Insights into the protein interactions with graphitic nanomaterials using computational modelling techniques

A Thesis submitted in fulfillment of the requirements for the degree of

Doctor of Philosophy

Adam J. Makarucha

B. App. Sci(Nanotechnology). & B. App. Sci(Physics).

School of Applied Science

College of Science, Engineering and Health

RMIT University

August 2015

Declaration of Candidature

I certify that except where due acknowledgement has been made, the work is that of the author alone; the work has not been submitted previously, in whole or in part, to qualify for any other academic award; the content of the thesis is the result of work which has been carried out since the official commencement date of the approved research program; any editorial work, paid or unpaid, carried out by a third party is acknowledged; and, ethics procedures and guidelines have been followed.

Adam J. Makarucha

August 2015

Acknowledgements

I would like to acknowledge all the support and advice that has made this candidature a possibility. First and foremost Prof. Irene Yarovsky for giving me the opportunity and support to work on such an important and interesting project. Her extensive knowledge and insight throughout the years has made this work possible and ever enjoyable.

I would also like to convey my deepest thanks to my other supervisor Dr. Nevena Todorova for her continued advice, encouragement and friendship throughout my candidature.

Thank you to my family, particularly my parents for their continued support, advice and guidance, it is always valued deeply.

Thank you to my friends for their patience and respect exceptionally through this final 8 months.

I would like to acknowledge Dr. Andrew Christofferson for always being available for a chat and some great advice. I have also been lucky to be a part of such a great, fun and professional research group, thanks for the Friday lunches and the banter.

This work has been funded by the Australian Research Council Discovery grant DP0984565. I acknowledge the generous allocation of high performance computational resources from the Australian National Computational Infrastructure (NCI) the Western Australian computational facility (iVEC), the Victorian Partnership for Advanced Computing (VPAC) and the Victorian Life Sciences Computational Initiative (VLSCI).

Finally but certainly not least to my partner Mahdi, who has supported me throughout this candidature. I thank you for your continued support, patience and when needed honesty. I could not have done this without you by my side, so I dedicated this thesis to you.

Publication List

- Adam J. Makarucha, Nevena Todorova, and Irene Yarovsky. "Nanomaterials in Biological Environment: A Review of Computer Modelling Studies." European Biophysics Journal 40 (2010): 103–15.

- Nevena Todorova, Adam J. Makarucha, Nicholas D. M. Hine, Arash A. Mostofi, and Irene Yarovsky. "Dimensionality of Carbon Nanomaterials Determines the Binding and Dynamics of Amyloidogenic Peptides: Multiscale Theoretical Simulations." PLoS Computational Biology 9, no. 12 (December 5, 2013): e1003360. doi:10.1371 journal.pcbi.1003360.

- Adam J. Makarucha, Nevena Todorova, and Irene Yarovsky. "Effects of Graphitic Nanomaterials on the Dissociation Pathway of Amyloidogenic Peptide Dimer." In 2014 International Conference on Nanoscience and Nanotechnology (ICONN), 31–34, 2014. doi:10.1109/ICONN.2014.6965254.

- Adam J. Makarucha, Nevena Todorova, and Irene Yarovsky. "To bind or not to bind: the effect of graphitic particles on amyloid fibril formation" *manuscript in preparation*

- Adam J. Makarucha, Nevena Todorova, and Irene Yarovsky. "The effect of graphitic nanomaterials on the full apoC-II fibril" *manuscript in preparation*

Contents

List of Figures

List of Tables

Abbreviations

AFM Atomic Force Microscopy

ApoC-II Apolipoprotein C-II

BE-META Bias Exchange Metadynamics

CC Coupled Cluster

CD Circular Dichroism

CI Configuration Interaction

CNT Carbon Nanotube

D5PC Dipentnoylphosphatidylcholine

DMD Discrete Molecular Dynamics

DNA Deoxyribonnucleic acid

FRET Fluorescence Resonance Energy Transfer

GROMACS GROningen MAchine for Chemical Simulation

HF Hartree Fock

MC Monte Carlo

MD Molecular Dynamics

MM Molecular Modelling

MP2/3/4 Moller-Plesset Perturbation Theory

MWCNT Multi-walled Carbon Nanotube

NMR Nuclear Magnetic Resonance

NPT Constant number of particles pressure and temperature

NVT Constant number of particles volume and temperature

ONETEP Order-N Electronic Total Energy Package

PBC Periodic boundary conditions

PDB Protein Data Bank

PME Particle Mesh Ewald

QD Quantum Dot

RDF Radial Distribution Function

REMD Replica Exchange Molecular Dynamics

REST Replica Exchange with Solute Tempering

RMSD Root Mean Square Displacement

RMSF Root Mean Square Fluctuation

SASA Solvent Accessible Surface Area

ThT Theoflavin T

VMD Visual Molecular Dynamics

WHAM Weighted Histogram Analysis Method

XRD X-ray Diffraction

Abstract

In this thesis computational modelling techniques were employed to investigate the behaviour of an amyloidogenic protein in the presence of dimensionally different carbonaceous nanomaterials. Experimental studies have demonstrated that nanoparticles can affect the rate of protein self-assembly, possibly interfering with the development of protein misfolding diseases such as Alzheimer's, Parkinson's and prion disease caused by aggregation and fibril formation of amyloid-prone proteins. An introduction into the aspects of protein folding and misfolding, and how nanomaterials can effect these processes is given in Chapter 1.

The computational techniques used in this thesis include large-scale density functional theory calculations and classical molecular dynamics simulations and their derivative methods such as umbrella sampling and replica exchange methods, these are described in Chapter 2. The behaviour, in solution and various fibril inhibiting and fibril favouring environments, of the amyloidogenic protein apolipoprotein C-II (ApoC-II) and its peptides derivatives are described in Chapter 3. Additionally the graphitic nanomaterials (carbon fullernes, single walled carbon nanotube and graphene) used throughout this thesis are also described in Chapter 3.

Initially the effect of the different carbon nanomaterials on the structure, dynamics and binding of the monomeric peptide apoC-II(60-70), all of which can influence its fibril formation capacity, were studied and compared to results obtained from previously characterised peptide behaviour in solution, in Chapter 4. A combination of computational methods, including large-scale electronic structure calculations and classical all-atom molecular dynamics was utilised. Additionally the simulations were conducted using a recently developed polarisable forcefield for graphitic nanomaterials and compared against the results

using the common non-polarisable forcefield to determine the effects of graphitic surface polarisation in solution on adsorption of biomolecules.

Understanding the effect nanomaterials may have on the early stages of fibril formation and in particular the small oligomeric species that drive the initial fibrillation behaviour is important in identifying how they can either inhibit or promote fibril growth. In Chapter 5, the adsorption and desorption mechanism of two preformed oligomeric composits of apoC-II(60-70) peptide (dimer and tetramer) were investigated. Initially the structure of water around the nanomaterial surface was examined, followed by a characterisation of the amphipathicity of the two oligomers. Subsequently the adsorption mechanism of the apoC-II(60-70) dimer and tetramer to each nanomaterial was conducted by utilising many short brute-force molecular dynamics simulations. The dynamic properties of the two oligomers while adsorbed to each nanomaterial were also investigated. Finally the free energy of dissociation of the apoC-II(60-70) dimer from each nanomaterial was calculated. The results were used to determine if there existed a favourable adsorption mechanism and if this could impact on the fibrillation ability of the oligomeric peptides.

It is often difficult to fully explore the conformational landscape of peptides and proteins especially while adsorbed to an interface, as a consequence many researchers have developed advanced sampling methods to overcome these sampling problems. In Chapter 6 the advanced sampling method known as replica exchange with solute tempering (REST) was applied to investigate the stability and interactions of the apoC-II(60-70) dimer and tetramer while adsorbed to the carbonaceous nanomaterials. Additionally the binding free energies of the apoC-II oligomers to each nanosurface was estimated. The results were used to rationalise how nanomaterial curvature, fibril seed size and peptide - nanomaterial binding energy impact the oligomers stability and thus fibrillation ability.

In Chapter 7 the aggregate dynamics and structure of the full length preformed apoC-II tetramer in the presence the different carbonaceous nanomaterials was explored. The conformational stability and structural dynamics of the apoC-II tetramer while adsorbed to each surface was examined along with an estimation of the binding free energy of the fibril seed to each nanomaterial. The results were compared to those obtained throughout the thesis of the peptide derivative apoC-II(60-70) and its oligomers in order to extrapolate the potential effect that these nanomaterials may have on influencing the fibril stability

of the full length apoC-II tetramer.

Chapter 8 summaries the overall findings of this thesis and how they may impact the wider research community.

To conclude, possible future research into the effect that other graphitic nanomaterials may have on fibrillation. Additionally another amyloidogenic peptide, amylin, is discussed as a future target for combating type II diabetes with nano therapeutics.

Chapter 1

Introduction

1.1 Overview

In this chapter, an overview of the structure, dynamics and (mis) folding of proteins is presented. A brief introduction on protein structure is presented in the first section 1.2. A short review of the current research into protein aggregation and amyloid fibril formation is presented in section 1.3. A literature review of the research efforts made to investigate the effect that nanomaterials have on biological systems including membranes, DNA and proteins is presented in section 1.4. The section has a focus on how nanomaterials can impact on protein aggregation and amyloid fibril formation, section 1.5.

1.2 Proteins

Proteins are a group of biological macromolecules that perform critical functions within living organisms. Functions of proteins include catalyzing chemical reactions important for many biological processes (enzymes), neutralizing foreign objects such as bacteria and viruses (antibodies) and for components of cartilage (collagen).

1.2.1 Protein structure

In its most basic form a protein is a strand of subunits known as amino acids or residues that are joined by peptide bonds. Amino acids are composed of a central carbon atom (α carbon) which is covalently bonded to a hydrogen atom (H), an amino group (NH_2), a

carboxyl group (COOH) and a side-chain R group. The amino group of an amino acid is referred to as the N-terminus and the carboxyl as the C-terminus, Figure 1.1.

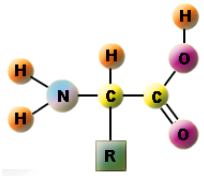

Figure 1.1: A schematic representation of the structure of amino acid, the amino group on the left, the carboxyl group on the right and the unqiue R-group sidechain bonded to the Cα atom.

There are 20 naturally occurring amino acids which are distinguished by the chemical nature of the unique R group side-chain. Amino acids with a strictly hydrophobic side-chain are Ala (A), Val (V), Leu (L), Ile (I), Phe (F), Pro (P), and Met (M). The charged amino acids are Asp (D), Glu (E), Lys (K), and Arg (R) and amino acids with polar side-chains, Ser (S), Thr (T), Cys (C), Asn (N), Gln (Q), His (H), Tyr (Y), and Trp (W). The Gly (G) amino acid is the simplest of the 20 amino acids having only a hydrogen atom as a side-chain making it unique and it is usually considered a member of the hydrophobic amino acids. Phe, Tyr and Trp all have an aromatic side-chain which is important in biological recognition and has the ability to form π - π interactions. These types of interactions are particularly strong non-specific interactions and important for binding to carbon based nanostructures (further discussion in section 1.3 and Chapter 3).

Proteins are synthesised through the formation of peptide bonds between amino acids. A condensation reaction between the carboxyl group of one amino acid and the amino group of another results in the formation of a peptide bond between amino acids and a free H_2O molecule, Figure 1.2. As the protein chain grows, the α-carbon atom and the carbon atoms that form the peptide bonds are referred to as the protein backbone. All amino acids with the exception of glycine can exist in two enantiomers which are mirror images of each other, called L or D amino acids. Amino acids almost always posses the L-configuration, while some D-amino acids exist in microorganisms, and can be found in cell walls of bacteria.

The unique sequence of amino acids that make up proteins is specified by the nucleotide sequence of DNA. Sets of three nucleotides called codons correspond to a specific amino

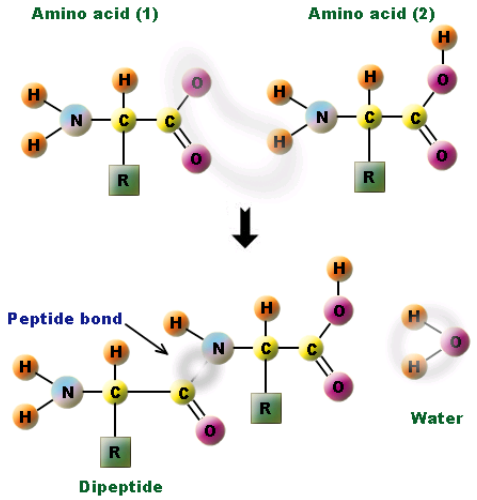

Figure 1.2: A schematic representation of the condensation reaction to form a peptide bond.

acid. The DNA sequence that relates to a specific protein is transcribed to messenger RNA (mRNA). mRNA binds to a ribosome which allows translation of the codons to occur and protein chain to be grown.

There are distinct the levels of protein structure are separated into four groups, Figure 1.3. The unique linear sequence of amino acids that make up a protein and dictates the final conformation is referred to as the primary structure. Highly regular local regions of structural motifs are referred to as secondary structure, such as α-helices and β-strands or β-sheets. The α-helix is a common structural protein motif, and is identifiable by its spiral-look. The α-helix is stabilised by the formation of parallel hydrogen bonds between the backbone atoms of consecutive amino acids in a protein. Another important secondary structure is the β-strand, which has the tendency to self-associate to form β-sheet structures, which are several β-strands bound together by hydrogen bonds between the backbone atoms. β-strands form pleated β-sheet with either parallel or anti-parallel orientations, Figure 1.4. The β-sheet structures have been associated with amyloid fibril formation, which is implicated in many degenerative diseases.

The overall 3D structure of a protein is referred to as the tertiary structure. The secondary structure motifs (α-helices and β-strands) are folded into a compact structure driven by non-specific hydrophobic interactions. These structural motifs are connected by turns and loop regions, enabling flexibilty in the protein, which is often related to its activity. Loop regions that connect two adjacent anti-parallel β-strands are called β-

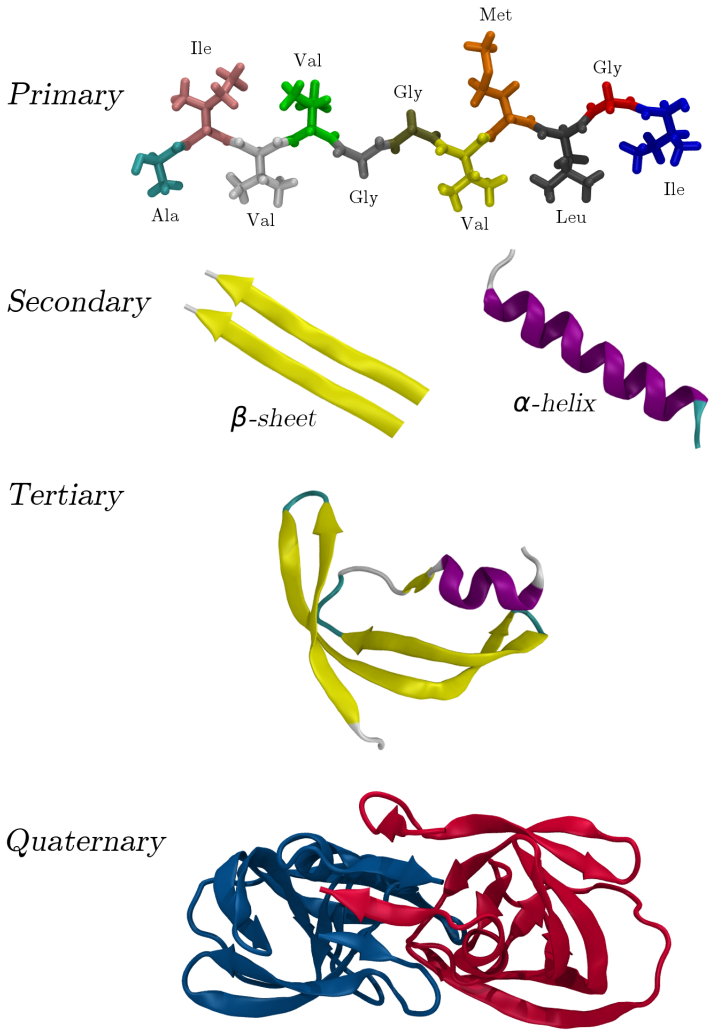

Figure 1.3: The amino acid sequence of a protein is called its primary structure. Local ordered regions of the protein strand are known as secondary structures, these include α-helices or β-sheets. The tertiary structure is formed by packing these secondary structural elements into a globular unit or domain. The quaternary structure is the final conformation with several globular units arranged in close proximity.

hairpins. Stable protein structures are maintained through specific interactions including salt-bridges, disulfide bonds and hydrogen bonding. The quaternary protein structure is the arrangement of multiple folded protein molecules in a multi-subunit complex, which is bonded together by the same specific interactions that stabilize protein tertiary structure.

The functional properties of proteins come from their native 3D structure, failure to fold into their functional form usually produces proteins with different properties that sometimes can be pathogenic, such as the human islet amyloid poly peptide (hIAPP), which when over expressed is implicated in the development of type-II diabetes. Several

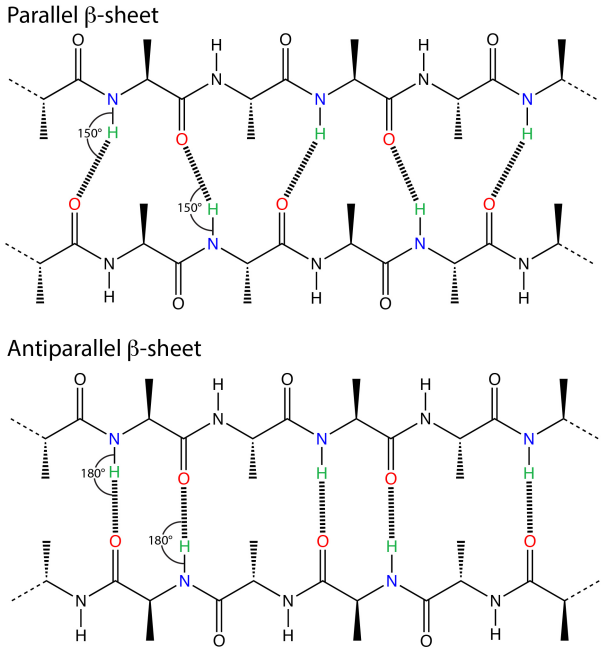

Figure 1.4: Schematic of the hydrogen bonding patterns represented by the dotted black lines in parallel and anti-parallel β-sheet.

neurodegenerative and other diseases are a result of the accumulation of misfolded proteins, these include Alzheimer's, Parkinson's and atherosclerosis.

1.2.2 Protein folding

The final 3D structure of a protein is dictated solely by its amino acid sequence, whereby a protein is able to fold *de novo* to its native functional conformation. This remarkable phenomenon has been the challenge in predicting protein structure ever since the first atomic resolution protein structure was determined by Kendrew and Perutz in 1960 [**Kendrew1960**]. The structure they identified was more complex and irregular than they expected, resulting in the realization that protein structure prediction was a more complex process than originally thought. A major milestone in protein science was the hypothesis of Christian Anfinsen and co-workers [1], who proposed that the native structure of a protein is the thermodynamically stable conformation, which depends only on the amino acid sequence and the conditions of the solution, not on the kinetic folding route. However random search of all possible conformations to reach the native state of a protein is unfeasible. An example of a 79 amino acid sized protein would have to potentially sample 3^{79} configurations before finding its native state, which could take years

to achieve. However, it is known that proteins fold within microseconds to seconds indicating that random searches are not an effective way to find the folded state of a protein [2], this is known as the Levinthal's paradox [3]. Computational and theoretical methods have been used to elucidate the mechanisms of protein folding at atomic detail. Recently the thermodynamically stable states of 12 small protein structures have been successfully reached using computational techniques [4]. However, successes like these are limited and the folding process of linear polypeptide strand into its 3D, biologically active conformation is poorly understood and the theoretical prediction of the folding pathway remains a challenge. Theoretical and computational methods that can be used to explore the conformational landscape of proteins and the interaction of proteins with nanomaterials are discussed in Chapter 2. A literature review of the current computational research investigating the interaction of amyloidogenic proteins with nanomaterials is discussed in Chapter 3.

1.3 Protein self-association and aggregation

While all the information needed for proteins to fold is encoded in their amino acid sequence, there are many more elements that play a part *in vivo*. In a crowded cellular environment, surrounded by interacting proteins, nascent polypeptides face a formidable challenge in finding the correct interactions that result in a folded functional protein. Many become trapped in meta-stable intermediate structures which are usually recognised by proteasomal machinery and degraded or refolded by chaperones. Alternatively, they can also misfold and self-associate leading to formation of either amorphous compounds or structures of elongated-unbranched morphology, known as amyloid fibrils. An accumulation of these fibrils can result in a range of human diseases commonly referred to as amyloidosis. Some of the diseases associated with amyloid fibrils are Alzheimer's, variant Creutzfeldt-Jakob disease, Parkinson's, type-II diabetes and many others.

1.3.1 Early history of amyloid diseases

The first use of the term "amyloid" was by Rudolf Virchow's paper from 1854 for the structural deposits discovered in human tissue [5]. Virchow identified cellulose like deposits in

cerebral corpora amylacea in the ependyma and choroid plexus of the brain, by using a water solution of iodine in combination with hydrated sulphuric acid, commonly used as a stain for cellulose [6]. Virchow and Meckel tested tissue samples, which exhibited what we call today systemic amyloidosis, and observed a similar reaction to iodine as had been observed with corpora amylacea [7], they determined these wax-like deposits had a degenerative affect on the spleen, liver and kidneys. Virchow concluded that these "amyloid" deposits present in the tissue samples were cellulose by nature. However, Friedreich and Kekulé conducted direct chemical analysis on amyloid-rich segments of a spleen from a patient with amyloidosis and found that the main substance of these deposits was in fact proteins [8]. The early staining method used, iodine staining, to identify amyloid deposits was replaced by metachromatic stains, an example of which is crystal violet. However it was Bennhold [9] who introduced the most important histological stain marker for amyloid, Congo red.

The strong affinity for amyloid deposits made Congo red a useful tool in diagnosing amyloidosis. Importantly, Divry and Florkin in 1927 made the discovery that amyloid deposits stained by Congo red resulted in enhanced birefringence (or double refraction) when examined using a cross polariser and light microscope [10]. It was suggested that this property of amyloid depends on an ordered arrangement of the elongated Congo red molecules in the amyloid, and that amyloid was not amorphous as earlier described, but has an organised structure [11]. The standardised Congo red staining method introduced by Puchtler et al. [12] is still in use today. Thioflavin T and S are two other common staining methods which are also frequently used.

The formation of extracellular amyloid fibrils or intracellular inclusions with amyloid characteristics has been implicated in many degenerative diseases, a list of these diseases is given in Table **??**. The proteins that are associated with each disease are listed, together with their chain length and known monomeric structure. The diseases can be categorised as follows, neurodegenerative conditions, in which aggregation occurs in the brain, non-neuropathic localized amyloidoses, where the aggregation occurs in a single tissue other than the brain, and finally nonneuropathic systemic amyloidosis, in which aggregation occurs in multiple tissues. The most well known amyloidogenic diseases are generally the neurodegenerative conditions which include Alzheimer's and Parkinson's diseases. Gen-

erally amyloidogenic conditions are sporadic (85%), however hereditary forms (10%) of some of these diseases have been documented. Spongiform encephalopathies can also be transmissible (5%) in humans as well as in other mammals, and has been reported to occur in mice injected with a type of prion protein [13].

Disease	Aggregating protein or peptide	Polypeptide length (number of residues)	Structure of protein or peptide
Neurodegenerative diseases			
Alzheimer's disease	Amyloid-β peptide	37-43	Intrinsically disordered
Spongiform encephalopathies	Prion protein or its fragments	230	Intrinsically disordered and α-helical
Parkinson's disease	α-synuclein	140	Intrinsically disordered
Amyotrophic lateral sclerisis	Superoxide disutase 1	153	β-sheet and lg-like
Huntington's disease	Huntingtin fragments	Variable	Mostly intrinsically disordered
Familial amyloidotic polyneuropathy	Transthyretin mutants	127	β-sheet
Non-neuropathic systemic amyloidosis			
Amyloid light chain (AL) amyloidosis	Immunoglobulin (lg) light chains or its fragments	90	β-sheet and lg-like
Amyloid A (AA) amyloidosis	Serum amyloid A1 protein fragments	76-104	α-helical and unknown fold
Senile systemic amyloidosis	Wild-type transthyretin	127	β-sheet
Haemodialysis-related amyloidosis	β_2-microglobulin	99	β-sheet and lg-like
Lysozyme amyloidosis	Lysozyme mutants	130	α-helical and β-sheet
Non-neuropathic systemic localized amyloidosis			
Apolipoprotein A1 (Apo A-1) amyloidosis	Apo A-1 fragments	80-93	Intrinsically disordered
Type II diabetes	Amylin	37	Intrinsically disordered
Injection-localized amyloidosis	Insulin	21 and 30	α-helical and insulin-like

Table 1.1: A selection of diseases associated with extracellular amyloid deposits or intracellular inclusions with amyloid-like characteristics. For a more comprehensive list of the approximately 50 human protein misfolding diseases and their associated proteins see [14]. The figure was reproduced from the detailed review presented by Knowles et al. [15]

1.3.2 Structure of amyloid fibrils

In 1959, Cohen and Cakins undertook electron microscopy studies to determine the possibility of amyloid having an ordered submicroscopic structure, as indicated by the birefringence associated with amyloid deposits stained with Congo red. Their study found that the amyloid, which is glassy(hyalin) and structureless under light microscopy, in fact has a characteristic fibrillar ultrastructure when analysed using an electron microscope [16]. Their findings were confirmed in several other studies [17, 18, 19, 20, 21] which gave further insight into the specific structural organisation of amyloid fibrils. These studies

revealed that, even though the proteins from which the amyloid fibrils developed were different, the final morphology of the fibrils was very similar, consisting of a cross-β structure with the β-strands perpendicular to the fibril axis, Figure 1.5. Overall amyloid fibrils tend to appear as unbranched filamentous structures only a few nanometers in diameter but often micrometres in length, when examined using electron microscopy or atomic force microscopy. These fibrils are typically observed to consist of multiple protofilaments that twist around each other to form mature fibrils. Significant progress has been made in determining the molecular structures of amyloid fibrils in atomic detail using experimental techniques [22, 23, 24, 25]. Advances in experimental solid state nuclear magnetic resonance (SSNMR) techniques have enabled the elucidation of the fibril architecture of amyloidogenic peptides, including Aβ1-40, Aβ1-42, the prion fibril, hIAPP20-27 fibril and $\beta_2$microglobulin.

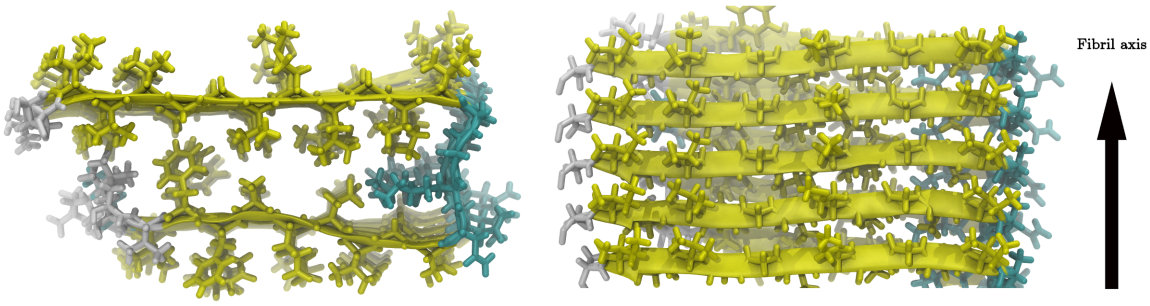

Figure 1.5: Experimentally determined crystal structures of Aβ 1-42

Mechanisms of fibril formation

Protein fibrillation is a complex process, which involves kinetic competition between the formation of amorphous aggregates and fibrillar species, including a variety of intermediates, multiple conformational states, and a number of filamentous forms [26, 27, 28]. A schematic diagram representing the various conformational states a protein can adopt during folding, misfolding and aggregation is presented in Figure 1.6.

Aggregation of amyloid fibrils is a cooperative process that in general adheres to a "nucleation-dependent polymerization" model involving two phases: a lag phase and an elongation phase, Figure 1.6 [29, 30, 31, 32]. Within the lag phase the protein undergoes a number of transitions including from monomeric structures to the formation of partially

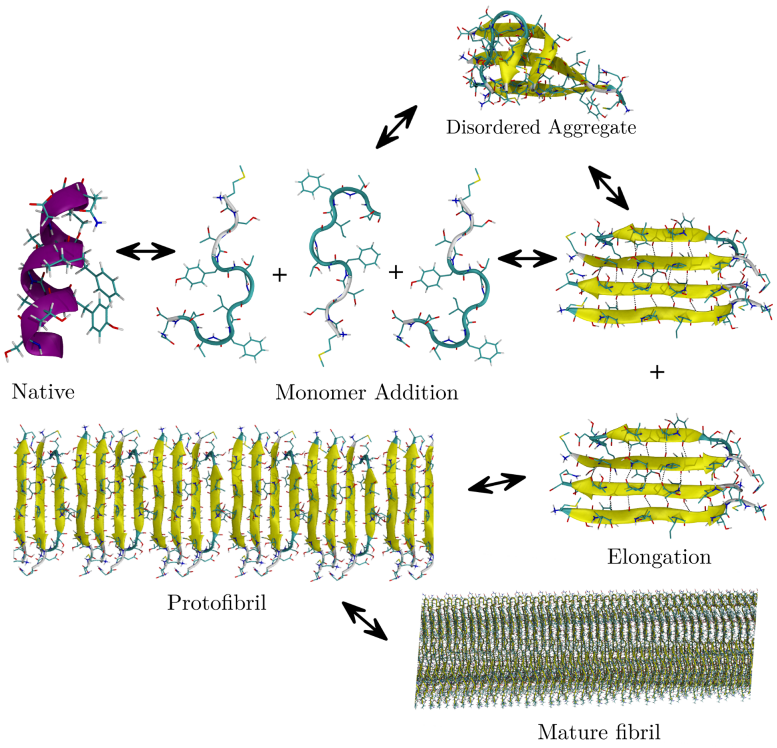

Figure 1.6: A schematic representing possible changes that polypeptides can experience when transitioning from a native state to mature amyloid fibril.

folded intermediates and nucleation which is subsequently followed by rapid fibril growth, the elongation phase. The time course of this conversion of a peptide or protein into its fibrillar form can be experimentally measured by ThT fluorescence or light scattering [14]. The lag phase is assumed to be the time required for nuclei to form. Once a nucleus is formed, fibril growth is thought to proceed rapidly by further association of either monomers or oligomers with the nucleus. Similarly to other processes that involve a nuclation step, such as crystallisation, the addition of a preformed nucleus or fibrillar species, known as a template, to a sample of protein under aggregation conditions causes the lag phase to be shortened and ultimately abolished [33]. At this stage the rate of the aggregation process is no longer limited by the need for nucleation [31]. All the models proposed so far for fibril formation involve significant conformation changes during the fibrillation process.

1.3.3 Oligomer formation and fibril growth

The growth of amyloid-like fibrils is inherently complex and involves many growth processes including monomer activation, primary nucleation, secondary growth processes, elongation by monomer addition and many more. It is impossible to obtain an all-encompassing analytical solution for such an elaborate growth scheme. As a consequence several kinetic models exist to explain the process of fibril formation and growth. These include primary nucleation-dependant models, that explain the initial nucleation process, the secondary growth processes, that explain the secondary *de novo* filament creation processes and finally the elongation phase.

Several primary nucleation-dependant models have been proposed including monomer addition, coagulation and 'lock and dock' mechanisms. Monomer addition refers to the process of nucleation by the addition of a single monomer species to the nucleus. This is thought to be a common process in the formation of amyloid fibrils. Coagulation is the end to end joining of two oligomers and has been observed experimentally [34, 35, 36]. In systems were the initial elongation is dominated by monomer addition it is possible for coagulation to become important in later processes. Finally the 'lock and dock' mechanism has been proposed in several studies [37, 38, 39], suggesting that the association of monomers to the amyloid fibril occurs by multi-step kinetics, based on the elongation of the fibril by a dock-lock mechanism [38, 40]. In this model, an initial reversible weak "docking" interaction is required to enable subsequent "locking" interactions to occur between the formed oligomer or fibril and the deposited monomer. The "locking" event is the rate limiting step in this kinetic model of fibril formation.

Primary nucleation processes are typically needed for the initial nucleation of oligomer structures however it is not the only pathway for new oligomer formation. Secondary growth processes are those in which creation of new oligomer species is dependent upon the existing oligomer population. If a secondary process is active then the rate of aggregation will accelerate and the aggregation population will increase exponentially. Secondary nucleation and branching can occur on the lateral surface of existing oligomers, whereby monomer additional to this surface results in the growth of an addition nucleus. This nucleus can remain attached or detach and diffuse into the solution [41]. Furthmore

branching has been observed on sickle haemoglobin [42], Aβ [43] and glucagon [41]. Another secondary growth process is the process of the oligomer breaking resulting in the creation of new ends for fibril growth, this process is known as fragmentation. Agitation and sonification of amyloidogenic species in solution has been shown to accelerate fibril growth as a result of increased oligomer ends produced by fragmentation [44, 45].

Understanding the mechanisms of fibril formation from the initial monomeric state is important because it is becoming increasingly evident that the nonfibrilllar intermediates may in fact be the toxic species in amyloid related diseases. This has been shown for amyloid-β and human Islet amyloid polypeptide [46, 47, 48, 27, 49, 50]. In particular, determination of the thermodynamics and kinetics of all the conformational changes that link these different species are of great importance. The characterisation of each transition in molecular detail and the identification of the residues and regions of sequence that promote fibrillation are crucial for the development of therapeutic methods. Recently research has begun to focus on how novel materials such as nanomaterials can effect the amyloid fibril formation process. The potential for these new materials to act as therapeutics to combat amyloid disease is great, however long term effects of nanomaterial deposits on biological systems is largely unknown and needs to be further explored.

1.4 Nanomaterials in biological environments

Nanotechnology is impacting numerous areas of development in science and technology, specifically with applications in materials science, medicine, bioimaging, sensing and electronics [51, 52, 53, 54]. Some of the more specific applications of nanotechnology in medicine include the use of nanoparticles for drug delivery [52, 55], biological labels and imaging [56]. While the most immediate near term benefits expected from the use of nanotechnology arise from the novel properties of nanomaterials due to their unique volume/surface ratios, and the ability to prepare and control their properties with greater precision and complexity, there is apprehension that nanoparticles used for medical applications may in fact induce cytotoxic effects, as has already been shown in eukaryotic and prokaryotic cells [57, 58, 59]. Moreover engineered nanoparticles, which are expected to be used increasingly in industry and the manufacture of household goods, can also interact

with biological molecules and have a potential to damage cells *in vivo* [60]. Modification of nanoparticles through functionalisation can allow a greater degree of control to target specific interactions, which can permit their use in a broader range of applications, from environmental [61], industrial [62] to biomedical uses [63, 56].

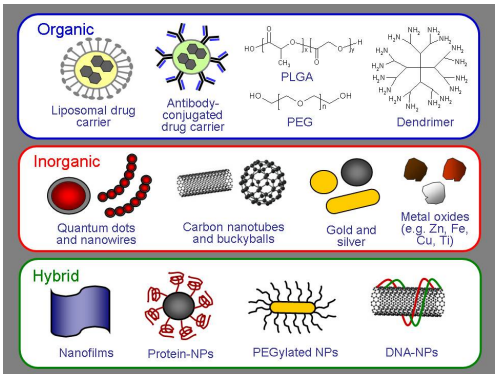

Figure 1.7: Most engineered nanomaterials in current use belong to three broad classes. Adapted from [64].

Generally nanoparticles can be considered to exist in one of three broad categories [64]: organic, inorganic and hybrid particles Figure 1.7. The organic particles are those created by simple monomeric building blocks, such as polymer based nanoparticles. The second and perhaps most well represented group is that of inorganic nanomaterials, these include carbon nanotubes, fullerene particles, metallic nanoparticles, including gold and silver nanoparticles, and many metal oxide species. Hybrid nanoparticles are the third group of engineered nanoparticles, consisting of a combination of organic and inorganic nanomaterials, such as peptide functionalised gold nanoparticles [65] and DNA-carbon nanotube arrays and include the nanoparticles intended for use as delivery vehicles illustrated in Figure 1.8 for membrane active peptides such as antimicrobial peptides [66] and references therein).

Nanomaterials are of the same size scale as typical cellular components (Figure 1.9) and thus offer an entirely unique point from which to view and manipulate fundamental biological pathways and processes. At the same time the size commensurability enables interatomic interactions between nanoparticles and biological molecules and has therefore a significant potential to interfere with biological function.

Currently the relationship between size, shape and surface chemistry of nanostructures and their correlation with intracellular and *in vivo* bio-distribution remains ambiguous [67]

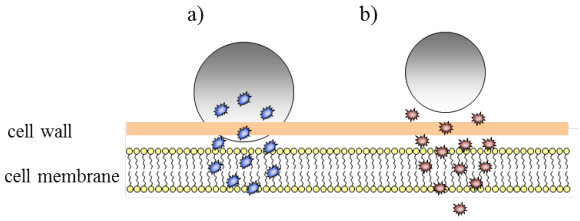

Figure 1.8: Nanoparticles used as carriers of membrane-active peptides in drug delivery: a Carried antimicrobial drugs are released across a cell membrane after nanoparticles fuse with the cell wall; b Drug molecules can diffuse into the interior of the microorganisms by crossing the cell membrane once the nanoparticles bind to the cell wall

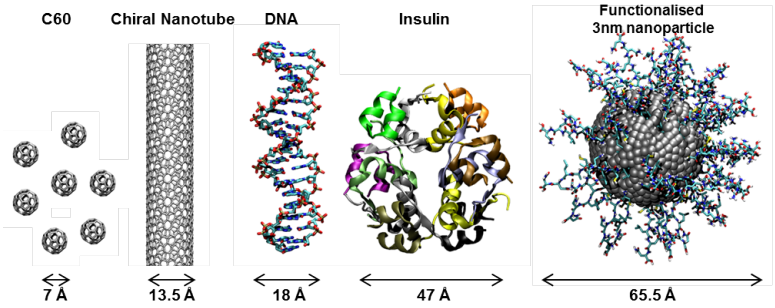

Figure 1.9: Size comparison of some common nanoparticles and biological molecules

as is our understanding of the interactions between nanomaterials and biological matter [68]. At the same time it has been demonstrated that nanoparticles could cross the lung, blood and brain barrier and enter the cardiovascular circulation thereby reaching many organs [69]. Various studies have shown airborne combustion generated carbon nanoparticles (<100 nm) are associated with increased pulmonary and cardiovascular mortality [70] alerting to a potential harm of both intentional (medicinal) and unintentional exposure to carbon nanotubes, fullerenes and their derivatives [71]. It is believed that cytotoxic nanoparticle effects emerge in a dose- and time-dependant manner for carbon, metal and semiconductor based nanoparticles [69] and the oxidative stress is the best developed paradigm to explain the toxic effects of inhaled nanoparticles [72]. It has also been shown that nanoparticles can nucleate protein fibrillation [73] and possibly contribute to the development of protein unfolding diseases such as Alzheimer's, Creutzfeld-Jacob disease, and dialysis-related amyloidosis [73]. In summary, the mechanisms of the interatomic interactions between the nanoparticles and biological molecules are not sufficiently understood. While little is known about possible effects of nanoparticles on molecular structure and function of biological molecules, specifically proteins, DNA and biological membranes,

numerous nanomaterials are enjoying a rapid growth in a number of applications, from industrial to medicinal. It has become apparent that health and safety aspects associated with the spread of nanomaterials need serious scientific scrutiny so that possible cytotoxic effects can be identified and prevented. Physicochemical mechanisms that nanoparticles undergo to affect biological molecules and complex systems are currently under investigation by experimental and theoretical methods. However current experimental techniques are limited [74] in their ability to study nanoparticle interactions with biological environments at the nanoscale. At the same time, the spatial and temporal resolutions that computational techniques currently allow [75] enable the investigation of specific interactions and dynamics that nanoparticles induce in biological molecules. This has led to an increasing use of computational methods to elucidate the fundamental aspects of intermolecular interactions within nanoparticle-biomaterial systems. Current computational techniques include electronic structure methods [76, 77], all-atom Monte Carlo [78] and molecular dynamics [79] methods and coarse grained methods [80] which have all been used to gain a better understanding of the interactions and dynamics of nanoparticles within biological systems. First-principles electronic structure techniques, such as density functional theory, compute the total energy and electron density of molecules using quantum mechanical techniques [77]. These methods can be used to accurately calculate a wide range of fundamental properties of various complexes, such as the chemical and electronic structure of a system. However these techniques are very computationally demanding, mostly limited by the systems size (few hundred atoms) and simulation time scales on the order of several picoseconds. The most widely applied computational techniques are the classical methods, which enable the exploration of the structural evolution and structure-activity relationships in biological systems with atomistic resolution. The all-atom molecular dynamics simulation method is based on Newton's laws of motion, whereby solving the differential equations embodied in Newton's second law it is possible to obtain a trajectory that describes the atomic positions, as they progress over time. All-atom simulations rely on the fundamental forces that govern the atomic motions, these are derived from pair-wise interatomic interaction potentials and are usually mathematically defined and empirically parameterised in the form of a forcefield. These forcefields describe bond stretching, bending, and rotation as well as the non-bonded interactions,

including electrostatic and van der Waals interactions [77]. The choice of a forcefield for each simulated system is important, as forcefields are developed with a specific environment/application in mind, and it will ultimately determine the quality of the results [81]. Using the molecular dynamics method it is currently feasible to investigate systems in solution with explicit representation of up to millions of atoms [75, 82] over nanoseconds-microseconds time scales. An advantage of this method is the ability to determine the structure and dynamics of complex systems at an atomic detail. However, some biological processes occur over longer periods of time and/or require modelling of larger systems, thus more simplistic techniques, such as the coarse grained methods need to be applied. Coarse grained methods are receiving significant focus at the moment due to their ability to simulate large complexes, such as protein-membranes systems [83, 84, 85]. In these models a small group of atoms is treated as a single interaction unit, where the interaction is governed by a simplistic forcefield [86] and then molecular dynamics is applied as in all-atom methods. As a result larger systems and simulation times are possible, however at the expense of accuracy. Recently there has been an increasing number of computational studies investigating the structure and dynamics of nanoparticles and their interactions with aqueous media [87, 88] and biomolecules including nucleotides and nucleic acids [89, 90, 91, 92], peptides and proteins [93, 94, 87, 95], and cell membranes [83, 96, 97, 98]. However, computer simulations in this field are still at an early stage. Here we present a review of recent computational studies investigating effects of nanostructured materials on biological environments and discuss their successes and limitations.

1.4.1 Effects of nanomaterials on the structure and dynamics of water

First, it is fundamental to understand how nanostructured materials interact with water molecules since biosystems function in a solvent environment, thus the interactions they have with the solvent, water, are crucial to how they behave. Therefore the way in which nanoparticles change the structure of the solvent can determine how they affect the surrounding biological molecules. It has been shown using coarse grained molecular dynamics that the size and thus curvature is crucial in determining the hydrophobic or hydrophilic character of the nanoparticle. This has implications for self assembly and aggregation of hydrated nanoparticles and colloidal particles [87]. Water mediated interactions be-

tween carbon nanoparticles have shown a similar dependency on surface curvature of the nanoparticle. A molecular dynamics study by Li et al. demonstrated that there was a high surface–water dispersion interaction due to the high density of surface atoms [99]. Another work investigating water molecules surrounding gold nanoparticles using molecular dynamics techniques found the formation of two hydration shells, where the first shell arranged regularly on small nanoparticles (0.8 nm-1.3 nm diameter) and irregularly on larger nanoparticles (>1.3 nm diameter). It was also shown that on the 0.8 nm gold nanoparticle the first hydration shell arranged in a bulk like water structure [74]. Comparably water has been found to form two hydration shells around fullerene (C60) nanoparticles indicating that the fullerene behaves as a large hydrophobic solute [100]. Furthermore, Yiapanis et al. [101] investigated the effects that surface modifications may have on the adhesion between polyester and amorphous carbon using molecular dynamics techniques. Accentuated roughness caused by the protruding modification groups, hydroxyl, carboxyl and fluorine, reduces the adhesion with the carbon surface. Whereas reorganization of the modifiers to energetically favourable regions results in a reduction in repulsive interactions and in some cases an increase in attractive interfacial interactions. This reorganization is dependant on structural topography of the carbon surface as well as the chemical type and concentrations of the modifiers on the polymer surface [101]. These studies offer a possible explanation for the hydrophobic nature of many nanoparticles where the curvature of the particle plays a crucial role in the degree of hydrophobicity. A recent molecular dynamics (MD) study revealed that when a surface has domains similar in size to solvent molecules the interfacial energy shows non-monotonic trends. Kuna et al. demonstrated that the solvent behaviour at the interface is controlled by the nanostructured surface, leading to possible implication in biological processes [88].

1.4.2 Effects of nanostructured materials on biological membranes

Detailed understanding of the effects of nanoparticles on biological membranes is crucial for the advancement of nanoparticles as drug delivery systems and reduction of possible cytotoxic effects [102]. Many theoretical studies have been conducted on the interactions of cell membranes and several types of nanoparticles including fullerenes [83, 96, 97, 98, 103], carbon nanotubes [84, 85] and gold nanoparticles [104]. Functionalised nanopar-

ticles have been used to select only particular cellular membranes so that only specific cells are labelled, as well as improve the uptake of the labeled nanoparticle [105]. These functionalised nanoparticles have used DNA [106] and peptides [107, 108] as receptors for particular cells and in some cases to assist with uptake of encapsulated drugs [109]. Carbon based nanoparticles, such as buckyballs and nanotubes have shown great potential for application in biomedicine due to their potential ability to permeate a lipid bilayer [110]. An excellent recent review has been published on the use of both classical molecular dynamics and coarse grained techniques on carbon nanoparticles-membrane systems [109]. It covers simulations of C60 fullerene nanoparticles and carbon nanotubes translocating across lipid bilayers. It was found that translocation of fullerene particles into a membrane is energetically favourable [83, 97] and that these particles tend to sit off the bilayer centre [96]. Functionalised derivatives of C60 were shown to prohibit translocation of the nanoparticle across the membrane layer, suggesting a method to control transport across a bilayer [98, 111], while incorporation of charged nanoparticles resulted in membrane breakage [112] due to the formation of micelle structures. Simulation studies have identified that carbon nanotubes enter a cell membrane either by wrapping into the membrane or by directly piercing through the membrane. A critical nanotube radius exists for the transition between the two modes of entry [84]. Furthermore lipids in the bilayer can block the nanotube upon piercing the membrane [85]. It was suggested that the cylindrical micelle of lipids surrounding the carbon nanotube may be used to solubilise carbon nanotubes [113]. Surfactant adsorption onto a carbon nanotube was found to be dependent on detergent concentration, while at low concentrations chirality of the carbon nanotube influences the wrapping angle and at higher concentrations the detergent molecule rotates away from the nanotube [114]. Molecular dynamics simulations have also been used to demonstrate that structure and packing of the lipids and peptides in pulmonary surfactant film can be affected by the nanoparticles $C_{188}H_{53}$ [115]. In addition, recent publications include simulation studies of charged nanoparticles with membrane systems aiming to understand how electrostatics can affect the adsorption and translocation of nanoparticles across a membrane. Using coarse grained simulations of hydrophobic and semihydrophilic nanoparticles in the presence of a cell membrane Li et al. found that a hydrophobic nanoparticle can result in the inclusion into the bilayer, whereas a semihydrophilic nanoparticle only adsorbs onto the

membrane. These results indicated that, the surface hydrophobicity can result in different response mechanisms in nanoparticle-biomembrane interactions [116]. Studies of charged nanoparticles on electro neutral phospholipid bilayers [117, 118], using coarse grained MD revealed, that electrostatic attraction improves the adhesion of a charged nanoparticle to the membrane, where the increase of electrostatic energy resulted in almost full wrapping of the charged nanoparticle by the membrane [117]. Furthermore, a study by Sachs et al. has found that large chaotropic anions penetrate deeply into the interfacial region of lipid bilyers [118]. Using molecular dynamics simulations it was shown that anion size alone can lead to such behaviour, where the larger anions are more hydrophobic and hence prefer the bilayer interior, thus accounting for the penetration into the membrane layer. Membrane swelling was found to occur in the presence of uncharged or hydrophobically modified nanoparticles. Another Monte Carlo investigation of the domain size of monolayers and the diffusion of nanoparticles demonstrated that dipole-dipole interactions could be fundamental in the control of membrane transport [119]. Dissipative particle dynamics (DPD) found that shape anisotropy and initial orientation of a nanoparticle can play a complicated role in the physical translocation of the particle across a lipid membrane [120]. It was further found that the volume of nanoparticles had little direct influence on translocation. This suggested that altering the geometry of particles could result in new applications of nanoparticles interacting with membranes [120]. Janus nanoparticles consisting of both hydrophobic and hydrophilic portions have been used to form a stable pore in a membrane system using DPD techniques [121]. It was found that once a stable pore was formed, small increases in membrane tension readily reopened the pore, thus allowing transport through the membrane. Additionally, the DPD investigation showed that the membrane tension could also be altered by changing the temperature or pH [121]. Gold nanoparticles have been found to repel, adhere to or penetrate lipid bilayers depending on the density and sign of the surface charge of the nanoparticle [122]. This coarse grained simulation study found gold nanoparticles readily adhere to and penetrate the bilayer, with a hydrophilic pore forming upon penetration of the lipid bilayer. Higher surface charge density was shown to increase membrane disruption whereas lower surface charge density resulted in increased penetration of the gold nanoparticles. Thus surface charge density was identified as a possible property that could be controlled to promote gold nanoparticle

cellular uptake while minimizing toxic effects. Recent coarse grained molecular dynamics simulations by Titov et al.[123] have shown that phospholipid molecules could isolate an embedded graphene layer. It was found that a micelle formed around a graphene sheet could self-insert into a lipid bilayer and remain stable in the interior of the membrane at room temperature. Furthermore stabilisation of composite graphene systems inside a lipid membrane was also suggested to be possible. This study has most relevance to in vitro phospholipid membranes, were graphene embedded membranes could have applications in biosensing and bioelectronic nanomaterials.

Classical molecular dynamics simulations have revealed that the interactions between single walled nanotubes and free dipalmitoylphosphatidylcholine (DPPC) lipids are concentration dependant [124]. At low concentrations of DPPC, the lipid molecules form a supramolecular two-layer cylindrical structure wrapped around the nanotube surface, whereas at higher concentrations the DPPC molecules form multilayered supramolecular structures. Hydrophobic tails of DPPC interact with the nanotube, with hydrogen bonding between the head groups of DPPC mediate self-organization of lipids. Overall, it was found that a membrane-like structure developed on the nanotube is typical of DPPC membrane [124].

1.4.3 Effects of nanomaterials on DNA structure

DNA molecules contain the genetic instructions used in the development and functioning of all known living organisms and are a fundamental component of life, thus it is important we have indepth understanding of the effects of various nanoparticles on the DNA structure/function. More recently, increasing studies are considering DNA molecules as a potential avenue for nanoparticle functionalisation. Investigation of nucleotides in the presence of carbon based nanoparticles such as nanotubes and buckyballs have been extensive as these nanoparticles are considered ideal for targeted drug delivery [110, 125]. This possible application has resulted in many simulation studies considering the translocation of DNA through carbon nanotubes. Gao et al. suggested that van der Waals and hydrophobic forces were the most important interactions in the insertion process of DNA into a carbon nanotube, with the former dominating the interaction between the DNA and carbon nanotube [90]. Several studies have investigated the effects of external fields on the

translocation of oligonucleotides through a carbon nanotube. These molecular dynamics simulation studies have shown that gravitational [79] and electric fields [126] can promote translocation through the carbon tube. It was concluded that translocation is tube size dependant and that critical field strength existed for which no translocation occurred [126]. Furthermore an energy barrier was found for an oligonucleotide passing from a nanotube of chirality ,14,14 into a nanotube of chirality 10,10, suggesting that translocation of DNA within a carbon nanotube channel is quite different from that of DNA translocation from the outside into a carbon nanotube [79].

Initial investigations into the effects of nanoparticles on DNA structure and function have also been conducted. For example, Johnson et al. 2008 investigated DNA-carbon nanotube hybrids using MD techniques, to study the self-assembly mechanisms, structure and energetic properties of these nano-complexes [91]. The single walled carbon nanotubes induce the single stranded DNA bases to undergo a spontaneous conformational change that enabled the hybrid to self-assemble via π-π stacking interactions between the DNA bases and carbon nanotube walls. Spontaneous wrapping about the carbon nanotube was also observed with the wrapping driven by electrostatic and torsional interactions within the sugar-phosphate backbone [91].

Replica Exchange Molecular Dynamics (REMD) method was applied to determine the free-energy landscape of a DNA-Carbon nanotube hybrid [127]. The global minimum was found to be a nonhelical loop structure of the single stranded DNA. Base adsorption is limited to steric effects, however upon adsorption nucleotides display considerable conformational disorder [127]. Similar work was conducted by Martin et al. with some discrepancies in the simulated structures, which suggested to be due to the differences in computational set up of the REMD method. This finding highlights the importance of proper conformational sampling [128]. Research has also focused on C60 buckyballs in the presence of single and double stranded DNA molecules [89]. The results of this MD study have demonstrated high binding energies between the fullerene and nucleotides which have been attributed to the hydrophobic forces present that dominate the interactions between the molecules [89]. In this study C60 was shown to be able to penetrate the double helix of double-stranded DNA to form stable hybrids which frustrated the hydrogen bonds between end-group basepairs of the DNA molecule [89]. Thus cytotoxic

effects could be induced if DNA replication is impacted by the stable complexes formed between the nanoparticles and DNA molecules. Molecular dynamics simulations and ab initio calculations have been used to investigate DNA-carbon nanotube arrays and to find the electronic structure of the combined system [92]. This study revealed that the array of carbon nanotubes arranged to fit into the major groove of the DNA is semiconducting and that the bands on either end of the gap are derived exclusively from either the DNA or nanotubes. This work has implications and possible applications in devices using electron switching and possibly for ultrafast DNA sequencing [92]. Functionalised nanoparticles have many applications, including in drug discovery [129], biosensing [130] and sequencing [129]. Thus research has been conducted on the effect of DNA functionalisation on a flat gold surface [131] and a gold nanoparticle [131] using MD simulations. It was found that both base stacking and non-Watson-Crick hydrogen bond formation are involved in the interactions between DNA strands on the gold surface, whereas no significant hydrogen bonding occurs on the gold nanoparticle surface. It was found that on both surfaces an increase in sodium concentration occurs, which is consistent with an observed increase in melting temperature of DNA [131, 131].

1.4.4 Effects of nanomaterials on the structure and dynamics of proteins

The study of protein interactions with various surfaces can serve as a precursor to understanding behaviour of proteins in the proximity of nanomaterials. Proteins have been studied in the presence of a vast array of surfaces. Studies of graphite, silicon and mica surfaces have all been used to gain an understanding of the interactions that can occur between hydrophobic/hydrophilic, neutral/charged surfaces and biological systems. Early work by Yarovsky et al. used all-atom MD and Monte Carlo simulations to reveal detail of peptide interactions with n-alkyl modified silica (SiO_2) surface used as reverse phase support on high performance liquid chromatography columns[132]. Recently [133] performed molecular dynamics studies of hen egg white lysozyme (HEWL) adsorption on negatively charged, hydrophilic, SiO2 surface (mimicking a mica surface). Their simulations showed that conformational alterations are required for HEWL adsorption, and that upon adsorption the protein loses some alpha-helical content. The main force governing adsorption is believed to be the electrostatic attraction between parts of the protein and the surface.

Further studies involving HEWL adsorption to mica surfaces have shown that lysozyme clusters diffuse across the substrate at a rate that varies inversely with size, suggesting that the molecular scale mechanisms are responsible for the mobility of the proteins on the substrate [134]. Monte Carlo simulations were applied to investigate lysozyme adsorption to charged surfaces at different protein concentrations, protein net charges, ionic strengths, and surface charge densities [78]. Although, the method used was quite simplistic (protein represented as hard-sphere, and charged surface described by a hard wall), the results compared favourably with experimental findings. The protein adsorption was favoured by high protein concentration, high protein net charge, low ionic strength, and high surface charge density. Interestingly, adsorption appeared possible for a weakly negatively charged protein to the negatively charged surface as a result of an electrostatically favourable protein reorientation at the surface [78]. Graphene surfaces have also been studied extensively because of its many uses in ultra fast and ultra low noise biological sensors [135, 136, 130]. Human insulin was used as a protein model in an MD study to investigate the conformational changes in the presence of free and fixed graphene surfaces [137]. The alpha-helices of insulin had selective protection from the free graphene surface as a consequence of the flexibility of the graphene surface, which resulted in a higher stability of the protein. This selective protection could improve the stability of proteins on the biosensors or biomaterials it is designed for. However it was shown that the tertiary structure of the protein was partially destroyed when adsorbed to the graphene surface [137]. Similarly further MD studies of graphene have revealed that the initial adsorption of fibronectin type I module can result in local rearrangements of the strands that were in contact with the surface. However it was found that the overall molecular structure did not change in the initial stages of adsorption. As the simulation progressed, the molecule spread along the graphene surface to maximise the surface coverage, and thus interaction energy [138]. These studies have shown that hydrophobic surfaces can induce tertiary and in some cases secondary structure loss by proteins adsorbed to these surfaces. It has been suggested that the rearrangement of protein on surfaces is dependent on the hydrophobicity, crystallinity, and smoothness of the surface. MD simulations using both classical and course grained approaches have been conducted by Hung et al. to study the effects of surface hydrophobicity and nanostructuring on protein absorption [139]. Hung et al.

modelled monolayer-protected gold nanoparticles (MPMNs), a newly-discovered class of nanoparticles whose surface is composed of well-ordered, parallel alternating stripes which circumscribe the metal core [140]. Their surface structures can be readily manipulated by altering the relative composition of the self-assembled hydrophobic (octanethiol, OT) and hydrophilic (mercaptohexanol, MH) ligands, rendering them uniquely suited to systematic studies of the role of surface nanometre structure in biomolecular adsorption [88]. Interactions of Cytochrome C with MPMN surfaces were studied using experimental protein assays and molecular dynamics simulations. Experimental microBCA assays revealed that Cyt C exhibited increased adsorption with increasing %MH, suggesting that Cyt C - surface interactions are largely hydrophilic. Protein-surface adsorption enthalpies calculated from simulations indicate increased adsorption with respect to %MH in agreement with experiments. Simulations identified energetically-favourable protein binding orientations on MPMNs and the major contributing residues. The strength of Cyt C binding to mixed-ligand surfaces directly related to the number of contacts between protein and surface; the intimacy and specificity of these contacts; the extent of registry between polar and non-polar regions of the protein binding site and the corresponding surface nanostructures. Simulations identified that the amphipathic nature of the lysine side-chain enables it to form simultaneous persistent contacts with both OT and MH at boundaries of phase-separated nanodomains.

Overall, with an understanding of how the nanostructuring of surfaces influences protein dynamics, control of their bound states can be achieved. This may give rise to an array of newly tailored materials/surface coatings for use as biosensors, hybrid materials, nanotechnology, and biocompatible surfaces. Further research has also been conducted in an attempt to elucidate possible nano-toxic effects by the investigation of the effects of various nanostructures and nanoparticles on the peptide and proteins structure and dynamics. Aggregation of peptides and proteins is a common precursor to some neurological diseases and as such investigations of the possible link between nanoparticles and aggregation are underway. One such study has been conducted using discontinuous molecular dynamics (DMD) on a nanoparticle-catalysed peptide to determine how nanoparticles may facilitate the peptides aggregation [141]. DMD is a technique used as a faster and computationally simpler alternative to standard molecular dynamics. DMD systems evolve on a collision

by collision basis, and require the calculation of the collision dynamics and the search for the next collision. Auer et al. used a modified version of the tube model, where residues are represented by their Calpha atoms connected into a chain with a distance of 3.8±0.2 Å between neighbouring atoms [141]. It was suggested by Auer and co-workers that the process of aggregation can be sped up by the presence of factors capable of increasing the local concentration of proteins, such as high surface area nanoparticles, thus promoting further formation of disordered oligomers.

Similarly, the MD study by Noon et al. showed significant hydrophobic interactions at the binding site of an antibody with a desolvated fullerene particle [93]. These interactions included extensive pi-stacking of the aromatic side chains with the carbon rings of the fullerene particle, suggesting that pi-stackings are very efficient and common modes of biological recognition of pi-electron rich carbon nanoparticles. Furthermore, the results demonstrated that, an ordinary protein binding site can readily bind to a carbon nanoparticle with high affinity and specificity through recognition modes that are common in protein-ligand recognition [93]. In general, carbon-carbon interactions are not considered specific, however these interactions have become more specific due to the nanostructuring of the particle allowing ordinary protein binding sites to be occupied by carbon nanoparticles. Adsorption of human serum albumin on the surface of carbon nanotubes [142] was investigated by MD simulations to understand possible conformational changes that the carbon nanotube may induce on the protein structure. It was found that the overall alpha-helical secondary structure of the protein was largely unchanged, whereas the random coils connecting these alpha-helices were strongly affected. This resulted in tertiary structure changes in the protein, mostly due to the orientational and conformational changes of the protein structure to fit the arrangement of carbon atoms on the nanotube surface. Similarly to the studies presented by Noon et al., adsorbed aromatic rings possessed the most favourable interactions between the protein and carbon nanotube surface [142]. It appears that nanoparticles can affect the overall structure and function of proteins, by hydrophobic interactions and pi-stacking between the aromatic residues and hexagonal carbon arrangement on some carbonaceous nanoparticles. Nanoparticles, and in particular nanotubes, have been highlighted as having a huge range of applications from field-effect transistors to biological application such as drug delivery vehicles. How-

ever dispersion of nanotubes within aqueous environments is problematic due to their high affinity for one another. As a result, peptides have been identified as possible nanotube dispersion mediators. One such designed peptide is nano-1 [94], an amphiphilic helical peptide which has been simulated using MD techniques in varying environments including water/oil, water/graphite and water/single walled carbon nanotube (SWNT) interfaces [94]. Further molecular dynamics simulations conducted by Chiu et al. showed that nano-1 has reduced its amphiphilic character at the water/oil interface and exhibited partial unfolding of the alpha-helix when adsorbed to graphite surface [94]. In contrast, the peptide was observed to curve on the SWNT external surface and retained its alpha-helix structure by maintaining hydrophobic contacts with the SWNT and hydrogen bonds with water [87]. Their results also showed that the inter-peptide hydrogen bonding through the peptide's lysine and glutamate residues help to stabilise the peptide-wrapped carbon nanotube. The peptides were found to collectively tilt along the nanotube surface resulting in peptide-peptide interactions that completely shield the nanotube from contact with water. All hydrophobic residues of the peptide interacted with the nanotube which allowed hydrogen bonding with water molecules to stabilise the multipeptide/SWNT complex [87]. Reversible cyclic peptides (RCP) have also been investigated, using MD simulations, for use as carbon nanotube dispersion mediators [143, 144]. Using free energy calculations and molecular dynamics simulations Chiu et al. showed that SWNT association is thermodynamically favourable with the reversible cyclic peptides preference to forming antiparallel beta-sheet-like structure [143]. These beta-sheet-like ring stacks form through peptide backbone hydrogen bonding along the SWNT surface. These structures can lead to the formation of tubular peptide stacks encasing the SWNT, which was also found to be a thermodynamically favourable process [143]. The limited diameter selectivity in carbon nanotube solubilisation is due to intra-peptide and inter-peptide disulfide bonds and not a result of single peptide wrapping [144]. As mentioned previously, carbon nanotubes have been considered as ideal drug delivery systems [110, 125], and work has been extended to study peptide encapsulation. Steered and classical molecular dynamics simulations were used to demonstrate the ability of carbon nanotubes to encapsulate peptides or proteins [145]. It was found that the van der Waals attractive forces were the driving force for the encapsulation of a peptide within the carbon nanotube. Furthermore, Chen et al. found

that longer nanotubes provide a broader area to trap peptides, while nanotubes with a smaller diameter are able to encapsulate the peptide with deeper interaction energy well [145]. Thus balancing the diameter and length of carbon nanotubes is important for their possible role as drug delivery devices [145]. Hydroxyapatite (HAP) is the main component of bones and teeth [95, 96]; synthetic HAP has medical applications as a bioinert coating [146] as well as a tool to investigate bone growth and formation [147]. As a result, investigations of the effects of HAP on the structure and function of fibronectin have been conducted. The steered MD and classical MD studies revealed that the charged C- and N-terminals interacted strongest with the surface [142]. Charged guanido groups, neutral amino groups and hydroxyl groups also have considerable interactions with the surface [142]. Further studies of hydroxyapatite (HAP) crystal and protein molecules (BMP-2) have used steered molecular dynamics [148]. The results agree with previous work which suggest that the –OH and the C- and N-terminals are the three groups through which the protein molecule BMP-2 interacts with HAP. It was also found that along with the Coulombic force, the water-bridged hydrogen bond is important in the adsorption process [148].

1.5 Nanomaterials effect on amyloid fibril formation

Recently research has focused on the influence of nanomaterials on protein conformation, including protein misfolding, self-assembly and aggregation into amyloid fibrils [149, 150]. Nanomaterials may inhibit or promote cytotoxicity at three different stages of the fibrillation process, (1) by disruption of the nucleation phase ie. the formation of fibril seeds, (2) by influencing the elongation/fibril growth ability and (3) by altering the amount of toxic species present and/or forming [151]. Nanomaterials of varying composition, functionalization, shape and size have been shown to effect the fibrillation of amyloidogenic peptides and proteins in many different ways. Factors such as shape, size, surface chemistry including concentration and composition of surface functionalization and charge have been shown to impact the ability of nanoparticles (NPs) to inhibit or promote aggregation. Much research has been undertaken recently to explore how specifically these factors can directly effect fibril formation. In the following section this literature is examined in

detail. In the discussion NPs are separated into three groups, organic nanomaterials (such as polymer nanoparticles and dendrimers), inorganic nanomaterials (such as gold NPs, quantum dots) and carbonaceous nanomaterials (such as fullerenes, nanotubes, graphene, and their derivatives).

1.5.1 Organic nanomaterials

Organic nanomaterials such as polymers, ie. nanoparticles and assemblies, are attractive for *in vivo* applications as they are easily produced, have a flexible design, and structure as well as a large variation of functional groups that allow easy modification of the particle surface. The ability to finely control physico-chemical properties of polymeric NPs makes them highly tunable nanomaterials. Additionally polymer based nanomaterials are often biodegradable and biocompatible *in vivo*, reducing potential cytotoxicity. Two classes of organic nanoparticles include, dendrimers, a type of polymer based material that has a highly ordered structure, and polymeric nanoparticles that can take on many configurations such as nanotubes, nanowires and vesicles.

Dendrimers

Dendrimers were first shown to effect fibrillation and the associated cytotoxicity of prion molecules in the infectious state (PrPSc). Surattapone et al. used cationic polyamine dendrimers (poly(propyleneimine, PPI), to show that these dendrimers effectively eliminated the PrPSc and cured prion-infected neuroblastoma cells. The PPI dendrimer reduced cytotoxicity in two ways, (1) the PPI bound with either the prion monomer or prion aggregates directly at certain sites that disrupted the β-sheet structure and caused dissociation or inhibition of the amyloid fibril. (2) the presence of PPI in lysosomes assists the transport of the prion molecules into secondary lysozymes allowing the clearance of these toxic species by proteolytic enzymes [152].

Poly(amidoamine), PAMAM is another dendrimer that has been shown to effect the fibrillation of Aβ1-28, the prion protein segment 185-208 (PrP185-208) and α-synuclein. Klajnert et al. showed that low dendrimer concentrations of PAMAM facilitated the formation of Aβ1-28 and PrP185-208 fibril nuclei while high concentrations of the same dendrimer delayed the elongation process [153]. PAMAM was even shown to break down

pre-existing fibrils of α-synuclein [154, 155]. Like PAMAM, gallic acid triethylene glycol (GATG) dendrimers showed the ability to accelerate the formation of Aβ fibrils which lead to a reduction in prefibrillar species and thus reduced overall toxicity [156].

Amyloid fibril formation can be affected by charged surface and proteins as it has recently been shown that Aβ is inhibited by the presence of hydrophilic charged proteins [157]. Surface charge effects of dendrimers on amyloid fibril formation have been investigated by Heegaard et al. [158]. Guanidino-modified and non-modified dendrimers were investigated with the prion protein (PrP106-126) and showed that the modified (charged) dendrimer acted as an inhibitor to fibril formation while the non-modified (uncharged) dendrimer had no remarkable influence on fibril formation [158]. Similarly Giehm et al. showed that guanidino-modified PAMAM dendrimers at a pH range of 6 to 10 destabilizes and precipitates insulin while unmodified diaminobutyrate, which is charged in the pH range 6 to 8, also destabilized insulin in the pH range 6 to 8 but much less at pH 10. Giehm et al. hypothesized that the interactions between dendrimers and proteins are mainly driven by electrostatic interactions as revealed by the pH-dependence phenomena [159]. In this way dendrimers may work by breaking up aggregates to release monomers which will lead to two fibrillation pathways depending on dendrimer concentration. At high concentrations the dendrimer either blocks further monomer association or binds the free monomers to the dendrimer surface while at low concentrations these free monomers will lead to the formation of new fibrils [160, 161].

Polymeric nanoparticles

Uncharged copolymer, N-isopropylacrylamide/N-*tert*-buty-lacrylamide (NIPAM/BAM) were investigated for their potential to impact on amyloid fibril formation of Aβ and hIAPP. NIPAM/BAM was chosen due to the ability to easily modulate its surface properties by simply varying the monomer ratio of NIPAM to BAM, where a higher NIPAM fraction results in a greater hydrogen bonding capacity [162, 163]. NIPAM/BAM nanoparticles were shown to retard Aβ and hIAPP amyloid fibril formation by blocking the binding sites of existing monomers and oligomers. Higher NIPAM ratio nanoparticles had a greater capacity to inhibit fibril formation, indicating that hydrogen bonding of the peptides with nanoparticles is an important consideration when designing amyloid fibril inhibitors.

In contrast, when NIPAM/BAM was studied in solution with $\beta_2$microglobulin there was an increased probability of a critical nucleus forming that could lead to the nucleation of protein fibrils [73]. The dual effect of the NIPAM/BAM nanoparticle on fibril formation was rationalized by examining the different protein structures, Aβ and hIAPP are largely unstructured wereas $\beta_2$microglobulin is a globular protein with a stable β-sheet conformation. Szczepankiewicz et al. suggest that the stability of the proteins native state can determine its propensity to form amyloid fibrils [164]. This concept was further explored by examining the fibrillation kinetics of single chain monellin mutants with NIPAM/BAM. By modulating the mutation of the monellin, the intrinsic stability and thus aggregation rate of the protein could be controlled. They found that, for monellin mutants with a high intrinsic stability and low intrinsic aggregation rate, amyloid fibril formation is accelerated by the NIPAM/BAM. In contrast, for peptides with a low intrinsic stability and high intrinsic aggregation rate, fibril formation was retarded by the presence of NIPAM/BAM [165].

Similarly recent work by Vacha and co-workers has shown that an attractive nanosurface retards fibril formation of peptides with a high intrinsic aggregation rate while the same surface accelerates fibril formation of peptides with a low propensity for fibril formation [166]. These results were produced using dynamic monte carlo simulations, a technique that enables the atomic detail to be removed but allows control of the attractive potential of the nanosurface and the model "fibrils". Systems comprised between 200-800 peptides, four wall binding strengths were tested, that is repulsive, weakly attractive, attractive and highly attractive. Interestingly they found that a weakly attractive surface decreases the nucleation rate more compared to a purely repulsive surface, this is due to a reduction in protein concentration in the bulk while the surface concentration is not high enough to nucleate fibril formation. The reverse behaviour is found for highly attractive surfaces, they lead to an acceleration in fibril formation, as the concentration at the surface is high enough to nucleate fibrils. The simulation results were validated by experimental ThT fluorescence results of α-synuclein and Aβ(1-42) in the presence of a polystyrene surface. As predicted by the model the α-synuclein has a low intrinsic aggregation rate and the presence of a surface resulted in an increase in fibril formation, while for Aβ, a high intrinsic aggregate, the presence of the surface reduces the fibrillation rate

[166].

1.5.2 Inorganic nanomaterials

Inorganic nanoparticles hold promise for many diverse applications ranging from chemical sensing to novel therapeutics. They can be easily and cheaply synthesized and are usually stable and resistant to decomposition especially when exposed to heat, light, acids and other factors. These features make them attractive for a vast array of applications. Two types of inorganic nanomaterials that have been used for in vivo applications are gold nanoparticles and quantum dots.

Gold nanomaterials

Gold nanoparticles are inert, biocompatible and easily functionalised through the Au-thiol bond, making them ideal for *in vivo* applications. Consequently gold nanoparticles are widely used to monitor protein-protein interactions in immunohistochemisty, in photothermal therapy and radiation therapy, in molecular imagining and recently as effective agents for screening amyloid aggregation inhibitors.

The peptide sequence CFGAILSS, which is based on the amyloidogenic region of the hIAPP protein, was found to form extended amyloid fibrils in aqueous solutions, with an anti-parallel configuration. When constrained to a AuNP surface, the peptide adopted parallel β-sheet configuration that was dependant on the NP curvature, that is at a lower curvature (larger AuNP) the peptide had a tendency to adopt this configuration [167]. Similarly Aβ monomers in the presence of bare AuNPs and carboxyl-conjugated AuNPs adopted different conformations, specifically it was found that they prefer to form short and fragmented fibrils along with spherical oligomers, which exhibited reduced cytotoxicity [168]. Furthermore Liao et al. showed that AuNPs could destabilize preformed Aβ aggregates and AuNPs preferentially bound to the fibril surface [168].

Lysozyme was also shown to adopt conformations that differed from its favoured solution structures in the presence of AuNPs. Lysozyme was found to form two types of extended aggregates, amorphous nanoparticle-protein complexes as well as large protein aggregates without embedded nanoparticles [169]. The lysozyme at the AuNPs interface was observed to undergo partial unfolding and this structure was hypothesized to catalyze

the fibril growth.Additionally it was shown that limited conformational changes occur while the lysozyme was adsorbed to the gold nanoparticle.

Functionalisation of gold NPs with glutathione (GSH) has been shown to disrupt amyloid aggregates formed in solution by lysozyme as well as inhibit any further aggregate growth [170]. Furthermore the disruptive effect of the AuNPs-GSH was found to be concentration dependant, where high concentrations lead to depolymerization of the lysozyme aggregates and lower concentrations just inhibit further aggregate growth. Interestingly GSH alone in solution with the lysozyme aggregates did not retain this disruption property [170].

Chan et al. conducted a systematic study to determine the effect that size, charge and surface functionalisation had on the elongation ability of Aβ1-40 fibril seeds [171]. By capping AuNPs with N-acetyl-L-cysteine (NAC), 3-mercaptopropionic acid (MPA) and citrate Chan et al. identifed that the less negatively charged NAC capped AuNPs resulted in stronger interactions with the Aβ1-40 which were mediated by hydrogen bonding, while the MPA and citrate capped particles discouraged peptide NP interactions. Chan et al. concluded that there was no significant effect on fibrillation of Aβ1-40 fibril seeds by the presence of AuNPs [171].

Molecular dynamics simulations examining the interaction of the extracellular matrix protein fibronectin (FN) with the Au(111) surface have used the GolP-OPLS-AA force field to examine the interactions between proteins and Au surfaces as well as the effect that adsorption has on the protein structure [172]. Hoefling et al. showed that the positively charged arginine residues initiated contact with the Au surface, this highlights the possibility of designed peptides to specifically bind to the Au surface [172]. While no protein unfolding was observed for the FN when it was adsorbed to the Au surface, significant domain shifts were seen resulting in the exposure of hidden epitopes that may lead to immunological threats [173, 172].

Another molecular dynamics study utilizing the GolP-OPLS-AA force field investigated the effect that thiol protected gold nanoparticles have on β_2-microglobulin's fibrillation propensity [174]. Initially rigid-body docking was conducted to identify the most favorable orientations of gold nanoparticle and β_2-microglobulin. The interaction energy of these complexes was also identified by determining the Lennard-Jones, electrostatic

interaction energy, and the desolvation energy. Subsequent all-atom simulations were conducted to refine the orientations identified by the docking simulations. The longest life complexes formed by the gold nanoparticle and the β_2-microglobulin were situated in the protein domains that may bind another protein. Brancolini et al. proposed this behaviour may potentially inhibit fibrillation activity [174]. This behaviour was further rationalized with previous simulation studies of a known fibril inhibitor, doxycycline. Doxycycline similarly reduces protein flexibility and conformational stability strongly favoring the native-like protein structure and was also shown to bind to the active sites of β_2-microglobulin [174].

Quantum dots

Quantum dots (QDs) have applications in cellular labelling and imaging as well as biodectection including detection of amyloid aggregates. These potential applications come about from the unique properties that QDs possess, including photoluminescence, high photostability, water-solubility and biocompatibility. CdTe quantum dots have been shown to be highly selective probes for prion proteins [175] and CdSe/ZnS core QDs have been shown to attach to various amyloid proteins for tracking the process of fibrillation [176, 177]. While QDs have been used as probes for tracking amyloid fibril formation they have also been shown to effect the fibrillation process [178, 179].

Dihydrolipoic acid (DHLA)-capped QDs were observed to accelerate the fibrillation of human serum albumin (HSA) and lead to the formation of mature fibrils. The researchers hypothesized that the DHLA-QDs acted like an existing fibril nucleus and thus seeded the nucleation phase [178]. In contrast N-acetyl-L-cysteine (NAC) capping of CdTe QDs (NAC-QDs) lead to drastic inhibition of Aβ fibrillization. Xiao and co-workers showed that NAC-QDs could inhibit the fibril formation at any point along the fibrillation pathway. They proposed the inhibition was a result of strong intermolecular interaction between the NAC-QDs and amyloid fibrils which resulted in blocking the active elongation sites [179].

1.5.3 Graphitic nanomaterials

Graphitic nanomaterials can adopt structures that are characterized by trivalent carbon atoms with a sp^2 hybridization placed in a two-dimensional lattice or the formation of car-

bon nanodiamonds that have a core of sp^3 bonded carbon atoms and surface of varied sp^2 bonded carbon atoms. The lattice of sp^2 bonded carbon atoms can adopt many structures three of which are spherical fullerenes, tubular carbon nanotubes and flat graphite and graphene surfaces, while carbon nanodiamonds take on a typically polyhedra with a diamond core. These unique structures give graphitic nanoparticles a lot of unique properties, such as high tensile strength, antioxidising behaviour and unique optical properties [180, 181, 182]. Graphitic nanomaterials have applications ranging from electronics, catalysis, chemical sensing, biosensors, drug and vaccine delivery, super capacitors cell detection and many more. A focus on the use for graphitic nanoparticles *in vivo* has highlighted their capability to effect amyloid fibril formation.

Fullerenes

Fullerenes are carbon molecules with a spherical shape, they consist of adjacent hexagonal and pentagonal rings. They have been created in a range of sizes from the small C20 to the soccer ball like C60 to much larger fullerenes consisting of over 120 carbon atoms. One of the unique properties of fullerenes, particularly C60, is it can act as an anti-oxidant, neutralizing free radicals in solution. This ability makes them an attractive therapeutic for to treating Alzheimer's disease as it has been shown that the biochemical path of Alzheimer's disease involves oxidative stress [183].

C60 derivatives functionalised with carboxylic acid, to enable solubility, have been shown to reduce apoptotic neuronal death induced by exposure to the Aβ1-42 protein [184]. Further investigations of the effect that C60 has on Aβ1-40 protein and Aβ11-25 peptides showed that it bound specifically in the central hydrophobic region, KVLFF, which is hypothesised to drive aggregation. By binding to this site further fibril growth would be inhibited, this was confirmed by ThT fluorescence which showed a 4 times increase for the Aβ1-40 protein in the presence of the C60 particle when compared to another common inhibitor, melatonin [185].

Lee and Huang functionalised C60 with PEG or pentoxifylline dyad (PTX) and showed that both particles reduced the A$\beta_2$5-35 cytotoxicity, while retaining the anti-oxidant ability of C60. This lead to a reduction in damage to mitochondrial membrane [186].

Fullerenes have also been functionalised with hydrophilic groups to improve water

solubility and biocompatibility. Hydrated fullerene C60 (C60HyFn) and sodium polyhydroxylated fullerenes (NaFL) were found to have anti-amyloid activity toward the fibrils of Aβ25-35 and Aβ1-42 peptides [187]. When C60HyFn was administered to control rats they showed improved cognitive performance and prevented impairment of performance of the cognitive tasks that is induced by A$\beta_2$5-35 [187]. Zhou et al. have examined a 1,2-(dimethoxymethano)fullerene (DMF), a water soluble fullerene derivative, in the presence of a preformed Aβ hexamer to determine the interaction, dynamics and binding mechanisms. Using classical molecular dynamics and the GROMOS43a1 force field Zhou et al. identified three favourable binding sites, the central hydrophobic region, residues 17-21, the turn site residues 27-31 and the C-terminal β-sheet site residues 31-41. Utilizing molecular mechanics generalized born surface area (MMGBSA), to produce binding free energies, they identified these sites to be the most energetically favorable for DMF adsorption. By decomposing the contributions to the binding energy per residue they determined that π-π-stacking and hydrophobic interactions were important for the strong binding to the Aβ hexamer. They also examined the curvature of the binding sites and found that curvatures that match the DMF molecule resulted in a tighter binding. Finally by binding to the turn region of the Aβ protofibril the DMF particle could disrupt the D23- K28 salt-bridge that is important for the Aβ fibrillation [188].

Huy and Li conducted a systematic investigation of the binding affinity of different sized fullerene particles Aβ9-40 and Aβ17-42 using a combination of docking and all-atom molecular dynamics [189]. Additionally the Hatree-Fock method and 6-31G* basis set was used to generate the bonded parameters and particle charges for each sized fullerene particle. The MMPBSA method was used to determine the binding free energy of each fullerene particle to the two Aβ peptides. The investigation revealed that the binding free energy is linearly dependant on fullerene size, that is the larger the fullerene the higher the binding affinity. Furthermore they identified that fullerenes bind to Aβ9-40 fibrils stronger than to Aβ17-42. Of the various fullerene sizes, C60 was identified as the biggest disrupter of Aβ17-42 fibrils. The MMPBSA results showed that van der Waals interactions dominate over the electrostatic interaction and non-polar residues of Aβ peptides play the most significant role in binding with fullerenes [189].

These studies suggest fullerenes could be a useful and effective therapeutics to combat

amyloid disease however the specific way in which fullerenes impact on amyloid fibril formation is still largely unknown.

Carbon nanotubes

Carbon nanotubes (CNTs) have been considered for many uses *in vivo* including as biosensors, as site-specific drug delivery vehicles or for direct interaction with disease-related biomolecules including those involved in amyloidosis [190].

Linse et al. conducted a systematic study investigating the effect that various nanomaterials have on the fibrillation of $\beta_2$microglobulin [73]. ThT fluorescence results showed that copolymer particles, quantum dots and carbon nanotubes all enhanced the probability of a critical nucleus for nucleation. They further showed that the shortened lag phase was dependant on the amount and surface chemistry of the particle. The results also indicated that $\beta_2$microglobulin may form multiple layers on the NPs, which indicated that multiple binding and dissociation cycles occured during the lag phase. This behaviour is indicative of a higher protein concentration occurring at the NP surface which promoted the formation of oligomers [73].

In contrast Ghule et al. found that multi-walled carbon nanotubes (MWCNTs) prevented 2,2,2-trifluoroethanol (TFE)-induced amyloid aggregation of the recombinant human acidic fibroblast growth factor protein (hFGF-1) [191]. They suggested the reduced aggregation in the presence of CNTs could be a result of adsorption and encapsulation of the protein on the surface of the CNT which may reduce the concentration of protein in solution. This work has been further rationalized by Luo et al. where they observed that the presence of CNTs resulted in a reduction of Aβ fibrils [192]. Using NMR, ThT/flouoresence spectroscopy with AFM imaging they showed that the presence of CNTs resulted in a reduction of the Aβ lag phase while leading to an increased transition time indicating that the CNTs allowed the quick formation of prefibrillar nuclei but inhibited growth of these Aβ nuclei into amyloid fibrils. They proposed a mechanism whereby the CNTs quickly bind the Aβ peptides that have adopted a parallel β-sheet conformation, this conformation is stabilised on the CNT surface which inhibits any further structural transitions that are required to transition from a small oligomer to a stable nucleus for fibrillation [192].

The Wei group have conducted a number of studies on the effect that CNTs have on Aβ

peptides. Initially they used all-atom molecular dynamics to simulate two preformed A$\beta_2$5-35 bilayer β-sheets that consist of either parrallel or mixed anti-parallel-parallel positioned either side of a CNT particle [193]. Their simulations showed that the two disjointed Aβ25-35 β-sheets with mixed sheet orientations assembled into a β-barrel, wrapping around the CNT. While the β-sheets that consisted purely of parrallel β-sheets formed disordered structures when adsorbed to the surface of the CNT. They proposed that the formation of the β-barrel is a two step process, (1) the Aβ25-35 β-sheet curving around the CNT due to hydrophobic interactions and dehydration, (2) fluctuating intersheet backbone hydrogen bonding [193]. A more recent publication utilised replica exchange molecular dynamics (REMD) to examine octomers of Aβ(16-22) in the presence and absence of a single walled carbon nanotube [194]. Initially, simulations of random chains in explicit solution were conducted, the simulated structures consisted mostly of disordered β-sheets. Subsequently the initial Aβ16-22 configuration of random peptide chains as well as the final disordered β-sheet structures of Aβ16-22 were simulated in the presence of the CNT. The simulation starting from the prefibrillar structure became destabilized in the presence of the CNT while the simulation starting with respect to the random chains was inhibited from forming β-sheet structures. Through analysis of the interactions between the Aβ16-22, CNT and water the authors identified that the interactions that drove destabilization of the prefibrillar structure and restricted the random chains from adopting β-sheet were hydrophobic and most importantly the π-stacking interactions. From these results it was suggested that CNTs will inhibit fibrillation of Aβ16-22 [194].

Jana and Sengupta investigated the collapse propensities of full length monomeric Aβ(1-42) in the presence and absence of a single-wall carbon nanotube using classical molecular dynamics [195, 186]. The propensity for Aβ to collapse and form hairpin-like structures [22, 196] has been suggested to be one of the key steps in Aβ self-assembly [195, 186]. As a consequence, conditions and/or modifications disrupting this collapse mechanism may impact on the overall propensity of Aβ to self-assemble into insoluble fibrils. Jana et al. characterized the peptide in relation to the behaviour of two important hydrophobic regions, the first, defined as HP1, comprised of residues 17-21 (LVFFA) and the second, defined as HP2, comprised of residues 30-35 (AIIGLM) [197]. They further defined Aβ collapse as the separation distance of the centre of mass of residues 17-26 and

residues 28-42, where a smaller distance indicated greater degrees of collapse. By utilising the adaptive biasing force method with the centre of mass separation distance of these two hydrophobic regions they were able to identify that it was not energetically favorable for the Aβ peptide to remain in an uncollapsed state in solution, with an energetic cost of $\tilde{1}5$ kcal/mol. While adsorbed to the CNT surface however, it was more energetically favorable to remain in an uncollapsed state, with an energy barrier of $\tilde{3}$ kcal/mol to reach a collapsed state [197].

Jana et al. continued this work to determine the roles of key domains on adsorption to the carbon nanotube surface utilising all-atom molecular dynamics simulations and point mutations of Aβ. To reduce the aromaticity and hydrophobicity of Aβ, the Phe residue at position 19 were mutated to either Ile or Tyr. Jana et al. showed that by reducing the hydrophobicity of the key hydrophobic region between residues 17-21 has a significant effect on the propensity for Aβ to collapse and its ability to adsorb to the CNT [198]. The reduced ability to adsorb may be due to its reduced ability to expunge water. Similarly reducing the aromaticity of the peptide resulted in a reduction in Aβ adsorption to the CNT. Jana et al. suggest that by targeting the specific hydrophobic core region of Aβ with either CNT or other drug targets Aβs propensity to form fibrils could be reduced [198].

Graphene and graphite

Graphite was initially used as a deposition substrate to examine protein aggregation using atomic force microscopy (AFM) or scanning tunneling microscopy (STM). It was noticed however that graphite influenced the fibrillation kinetics and also the final fibrillar morphologies.

Early work by Kowalewski and Holtzman investigated the effect that deposition of Aβ1-42 onto graphite surface had on the fibril morphology. They found that the peptide formed elongated β-sheets with extended peptide chains perpendicular to the long axis of the aggregate [199]. These β-sheets form along the crystallographic symmetry of the graphite surface and are oriented along the three directions at 120° to each other [199].

Human amylin-derived peptides were also observed to undergo the same template driven assembly [200]. Further analysis of fibrils that form along the 3-fold symmetry of

graphite showed that, for an unfolded sequence, the peptides formed parallel β-sheets with the polar side chains solvent exposed and the nonpolar side chains pointed down towards the graphite surface [201].

Investigation of Aβ17-42 on graphite surfaces showed that at high concentration Aβ favoured the formation of amyloid filaments with a U-shaped β-strand-turn-β-strand structure, similar to the previous work this filament was found to follow the graphite's hexagonal lattice symmetry [202]. Losic et al. investigated low concentration Aβ1-40 on graphite which formed fibrils along the step edges of the graphite. They hypothesised that hydrophobic and electrostatic interactions at the edge planes promoted and directed the fibrillation effect [203].

Guo et al. utilised classical all-atom molecular dynamics to examine the effect that various carbon nanomaterials may have on islet amyloid polypeptide (IAPP) [204]. They simulated four and eight IAPP(22-28) peptides in explicit solvent without and with a C60 particle, single walled carbon nanotube and graphene surface. They showed that the peptides adopted various conformations on the different carbon nanosurfaces, highlighting the fact the interactions and adsorption was dominated by π-π stacking and hydrophobic interactions. They determined through analysis of probability distribution of the minimum distance of side chains of the peptide to the nanosurface, that the strongest adsorption was to the CNT and graphene surface. Analysis revealed that on both these surfaces β-sheet content was reduced when compared to the IAPP(22-28) peptides in solution and in the presence of C60. Guo et al. concluded that the adsorption interaction had competitive advantage over the interaction between peptides, and they suggested that the extended CNT and graphene surfaces may inhibit early stages of fibrillation of IAPP(22-28) [204].

A recent investigation examined the effect that graphene has on the adsorption of human islet amyloid polypeptides (hIAPP(22-28)) fibrils and monomers to a cell like membrane. Utilising molecular dynamics with the OPLS forcefield the authors first equilibrated two systems, (1) a fibril like hIAPP(22-28) octomer and (2) eight individual hIAPP(22-28) monomers on the surface of the membrane. Subsequently they introduced a graphene sheet to determine the ability of the sheet to remove the peptides from the membrane surface. They found that desorption of the fibril (1) from the membrane surface onto the graphene took place rapidly within 14 ns. This process was assisted by dewetting of the graphene

surface by the fibril as it approached the graphene surface, resulting in a drying-induced attraction between the fibril and the graphene. Introduction of a graphene surface in the monomer system (2) also resulted in the desorption of some of the monomers on to the surface of the graphene, this behaviour was proposed to be driven by π-π stacking of the F23 residue with the graphene sheet [205].

Recent research highlighted that nanomaterials can impact protein self-assembly and amyloid fibril formation both by inhibiting fibril growth or accelerating it. However the molecular mechanisms that are behind these effects have yet to be fully explained. Additionally the recent literature indicated that the effect nanomaterials have on the propensity for certain peptides and proteins may have more to do with the intrinsic aggregation propensity of the protein itself. This highlights the need to investigate fibril forming peptides and proteins in solution as a benchmark to determine the effect that nanomaterials have on their aggregation propensity. Furthermore by elucidation of the mechanisms that may impact fibril formation in the presence of nanomaterials, of various shape, size, interaction strength and surface chemistry, these properties can be harnessed to design novel and safe nano theranostic materials and devices.

Computational techniques provide a complementary approach to explore these molecular mechanisms at length and time scales that are not yet accessible to experiments, they enable the systematic characterisation of the molecular level effect that nanomaterials have on amyloid fibril formation. Computational methods that are relevant to this pursuit are described in Chapter 2, while the amyloidogenic protein model and the nanomaterials investigated in this study are presented in Chapter 3.

1.6 Project aims

The intent of this project is to apply molecular dynamics techniques and derivative methods to investigate the folding, misfolding and aggregation of amyloidogenic peptides in the presence of three dimensionally different carbon nanomaterials, as well as determining and characterising the fundamental interactions between the peptide and the nanomaterials. The specific aims of the project are categorised below:

1. Investigate the effect that dimensionally different carbonaceous nanomaterials have

on the interactions and dynamics of an apoC-II(60-70) monomer using classical molecular dynamics in combination with umbrella sampling and density functional theory.

2. Determine the influence of polarization of the carbon nanomaterial on the interactions, dynamics and structure of the apoC-II(60-70) monomer. The use of polarization in simulation of carbon nanomaterials is an important consideration and may influence the quality of the results.

3. Investigate the dissociation pathway of a preformed apoC-II(60-70) dimer adsorbed to dimensionally different carbonaceous nanomaterials to identify the dissociation pathways and identify the nanomaterials capacity to disrupt the dimers.

4. Investigate the structure, dynamics and stability of preformed larger apoC-II(60-70) fibril seeds in the presence of carbonaceous nanomaterials using the replica exchange with solute tempering (REST) method, in order to identify the effect each nanomaterial has on aggregate stability and whether it can induce fibril inhibiting or promoting conformations.

5. Investigate the stability and interactions of the full apoC-II fibril tetramer in the presence of the various carbonaceous nanomaterials to elucidate the effect that these nanomaterials have on a stable fibril structure.

6. Draw conclusions on generalised effects of carbon nanoparticles and amyloid forming capacity of intrinsically amyloidogenic proteins.

Chapter 2

Computational techniques

2.1 Overview

Computational modelling is a useful tool to examine atomic level interactions that govern the behaviour of nanoscale systems. The modelling techniques are perfectly suited to probe the atomic level interactions that take place between nanomaterials and biological milieu that are not yet accessible to experiment. This chapter provides an overview of the computational methods and techniques commonly used to investigate biological systems including those in the presence of nanomaterials. The application of these methods in the studies presented in this thesis is also noted. Initially an introduction into molecular modelling and its underlying ideas is presented, a brief discussion of quantum mechanical techniques follow, discussing their history and evolution. Section 2.4, discusses the classical simulation techniques including their underlying methodologies, specific focus is given to molecular dynamics (MD) simulation, a method applied extensively throughout this thesis. Section 2.6 discusses the conformational sampling problem with respect to protein simulations and MD derivative methods developed to overcome some of these limitations, such as umbrella sampling and replica exchange methods.

2.2 Introduction

Computational modelling and simulation leverage the processing power of modern CPUs, GPUs and co-processors to explore problems that are often difficult or impossible to ex-

amine using traditional experimental techniques. Molecular modelling (MM) is one major field that utilises the fast growing computational power. MM is the collective term describing a large array of techniques that can be applied to model the behaviour of molecules, ranging from the very small scale (100 atoms or less, equivalent to a nanomaterial surface a few atoms across) to the very large (greater than 1,000,000 atoms, equivalent to a nanomaterial surface of 30 nm x 30 nm). The advantage of MM methods over currently available experimental techniques is the ability to explore the time evolution in a controlled system of atomic detail from the femto to micro or even millisecond time scale.

Computational methods have been developed to explore the electronic, atomic and molecular level interactions of a variety of systems. These methods range from the most accurate and computationally intensive description of the electronic structure using quantum mechanics (QM), including *ab initio* and density functional theory (DFT) methods, to the atomistic force field methods that apply Newtonian mechanics to examine the time evolution of the physical (rather than chemical) interactions and dynamics of a many atom system, to coarse-grained methods that consider a group of atoms as a single interaction sight and are thus able to explore micro and millisecond timescales.

The most precise "*ab-initio*" (from the first principles) description of a system of particles begins with the Schrödinger equation, which describes the quantum state of the system. Solutions of this equation provides molecular, atomic and electronic level information about the system. The non-relativistic time independent form of the equation is,

$$\mathbf{H}\Psi(\mathbf{r}) = E\Psi(\mathbf{r}), \tag{2.1}$$

where $\mathbf{H}$ is the Hamiltonian operator acting on the wave function Ψ, and E is the total energy of the system. The Schröedinger equation can in theory be used to explicitly represent any physical system, however solving the equation explicitly for more than the hydrogen atom is extremely difficult. This obstacle is termed the *many body problem*. Methods and approximations have been developed to allow larger systems to be solved while retaining various degrees of accuracy.

The *Born-Oppenheimer approximation* (BA) alleviates this problem by splitting the

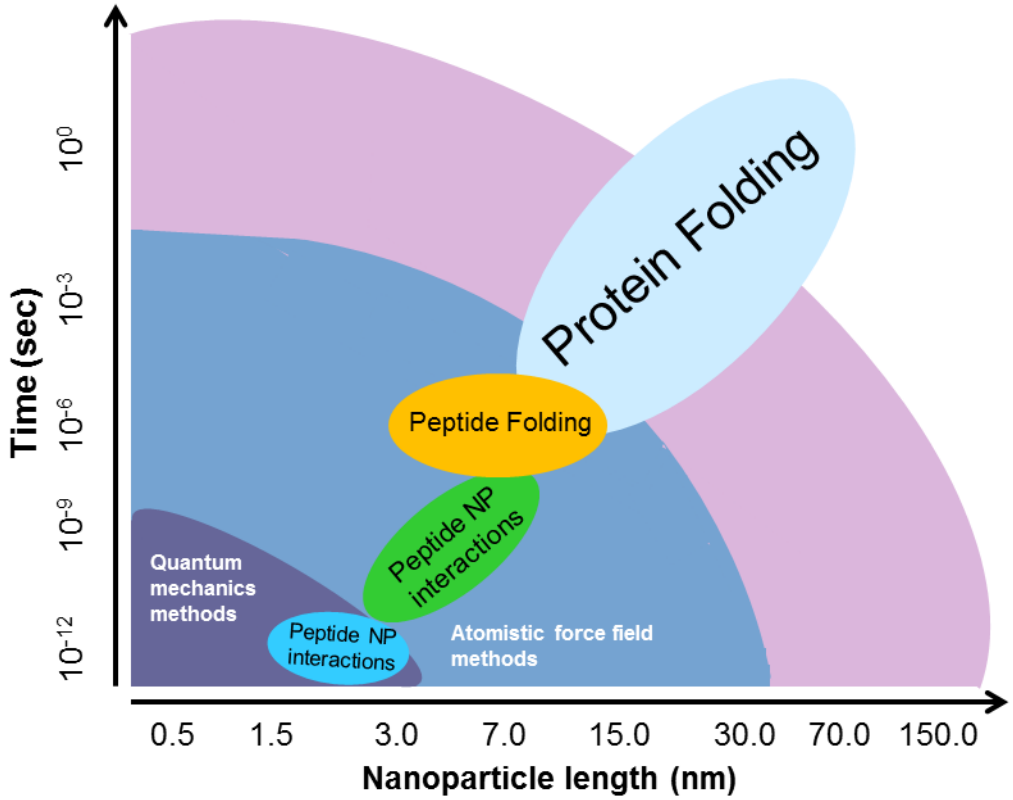

Figure 2.1: A schematic of the accessible system size and time scale for different types molecular modelling techniques.

wave function of an atom into its electronic and nuclear components. This approximation can be made as the masses of the atomic nuclei are significantly larger than that of the electrons, by a factor of ≈2000. As mass is inversely applied to the operator in the Schröedinger equation, the kinetic energy of the nuclei, T^N, is an equivalent factor less than that of the electrons. Thus by approximating the kinetic energy of the nuclei to zero, their positions can be considered fixed. This allows the calculation of the electronic ground state energy E^N. The BA also makes the approximation that the velocity of the electrons is much greater than that of the nuclei which allows the nuclear ground state energy of the system to be solved. As the electrons are assumed to have instantaneously reached their ground state positions, a wavefunction can be employed that is *only* dependent on the motions of the nuclei. The Hamiltonian operator now includes the kinetic energy of the nuclei T^N, a nucleus-nucleus interaction potential V^{NN} and the electronic potential is represented by E^N. As V^{NN} and E^N have already been calculated for the positions of the nuclei, the ground state wave function of a molecule can be calculated as a function of

nuclear coordinates only.

While the BA greatly simplifies the Schrödinger equation for light atoms, solving for the electronic ground state energy of a molecular system is still a formidable task computationally and impossible analytically. However, BA forms the basis of a number of *ab-initio* methods as well as the classical molecular modelling methods, these are discussed below.

2.3 *Ab-initio* methods

Ab-initio methods or otherwise known as the first principles approaches describe molecular systems by solving the Schröedinger equation to various degrees of accuracy. Several mathematical theorems have been developed with the aim of solving the Schröedinger equation for larger systems while retaining accuracy. The methods, developed in the late 1920s, by Douglas Hartree and Vladimir Fock solve equation 2.1 from first principles. Termed the Hartree-Fock approximation, this method assumes that electrons move independently of each other and are confined to the molecular orbitals. These orbitals are determined by assuming that the electron is moving within an average field of all the other electrons. The total wavefunction is written in the form of a single "Slater" determinant, χ_{i}.

$$\Psi = \frac{1}{\sqrt{N!}} \begin{vmatrix} \chi_1(1) & \chi_2(1) & ... & \chi_n(1) \\ \chi_1(2) & \chi_2(2) & ... & \chi_n(2) \\ ... & ... & & ... \\ \chi_1(N) & \chi_2(N) & ... & \chi_n(N) \end{vmatrix} \tag{2.2}$$

Where equation 2.2 is termed a spin orbital and is the product of a molecular orbital, Ψ_{i}, and a spin function, α or β. The lowest energy of the molecular orbitals can be obtained by the self-consistent-field procedure. The Hartree-Fock approximation leads to a set of coupled differential equations (the Hartree-Fock equations), that represent the coordinates of a single electron. By introducing the Linear Combination of Atomic Orbitals (LCAO) approximation, the molecular orbitals are expressed as linear combinations of a finite set

(a basis set) of prescribed functions known as basis functions, ϕ.

$$\Psi_i = \sum_{\mu} c_{\mu i} \phi_{\mu} \tag{2.3}$$

where ϕ_{μ} is one of K atomic orbitals and $C_{\mu i}$ is a coeffiecent. As the Hartree-Fock equations represents these interactions as a linear combination of (one-electron) atomic orbitals, it is able to avoid the many-body problem. The HF wavefunction can then be solved for the ground state energy using the variational principle [206, 207, 208]. The principle states that the energy calculated from an approximation to the true wavefunction will always be greater than the true energy. Thus by using the self-consistent-field procedure described above the wavefunction can be improved to result in the lowest energy for the molecular orbital.

The Post Hartree-Fock methods (CI [209], CPP [210], MP [211, 212]) have emerged to remedy the electron correlation absent from HF methods, albeit to a limited degree. A further limitation of standard HF is its inability to account for dispersion forces, which Post Hartree-Fock (PHF) methods go some way to fixing [213]. The results are generally more accurate than the corresponding HF calculation, although at a greater computational cost [214]. HF and PHF methods are employed in the study of molecular structure, NMR and, vibrational, electronic and photoelectron spectra of systems where a small number of atoms can be modelled periodically, such as semiconductors [215, 216, 217].

Another approach to describing electron correlation is to consider the fact that the sum of the exchange and correlation energies of a uniform electron gas can be calculated exactly knowing only its density (4). This approach forms a foundation of density functional theory (DFT) and overcomes the many body problem by treating the ground state electrons not as individual particles with dimensions 3N, but as an electron density with only the three spatial dimensions. In the Kohn-Sham formalism, the ground-state electronic energy, E, is written as a sum of the kinetic energy, E_T, the electron-nuclear interaction energy, E_V, the Coulomb energy, E_J, and the exchange/correlation energy, E_{XC}.

$$E = E_T + E_V + E_J + E_{XC} \tag{2.4}$$

All the components depend on the total electron density, $\rho(\mathbf{r})$, with the exception of

the kinetic energy, E_T.

$$\rho(\mathbf{r}, \mathbf{r}') = \sum_{i}^{orbitals} f_i \psi_i(\mathbf{r}) \psi_i^*(\mathbf{r}') \tag{2.5}$$

All the information about the ground state of a system is contained in the *single-particle* density matrix $\rho(\mathbf{r}, \mathbf{r}')$, equation 2.5. Here, f_i is the occupancy of state ψ_i where at zero temperature it is restricted to either 0 or 1. The charge density $n(\mathbf{r})$, is given by the diagonal elements of the density matrix

$$n(\mathbf{r}) = 2\rho(\mathbf{r}, \mathbf{r}). \tag{2.6}$$

This work led to a Nobel prize in 1988 and the popularity and versatility of DFT is reflected in the diverse number of fields where it is employed; molecular biology, geophysics, quantum chemistry and solid-state physics. Similar to Hartree-Fock calculations, DFT has not originally included the physics necessary to properly describe dispersion forces [218, 219], although efforts are being made to overcome these limitations [220, 221, 222, 223] and references therein. Despite the success of DFT approaches, the technique is usually limited to system sizes of < 1000 atoms.

ONETEP

To extend the applicability of DFT to systems that consist of many thousands of atoms research in the last decade has focused on constructing *linear-scaling* DFT codes [224, 225]. These methods exploit the electronic localization [226, 227] that is inherent in systems with a band gap. They also seek to optimize quantities that in principle, are infinite in extent, but decay exponentially, i.e the single-particle density matrix [228] or Wannier functions [229, 230]. One such linear-scaling method is implemented in ONETEP (order-N electronic total energy package) and has been implemented within this thesis to determine the electronic structure and properties of the interface between the protein and nanomaterial. ONETEP's implementation of linear scaling [231] exploits the electronic localization that is inherent in systems with a nonvanishing band gap [232].

The density matrix, equation 2.5, will decay exponentially as a function of the distance between $\mathbf{r}$' and $\mathbf{r}$, given that a band gap exists within the system [233, 234, 235]. This is

the property that is exploited by many linear-scaling DFT methods, whereby the density matrix is truncated to a sparse band-diagonal form such that the amount of information it contains increases linearly with size. With this in mind the density matrix can be expressed as,

$$\rho(\mathbf{r},\mathbf{r}') = \phi_\alpha(\mathbf{r}) K^{\alpha\beta} \phi^*_\beta(\mathbf{r}'), \tag{2.7}$$

where, ϕ_α are a set of *spatially localized nonorthogonal* basis functions and the matrix $\mathbf{K}$ is called the *density kernel* [236]. Thus a "coarse-grained" truncation of the density matrix can be achieved by truncating the new density kernel by,

$$K^{\alpha\beta} = 0 \tag{2.8}$$

when

$$|\mathbf{R}_\alpha - \mathbf{R}_\beta| > r_{cut}, \tag{2.9}$$

where $\mathbf{R}_\alpha$ and $\mathbf{R}_\beta$ are the "centres" of the localization regions of the functions $\phi_\alpha(\mathbf{r})$ and $\phi_\beta(\mathbf{r}')$. Often linear-scaling techniques use a LCAO approach, where the basis ϕ_α consists of atomic orbitals. Their radial shapes can be expanded in using a number of different functions [237, 238, 239, 240] and they are truncated either by "thresholding" [241] or by truncation of orthogonal Wannier-like functions [240]. However, these methods are subject to problems of *transferability* of the basis set used and the fact that the size of the sparse matrices increases with the square of the number of atomic orbitals per atom for a given $\mathrm{r_{cut}}$. These problems can be overcome by conducting preliminary calculations with a number of basis sets.

ONETEP overcomes these problems by utilising a minimal number of ϕ_α localized functions per atom to reduce the matrix size and optimizing these functions during the calculation. Thus ϕ_α are no longer a basis set, rather they are quantities to be determined during the calculation along with the density kernel $\mathbf{K}$. In ONETEP the ϕ_α are called nonorthogonal generalized Wannier functions (NGWFs) [231]. Strict localization is enforced on the NGWFs by confining them to spherical regions centered on atoms and by constantly truncating any contributions that may develop outside these *localization sphere*

during the *conjugate gradient* optimization procedure.

Thus by exploiting the real space localization of the electronic system that is inherent in nonmetallic materials, ONETEP is able to produce the same accuracy as conventional cubic-scaling plane wave approaches while offering linear scalability [242]. The method has been shown to be efficient for biological systems, up to $\approx$ 41,000 atoms in size [243] at the time of writing.

2.4 Classical simulation methods

Classical simulations, are not as accurate or robust as the quantum mechanically derived methods, however they enable the investigation of larger systems at atomic or near atomic detail. Empirical force field methods are a classical technique that can be applied to theoretically investigate the interactions between many particle systems including biological and inorganic complexes.

2.4.1 Force fields

Fundamental to classical simulation methods are the forces that govern the atomic motions and pair-wise atom-atom interactions. These forces are described by empirical or QM derived potential energy function. The combination of the potential energy function with the geometric and energetic parameters used, yield what is known as a force field (FF). FF's are usually developed in the context of a specific environment, such as biological milieu which includes water, ions and macromolecules (proteins, lipids and DNA). Many of these FF's have been specifically developed to replicate experimental data associated with the behaviour of water in these biological environments. Several different types of water models exist fitting into 3 groups, the simple interaction site rigid water models, flexible water models and models that explicitly include the effects of polarisation. The simple rigid water models typically use between three and five interaction sites, TIP3P [244] and SPC [245] are commonly used 3 site models. FFs that have been developed to enable an accurate description of proteins in these explicitly solvated environments include the all-atom CHARMM [246], AMBER [247] FFs that were developed with the TIP3P water model and the all-atom OPLS-AA [248] and united-atom GROMOS [249] FFs, which

were parameterised with the SPC water model. The all-atom FFs, as the name suggests, describe every atom explicitly while the united-atom FFs treat hydrogens bonded to an aliphatic carbon as a single interaction site, which can reduce the computational cost of these simulations. Recently FFs have been developed to accurately capture the interactions between proteins and nanomaterial interfaces. Golp-CHARMM [250], GRAPPA [251] and an extension to the AMOEBA PRO FF [252] are a few examples specifically developed to simulate gold-protein (Golp-CHARMM) and graphitic-protein interactions (GRAPPA, AMOEBA PRO). These FFs are required to accurately model the polarisabilty of these nanomaterials and its effect on protein adsorption and dynamics. The treatment of polarisation in these FFs is discussed in section 2.4.2. In general FFs are grouped as either class I or class II, where a class I FF is restricted to the inclusion of harmonic terms to describe bond stretching, angle bending and torsion rotation, this type of FF is described below. Class II FFs additionally include terms to describe the coupling between the internal coordinates of atomic systems, known as cross terms. These terms can reproduce structural properties accurately such as vibrational frequencies. Examples of class II FFs are the COMPASS [253] and CFF95 [254] force fields.

In this thesis the class I GROMOS FF has been used throughout, it has been previously validated [81] and used extensively to explore the structure and dynamics of the protein model employed in this study [255, 256, 257, 258]. Extensive details of these studies are presented in Chapter 3. The functional form of each force field contains energy terms describing the bonded (E_{bonded}) and nonbonded ($E_{nonbonded}$) interactions between the atoms of a system. The terms representing bonded interactions account for the stretching of bonds, the bending of valence angles, and the rotation of dihedrals. The nonbonded terms represent the electrostatic and van der Waals interactions. An example of a force field equation is given in equations 2.10-2.12.

$$E_{bonded} = \sum_{bonds} K_b(b - b_0)^2 + \sum_{angles} K_\theta(\theta - \theta_0)^2 + \sum_{dihedrals} K_\chi(1 + cos(n\chi - \sigma)) \quad (2.10)$$

and

$$E_{nonbonded} = \sum_{\text{nonbonded pairs ij}} \left(4\varepsilon_{ij} \left[(\frac{\sigma_{ij}}{r_{ij}})^{12} - \frac{\sigma_{ij}}{r_{ij}})^{6} \right] + \frac{q_i q_j}{4\pi\varepsilon_0 r_{ij}} \right) \tag{2.11}$$

The total potential energy function is in the form of,

$$E_{total} = E_{bonded} + E_{nonbonded} \tag{2.12}$$

where E_{bonded} is the contribution from the bonded interactions, $E_{nonbonded}$ is the contribution from the nonbonded interactions, to the total energy. The first term in equation 2.10 describes the stretching of bonds summed over all bonded pairs, where each bonded pair is represented by a Hooke's law formula. K_b and b_0 are the parameters describing the stiffness and reference bond length respectively, and b represents the interaction distance between atom pairs. The second term is also represented by a Hooke's law formula and describes the deviation/bending of the angle (θ), summed over all triplets of bonded atoms. Similar to the bonded term, K_θ and θ_0 are the parameters describing the stiffness and reference angle position respectively, while θ represents the angle formed by the three consecutively bonded atoms. The final term describes the rotation of the dihedral around the cenrel bond of any four consecutively bonded particles, these rotations are a periodic function described by a cosine function. K_χ, n and σ represent the barrier height for the rotation of the dihedral, the periodicity and the phase respectively.

The nonbonded potential energy equation, describes the intermolecular or nonbonded interactions. Generally, nonbonded interactions between atoms are calculated between atoms in separate molecules or between atoms separated by three or more bonds in the same molecule. The first part of the equation is the van der Waals term, described by the Lennard-Jones equation, which models the attractive dispersion and repulsive interactions. The ϵ_{ij} parameter is the well depth of the interaction between atoms i and j, r_{ij} is the distance between the two interacting atoms. σ parameter defines the separation for which the Lennard-Jones energy is zero for the combination of atoms i and j, which is also known as the collision diameter. The second part of the nonbonded energy equation models the electrostatic interactions between the nonbonded pairs of atoms. The electrostatic interactions are based on Coulomb's law, where the product of the particle charges of the atoms i and j, that is q_i and q_j, divided by the separation distance of the two atoms and

the dielectric of the medium ϵ_0 results in the electrostatic contribution to the nonbonded energy. The partial charges on these atoms are noninteger values that are selected to represent the overall charge distribution of a molecule. The sum of the partial charges in a molecule must equal the molecule's net formal charge. While the previous applies generally to all FF's there are some variations that are important to consider. One important difference between FF's is the variable of "improper" dihedrals, which can be applied to maintain chirality or planarity at an atom centre bonded to three other atoms, an example is for cyclic molecules like benzene. The CHARMM and GROMOS FF's add a separate term for improper dihedral energy that has a quadratic dependence on the value of the improper dihedral, similar to the terms for bonds and angles. The additional separate term is important for the united-atom GROMOS FF, as it does not include particle positions for the hydrogen atoms bonded to aliphatic carbons, the improper dihedral term serves to preserve chirality at these carbon centres.

2.4.2 Treatment of polarization

In general the description of the FFs above do not account specifically for non-bonded interactions that are not pair-additive, the most important example of which is interaction through atomic polarisability. In these FFs, the average non pair-additive contributions, i.e polarisation, are included within the effective pair potentials. While in general the effective pair potentials are a reasonable approximation, in practice, they can be insufficient for the modelling of the interaction of proteins with polarisable surfaces, such as those of nanomaterials where polarization is induced by the presence of the solute and solvent. Examples include gold and graphitic nanomaterials such as carbon nanotubes and graphene surfaces.

Polarisability within an all-atom molecular modelled system can be described by either the Shell model of Dick and Overhauser [259] or by using the Rod model introduced by Iori and Corni [260]. In both models an additional shell particle representing the electronic degrees of freedom is introduced. This additional site has no van der Waals interactions with other atoms and is characterised by the mass m and the charge q. In the case of polarisable nanomaterials, the atom that is attached to this additional shell particle is assigned a charge of -q. The interaction between the shell particle and its respective

nucleus is not included in the energy and force calculations.

The two models differ by how they connect the shell particle to the nucleus. The Shell model uses a harmonic bond with a force constant k, the polarizability (α) is determined using this force constant, the mass m and charge q to produce,

$$\alpha = \frac{q^2}{k}, \tag{2.13}$$

and the harmonic oscillator frequency (ω),

$$\omega = \sqrt{\frac{k}{m}}. \tag{2.14}$$

For the Shell model the potential energy is minimised with respect to the shell position at every step of the simulation. To produce the correct adiabatic decoupling between the fictitious oscillators and the real nuclei dynamics, small timesteps, < 0.5 fs, may need to be applied. This drawback can be overcome by coupling to a low temperature thermostat [261] keeping the oscillator close to its minimum, although this may artificially affect the energy distribution of the real system. Even with these optimisations the minimisation can add significantly to the computational time required to simulate the system.

Alternatively the Rod model can be applied to a nanosurface that has a set of fixed atoms, without the need to apply a low temperature thermostat to the shell particle. Where the Shell model uses a harmonic bond to connect the shell particle to the nucleus the rod model forces the shell particle to be at a given distance l_0, with a free orientation. Unlike the Drude oscillator, the rod always has a finite dipole moment, $\mu{=}ql_0$. As a consequence T must be greater than zero to produce an orientational average and thus physically meaningful results. The polarizability is given by,

$$\alpha = \frac{\mu^2}{3k_bT}, \tag{2.15}$$

where, μ is as described earlier, k_b is the Boltzmann constant and T is the temperature. The typical intrinsic time-scale is determined by the rotation frequency at a given temperature,

$$\omega = \sqrt{\frac{2k_bT}{l_0^2 m}}. \tag{2.16}$$

Recently the rod model has been used to describe polarisable nanomaterial surfaces, including the gold (111) and (100) surfaces [250] and graphitic nanomaterials, specifically carbon nanotubes and graphene [251]. These two implementations have been combined with the well validated CHARMM FF, producing GolP-CHARMM and GRAPPA respectively. GRAPPA was validated against high level *ab initio* calculations, experimental data and the AMBERPRO polarised forcefield [251]. In this work the GRAPPA FF has been implemented and compared to the GROMOS FF in Chapter 4 to determine the effect that polarisation has on adsorption and dynamics of a protein in the presence of a carbon nanotube and graphene surface.

2.4.3 Periodic boundary conditions

One of the limitations of forcefield based simulations is the size of the system, where very large systems, greater than 200,000 atoms, can become computationally unfeasible to explore. By efficient approximation of boundaries and border effects of a system, "macroscopic" properties can be identified by using relatively smaller system sizes. Periodic boundary conditions are traditionally used to minimise the edge effects in a finite system enabling the particles to experience forces as if they were in bulk fluid. The atoms of the system to be simulated are placed into a space-filling box, which is surrounded in three dimensions by translated copies of it self. If a particle leaves the box during the simulations, it will be replaced by an image particle that enters from the opposite side. The number of particles within the central box thus remains constant. Depending on the system to be examined, there are several space-filling type boxes that may be more computationally efficient for running molecular dynamics calculations. There is the cubic unit cell, rhombic dodecahedron, truncated octahedrons, and the most general space-filling shape, the triclinic unit-cell [262].

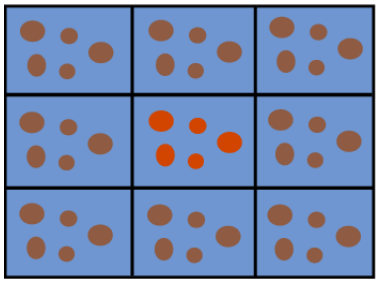

Figure 2.2: A two-dimensional schematic of periodic boundary conditions

2.4.4 Treatment of non-bonded interactions

Integration of the non-bonded potential (electrostatic and van der Waals forces) between particles in the system is the most computationally expensive task for each MD time step. This is a result of the pair additive nature of the interactions, that is as the system increases in size the number of non-bonded interactions to calculate becomes significantly larger. In comparison, the bonded interactions are almost trivial to calculate. For a given pair of non-bonded particles the LJ potential rapidly decays to a negligible value at 1.5 nm, with this in mind a distance cutoff can be implemented that restricts the number of non-bonded pairs contributing to the vdW potential of each atom. The pairs of atoms that contribute to the vdW for a given atom within the cutoff are placed on a neighbour list, this list is updated after a defined number of time steps. A similar cutoff and neighbour list method can be applied to the electrostatic interactions. However the electrostatic interactions decay much slower than the LJ, at a rate of r^{-1}, as a consequence this Coulombic interaction can extend into the adjacent unit cell and result in self interactions. To avoid cut-off artifacts such as splitting dipoles and prevent self interaction, a tail correction can be applied, which allows the electrostatic interactions to decay smoothly to zero. There exist a number of algorithms that have been developed to sum the electrostatic potential more efficiently, including the Ewald summation [263], Particle Mesh Ewald (PME) [264, 265] and Particle-Particle Particle Mesh Ewald (PPPME) [266]. PME and PPPME are extensions of the Ewald summation, and are both commonly implemented in modern MD simulations, in this thesis the PME method has been used throughout. In the Ewald summation method, the electrostatic interaction is broken up into two terms shown in equation 2.17; a short range term below the cutoff and a long range term above the cutoff, which are solved in real space and reciprocal space, respectively. The long range interactions can be treated

as periodic waves in the unit cells, so V_{lr} can be Fourier transformed and summed in reciprocal space, then inverse Fourier transformed to give the long range electrostatic potential.

$$V = V_{sr} + V_{lr} \tag{2.17}$$

While Ewald summation is able to reduce the computational expense it is only suitable for systems with $<10^3$ particles, and with modern MD simulations approaching millions of atoms this method is impractical. Particle Mesh Ewald (PME) and Particle-Particle Particle Mesh Ewald (PPPME) extend the Ewald summation method to allow calculations of much larger systems. In the PME method the particle charges are mapped onto a 3D grid which allows the use of Discrete Fourier Transform functions for V_{lr} instead of Fourier transforms as used in the Ewald summation method. Fast Fourier Transform (FFT) algorithms can be implemented to calculate the DFTs, which is the main advantage of PME since FFTs are computed very quickly compared to ordinary Fourier transforms. The short range term is calculated explicitly.

2.4.5 Thermodynamics ensembles

The simplest simulations with periodic boundary conditions, are performed under constant number of particles (N), energy (E) and volume conditions (V), known as the *microcanonical* ensemble (NVE). This ensemble represents a thermally isolated system where the temperature can be calculated, but not controlled. Therefore it is desirable to perform the simulations in a different ensemble, such as the canonical ensemble (NVT) and isothermal-isobaric ensemble (NPT). Furthermore experimental measurements are made in environments of constant temperature and pressure, and so simulations in the isothermal-isobaric (NPT) ensemble are more directly relevant to experimental data.

2.4.6 Energy minimisation

The potential energy function of a macromolecular system has a complex landscape in a large number of dimensions (3N-3). This function has many minima, with the deepest point represents the *global minimum* and many other *local minima*. Knowledge of all the

local and the sole *global minimum* would allow a complete description of the system. Energy minimisation is a technique that can be used to find only the nearest *local minimum*, while methods that attempt to find the *global minimum* are discussed in section 2.6.

Given a starting atomic configuration, it is possible to find the nearest *local minimum* of the potential energy function described by a forcefield. It is often required to start a molecular dynamics simulation from a configuration that has been energetically minimized. This has the benefit of reducing the forces, and kinetic energy within the initial configuration. A number of methods exist to minimize the energy and find the nearest *local minimum*, they use the derivative(s) of the potential energy function (FF) with respect to the atomic coordinates. This produces the energy gradient, which provides information regarding the location of the *minimum* which is based on the direction of the gradient, while the magnitude of the gradient indicates the steepness of the slope. Three common first-order minimisation methods used to minimize the energy include, the steepest descent, the conjugate gradient and L-BFGS methods. Additionally second-order derivative methods can be used to precisely find the local minimum, an example of this is the Newton-Raphson method.

The steepest descent method simply takes a step in the direction of the negative gradient, the same direction as the force, without any consideration of the history built up in previous steps. The step size is adjusted such that the search is fast, but the motion is always downhill. The faster-converging conjugate gradient method uses gradient information from previous steps [267]. L-BFGS minimizer is mostly comparable to conjugate gradient method, but in some cases converges faster. The Newton-Raphson method is often slow for many atomic systems, however a precise minimum is found, this type of minimization can be necessary for the determination of vibration frequency. The local energy minimum is attained when the user specified convergence criteria for energy and/or force are met.

2.5 Molecular dynamics

Molecular dynamics allows the determination of the dynamic and time averaged ensemble properties of a system. Newton's equations of motion are used in order to observe the

evolution of the system with time. For a system of N particles, Newton's second law takes the form,

$$m_i \mathbf{r}_i = \mathbf{F}_i(\mathbf{r}_1, ..., \mathbf{r}_N) = -\frac{d\mathbf{E}_i}{d\mathbf{r}_i} \tag{2.18}$$

where $\mathbf{E}$ is the total potential energy function, described by a forcefield equation, 2.12). $\mathbf{F}_\mathrm{i}$ is the force acting on the particles in the system derived from $\mathbf{E}$, and $r^N = (r_1, r_2, ..., r_N)$ represents the complete set of atomic coordinates. As eluded to in section 2.2 the many-body problem dictates that their is no analytical solution to the equation of motion for systems of more than two particles, it can however be solved numerically. Various algorithms have been developed in order to find the numerical solution of a system of many particles as efficiently and accurately as possible, including the Verlet algorithm [268], leap-frog algorithm [269] and velocity Verlet algorithms [270].

A molecular dynamics simulation begins with an initial set of atomic positions and initial velocity, usually after an energy minimisation step has been conducted (discussed in section 2.4.6). Initial velocities can be randomly assigned to the particles from the Maxwell-Boltzmann distribution at the target temperature. Then Newton's second law in equation 2.18 is integrated in small time steps, typically 1-10 fs for MD, depends on the fastest vibration in the system (eg. 1 fs for hydrogen containing bonds). The time step can be increased by applying constraints to these fast vibrations, common methods to achieve this are described in section 2.5.3. The positions and velocities can be extracted from the equation 2.18, and the initial process is repeated, producing a set of atomic coordinates as a function of time, often referred to as a trajectory. The integration of the forces is the most time consuming part of MD simulations, as a consequence the integrator algorithms mentioned previously have been developed to reduce the computational cost as much as possible. The Verlet [268] integrator described below, and its derivatives are the most widely applied algorithms. Given a time step δt, the Verlet algorithm calculates the new atomic coordinates at time $t + \delta t$ using the acceleration and positions at time t, as well as the coordinates from the previous time step $t - \delta t$. A Taylor expansion of the position r(t) around some small increment in time δt is given by,

$$\mathbf{r}(t+\delta t) = \mathbf{r}(t) - \mathbf{r}(t)\delta t + \frac{1}{2}\mathbf{a}(t)\delta t^2 + ... \tag{2.19}$$

and similarly

$$\mathbf{r}(t-\delta t) = \mathbf{r}(t) - \mathbf{r}(t)\delta t + \frac{1}{2}\mathbf{a}(t)\delta t^2 + ... \tag{2.20}$$

and the addition of these two equations gives

$$\mathbf{r}(t+\delta t) = 2\mathbf{r}(t) - \mathbf{r}(t-\delta t) + \mathbf{a}(t)\delta t^2 \tag{2.21}$$

The new positions of the particles are generated by the equation 2.21, and the new potentials are calculated from equation 2.18. A limitation of the Verlet algorithm is that the velocity term is eliminated in the equation, which is sometimes desired. Other algorithms have been developed to include the velocity, including the velocity Verlet [270], and the leap-frog algorithm (used in this research). The leap-frog algorithm by Hockney et al. is fast and accurate for most types of MD, and calculates the velocity during the integration procedure [269]. The velocities at time $t + \frac{1}{2}\delta t$ are calculated as

$$\mathbf{v}(t+\frac{\delta t}{2}) = \mathbf{v}(t-\frac{\delta t}{2}) + \mathbf{a}(\mathbf{r}(t))\delta t \tag{2.22}$$

and the Taylor expansion of $\mathbf{r}$(t) at time $t = t + \delta t$ yields

$$\mathbf{r}(t+\delta t) = \mathbf{r}(t) - \mathbf{v}(t+\frac{1}{2}\delta t)\delta t \tag{2.23}$$

The velocity at time $t = t + \frac{1}{2}\delta t$ is calculated from the position and acceleration at time t as well as the previous velocity at $t = t - \frac{1}{2}\delta t$. Now the values have been derived for the position $r(t + \frac{1}{2}\delta t)$, which themselves provide the values needed for the next velocity step. In this way, the velocity and the positions leap-frog over each other.

2.5.1 Temperature coupling

Controlling the temperature of a system is often wanted and necessary due to solute drift during equilibration, drift due to force truncation and integration errors and as a result

of heating through external or frictional forces. There are several methods that have been proposed to apply temperature coupling to the system, these include the extended-ensemble Nosé-Hoover scheme [271, 272], the weak coupling scheme of Berendsen [273], and the more recently developed weak coupling with velocity-rescale method [274]. The extended-ensemble approach first proposed by Nosé [271] and later modified by Hoover [272] produces the correct description of the canonical ensemble and is now known as the *Nosé-Hoover temperature coupling* algorithm. This algorithm couples the temperature by introducing a thermal reservoir and frictional term to the system Hamiltonian (equation 2.18). This effects the thermal bath coupling of the system and ensures a proper ensemble is sampled. However, because this thermostat is strongly coupled to the system, it is more difficult to reach equilibrium, often oscillating around it. For this reason, it is common to begin a simulation with weakly coupled thermostat, such at the Berendsen thermostat [273].

The *Berendsen temperature coupling* algorithm mimics weak coupling with first-order kinetics to an external heat bath with a given temperature T_0. The effect of this algorithm is that a deviation of the system temperature from T_0 is slowly corrected according to,

$$\frac{dT}{dt} = \frac{T_0 - T}{\tau}. \tag{2.24}$$

which means that a temperature deviation decays exponentially with a time constant τ. The Berendsen weak coupling method has the strength that coupling can be varied and adapted depending on the simulation requirements, additionally it is extremely efficient for relaxing a system at a target temperature. While the Berendsen thermostat is simple and stable, it does not sample a well defined ensemble [274].

The thermostat algorithm developed by Bussi et al. [274] is an extension of the Berendsen thermostat with an additional stochastic term to enforce the correct distribution for the kinetic energy. The additional term ensures the correct canonical ensemble is sampled, and like the Berendsen thermostat it is weakly coupled, such that it easily equilibrates. The velocities are scaled according to

$$dK = (K_0 - K)\frac{dt}{\tau} + 2\sqrt{\frac{KK_0}{N_f}}\frac{dW}{\sqrt{\tau}} \tag{2.25}$$

where K is a value proportional to the temperature T in equation 2.24, N_f is the number of degrees of freedom and dW is a stochastic term.

Throughout this thesis the Berendsen and Bussi thermostat implementations have been used.

2.5.2 Pressure coupling

With similar reasoning to that behind the need for temperature coupling, a system can also be coupled to a pressure bath to give the correct representation of a molecular system. The two most widely used methods are the Berendsen algorithm [275] and the extended-ensemble Parrinello-Rahman approach [276]. Both these methods couple to a *pressure bath* such that the dimensions of the unit cell will be scaled to simulate a given pressure.

In the *Parrinello-Rahman* barostat the equations of motion are extended to include a box vector term, similar to the addition of a frictional term in the *Nose-Hoover* thermostat. By combining these two algorithms, in theory, the true NPT ensemble can be obtained.

Alternatively, the *Berendsen pressure coupling* algorithm rescales the cell dimensions at a rate inversely proportional to a user defined time constant τ_p in equation 2.26. If τ_p is large, the rate of change in pressure will be small. If τ_p is too small however this can lead to large jumps in the dimensions of the system.

$$\frac{dP}{dt} = \frac{P_0 - P}{\tau_p} \tag{2.26}$$

2.5.3 Bond constraint algorithms

As previously discussed, one of the most demanding aspects of simulation is the computation of nonbonded interactions because for some large systems, millions of pairs have to be evaluated for each time step. One way to enhance computational efficiency is by extending the time step used for each calculation. However, this will introduce systematic errors, as the shortest timescale in biological simulations are the hydrogen bond vibrations at 1 fs. Fortunately, in most simulations the bond vibrations are not of interest *per se*, and can be removed entirely by introducing bond constraint algorithms such as SHAKE [277] or LINCS [278]. Constraints make it possible to extend time steps to 2 fs.

The most widely used algorithm for large molecules is SHAKE, in which the bonds and

angles are reset to prescribed values by moving the bonded particles parallel to the old bond directions. SHAKE is an iterative method, where all the bonds are reset sequentially to the correct length. Because the bonds are coupled, this procedure has to be repeated until the desired accuracy is reached. SHAKE is simple and numerically stable since it resets all constraints within a prescribed tolerance, however this method has the drawback that no solutions may be found when displacements are large. This is due to the coupled bonds being handled one by one, thus correcting one bond may tilt a coupled bond so far that the method does not converge. A fast, reliable Linear Constraint Solver (LINCS) algorithm for molecular simulations was developed by Hess *et al.* where the constraints themselves are explicitly reset instead of the derivatives of the constraints [278]. The derivation of the algorithm is presented in terms of matrices; however no matrix multiplications are needed, making the method applicable to very large molecules. Although the LINCS algorithm shows the same accuracy as SHAKE, it is three to four times faster [278].

2.6 Conformational Sampling problem

Knowledge of the entire potential energy landscape, including all minima *local* and the *global minimum* of a system would enable the complete description of the relevant structures, conformations and their free energies. However, the dimensionality of the configurational space and the number of *local minima* is often so high that it is impossible to sample the complete potential energy landscape. Currently, there is no method that guarantees the determination of the *global minimum* in any practical amount of time. However, there are methods that can be used to accelerate the exploration of the potential energy landscape in an attempt to overcome potential energy barriers between local minima and ultimately obtain the *global minimum*. Molecular dynamics is a useful method for simulating the time evolution of a system and exploring the free energy landscape in the neighbourhood of a local minimum, it can however be difficult to extensively explore the free energy landscape of protein folding, misfolding and aggregation, using classical MD. For instance the system can easily be trapped in one of the local minima and fail to properly sample the entire conformational space. To overcome this inherent limitation it is necessary to apply methodologies that are capable of accelerating rare events, specifically,

configurational changes that involve the crossing of large free energy barriers. Many of these so called advanced sampling techniques were developed with a specific goal or purpose, generally these techniques fit into three search and sampling enhancement methods. One group of methods performs deformations or smoothing of the potential energy surface, such as local potential energy elevation [279] or conformational flooding [280]. The second type consists of methods that scale the system or simulation parameters, such as temperature annealing [281] or mass scaling [282]. And the third type are multi-copy searching and sampling algorithms, such as replica-exchange and multicanonical algorithms [283]. Three of the most widely used methodologies capable of exploring wider conformational space are Metadynamics [284], Umbrella Sampling [285] and Replica Exchange Molecular Dynamics methods [286].

2.6.1 Metadynamics

Metadynamics [285] is a powerful technique in which the free energy of the system is obtained from non-equilibrium simulations. Recently it has been used to determine the free energy of adsorption of amino acids at the aqueous graphene interface [251]. The metadynamics algorithm encourages the system to visit new conformational space rather than be confined to regions of local minima. This is achieved by introducing an additional bias potential (or force) that acts on a selected number of degrees of freedom, referred to as the collective variables (CVs). The CVs, are assumed to provide a coarse-grained description of the system, and are explicit functions, s($\mathbf{x}$) of the atomic coordinates, $\mathbf{x}$. The dynamics of the system is biased by a history dependent potential constructed as a sum of Gaussians centred on the trajectory of the collective variables,

$$V_b(s(\mathbf{x}),t) = \int_0^t d\acute{t} \frac{W}{\tau_G} exp \frac{-[s(\mathbf{x}) - s(\mathbf{x}(\acute{t}))]^2}{2\delta\sigma^2} \tag{2.27}$$

where W is the height, $\delta\sigma$ is the width of the gaussians and τ_{G} is the rate of their deposition. After a transient period, the Gaussian potential compensates the free energy, allowing the system to efficiently explore the space defined by the CVs. An accurate free energy reconstruction in several, CVs can be obtained with this method, however its performance deteriorates with increased dimensionality [285]. Thus when using a larger

number of CVs the effectiveness in conformational sampling of the method decreases, limiting its usefulness.

To alleviate this drawback several extensions of metadynamics have been proposed, these include the *multiple walkers* metadynamics version [287], *parallel tempering* metadynamics [288] and *bias exchange* metadynamics [289]. The *multiple walkers* technique introduces N replicas of the same system whereby each replica adds to the history dependent potential thus a free energy profile can be produced in 1/N of the time. Similarly the *parallel tempering* metadynamics technique introduces multiple replicas of the same system, however each replica is simulated at an increased temperature, this method of swapping configuration is also referred to as replica exchange and is discussed in more detail later in this section. The configuration of replicas, at adjacent temperatures, are exchanged while the potential energy is increased. This technique allows the system to quickly explore the free energy landscape and overcome large energy barriers, additionally the tempering of the system enables the sampling over degrees of freedom not explicitly included in the CV space. An extension of the replica exchange metadynamics approach is the bias exchange method. This technique also simulates multiple replicas, however these replicas differ by the CV that the biasing potential is applied to. At a fixed time interval a swap of the bias potentials between pairs of replicas is attempted. In this way it enables the exploration of a high dimensionality free energy landscape while only biasing a few dimensions of each replica.

2.6.2 Umbrella Sampling

Another biasing technique is umbrella sampling, whereby the free energy as a function of an inter- or intra-molecular "reaction" coordinates can be produced. Examples of the reaction coordinate include the distance between two atoms, or the distance between the COM of a peptide and a nanomaterials surface are often of interest when investigating molecular association/dissociation at nano interfaces. The free energy profile along a chosen coordinate is known as the potential of mean force (PMF). Various methods have been proposed for calculating potentials of mean force, one simple formulation is,

$$A(x) = -k_B T ln[P(x)] \tag{2.28}$$

where P(x) is the probability density over the coordinate x. It is possible to obtained this property from long timescale MD simulation, it is often in practically impossible, as a large region of the PMF corresponds to a region of low occupancy. Thus the PMF can be obtained by appling a biasing potentially that ensures the peptide is conformation is sampled along the reaction coordinate, one such technique is called umbrella sampling. The umbrella sampling method of Torrie and Valleau [285] overcomes the problem of insufficient sampling of certain regions of the reaction coordinate x by introducing an the biasing potential $W(x^N)$. Using a simple example of two interacting particles, the biasing potential would force the two bodies to sample prescribed separation distances.

$$V'(x^N) = V(x^N) + W(x^N) \tag{2.29}$$

Usually, a number of simulations with different reaction coordinate location are carried out, each one confining the position of the particle by applying the bias, $W(x^N)$, each new position is called a "window". Often a harmonic potential is used to restrain the particle at the reaction coordinate location of the specified window. The resultant probability density over the reaction coordinate is the biased density P(x'). The unbiased density, P(x), and thus the unbiased PMF is obtained by using the Weighted Histogram Analysis Method (WHAM) of Kumar et al. [290].

2.6.3 Replica exchange molecular dynamics

One way to overcome the energy barriers inherient in protein folding and protein nanomaterial interactions is to provide addition energy to the system, resulting in accelerated sampling. Additional energy can be introduced by increasing the temperature of the system, a common approach that uses this method is temperature based replica exchange molecular dynamics (REMD) [286]. REMD is a powerful technique able to enhance conformational sampling, compared to running parallel simulations at constant temperatures. This method uses several noninteracting replicas of the same system simulated at different temperatures all running concurrently. At a selected exchange time a Monte Carlo temperature exchange is performed between the replicas, with the exchange of configuration accepted or rejected based on a Metropolis acceptance criterion [291]. The Metropo-

lis acceptance criterion states that if the difference between the energy of the resulting conformation and the energy of the current conformation is negative, then the move to another temperature is accepted. However, if the difference in energy between the two states is positive, the random probability check will be conduced and if the result is below a specific probability (determined by the difference in energy between the resultant and current states) a swap will occur. High free energy barriers are crossed by the high temperature replicas while the exchanges allow the low temperature replicas to sample a larger conformational space. To ensure that each replica follows a Boltzmann distribution only neighbouring temperatures are probed for exchanges. While enhancing the exploration of conformational space, useful kinetic information cannot easily be extracted using the REMD method, such as the adsorption or desorption from interfaces. In order to effectively sample the energy landscape of a protein in explicit solvent, temperature REMD requires a large number of replicas and such can limit the computational effectiveness of this method. More recent formulations of the REMD method have been aiming to overcome this limitation.

Replica exchange with solute tempering

An alternative to the temperature-REM is the Hamiltonian-REM, which transforms the Hamiltonian at each replica level rather than the temperature. Fukunishi et al. showed that for a simple transformed Hamiltonian the sampling efficiency can be comparable or superior to T-REM [292]. A unique feature of the Hamiltonian REM formalization is the ability to modulate (increase the energy of) a part of the system. Liu et al. developed a H-REM that used this feature to only modulate the solute in the simulation [293]. The acceptance probability in this new method only scales with the number of degrees of freedom of the solute. As a result the number of replicas required to achieve a similar efficiency as T-REM is significantly reduced, overcoming one of the major limitations of the T-REM. Liu et al. termed the new method, replica exchange with solute tempering (REST). The REST method has been implemented in Gromacs following the method outlined by Terakawa et al [294]. Firstly a potential energy function V is divided up into three terms,

$$V = V_{ss} + V_{sw} + V_{ww}, \tag{2.30}$$

where V_{ss}, V_{sw} and V_{ww} are the intra solute potential, the solute-solvent interaction potential and the solvent-solvent potential respectively. Two end point potentials, V_L and V_H, are then defined,

$$V_L = \frac{\beta_L}{\beta} V_{ss} + \sqrt{\frac{\beta_L}{\beta}} V_{sw} + V_{ww} \tag{2.31}$$

and

$$V_H = \frac{\beta_H}{\beta} V_{ss} + \sqrt{\frac{\beta_H}{\beta}} V_{sw} + V_{ww} \tag{2.32}$$

where β is the inverse of the system temperature, β_L is the inverse of the lowest temperature usually the system temperature, while β_H is the inverse of the highest "effective temperature". The factor,

$$\frac{\beta_H}{\beta} < 1, \tag{2.33}$$

reduces the intra solute interactions thus enhances the solute dynamics. The solute-solvent interaction term is scaled by the square root of this ratio and the solvent-solvent term is not scaled. Using the two potentials V_L and V_H as two-ends, the replica potentials, V_i, can be introduced as their linear combination. The potential for the replica i is determined as,

$$V_i = (1-\lambda_i)V_L + \lambda_i V_H = \frac{\beta_L(1-\lambda_i) + \beta_H \lambda_i}{\beta} V_{ss} + \left(\sqrt{\frac{\beta_L}{\beta}}(1-\lambda_i) + \sqrt{\frac{\beta_H}{\beta}}\lambda_i \right) V_{sw} + V_{ww} \tag{2.34}$$

This series of potential defines the replicas within the Hamiltonian REM formulation. The replica with λ_i corresponds to the real Hamiltonian which we are interested in, and all other replicas are artificial ones introduced solely for enhancement of the solute conformational sampling. The effective temperature of each replica is determined by,

$$\beta_i = \beta_L(1 - \lambda_i) + \beta_H\lambda_i \tag{2.35}$$

which is the simple interpolation of the two-ends inverse temperatures β_{L} and β_{H}. Where β_{i} is the inverse of the system temperature for each of the replicas. This new implementation of replica exchange enables significantly less replicas to be used and thus can be applied to much larger system sizes at a lower computational cost compared to other replica exchange methods.

2.7 Simulation procedures employed in this work

The general procedure for the construction and the simulation of the protein-nanomaterial complexes in solution employed in this thesis is briefly described in this section. The details such as specific parameters used, cutoffs, box dimensions, specific methodologies implemented, simulation times etc. are described in the Computational Details section of each chapter. Generally, the simulation systems were built and calculations were performed using the simulation package Gromacs 4.6 [13]. The starting coordinate for peptides modelled were obtained from the Protein Data Bank (PDB, http://www.rcsb.org/pdb/) for the monomeric apoC-II(60-70) peptide, the oligomer structures of apoC-II(60-70) were obtained from the previous work in the group [257, 258] to determine the stability of these oligomers under various conditions, see Chapter 3 for more details. The structure of the full apoC-II fibril has also been obtained from previous work based on NMR studies and molecular dynamic simulations, see Chapter 3 for more details. The protein under study was initially stripped of all the hydrogens, before it was re-built with the new parameters from the selected force field. The graphitic nanomaterials were produced by using the nanotube and graphene surface builder implemented in the Visual Molecular Dynamics (VMD) program. The nanomaterials were parameterised using the sp_2 carbon parameters in the GROMOS43a1 parameter set. After the topology files for the protein and nanoparticles were compiled and the two structure files combined, a simulation box was constructed with chosen proportions, to produce a perfectly periodic nanomaterial, in the case of graphene and the CNT. The dimensions of the box can vary depending on the system's size, however a minimum distance of 10 Å was set from the periphery of the

protein to the edge of the box to eliminate cross-interactions. The nanomaterials were frozen in their initial position in all simulations. The simulation box was then filled with explicitly represented water molecules until water density of 1.0 g/cm^3 was obtained. If the solutes (peptides) had a non-zero total charge, counterions were incorporated in the simulation box to neutralise the system. Once the construction of the system had been finalised, energy minimisation was performed to eliminate bad van der Waals contacts or steric clashes between the protein, nanomaterial and water. The first-order minimisation method of steepest descent was applied to reach the lowest local energy point, where minimisation was considered converged when the maximum force exerted on the system was smaller than 20 kJ/mol/nm. The solvent equilibration stage involved constant volume/temperature (NVT) molecular dynamics simulation at T = 300 K with protein atoms restrained to allow the solvent to relax around the solute. Following the equilibration stages, data collection for analysis was performed in the NVT ensemble with constant temperature of 300 K, for total times specified in each results chapter. The leap-frog algorithm is utilised by default in the Gromacs package to integrate Newton's equations of motion, with a timestep of 2 fs unless otherwise specified. Additionally the LINCS algorithm was used to constrain the bond lengths to their equilibrium values [278].

Chapter 3

Protein and nanomaterials investigated

3.1 Overview

In this thesis computational methods were applied to gain insight into the interactions, dynamics and aggregation of an amyloidogenic peptides and proteins in the presence of dimensionally different graphitic nanomaterials. The protein of interest, apolipoprotein C-II (apoC-II), and its derivative peptides has been investigated with three different carbon nanomaterials: C60 fullerene, a single walled carbon nanotube and a graphene sheet.

ApoC-II has been extensively studied under a range of conditions both experimentally and computationally, making it a suitable model to explore the impact that nanomaterials may have on its behaviour. The different dimensionality and curvature of these carbonaceous nanomaterials enable us to identity the impact that curvature and shape of nanomaterials with similar surface chemistry has on protein interactions, dynamics and aggregation propensity.

3.2 Apolipoprotein C-II

Apolipoproteins are an important class of serum proteins that are found in protein-lipid complexes known as lipoprotein particles. Lipoprotein particles, such as low-density lipoprotein (LDL) and high-density lipoprotein (HDL) are responsible for the transport

of triacylglycerols, cholesterol and phospholipids in the blood stream [295]. A particular type of apolipoprotein is apolipoprotein C-II (apoC-II), this protein is a 79 residue co-factor of the very-low-density lipoproteins. ApoC-II is key in the activation of lipoprotein lipase [296], this enzyme is found in capillaries and catalyses the hydrolysis reaction of triacylglycerols to glycerol and fatty acids [297]. A human deficiency of apoC-II is associated with elevated triacylglycerol levels in the blood, which is consequently linked to atherosclerosis and, by extension, the risk of heart disease and stroke [298, 299].

3.2.1 ApoC-II structure

	1	2	3	4	5	6	7	8	9	10
0	Thr	Gln	Gln	Pro	Gln	Gln	Asp	Glu	Met	Pro
10	Ser	Pro	Thr	Phe	Leu	Thr	Gln	Val	Lys	Glu
20	Ser	Leu	Ser	Ser	Tyr	Trp	Glu	Ser	Ala	Lys
30	Thr	Ala	Ala	Gln	Asn	Leu	Tyr	Glu	Lys	Thr
40	Tyr	Leu	Pro	Ala	Val	Asp	Glu	Lys	Leu	Arg
50	Asp	Leu	Tyr	Ser	Lys	Ser	Thr	Ala	Ala	Met
60	Ser	Thr	Tyr	Thr	Gly	Ile	Phe	Thr	Asp	Gln
70	Val	Leu	Ser	Val	Leu	Lys	Gly	Glu	Glu	

Table 3.1: Primary sequence of apoC-II (PDB code 1SOH).

The initial determination of the apoC-II structure was conducted using nuclear magnetic resonance (NMR) techniques in the presence of sodium dodecyl sulphate (SDS) micelles by MacRaild et al. [300] and Zdunek et al. [301]. Further work utilising dodecylphosphocholine (DPC) micelles enabled the elucidation of the lipid bound apoC-II structure [302].

The primary sequence of human apoC-II is listed in table 3.1. NMR showed that the first 12 residues of apoC-II are structurally heterogeneous, while the rest of the protein forms predominately amphipathic helical structures [301, 302], with opposing polar faces oriented along the long axis of the helix. The amphipathic N-terminal region of apoC-II and α-helical regions that span the residues 16 to 38, 45 to 57 and 65 to 74 [301], mediate reversible binding to lipoprotein surfaces [303, 304]. While the C-terminal region

of apoC-II residues 63, 66, 69 and 70 played an important role in the activating lipoprotein lipase [305, 306, 307, 301]. A representation of the secondary structure of the lipid bound apoC-II(13-79) is shown in Figure 3.1.

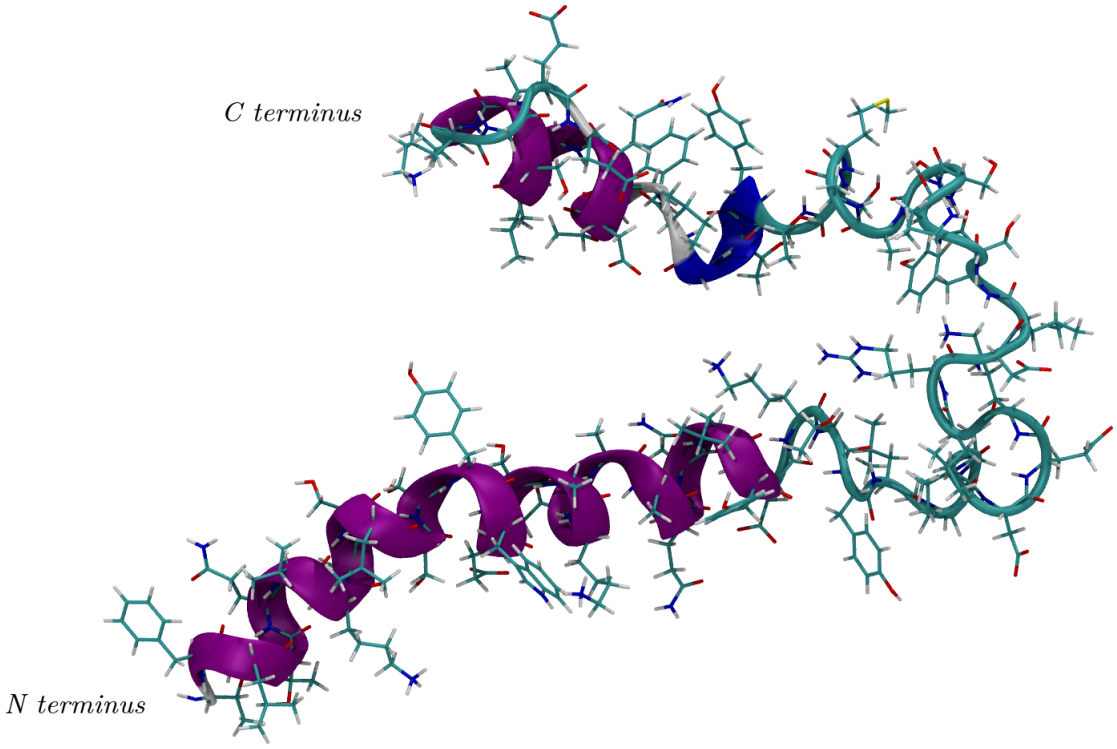

Figure 3.1: Cartoon representation of apoC-II(13-79) showing secondary structure and side chains. Secondary structure colour codes: magenta=α-helix, cyan=turn, white=coil, blue=3-10 helix.

3.2.2 ApoC-II misfolding and aggregation studies

ApoC-II is comprised of mostly α-helical structures in high lipid concentration environment, however it readily aggregates under lipid depleted conditions. X-ray diffraction has shown that apoC-II forms fibrils with the characteristic cross-β structure of amyloid fibrils [308]. These fibrils accumulate as amyloid deposits located within atherosclerotic plaques *in vivo* [309].

Interestingly apoC-II fibrils are relatively soluble, as such they have been characterised extensively by biophysical techniques [310, 302, 311]. Binger and co-workers used analytical ultracentrifugation to show that mature fibrils assemble via a reversible pathway that includes fibril breaking and joining [311]. A number of conditions were identified to

affect the fibrillation of apoC-II including the presence of auxiliary proteins [312], macromolecular crowding agents [313] and the presence of phospholipids below and above the critical micelle concentrations (CMC) [314, 313]. Additionally *in vitro* studies showed that oxidized cholesterol metabolites can trigger the aggregation of apoC-II to form amyloid deposits [315]. Similarly shear flow induced irreversible change in apoC-II secondary structure and accelerated fibril formation [299]. Alternatively, the oxidation of methionine residues, Met9 and Met60, has been demonstrated to inhibit fibril formation of the mature apoC-II [316]. The oxidized methionines are structurally less flexible, which possibly leads to a perturbation of the hydrophobic core [316]. Similarly chaperones, such as clusterin or α-crystallin, have been shown to suppress apoC-II amyloid formation [313, 312].

A simple 'letter G-like' β-strand-loop-β-strand model of the apoC-II fibril was recently proposed, Figure 3.2, by combining electron microscopy, single-cystein substitution mutantions, fluorescence resonance energy transfer (FRET) analysis and optimised using molecular dynamics [299]. Initial X-ray diffraction analysis indicated a simple cross-β-structure composed of two parallel β-sheets [299]. Further examination utilising advanced microscopy techniques such as transmission electron microscopy, scanning transmission electron microscopy and atomic force microscopy indicated that the fibrils are flat ribbons and are composed of one apoC-II molecule per 4.7 Å rise of the fibril structure [299]. The β-sheets were determined to be parallel in-register by analysis of cross-linking results from single-cystein substitution mutants. FRET analysis of the apoC-II fibrils provided distance constraints between selected donor and acceptor pairs located within the fibrils, allowing the development of the proposed model [299]. Subsequent all-atom molecular dynamics simulations showed that the model contained a stable cross-β-core with a flexible connecting loop devoid of persistent secondary structure [299]. The regions of apoC-II that are involved in hydrogen bonding within β-sheets of amyloid fibrils were identifed using hydrogen/deuterium exchange and proteolysis studies [317]. Wilson and co-workers showed that the bonding was between residues 19-37 and 57-74. Additionally, peptide fragments, composed of residues 60 to 70 and 56 to 76, have been shown to exhibit an inherent propensity for amyloid fibril formation in solution. In fact apoC-II(56-76) readily formed fibrils, although with a different morphology and different thioflavin T (ThT) fluorescence yield compared to the full-length apoC-II.

Wilson et al. proposed that the apoC-II(60-70) segment may be the driving factor in the propensity of apoC-II and its peptide derivatives to aggregate and accumulate in amyloid deposits *in vivo* [317]. The central region, 60-70, of the apoC-II(56-76) peptide derivative, retains the ability to form fibrils in lipid depleted conditions [256]. The effect that various environmental conditions, including different pH, concentration of lipids, the methionine oxidation and residue mutation had on the fibrillation kinetics of these small peptide derivatives of apoC-II, have been investigated both *in silico* and *in vitro* [316, 257, 258, 256, 255].

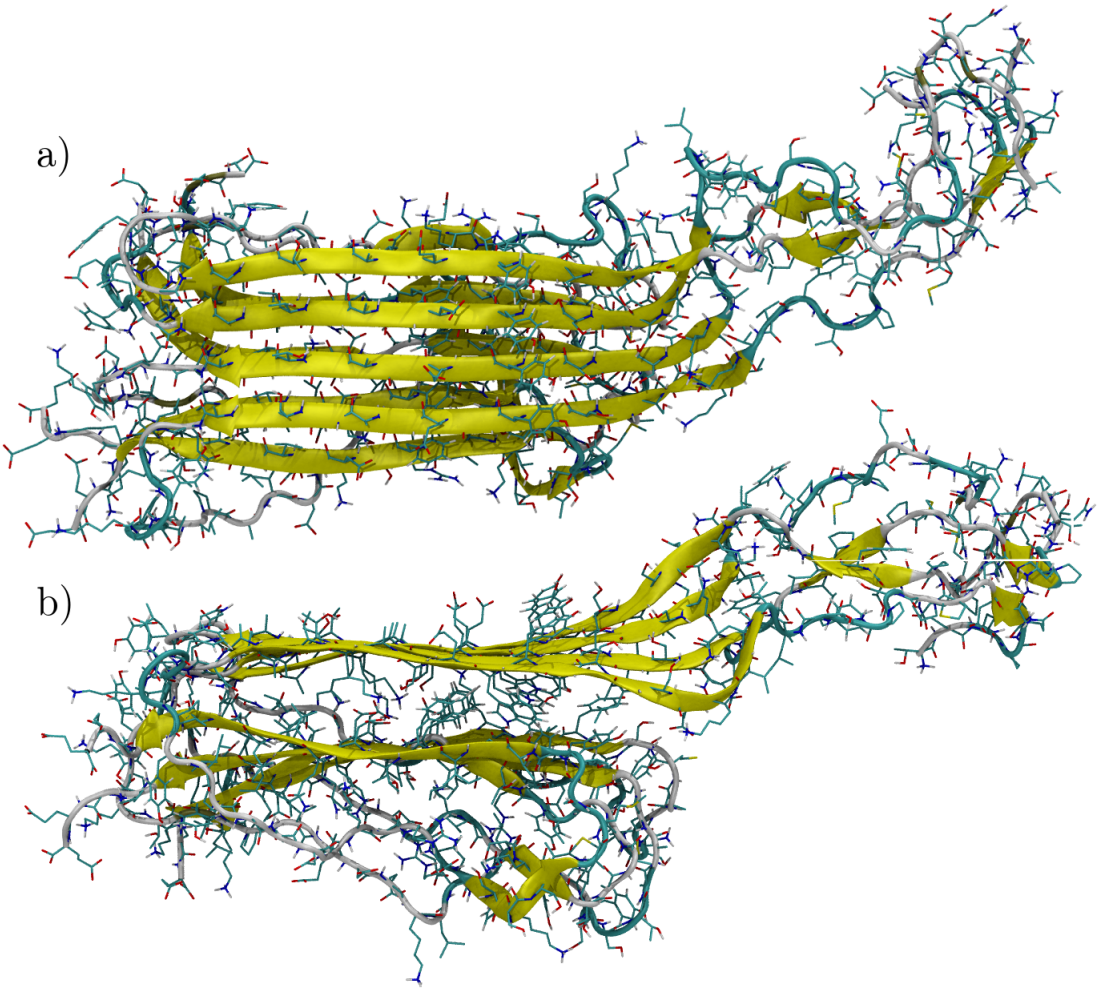

Figure 3.2: All-atom representation of apoC-II(1-79) fibril, optimised through molecular dynamics simulations [299], showing secondary structure and side chains. Top a) and side b) view of the apoC-II(1-79) fibril. Secondary structure colour codes: yellow=extended β-sheet, magenta=α-helix, cyan=turn, white=coil, blue=3-10 helix.

Oxidation and mutation of Met60 of the apoC-II(56-76), apoC-II(60-70) peptide deriva-

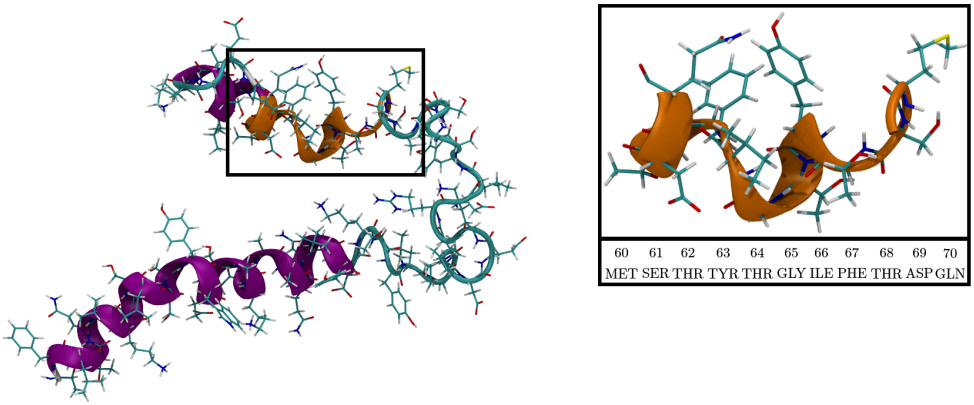

Figure 3.3: ApoC-II(13-79) and amyloidogenic peptide apoC-II(60-70).

tives and apoC-II(60-70) oligomers has been shown to effect their fibril formation kinetics, dynamics and stability in different ways [316, 258, 256]. Met60 was mutated to the hydrophillic Gln and hydrophobic Val. The wild-type apoC-II(56-76) and (56-76)Met60Gln peptides readily assembled into fibrils with similar lag phase, whereas oxidation of the Met resulted in slower fibril formation kinetics of apoC-II(56-76) and a less flexible structure, however fibril formation was not completely inhibited. Mutation of Met60 to Val resulted in the slowest fibril formation kinetics of apoC-II(56-76) and a tendency to explore a wider range of conformational space, however this mutation exhibited totally different aggregation kinetics compared to the full-length apoC-II with the same mutation. Simulation studies showed the behaviour of apoC-II(56-76) was different to that of the full length apoC-II suggesting that the mechanism of fibril formation may also be different [316].

The shorter apoC-II(60-70) peptide derivatives fibrillation kinetics were also investigated at different conditions including, the same Met60 oxidation as the apoC-II(56-76) as well as in different pH environments and in the presence of lipids. Distinct differences in apoC-II(60-70) secondary structure with the mutations and under environmental effects, were identified by molecular dynamics and correlated with the same fibril-favouring or fibril-disrupting conditions, as determined experimentally. At fibril-favouring conditions (neutral and low pH), the peptide preferentially adopts structures similar in shape to a β-hairpin, with the aromatic residues Tyr63 and Phe67 lying on the opposite faces of the hairpin, while under fibril-disruptive conditions (lipid-rich and oxidised Met) significantly different structures were obtained, with the aromatic residues Tyr63 and Phe67

orientations at the same face of the hairpin. The formation of a strong hydrophobic core, as exhibited in a β-hairpin structure, has been suggested to be favourable for peptide interaction and subsequent fibril formation [256].

Interestingly when the apoC-II(60-70) peptide undergoes the same set of Met60 mutations as tested for the longer apoC-II(56-76) peptide, it exhibits different fibrillation kinetics [258]. ThT fluorescence measurements determined the fibril formation kinetics of apoC-II(60-70) wild-type the and mutated variants. Reduced kinetics were observed for the oxi-Met and Met60Gln peptides, resulting in a longer lag phase, while the wild-type and Met60Val peptides formed fibrils faster. Molecular dynamics simulations revealed that fibril forming structures, specifically the formation of a β-hairpin, were adopted by the mutated and oxidised apoC-II(60-70) monomer [258]. However, the two mutations that experimentally showed a longer lag phase displayed increased structural flexibility and aromatic angle orientation, where the aromatic side-chains were located on opposite faces of the hairpin structure albeit with more freedom than the wild-type peptide. These difference were suggested to explain the different fibrillation kinetics observed for these mutations experimentally, indicating that the aromatic residues play a critical role in the fibrillation of apoC-II(60-70) [258]. Further investigation of oligomeric apoC-II(60-70) aggregates showed that extended β-sheet structures stabilize preformed dimers and tetramers of apoC-II(60-70), these oligomers and the monomeric apoC-II(60-70) are shown in Figure 3.4. The results suggested that a tetrameric species in anti-parallel configuration can serve as a possible seed for fibril formation of apoC-II(60-70), where side-chain-side-chain contacts contribute to the fibril stability, while the maximum exposure capacity of the whole peptide (backbone and aromatic side-chains) promotes the growth of the fibril-seed due to the increase in surface area available for interactions with other peptides [258].

Determination of the effect that sub-micellar concentrations of lipids had on amyloid fibril formation of the apoC-II(60-70) peptide was conducted utilising ThT fluorescense and molecular dynamics [255]. The ThT studies showed that sub-micellar levels of the short-chain phospholipids D5PC and D6PC strongly inhibited amyloid formation of apoC-II(60-70) peptide. In contrast, the sedimentation equilibrium analysis of these peptide-lipid mixtures indicated the presence of soluble oligomeric complexes. Hung et al. determined the dimerisation free energy, utilising the umbrella sampling method, of several

dimer complexes in the presence and absence of lipids [255]. They showed that short-chained phospholipids promote the formation and stabilisation of dimers by enhancing their inter-subunit hydrophobic interactions. The experimental and computational results suggested that peptide-bound lipids inhibit amyloid fibril formation by trapping of dimers and other oligomeric species in diverse non-fibril competent conformations. This in turn reduced their likelihood of acquiring subunit conformations capable of fibril nucleation and growth [255]. Additionally, increased lipid concentration led to a progressive decrease in solvent accessible surface area of monomeric apoC-II(60-70), while at the same time an increase in lipid-peptide interactions was observed. The aromatic residues, Tyr63 and Phe67, were involved in the most favourable interactions between the lipids and peptide, these interactions reduced the conformational lability of the peptide, which in turn could potentially slow the aggregation rate. Interestingly, the peptide conformations were affected by lipid concentration where low lipid concentrations resulted in extended β-strand configurations while at higher concentrations the peptide was trapped into fibril incompetent conformations [257].

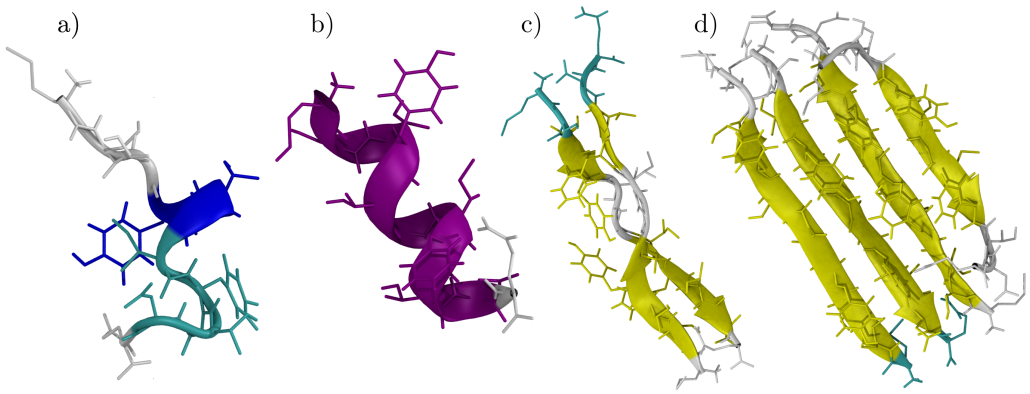

Figure 3.4: ApoC-II(60-70) peptide configurations, a) apoC-II(60-70) wild-type monomer, b) apoC-II(60-70) helix monomer, c) apoC-II(60-70) anti-parallel dimer and d) apoC-II(60-70) anti-parallel tetramer. Secondary structure colour codes: magenta=α-helix, cyan=turn, white=coil, blue=3-10 helix, yellow=extended β-sheet.

More recently a cyclic peptide, cyc(60-70), derived by disulfide cross-linking of cysteine residues added to the termini of the apoC-II(60-70) peptide, has been demonstrated as an effective inhibitor of apoC-II(56-76) and apoC-II(60-70) peptide fibril formation [318]. NMR spectroscopy revealed a well-defined structure of cyc(60-70) comprised of two faces, a hydrophillic and a more hydrophobic face, containing Met60, Tyr63, Ile66 and Phe67

side chains. Reduction of the disulfide bond or scrambling of the amino acid sequence within cyc(60-70) impaired its ability to inhibit fibril formation. Molecular dynamics was conducted to determine the structural and dynamic differences of the native and scrambled cyc(60-70). This study showed the native cyc(60-70) consisted of a flexible central region while the scrambled sequence had much reduced flexibility and greater number of intramolecular hydrogen bonds. These results suggested that the inhibiting effect of the cyc(60-70) peptide on the apoC-II peptide fibrillation was related to the distinct hydrophobic and hydrophilic faces of cyc(60-70) enabling it to interact transiently with fibrillogenic peptides and inhibit fibril assembly [318]. Additional all-atom molecular dynamics simulations and electronic structure calculations, were used to determine the mechanism of cyc(60-70)'s ability to inhibit apoC-II(60-70) fibril formation [319]. The results showed that the cyclic peptide induced flexibility in the apoC-II(60-70), suggesting that one mechanism by which the cyc(60-70) inhibits fibrillation a disruption of configurations that are required to be adopted for fibril formation. Interestingly, the cyc(60-70) itself has reduced conformational flexibility upon complexation with the apoC-II(60-70), this behaviour was mediated by hydrophobic interactions, leading to the capping of the fibril-forming region of apoC-II(60-70) generating an outer hydrophillic shell that would not have been favorable for further peptide association. The electronic structure calculations revealed that the apoC-II(60-70) bound most strongly to the hydrophobic side of the cyc(60-70) and weakest to the hydrophilic side. This amphipathic character for which it was named a "Janus" peptide, enables the cyc(60-70) to be an effective inhibitor of apoC-II(60-70) fibrillation [319]. The work lead to a hypothesis that Janus peptides (or their mimics) can potentially serve as amyloid fibril inhibitors.

3.3 Carbonaceous nanomaterials

The element carbon is ubiquitous in nature, present in most of the chemical substances found to this date, it is the basic building block within all organic matter and it is even a fundamental catalytic component of the fusion of hydrogen into helium within the sun. Carbon can exist in almost pure forms, these take on the form of several allotropes, such as diamond, graphite and some that are nano in scale such as fullerenes, which consist of

buckyballs and nanotubes, as well as the single or few layered graphite known as graphene. These nanoscaled carbon materials effectively contain 100% carbon and dimensions often between a few and hundreds of nanometers. While it is often thought that carbon nanomaterials are a recent discovery they have actually been used for more than 3000 years, in the form of carbon black which is used in rubber tires and the pigment industry. However, compared to the amorphous carbon materials, crystalline carbon nanomaterials (CNM) are a more modern creation. In general crystalline CNM have been produced using advanced techniques such as high voltage arc, laser ablation, and chemical vapor deposition [320]. They are characterized by trivalent carbon atoms with an sp^2 hybridization placed in a two-dimensional lattice, which can close into spheres (fullerenes), or cylinders (single-walled/multi-walled carbon nanotubes, SWCNTs/MWCNTs) or remain in a fully planar geometry (graphene), mimicking zero (0D), one (1D) or two-dimensional (2D) structures, respectively [320].

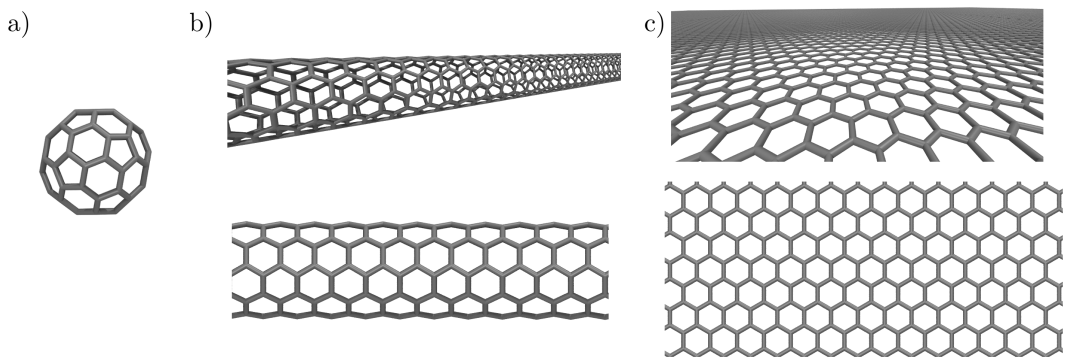

Figure 3.5: Atomistic representative of the three graphitic nanomaterials explored in this thesis, a) 0D C60 fullerene, b) 1D single wall carbon nanotube and c) 2D graphene.

3.3.1 Fullerenes

Fullerenes encompass any molecule that is entirely composed of carbon in the form of an ellisoid, tube or hollow sphere. They were first discovered in 1985 by Richard Smalley and Harry Kroto, who were awarded the 1996 Nobel prize in chemistry. The first discovered and perhaps the most well known fullerene particle is the C60 or ”buckyball”. C60 adopts a soccer ball like shape and is composed of 20 hexagons and 12 pentagons, and is the smallest fullerene molecule in which no two pentagons share an edge (as this is highly

destabilising), Figure 3.5a. Smalley and Kroto named the hollow spherical fullerenes after the famous architect that created geodesic like domes, Rickard Buckminster Fuller, hence the name "buckyball".

Thousands of fullerene molecules have been synthesized since the first discovery of the fullerene in the 1980s. Interestingly C60 is still the most stable and the most commonly occurring fullerene in the environment and can be easily found in various materials such as soot. Due to the rings of fullerenes being fused and double bonds being conjugated, they normally have unoccupied molecular orbitals and are thus capable of efficiently accepting electrons and entrapping various radical species [321]. This property makes them promising medical antioxidants to be used to protect cell growth from various toxins [322] and UVA irradiation [323]. Their unique molecular architecture and high antioxidant activity had been demonstrated to provide good antiviral activity [324] and their ability to cross cellular membranes, may enable their use as drug delivery vehicles [325].

3.3.2 Carbon nanotubes

In 1991, Sumio Iijima published the first synthesis of carbon nanotubes (CNTs), a type of fullerene, in the shape of a hollow cylinder composed of rolled sheets of sp^2 bonded carbon, Figure 3.5b [326]. CNTs can exist as a single walled CNT (SWCNT) or many concentric CNTs inside one another (multi walled CNTs) with diameters ranging from 0.4 nm up to 100 nm respectively and lengths that can go up to several micrometers. CNTs have unique structures and exceptional mechanical, thermal, magnetic, optical, electrical, surface, and chemical properties [327]. Due to these unique properties, CNTs have been used for applications in electronics, catalysis, and chemical sensing [328]. Like all pure carbon nanomaterials; CNTs have poor solubility [329] and are typically functionalised to enable dispersion in solution [330, 329]. As a consequence they have been well investigated [330] for uses in biological settings, with potential applications as biosensors, drug and vaccine delivery and novel biomaterials [331]. Recently however research has highlighted the potential toxic effects that these novel nanomaterials may have *in vivo*, in particular it has been demonstrated that inhaled CNTs can migrate to other organs within mice models [332]. Additionally these inhaled CNTs can also enter cells and accumulate in the cytoplasm [333, 334], leading to lung insult [335, 336], immunological toxicity [337] and

adverse cardiovascular effects [96].

3.3.3 Graphene

Graphite occurs naturally in sediment and rock and has been used for hundreds of years. It is a 3D structure that consists of many layers of a one atom thick 2D sp^2 bonded carbon atoms, Figure 3.5c. While studies of graphite of only a few layers had been conducted for some time [338] it was not till Geim and co-workers isolated a single-layer to produce graphene [339]. They used a mechanical exfoliation technique to isolate 2D crystals from the 3D graphite, essentially using Sellotape to peel away layers of graphite to eventually produce single layered graphene. This technique produced single or few layered flakes pinned to the substrate by only van der Waals forces and could be made free-standing by etching away the substrate.

Since this initial discovery of graphene an explosive interest in the material has led to the development of many new manufacturing techniques including micromechanical exfoliation, chemical vapor deposition, epitaxial growth, or chemical synthesis [340]. Characterisation of graphene revealed that because of the long-range 2D π-conjugation, it has extraordinary thermal, mechanical, and electrical properties [340]. These unique properties have driven the development of graphene based devices and the inclusion of graphene within devices and composite materials such as transistors, antibacterial papers, super capacitors, battery electrodes, and structural composites [340]. In bionanotechnology graphene has been proposed for applications in biosensors, drug delivery, cell detection and cell imaging [182, 341]. However graphene has been shown to induce cytotoxic effects both *it vitro* [342, 343, 344] and *in vivo* [344, 175, 345]. The current research investigating the effect that graphene and the graphitic nanomaterials have on amyloid fibril forming proteins has been presented in Chapter 1 Section 1.5

Typically graphene is functionalised around its edges when used for biological applications, this allows it to be soluble in solution as well as providing specificity when targeting a certain cell *in vivo* [346]. The size of graphene for these applications ranges from 20 nm to 500 nm [347], at this size scale edge effects are a small site for biological interaction. Additionally graphene adopts a rippled structure *in vacuo* with a typical wavelength of the order of $>$ 10 nm with an amplitude of 1 nm [348, 349]. This rippled structure has

not yet been characterised in solution.

In this work the various carbon nanomaterials were modelled as fixed particles using the sp^2 carbon type in the GROMOS43a1 force field. The CNT and graphene surfaces were modelled as infinite periodic, with the assumption made that while solubilisation of bare carbon nanomaterials may not be possible, the surface modelled, $\approx$ 7 nm x $\approx$ 7 nm is small enough to consider it the central bare site of a much larger solublisable surface. Furthermore the ripple effect of the CNT and graphene would be mostly predominate at much greater sizes and thus can also be ignored at the length scale employed here.

Chapter 4

The effect of carbonaceous nanomaterials on the binding and dynamics of amyloidogenic apoC-II(60-70) peptide

4.1 Overview

Recently it has been shown that nanomaterials can impact the formation of amyloid fibrils (as discussed in section 1.5) [73, 350, 351, 352]. There is evidence that suggests these nanomaterials can either inhibit or promote the formation of these fibrils, however the mechanisms behind this behaviour remain unclear. Thus, it is crucial to understand how nanomaterial shape and size as well as the external conditions (solvent) can affect the adsorption and dynamic behaviour of proteins at the nanoparticle interface.

In this chapter the behaviour of apoC-II(60-70) in the presence of three carbonaceous nanomaterials: a spherical C60 fullerene, a tubular single-wall carbon nanotube and a graphene surface, is investigated. The peptide's structure, dynamics and binding, all of which can influence its fibril formation capacity are studied and compared to results obtained from previously characterised peptide behaviour in solution (discussed in section 3.2). A combination of computational methods, including large-scale electronic

structure calculations and classical all-atom molecular dynamics is utilised. Furthermore, additional simulations were conducted using a recently developed polarisable forcefield for graphitic nanomaterials and compared against the results using the common non-polarisable forcefield to determine the effects of graphitic surface polarisation in solution on adsorption of biomolecules.

4.2 Introduction

The fast-developing field of nanotechnology has already had a significant impact in numerous areas of science and technology due to the ability to control properties of nanomaterials with greater precision [51, 54, 353]. Despite the remarkable speed of developments in nanoscience, little is known about the effects of nanomaterials on biological matter (discussed in section 1.4) [354]. There is a growing concern that nanomaterials, specifically those used for medical applications, may induce cytotoxic effects [355]. In addition, engineered nanomaterials, which are increasingly being used in industry and the manufacture of household goods have the ability to permeate blood-brain barriers and thus have the potential to damage cells *in vivo* [356]. The toxicity of nanoparticles has been associated with fibril formation, where nanoparticles can cause localisation of peptides and proteins on their surfaces and promote undesirable aggregation that can favour formation of amyloid fibrils (section 1.5). These highly-structured protein aggregates are associated with many degenerative diseases such as Alzheimer's, Creutzfeld-Jacob disease, and dialysis-related amyloidosis (section 1.3) [73, 350, 351, 352].

Carbonaceous nanoparticles are one of the most prevalent types of nanomaterials present in the environment. These air-borne particles are continuously injected into the atmosphere in large quantities through the process of combustion and, at the smallest scale, are in the form of clusters with nanometric dimensions. Carbon based nanomaterials, such as fullerenes, nanotubes and graphene surfaces, have been widely studied for a variety of applications due to their outstanding mechanical, thermal and electronic properties. There is, however, a growing volume of literature that alerts to the potential harm from both intentional (medicinal) and unintentional (environmental) exposure of living organisms to such particles [356, 357, 358]. Comprehensive understanding of organic-inorganic

interactions is crucial in order to minimise the potential toxicological effects associated with advances in the development and use of such nanomaterials [67, 359].

Computational modelling has been used extensively to study the dynamic, thermodynamic and mechanical properties of biological systems under different conditions. Several reviews summarise the application of computer simulations to the study of biological matter in the presence of nanomaterials, specifically the common modes by which nanomaterials interact with proteins, DNA and lipid membranes [360, 361, 362, 151, 150]. Physicochemical properties that may be important in understanding the toxic effects of nanomaterials include particle size and size distribution, shape, exposed surface area, internal structure and surface chemistry [363]. Much research has focused on the characterisation of carbon-based nanomaterials such as fullerenes, carbon nanotubes and graphene surfaces [364, 182, 365]. At the same time, experiments involving carbonaceous nanomaterials in biological milieu are still limited and the interactions involved are not well understood [366]. Specifically, there are some contrasting findings that have recently been published on the role of carbon nanotubes in fibril formation. Linse et al. found an increase in the rate of fibrillation by β_2-microglobulin in the presence of carbon nanotubes, where they suggested that a locally increased concentration of protein on the carbon nanotubes surface promotes oligomer formation [73]. Two other separate studies also suggested that carbon nanotubes act as a catalyst for fibril formation [367, 368]. In contrast, Ghule et al. found that multi-walled carbon nanotubes inhibit amyloid aggregation of the human growth factor protein, hFGF-1 by encapsulating the protein structure and suppressing like-protein interactions [191]. Furthermore, recent computational studies of Aβ peptides found that carbon nanotubes drive the formation of β-barrels around the nanoparticle [193, 194]. The authors suggested that this type of aggregation would lead to; 1) blocking of the peptide structure for further peptide association; 2) reducing the population of monomers/oligomers available for fibril growth, and thus resulting in an inhibition of Aβ fibrillation [193]. In addition, they proposed that the hydrophobic and π-π interactions between the Aβ peptide and carbon nanotube inhibit β-sheet formation and destabilise fibril-seeds into random coil aggregates, which would increase the nucleation lag-time and possibly reverse the fibrillation process [194]. It is evident from the works presented above that there are contrasting views on the role of carbon nanomaterials in fibril formation.

However, there is substantial evidence that suggests carbon nanomaterials can have fibril inducing and inhibiting capabilities depending on the structural architecture of the nanoparticle itself and more importantly, the affinity of the peptide/protein under investigation, which plays a crucial role in the resultant propensity for aggregation on the nanoparticle surfaces [151, 150, 166].

While advances in experimental techniques are able to probe ever-smaller length-scales and ever-shorter timescales, atomistic modelling is a valuable complementary approach for a systematic investigation of detailed mechanisms of nanoscale phenomena at the atomistic and electronic levels [365, 94, 87, 252, 256, 255, 369, 370, 258, 257, 319, 371]. This is even more evident with the recent development of several forcefields specifically parameterised to accurately capture the interactions between proteins and nanomaterials, including the polarisablility of nanomaterials, which is often ignored in classical simulations [372, 250, 251]. In this chapter, a computational study is presented, investigating the effects of curvature and shape of carbonaceous nanomaterials on the structure, dynamics and binding of an amyloidogenic apolipoprotein C-II (apoC-II) derived peptide.

As described in Chapter 3, apoC-II is a 79 amino acid protein, with an important role in lipid transport [373, 374]. Under lipid-depleted conditions, apoC-II readily forms homogeneous fibrils with all of the characteristics of amyloid fibrils [308]. These amyloid fibrils are commonly associated with atherosclerotic plaques, where they have been found to co-localise with other apolipoproteins and initiate early events in heart disease [299]. Studies have shown that airway exposure to concentrated ambient particles and single-wall carbon nanotubes can promote progression of the atherosclerosis process in apolipoprotein-E knockout mice that develop plaques in blood vessels at early age [96, 375]. Similarly, a study by Vesterdal et al. demonstrated that intraperitoneal administration of pristine C60 fullerenes is associated with a moderate decrease in the vascular function of mice with atherosclerosis [376].

The apoC-II peptide derivative, apoC-II(60-70), was found to have the ability to form amyloid fibrils independently [317]. Numerous studies of this peptide have identified fibril-inhibiting and fibril-promoting configurations in a range of conditions and in different environments using experimental and computational techniques (section 3.2) [256, 255, 258, 257, 318, 370]. Monomeric wild-type apoC-II(60-70) peptide was identified to adopt

hairpin-like structures in solution, which was defined as an intermediate state on-pathway for the formation of fibril-seeds. Furthermore increased solvent accessible surface area and the relative orientation of the aromatic side chains were identified as fibril-favouring, while increased flexibility and the broader distribution of angles between the aromatic residues of mutated apoC-II(60-70) were identified as fibril-inhibiting [256, 258]. Overall, the solution based studies on the behaviour of apoC-II(60-70) in different environments provide benchmark data for identifying the effects of nanomaterials on the structure and dynamics of this amyloidogenic peptide.

In this chapter, the interactions, dynamics and binding energies of apoC-II(60-70) in the presence of three dimensionally different carbonaceous nanomaterials explored. The results are rationalised with respect to previously characterised peptide behaviour in solution to determine the effect that the nanomaterials may have on the fibrillation capacity of this peptide. In this work, a combination of computational methods is employed, including large-scale electronic structure calculations and classical all-atom molecular dynamics, using both non-polarisable and polarisable force fields. This combined DFT and classical molecular dynamics approach was used for the first time to investigate the fibril inhibition mechanisms of cyclic apoC-II(60-70) and its linear analogue [319]. The application of this multiscale modelling approach enables investigation of the fundamental driving forces behind the interactions of the peptide with nanomaterials and their effects on the peptide structure, dynamics and amyloidogenic capacity.

4.3 Computational details

4.3.1 Atomistic simulations of peptide-nanomaterial systems

To investigate the effects of carbonaceous nanomaterials on the structure and dynamics of apoC-II(60-70) (MSTYTGIFTDQ, 169 atoms) a series of simulations were performed with different starting peptide conformations and arrangements. The fullerene particle consisted of 60 carbon atoms with a radius of 3.5 Å. The nanotube was modelled as a (5,5) single-walled tube with 320 atoms in an open ended armchair arrangement, 6.78 Å in diameter and 38 Å in length, which was sufficiently long to prevent interactions between the peptide and the edges. Graphene was modelled as a periodic single sheet of 2160 carbon

atoms in a hexagonal arrangement to represent an infinite graphene surface. The starting configurations were constructed by positioning the peptide in different conformations with a minimum distance between the peptide and nanomaterials of <10 Å in different initial orientations, Figure 4.1 and Figure 4.2. The peptide together with the nanomaterial was then placed in a periodic simulation cell of at least 60 Å x 60 Å x 60 Å in dimension.

Initial peptide conformation	System	Starting structure	Simulation Time
Wild-type (wt) 	c60-wt-o1	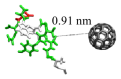	100 ns
	c60-wt-o2	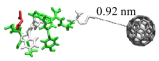	100 ns
	nt-wt-o1	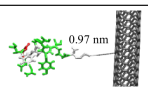	100 ns
	nt-wt-o2	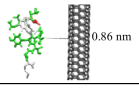	100 ns
	graph-wt-o1	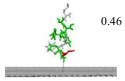	100 ns
	graph-wt-o2	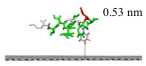	100 ns

Figure 4.1: Starting orientations of the wild-type apoC-II(60-70) peptide relative to each nanoparticle. The system names and total simulation time are also shown.

Initial peptide conformation	System	Starting structure	Simulation Time
Helix (h) 	c60-h-o1	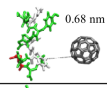	100 ns
	c60-h-o2	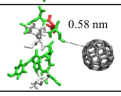	100 ns
	nt-h-o1	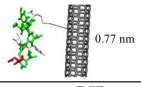	100 ns
	nt-h-o2	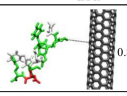	100 ns
	graph-h-o1	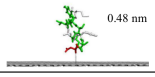	100 ns
	graph-h-o2	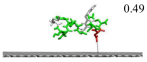	100 ns

Figure 4.2: Starting orientations of the helical apoC-II(60-70) peptide relative to each nanoparticle. The system names and total simulation time are also shown

Two forcefields were employed to simulate these peptide - nanomaterial systems, a non-

polarisable (GROMOS) and a polarisable (GRAPPA) forcefield. The GRAPPA forcefield differs from the GROMOS forcefield by implementing polarisable carbon nanomaterials within the CHARMM environment. Polarisation can be employed by describing the electrostatic interactions with the use of distributed multipoles [252, 371, 377] or by using the recently validated Rod Model [372, 250, 251]. GRAPPA utilises the Rod Model to provide the graphene and CNT surfaces with polarisation, whereby a single dummy atom is attached to each carbon of the nanosurface. This dummy atom has a small charge (0.1e), exactly opposite to that of the carbon atoms (-0.1e), and is free to rotate at a specified length [251]. For a further description of polarisability forcefield models refer to section 2.4.2. Both sets of classical molecular dynamics (MD) simulations were performed using the Gromacs [378] simulation package.

The non-polaraisable forcefield simulations utilised the united-atom Gromos forcefield and the 43A1 parameter set. The carbonaceous nanomaterials were modelled using the aromatic sp^2 carbon parameters and water was modelled using SPC water model [245]. The Lennard-Jones interactions were truncated at 10 Å with the long-range electrostatic interactions accounted for by the Particle Mesh Ewald (PME) method [379]. The LINCS algorithm was used to constrain the bond lengths to their equilibrium values [278], enabling a timestep of 2 fs to be applied for all simulations. These simulations were conducted in an NVT ensemble with the Berendsen thermostat [275] at a temperature of 300 K.

As described above, polarised carbon nanomaterials were simulated by employing the GRAPPA forcefield, which has been implemented with the CHARMM22 forcefield, thus the CHARMM-modified version of TIP3P [244, 380] water model was used and the CHARMM22 forcefield parameters used for the amino acids of apoC-II(60-70) [381, 382]. A time step of 1 fs was used with a Lennard-Jones non-bonded interactions switched off between 10.0 and 11.0 Å and a cut-off of 13.0 Å used for the PME summation. Constant temperature was maintained using the Nose-Hoover thermostat [383].

The energy minimisation and equilibration stages started with an *in vacuo* energy minimisation using steepest descent algorithm performed on the peptide-nanoparticle systems to remove steric clashes. The optimised system was then solvated using the water models mentioned earlier at a water density of 1 g/cm^3. To neutralise the overall negative charge of the system, an unrestrained counterion (Na+) was included in the simulation cell. En-

ergy minimisation on the solvated system was performed to relax all of the atomic degrees of freedom. Subsequently, MD was conducted to allow the solvent to equilibrate around the solutes by keeping the peptide and nanomaterial restrained. In all simulations the geometry of the nanomaterial was restrained for ease of monitoring the peptide dynamics. The VMD software package was used for visualization of the dynamics and analysis of the molecular trajectories [384].

Two initial non-fibrillar conformations (native and helical) of apoC-II(60-70) peptide were simulated in the presence of each nanomaterial. To further enhance conformational sampling simulations were repeated six times with different starting orientations of apoC-II(60-70) with respect to the nanomaterial, yielding a total 800 ns of data per nanomaterial-peptide complex. The behaviour and structures observed in multiple simulations of each system exhibited consistent trends, therefore the results from representative simulations are shown for comparison between the systems.

4.3.2 Potential of mean force calculations

The potential of mean force calculations were conducted using the Gromos forcefield using umbrella sampling and the weighted histogram analysis method (WHAM) [385], potential of mean force (PMF) profiles were generated to evaluate the free energy of dissociation (ΔG) for apoC-II(60-70) bound to each nanomaterial in solution. This method was applied to explicitly solvated systems and therefore accounts for the entropic contributions in the determination of the dissociation free energies. We determined the PMF as a function of separation distance between the centre of mass of the nanomaterial and the α-carbon of the glycine residue in apoC-II(60-70). To acquire the PMF profiles, a series of simulations (windows) were performed at increasing distance between the peptide and nanomaterial, starting from typical equilibrium structures of the peptide-nanomaterial complex obtained via "spontaneous" MD simulations. The peptide was restrained at each window using Hookean functions with a force constant of 8000 $kJmol^{-1}nm^{-2}$. In the present work, ΔG and PMF both refer to the free energy required to bring the peptide and nanomaterial from an associated form, which defines our zero of free energy, to some separation d. Adjacent windows were separated by 0.5 Å and each window was simulated for 15 ns with at least 30 windows used (until the peptide was fully dissociated from the nanomaterial),

resulting in a total simulation time of at least 450 ns per nanomaterial complex. WHAM was subsequently applied on the final 5 ns of simulations to remove the biasing potentials and obtain the unbiased PMF profiles.

4.3.3 Electronic structure and binding energy calculations

Binding energy calculations were performed on multiple structures selected from the classical forcefield trajectories of each peptide-nanomaterial system (more details in aromatic tracking section). Based on the findings of a recent methodological study, classical energy minimisation was performed on selected frames in solution prior to electronic structure calculations [386]. This procedure reduced any electrostatic artifacts that may arise due to the electronic structure calculations being performed in vacuum while retaining the major structural features of the system obtained during the fully solvated MD simulations. Single point electronic energy calculations performed on the resultant frames were used to calculate *in vacuo* binding energies between the peptide and nanomaterials. We determined the binding energy (E_b) of apoC-II(60-70) peptide on each nanomaterial, as

$$E_b = E_{P+N} - E_P - E_N, \tag{4.1}$$

where E_{P+N} is the total energy for the peptide-nanomaterial complex, E_P is the total energy of the apoC-II(60-70) peptide and E_N is the total energy of the isolated nanomaterial.

The linear-scaling DFT code ONETEP [242] was used, which combines linear scaling computational efficiency with accuracy that is comparable to traditional plane-wave DFT codes. Such efficiency opens up the possibility of performing accurate DFT calculations on thousands and tens of thousands of atoms, including proteins [387, 388, 389] and various nanomaterials [390, 242]. ONETEP achieves linear scaling by exploiting the 'near-sightedness' of the single-particle density matrix $\rho(\mathbf{r}, \mathbf{r}')$ in non-metallic systems,

$$\rho(\mathbf{r}, \mathbf{r}') = \sum_{\alpha\beta} \phi_\alpha(\mathbf{r}) K^{\alpha\beta} \phi^*_\beta(\mathbf{r}'), \tag{4.2}$$

where K is the density kernel and ϕ_α are a set of strictly localised non-orthogonal generalised Wannier functions (NGWFs) [231]. The total energy is self-consistently minimised

with respect to both the density kernel and the NGWFs. The NGWFs are expanded in a basis set of periodic sinc (psinc) functions [391], which are equivalent to a plane-wave basis, and are optimised *in situ*, giving plane-wave accuracy and allowing the accuracy to be systematically improved with a single kinetic energy cut-off parameter. The PBE generalised-gradient approximation was used to describe exchange and correlation [392], and norm-conserving pseudopotentials were employed to describe the interactions between electrons and nuclei. Dispersion interactions were accounted for using a DFT+D approach [393]. Dispersion-corrected DFT has been shown to produce accurate results for weakly interacting systems, such as aromatic composites [394] and protein-ligand complexes [395]. The supercell dimensions for each system were sufficiently large to prevent interactions between periodic images. In all cases, NGWF radii of 8 bohr were used for all atoms, no truncation was applied to the density kernel, the kinetic energy cut-off for the psinc basis was 880 eV, and the Brillouin zone was sampled at the Γ-point only.

4.3.4 Aromatic tracking

The role of aromatic residues in the adsorption of apoC-II(60-70) to each nanomaterial was investigated by tracking the placement of the peptide‘s aromatic rings across each graphitic surface. This technique determines the position and orientation of the aromatic rings in amino acids relative to the rings within the nanomaterials' surface at every step of the MD trajectories. The aromatic ring arrangement was categorised into three groups: no π-stacking, offset π-stacking and face-to-face π-stacking (Figure 4.3), T-stacking or edge-to-face stacking was not considered in the present study. The criteria to determine no π-stack register is a pair-wise contact distance over 4.5 Å between any two atoms of the aromatic ring and nanomaterial; or an angle greater than 30° between the plane normal of the aromatic ring and nanomaterial surface [396]. Face-to-face π-stacking was accounted for when the displacement between the centroids of the phenyl rings of the aromatic residues and centroid of the nearest hexagonal/pentagonal carbon ring was less than 0.71 Å (half the carbon-carbon bond length). A displacement greater than 0.71 Å was considered as offset π-stacking. ApoC-II(60-70) peptide having two aromatic rings in its sequence (Tyr63 and Phe67) resulted in six possible ring arrangements relative to the nanomaterials surface. The categories were defined as: (1) no π-stacking by both rings; (2) offset π-stacking by

one ring and no π-stacking by the other; (3) offset π-stacking by both rings; (4) face-to-face π-stacking by one ring and no π-stacking by the other; (5) face-to-face π-stacking by one ring and offset π-stacking by the other; (6) face-to-face π-stacking by both rings. Once the aromatic arrangement was categorised, each group underwent structural clustering with RMSD cut-off of 2 Å for the entire peptide using the single linkage clustering method to determine the most frequently sampled structure within each π-stacking category. Three representative peptide-nanoparticle complex structures featuring each π-stacking group were selected and underwent electronic structure calculations to determine their binding energies.

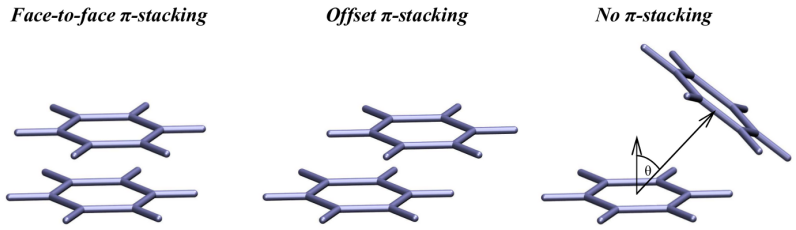

Figure 4.3: Phenyl rings demonstrating the aromatic ring arrangement categorised in three groups: face-to-face π-stacking, offset π-stacking and no π-stacking. To help in the interpretation of the cut-offs applied to categorise each aromatic arrangement, only the angle between the plane normal of the rings is shown (image on the right), while all other distance cut-offs are pair-wise in nature.

4.4 Results and discussions

Explicitly solvated molecular dynamics simulations were used to characterise the interactions between the amyloidogenic peptide apoC-II(60-70) and three exemplar carbonaceous nanomaterials. ApoC-II(60-70) showed a strong affinity to the nanomaterials, where the peptide came in contact with each nanomaterial within the first 20 ns of simulation and remained adsorbed for the entire trajectory. Below we analyse the bound states and the mechanisms responsible for the binding.

4.4.1 Secondary structure evolution and interactions

Secondary structure analysis was performed to investigate the effects of the nanomaterial curvature on the peptide's conformation. The STRuctural IDEntification (STRIDE) [397]

algorithm was utilised to classify the peptide's secondary structure as a function of time. Secondary structure evolution plots depicting typical conformational trends exhibited by apoC-II(60-70) in the presence of C60, nanotube and graphene are shown in Figure 4.4. The initial 20 ns of simulation (equilibration) are also shown to highlight the conformational changes in the peptide induced by adsorption onto the nanomaterial surface.

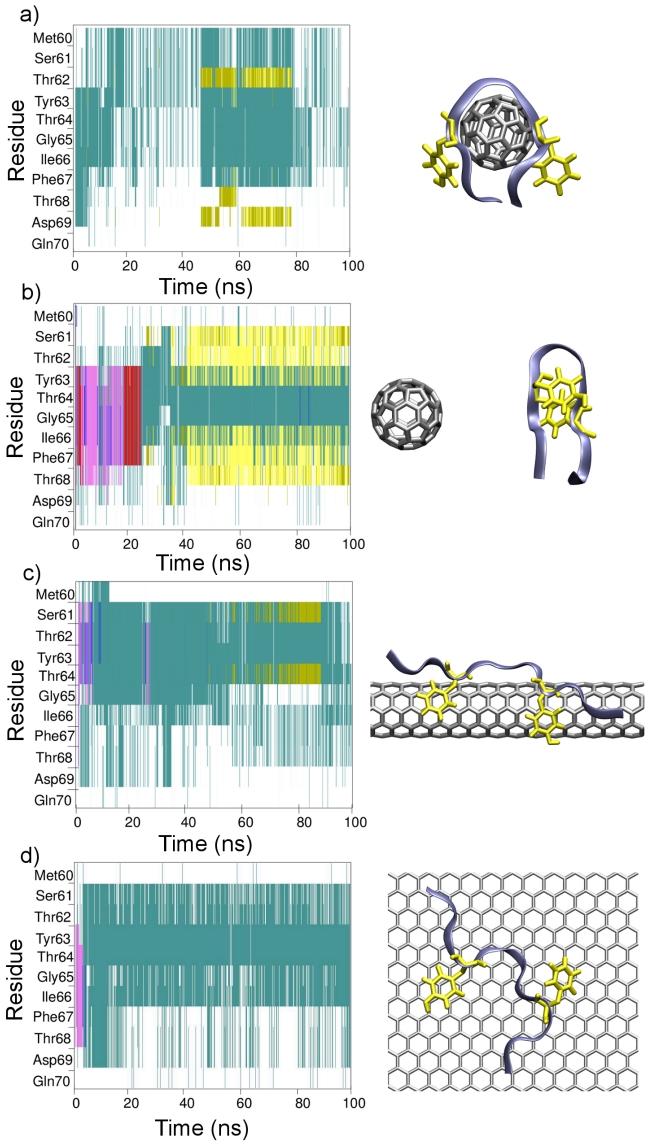

Figure 4.4: Secondary structure evolution plots for typical behaviours observed of apoC-II(60-70) in the presence of (a and b) C60, (c) nanotube and (d) graphene surface. Secondary structure colour codes: magenta = α-helix; red = π-helix; cyan = turn; white = coil; yellow = extended conformation; green = hydrogen bridge. Screen shots depicting the typical (most populated) peptide structure and aromatic residues arrangement for each system are shown as insets.

The results show a structural transformation of the peptide upon adsorption to the

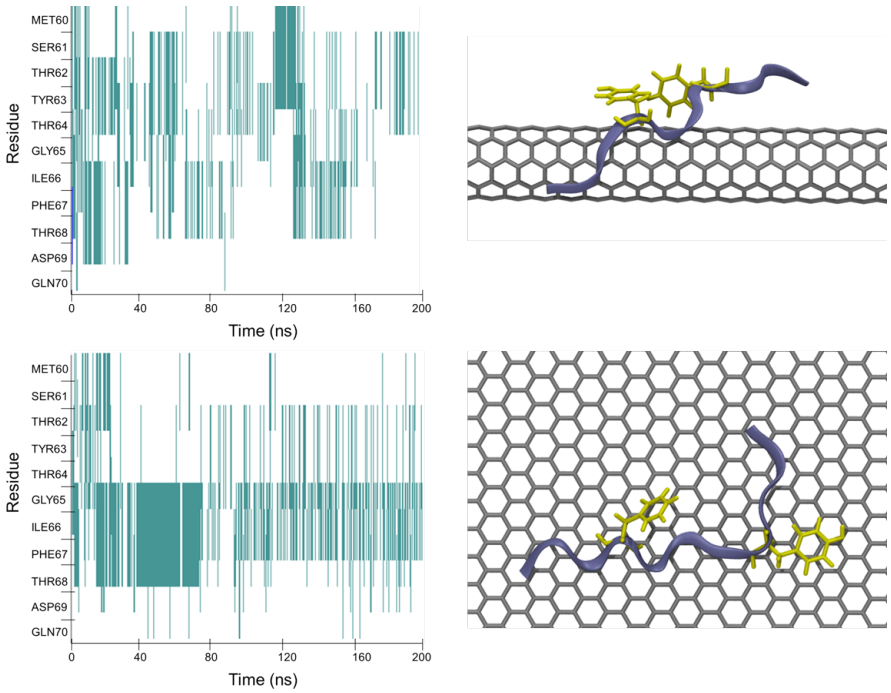

Figure 4.5: Secondary structure evolution plots for typical behaviours observed of apoC-II(60-70) in the presence of (a), nanotube and (b) graphene surface using the GRAPPA forcefield. Secondary structure colour codes: magenta = α-helix; red = π-helix; cyan = turn; white = coil; yellow = extended conformation; green = hydrogen bridge. Screen shots depicting the favourable peptide structure and aromatic residues arrangement for each system are shown as insets.

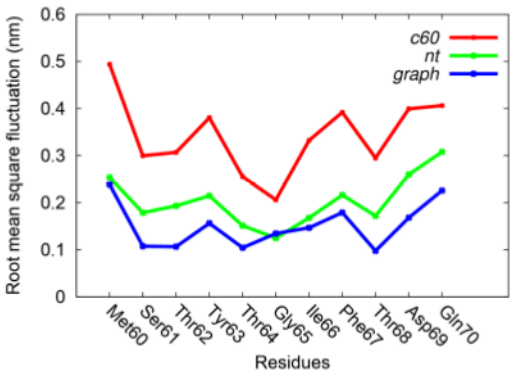

Figure 4.6: Root mean square fluctuation of the atomic positions in each residue in the presence of C60 (red), nanotube (green) and graphene (blue).

nanomaterial surface. ApoC-II(60-70) in the presence of C60 was observed to curve around the particle, with a turn region around Gly65, as shown in the picture inset of Figure 4.4a. This structure allows for a large number of contacts to be made with the nanoparticle, dominated by π-π interactions between the aromatic residues (Tyr63 and Phe67) and the C60 surface. Due to the presence of C60, apoC-II(60-70) is unable to form the inherent

solution β-hairpin conformation [256, 258]. In one out of six simulations the peptide was able to dissociate within 10 ns of contact with the C60 particle. This suggests that the peptide can be weakly bound to the surface of the nanoparticle, see Sections 4.4.3 and 4.4.4 for details. Upon desorption apoC-II(60-70) was able to form a β-hairpin conformation (picture inset of Figure 4.4b). We note that the β-hairpin structure was found favourable for monomeric apoC-II(60-70) peptide in solution, and identified as an intermediate state on-pathway for fibril formation [255, 258, 36]. The results show that the presence of C60 inhibits the formation of the characteristic fibril favouring β-hairpin as well as the extended conformation suggesting that the interactions with the C60 may contribute to an increase in peptide mobility (see Figure 4.6) and facilitate the formation of fibril incompetent conformations. A recent study by Andujar et al. is in line with our findings, where they showed that C60 induced significant destabilization of the amyloid-β fibrils by disrupting the hydrophobic contacts and salt-bridges between the β-sheets [398]. This suggests that C60 can be used as a prototype for the design of potential fibril inhibitors.

The secondary structure evolution plot of apoC-II(60-70) in the presence of a nanotube shows that the peptide exhibits different structural features compared to those in the presence of C60. The peptide tends to elongate across the surface of the nanotube, while adopting mostly turn and coil motifs. This behaviour is a result of the large surface area available for contact on the nanotube (Figure 4.4c). The strong affinity between the nanotube and peptide is facilitated by π-π interactions between the aromatic rings of the peptide and the nanotube, see Sections 4.4.3 and 4.4.4 for futher details. The curvature of the nanotube enables the peptide to arch, which enables the short-lived formation of a hydrogen bond between Ser61 and Thr64. In comparison to the C60 simulations, the peptide was less dynamic on the surface of the nanotube, as seen from the smaller number of conformations sampled by the peptide following the adsorption and immobilisation on the nanotube surface (Figure 4.4c and Figure 4.6.

The simulations of apoC-II(60-70) in the presence of graphene exhibited similar structural features to those seen in the presence of the nanotube. Upon adsorption, the peptide elongates along the graphene surface and features predominantly turn and coil structures (Figure 4.4d). The large surface area available for interactions enables the peptide to freely slide on the surface, while the favourable π-π stacking interactions between the

aromatic residues of the peptide and the surface define its conformational features. Linse et al. showed extended nanoparticles enhance the probability of appearance of a critical nucleus for nucleation of protein fibrils, albeit for a different combination of nanomaterials and peptides [73]. This feature was determined as fibril-favouring in previous works on apoC-II(60-70) oligomers [256, 258]. Other studies have also shown that carbon nanotubes and graphene surfaces facilitate a change in the conformation of peptides [94, 137] and π-stacking is an efficient mode of biological recognition of π-electron-rich carbon nanoparticles [365, 94, 87, 252, 377, 137, 93].

A common feature in all secondary structure plots is the presence of a persistent coil motif at the C-terminal end of the peptide, where predominantly hydrophilic residues reside. This suggests that the inherent preference for interaction with the polar environment by these residues is suppressed by the attractive van der Waals forces between the large surfaces presented by the nanomaterial and the peptide, preventing the peptide dissociation from the nanomaterial. Strong hydrophobic interactions between the WW domains and carbon nanotubes have also been associated with protein function "poisoning" and disruption of the protein active site [399]. Overall, it should be noted that the adsorbed peptide may adopt both fibril initiating as well as fibril incompetent conformations. However, our analyses indicate that the extended conformation adopted on the extended nanosurfaces is in line with the fibril competent structures found through previous modelling and experimental studies [255, 256, 257, 258, 318, 370]. In contrast the mobility and lack of secondary structure elements needed for the fibril formation by the C60 adsorbed peptide suggests the inhibiting role of this nanoparticle in the fibril formation of apoC-II(60-70) peptide.

To gain a more detailed understanding of the interactions involved in adsorption of apoC-II(60-70), the contact stabilities of the peptide's residues with each nanomaterial were investigated (Figure 4.7). Contact stabilities were calculated as the percentage of simulation time during which a contact was maintained between each residue and the respective nanomaterial. A contact was counted when the distance between a pair of atoms was less than 4 Å which enabled us to account for van der Waals interactions between the peptide and the nanoparticle.

High contact stabilities were found for both the aromatic tyrosine (Tyr63) and pheny-

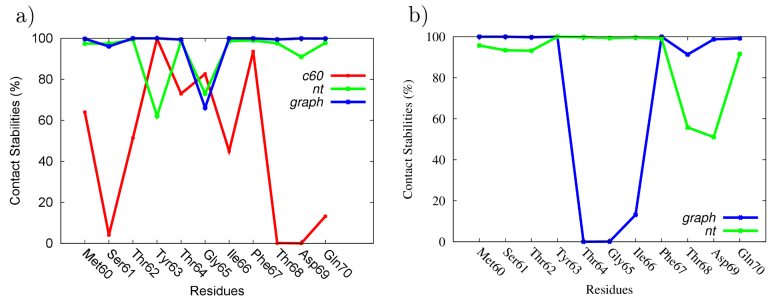

Figure 4.7: Contact stability plot of apoC-II adsorbed to C60 (red), carbon nanotubes (green) and graphene (blue), for the Gromos (a) and GRAPPA (b) forcefields.

lalanine (Phe67) residues with all nanomaterials. The stable π-stacking arrangements between the aromatic rings of the peptide and the electron-rich carbon rings of the surface, suggest that these are the key residues that contribute to the strong interactions between the peptide and the carbonaceous nanomaterials, in line with other studies [365, 94, 87, 252, 377, 137, 93].

This effect is evident in all simulations, however in the C60 complex the aromatic residues dominate the interactions between the peptide and C60 surface, while the other residues exhibit less persistent contacts. Interestingly, Tyr63 exhibits higher binding affinity to C60 compared to Phe67, in accordance with a DFT study that showed Phe and Tyr bind with a similar strength to the nanotube, while Tyr exhibits a stronger binding to C60 [400, 401]. In contrast, the large contact area presented by the carbon nanotubes and graphene results in higher contact stabilities with all (not just the aromatic) residues, this effect being most evident on the graphene surface.

In recent studies it was shown that the orientation of the aromatic side chains is different in the fibril-forming and fibril-inhibiting arrangements [256, 258]. The simulations of apoC-II(60-70) in the presence of C60 exhibited structures where the aromatic rings were positioned on the same side of the peptide which enhance the π-stacking interactions with the small, highly curved C60 particle. This ring arrangement was postulated to inhibit fibril formation [256, 258]. In contrast, the aromatic rings did not show a specific facial preference in the nanotube and graphene complex simulations (Figure 4.4c,d). This was due to the large contact area and stronger hydrophobic interactions presented by these materials, which formed the aromatic ring stacking upon adsorption of the peptide.

A series of radial distribution functions (RDF) were calculated to determine the degree

of water structuring around the peptide in solution and when bound to the nanomaterial surface. The results provide an insight into the extent of desolvation of the peptide conformation upon binding to the different nanomaterials. Typical RDFs of the peptide side chain hydrogen atoms (H) with respect to the water oxygen atoms (O) are shown in Figure 4.8. For all systems, the RDF profiles show a peak at ≈ 2 Å representing the first hydration shell, indicating hydrogen bonding between water and the apoC-II(60-70) side chains. The results also show the presence of a second hydration shell at ≈ 4 Å. The RDFs of peptide-nanomaterial complexes exhibit an attenuation of the overall probability density, suggesting the exclusion of water due to the hydrophobic contact between the peptide and nanoparticle manifests in the RDFs through the lowering of the occurrence of water at larger separation distances in the bound state. Indeed, desolvation effects have been shown to be favourable in the self-assembly of cyclic peptides on carbon nanotubes [87].

4.4.2 Polarisable forcefield simulations

The effects of polarisability of graphitic surfaces, CNT and graphene specifically, on the adsorption and structural evolution of apoC-II(60-70) were also explored using a newly developed forcefields [251]. In these simulations the apoC-II(60-70) monomer spontaneously adsorbed to the nanomaterials within 20 ns. On both the curved CNT and flat graphene surfaces the apoC-II(60-70) peptide adopts mostly random turn and coil motifs. Examination of the trajectories shows that in general the apoC-II(60-70) adopts elongated conformations with similar secondary structure profiles to those obtained when using the standard GROMOS forcefield, Figure 4.5. With both forcefields the conformations adopted by the peptide are mediated through the interaction of the two aromatic residues, Tyr63 and Phe67, with the nanosurface, which encourages the elongation of apoC-II(60-70) across the surfaces. These configurations are present on the surface of the CNT and graphene and typically coincide with aromatic residues positioned on opposite sides of the peptide.

Contact stabilities of the apoC-II(60-70)'s residues adsorbed to the polarised CNT and graphene were obtain to get a more detailed understanding of the interactions between the peptide and the polarised surfaces, Figure 4.7b. Overall, the results for the CNT and

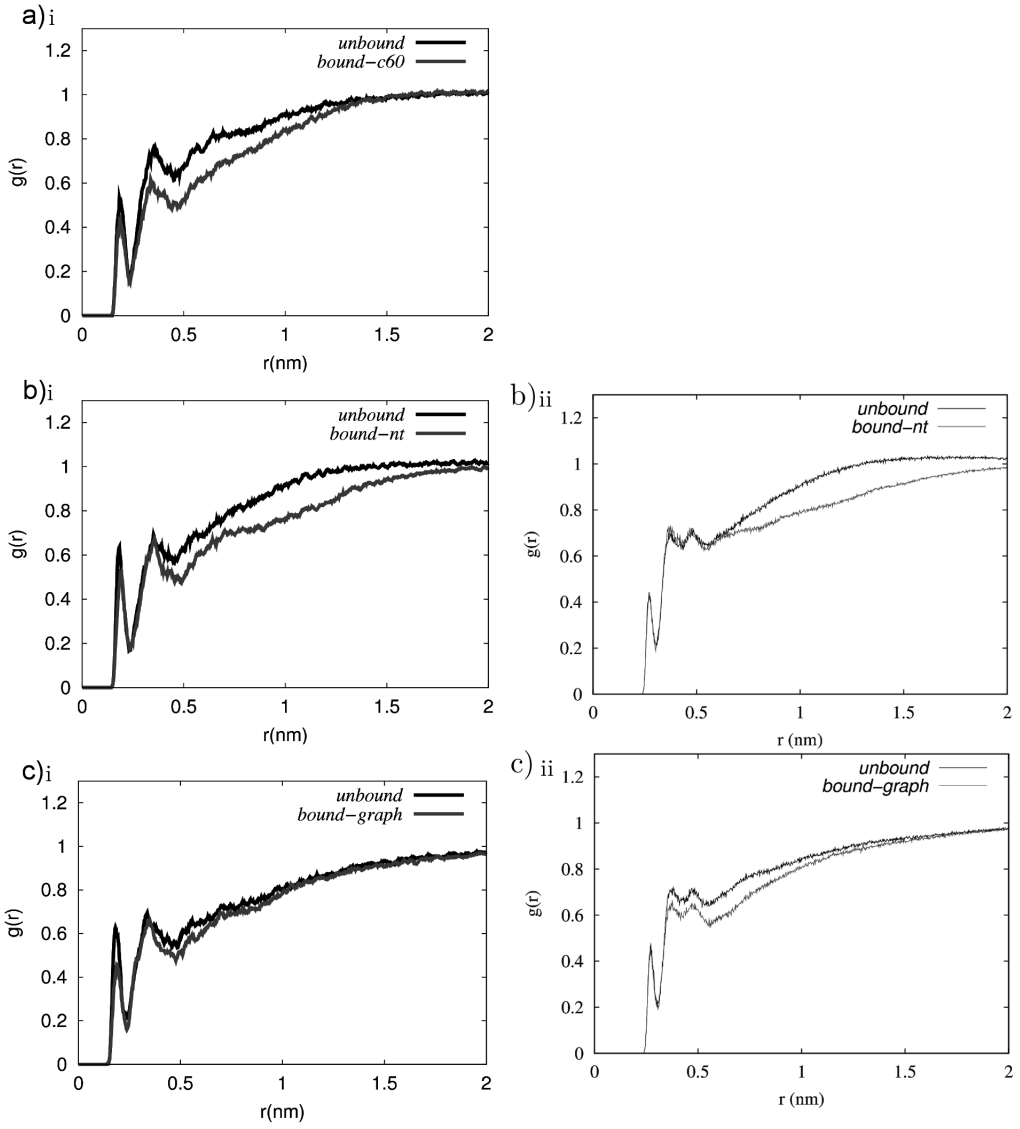

Figure 4.8: Radial distribution functions (RDF) of the water probability density, g(r), as a function of the distance, r, of water (O) from the side chain (H) atoms of apoC-II(60-70). RDFs for the peptide in a free (unbound) and adsorbed (bound) to a) C60, b) nanotube and c) graphene are shown, for the Gromos (i) and GRAPPA (ii) forcefields.

graphene showed similar trends to the results obtained when using the GROMOS forcefield, which highlighted the π-stacking arrangements between the aromatic residues, Tyr63 and Phe67, and the nanosurfaces were the most stable interactions, albeit with the Phe67 - nanomaterial stacking reduced in comparison (Figure 4.9). Additionally stable contacts were observed between the terminal residues, Met60 and Gln70, and both nanosurfaces, which was also observed in the GROMOS forcefield simulations. In contrast however the Ile66 residue displayed a significant "snorkeling" effect, Figure 4.9. These results correlate

well with recently published work employing the GRAPPA forcefield, investigating the intrinsically disordered peptide, P1 (HSSYWYAFNNKT), which is a known strong binder to graphene surfaces. It was found that it bound strongly through the residues Arg, Tyr, Trp and Gln and weakest through Ile [402].

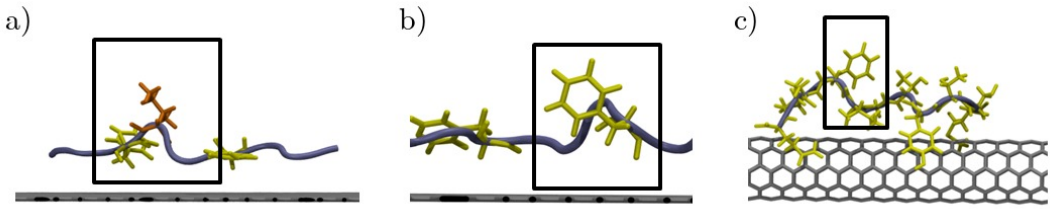

Figure 4.9: Images showing the snorkeling effect of Ile66 while apoC-II(60-70) is adsorbed to the graphene (a) and the reduced aromatic stacking of Phe67 while the apoC-II(60-70) peptide is adsorbed to the graphene (b) and CNT (c).

Finally, RDF profiles were investigated to determine if the desolvation of the peptide upon binding to the polarised nanomaterial were any different to the GROMOS forcefield results. Like the GROMOS forcefield RDFs, the RDFs here were calculated between the peptide side chain hydrogen atoms (H) with respect to the water oxygen atoms (O) and are shown in Figure 4.8ii. Upon adsorption to the nanosurface apoC-II(60-70) undergoes a similar desolvation behaviour where water is excluded due to the hydrophobic contacts between the peptide and nanosurface. Additionally the first two water shells that form around the peptide when using the GROMOS forcefield, present as peaks at 2 Å and 4 Å are also present here.

Overall the inclusion of a polarisable representation of the CNT and graphene nanomaterials has had no significant effect on the adsorption and conformations of apoC-II(60-70) when in the presence of these two nanomaterials. This suggests that while polarisation can be an important factor in peptide - nanomaterial interactions, with the apoC-II(60-70) peptide, it does not appear to have a major influence. Additionally a polarised description of the C60 particle is not available yet and as such does not allow the comparison with a spherical particle. Further validation is provided in this chapter by comparing the potential of mean force of dissociation in solution with binding energies obtained using density functional theory in vacuum.

4.4.3 Peptide-nanomaterial dissociation free energies in solution

To characterise the binding of apoC-II(60-70) peptide to each nanomaterial in the presence of solvent, the free energy of dissociation was calculated using umbrella sampling (potential of mean force, PMF) together with the weighted histogram analysis method (WHAM) [385]. This approach is applied to explicitly solvated systems and accounts for both the enthalpic and entropic contributions to the dissociation free energies. Two bound equilibrium complex structures were studied for each system to enhance sampling. The PMFs detailing the dissociation pathway of apoC-II(60-70) from each nanomaterial are presented in Figure 4.10.

The results demonstrate that higher degree of curvature reduces the surface area available for adsorption, and the dissociation free energy indicates that binding to C60 is weakest and binding to graphene is strongest of the systems investigated. Here, a lower value indicates a weaker binding. The size of the peptide does not allow for complete wrapping of the C60, therefore in this complex the peptide is quite mobile with terminal residues remaining free and not forming close contacts with the nanoparticle, as can be seen in the residue contact stability plot in Figure 4.7. Figure 4.10a indicates that the dissociation energy is dependent on the adsorbed peptide conformation. This suggests that C60 induces significant structural lability in apoC-II(60-70) preventing it from adopting stable conformations, in line with the peptide evolution observed through molecular dynamics trajectories (Figure 4.4 and Figure S1). A higher free energy of dissociation ($\approx$ 1.8 kcal/mol) was obtained for the peptide that had a larger number of contacts with C60 and whose aromatic rings were continuously interacting with the C60 particle. In contrast, the system where the two aromatic rings of the peptide predominantly formed π-stacking between themselves rather than with the nanoparticle resulted in a lower dissociation energy ($\approx$ 1.1 kcal/mol). The peaks and troughs are caused mostly by the transient π-stacking interactions, with peaks observed when contacts are broken, as illustrated by the insets in Figure 4.10. In our previous work on apoC-II(60-70) we showed that an increase in conformational flexibility and dynamics can slow down or even inhibit fibril formation [255], therefore it appears that interactions with the C60 can induce a similar, fibril inhibiting effect. We note that generally PMF plots for the C60-peptide system are noisier than

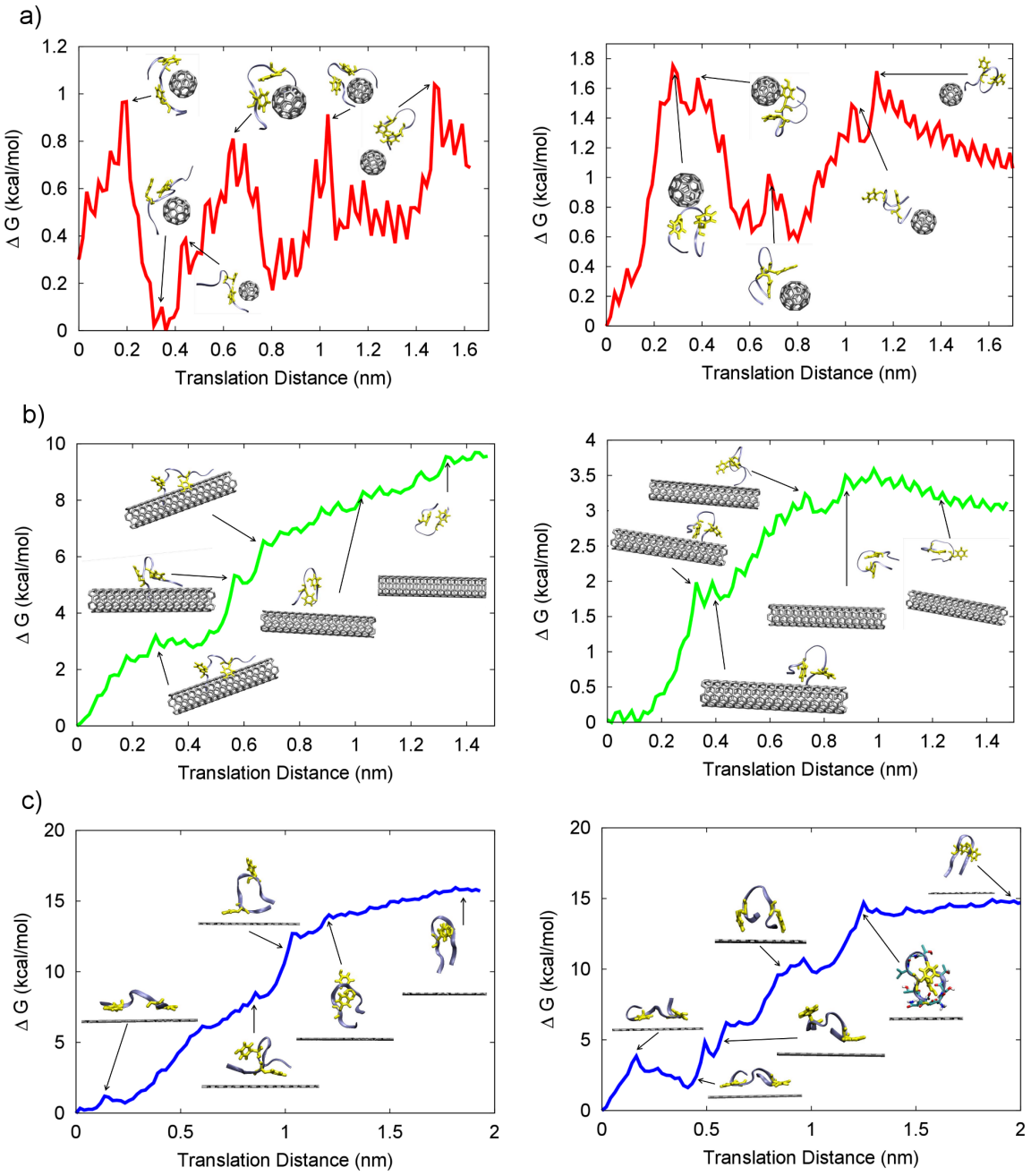

Figure 4.10: The free energy of dissociation of apoC-II(60-70) peptide from a) C60 (red), b) nanotube (green), and c) graphene (blue) surface, plotted with respect to the translation distance of the C_α of the glycine residue. Inserts depicting typical representative structures of transition states on the free energy surface are shown. For clarity the peptide structure is drawn as ribbon (iceblue) and the aromatic residues are shown as licorice (yellow).

those for the nanotube and graphene systems which is due to the transient nature of the contacts and increased mobility of apoC-II(60-70) when in contact with C60, rather than due to insufficient conformational sampling. Similarly, the free energy differences seen

between the multiple simulations of the peptide-nanotube system are due to the variety of structures sampled along each dissociation pathway. As expected, the predominantly elongated peptide conformations (Figure 4.10b, left) enabled a larger number of contacts between the peptide and the nanotube, which resulted in a higher free energy of dissociation ($\approx$ 8.6 kcal/mol). The peptide exhibiting mostly coiled structures made fewer contacts with the nanotube (Figure 4.10b, right) which in turn required less energy ($\approx$ 3.5 kcal/mol) to dissociate from it. The smoother PMF plots for the peptide-nanotube systems are a result of the persistent interactions between the components, in keeping with the results of the spontaneous MD simulations. The PMF plots representing the dissociation free energy of apoC-II(60-70) from graphene exhibited conformation independent pathways. As seen from the MD results, the π-stacking between apoC-II(60-70) and graphene contributes to the formation of elongated peptide structures and restricts the conformational flexibility of the peptide. Repeat simulations resulted in dissociation free energies of $\approx$ 15 kcal/mol irrespective of the conformations sampled along the dissociation pathway. We note that dissociation energy peaks occur when a large number of contacts are broken, such as during the illustrated dislocation of the aromatic residues from the graphene surface (see insets of Figure 4.10c). In contrast, as the peptide is slowly pulled away from the surfaces a characteristic smooth dissociation energy profile is observed.

4.4.4 Aromatic stacking and *in vacuo* binding energies

In addition to the classical simulation-derived dissociation free energies discussed above, we have used electronic structure calculations based on DFT to calculate *in vacuo* binding energies of selected frames derived from classical all-atom simulations. To investigate the role of aromatic residues (Tyr63 and Phe67) in driving the adsorption of apoC-II(60-70) onto carbon based nanomaterials, we employed our algorithm tracking the position and orientation of the phenyl rings of the aromatic amino acids with respect to the aromatic rings of the nanomaterials' surface at every step of the MD trajectories, described in section 4.3.4. The *in vacuo* binding energy of three representative frames from each π-stacking arrangement was obtained by DFT calculations using the ONETEP linear-scaling code [242], comprising a total of eighteen typical structures per peptide-nanoparticle complex. This analysis provides a measure of the relative binding of apoC-II(60-70) to a nanomate-

rial surface with respect to the contact area. The binding energy differences between the representative structures for each π-stacking configuration versus the peptide-nanomaterial contact area are shown in Figure 4.11. The vacuum binding energies are shown relatively to the strongest bound state (apoC-II(60-70) on graphene). In this case, higher absolute values indicate a weaker binding (left y-axis, Figure 4.11).

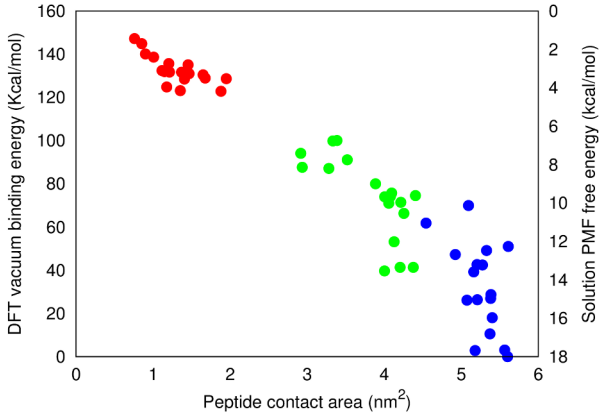

Figure 4.11: Relative DFT vacuum binding energies of apoC-II(60-70) adsorbed to C60 (red), carbon nanotube (green) and graphene (blue) vs the total contact area between the peptide and nanomaterial surface. The solution PMF free energy range for each nanomaterial is also shown (right axis, higher energy=stronger binding) to illustrate the correlation in binding strength between the classical and electronic structure methods.

The *in vacuo* binding energy results confirm the trends observed in our explicitly solvated PMF free energies showing the strength of binding between apoC-II(60-70) and the nanomaterials to follow: C60 <nanotube <graphene. In all systems the aromatic rings act like "anchors" for binding the peptide to the carbon nanomaterials via π-π interactions. DFT binding energy calculations confirm the finding from classical MD that apoC-II(60-70) exhibits strongest binding on graphene with a predominant face-to-face π-stacking arrangement made by the two aromatic rings of the peptide and the surface. The all-atom MD simulations show that the flat graphene surface promoted sliding of the peptide, Figure 4.12, and backbone elongation to optimise the π-stacking arrangement between the aromatic rings of the peptide and the substrate. This contributes to the peptide-graphene system having the largest aromatic and total contact area, which results in the strongest binding. The DFT binding energy also confirmed that apoC-II(60-70) exhibits a weaker binding to the nanotube and the weakest binding to C60, attributed to the increased nanosurface curvature which stimulates the formation of turns and loops in apoC-II(60-

70) leading to a lower contact area between the peptide and nanoparticle. We note that C60 comprises both hexagonal and pentagonal carbon rings and, therefore, has a lower probability of face-to-face π-stacking with the six-membered aromatic rings of the peptide (statistical data shown in Tables in the appendix A). This provides a further explanation for the significantly smaller contact area and weaker binding obtained for the peptide and C60 nanoparticle, compared to the nanotube and graphene systems (Figure 4.11 and Tables in appendix A).

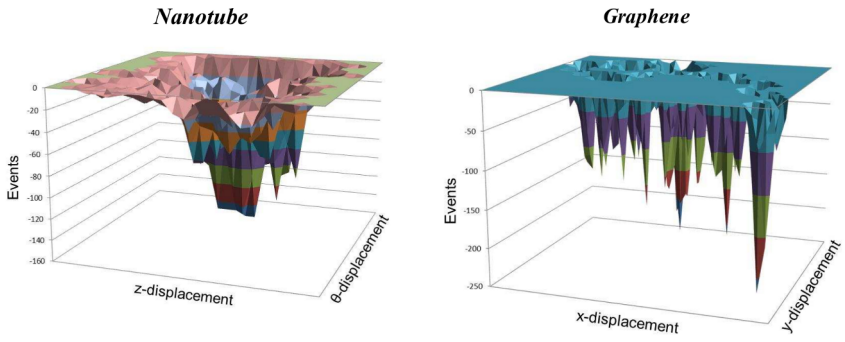

Figure 4.12: Aromatic tracking results showing the position of the center of mass of the apoC-II(60-70) with respect to the number of aromatic contacts (face-to-face and offset π-stacking) occurring at this position.

Furthermore, using our DFT calculations we were able to examine the intra-peptide electrostatic interactions which play a significant role in determining the peptide's secondary structure and consequently the binding affinity to other materials. Electron density difference ($\Delta\rho$) maps showing charge accumulation (red) and depletion (blue) upon peptide adsorption on each nanomaterial are presented in Figure 4.13. We can see that intra-peptide interactions are more significant in the proximity of nanoparticles with high curvature which have a reduced nanoparticle-peptide contact surface area, as Figures 4.11 and 4.13 demonstrate.

The greater surface area available on the flatter "hexagonal-only" surface of graphene allows for a more efficient π-stacking and a stronger peptide binding as shown in Figures 4.13c. Moreover, surface adsorbed elongated peptide conformations enable polar residues such as Thr, Ser and Gln to become more solvent exposed, thus exhibiting the "snorkeling effect" [403, 404] (see inset of Figure 4.13b), where the hydrophobic backbone interacts with the graphitic surface, while the polar side chains are protruding to the solvent. This

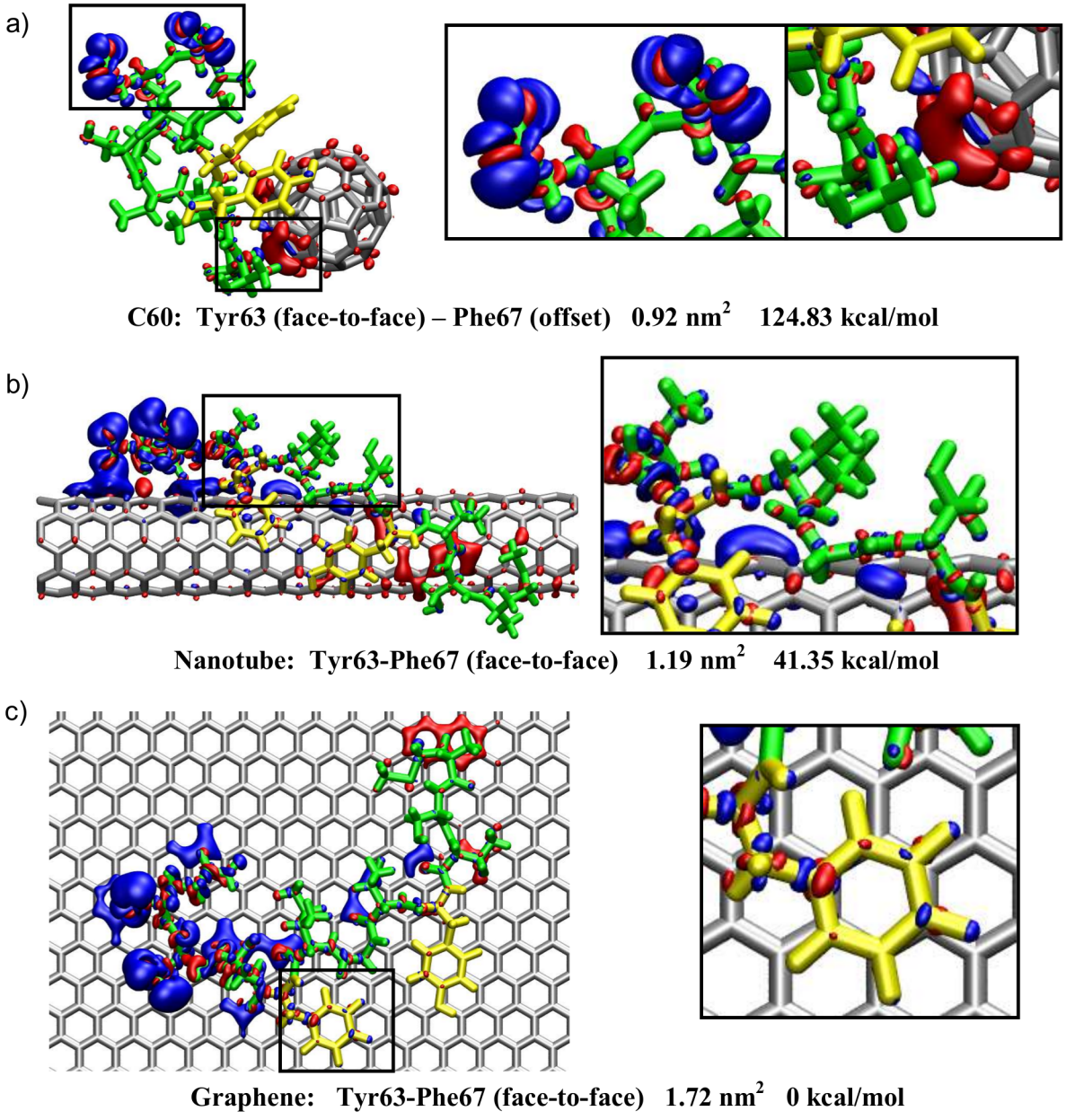

Figure 4.13: Electron density difference maps of representative frames from the clustering analysis shown by an isosurface with isovalues of $\Delta\rho$= +0.005e/Å^3 and -0.005e/Å^3. Red represents charge accumulation, and blue represents charge depletion. The aromatic rings are coloured yellow for clarity. The respective structures' π-stacking arrangement, aromatic contact area and binding energy differences relative to the strongest bound state (face-to-face π arrangement on graphene, Figure c) are also shown together with close-up insets of specific features to aid interpretations of the results.

lowers the overall contact area between the peptide and nanomaterial, and ultimately reduces the binding affinity. Figure 4.13 shows small electron density differences between the aromatic groups and the graphitic surfaces. This is in agreement with the study of

Poenitzsch et al. where they observed weak charge-transfer interactions between aromatic groups and carbon nanotubes using scanning tunneling spectroscopy and Raman experiments [405]. Our electron density analysis shows that, generally, a weaker binding is a result of inefficient π-stacking arrangements and intra-peptide electrostatic interactions that reduce the peptide-surface interactions, as Table 1A demonstrates. Charge redistribution can also be seen between the peptide and nanoparticle surface (Figure 4.13), suggesting some polarisability effects occur between the peptide and nanomaterial. Specifically, a charge depletion can be seen at Asp69 and Gln70 in all systems, while a charge accumulation develops at the closely interacting sites of the peptide and nanomaterial surface. Figure 4.13a shows charge accumulation at Gly65 for the C60 complex, while the nanotube and graphene exhibit charge buildup in close proximity to the predominantly hydrophilic N-terminal region of the peptide (Met60, Ser61 and Thr62). We note that the agreement between our classical non-polarisable simulations and both the polarisable FF and DFT studies suggest that the classical non-polarisable forcefield potentials employed here are able to capture the polarisation effects inherent to peptide-nanoparticle systems. Moreover, a recent study using the dispersion corrected DFTB-D method, showed that although molecular mechanics techniques with fixed-charge forcefields do not explicitly incorporate polarisability, they can predict the strength of π-π interactions between aromatic moieties and carbon nanotubes [36]. This reassures that molecular dynamics simulations utilising fixed charge forcefields provide a reasonable representation of the interactions between peptides and graphitic surfaces.

4.5 Conclusions

Using both non-polarisable and polarisable classical forcefields and electronic structure calculations, it has been shown that an amyloidogenic apoC-II(60-70) peptide exhibits a strong affinity for graphitic nanomaterials where binding is facilitated through π-π interactions between the aromatic residues of the peptide and the surface of the nanomaterial. This is generally achieved by the exclusion of water molecules from the peptide-nanomaterial interface. The proximity of the C60 fullerene contributed to an increase in conformational lability of apoC-II(60-70), which was shown to prevent it from adopt-

ing fibril-favouring structural features. This finding is in line with the previous studies of oxidised apoC-II(60-70), where increased structural flexibility and dynamics were the key factors prohibiting this peptide to form fibrils, confirmed experimentally. Conversely, our non-polarisable and polarisable data showed that the less curved nanotube and flat graphene nanomaterials promote elongated peptide conformations previously shown to form fibril seeds, which confirms recent findings that extended carbon nanosurfaces can act as templates able to encourage peptide fibril formation and growth. The electronic binding energy and solution free energy calculations showed the binding affinity of apoC-II(60-70) was weakest for the C60 particle, followed by the nanotube, and strongest for the graphene. In all simulations these trends are due to the larger contact area available for peptide adsorption to the flatter graphene and nanotube than the highly curved C60. The increased curvature also results in reduced efficiency of aromatic π-stacking and higher intra-peptide electrostatic interactions which contributes to its weaker binding to the nanomaterials. The electronic structure calculations show that dimensionality determines the electronic properties of the nanoparticle as well as size and curvature play a significant role in the contact area and binding mechanisms of the peptide. At the same time the intra-peptide interactions determined by the peptide sequence (i.e. presence of aromatic, aliphatic, polar/apolar amino acids) affect the binding mechanism of peptides to nanoparticles. The observed agreement between the classical non-polarisable, polarisable forcefields and electronic structure calculations show that molecular dynamics simulations utilising fixed charge forcefields provide reasonable representation of the interactions between peptides and graphitic surfaces. In summary, our results highlight that hydrophobic nanoparticles have multiple notable effects on the peptide structure, dynamics and binding affinity. We have demonstrated that dimensionality and different degree of curvature can either facilitate or hinder the interaction of amyloidogenic peptides with the nanosurfaces and make them adopt conformations capable of inhibiting or promoting fibril development. In the subsequent chapters the behaviour of oligomeric species of apoC-II(60-70) in the presence of the same carbon nanoparticles as studied herein, is examined. These findings can be important for rational design of amyloid fibril inhibitors as well as for clarification of possible toxic effects of carbon based nanomaterials.

Chapter 5

The adsorption-desorption mechanism of apoC-II(60-70) oligomers at the interface with carbonaceous nanomaterials

5.1 Overview

The formation of a fibril nucleus is a critical step in the development of amyloid fibrils. It is believed that these small fibrillar seeds or oligomers are the cytotoxic species of amyloid diseases [46, 47]. Understanding how these oligomers interact with nanomaterials is important to determine the potential for nanomaterials to act as either the amyloid seed formation inhibitors or promoters.

In this chapter spontaneous adsorption of two smallest amyloid seeds, a dimer and tetramer, of apoC-II(60-70) on the three carbonaceous nanomaterials was explored. Initially the water structuring around the nanomaterials is quantified and used to rationalise the initial adsorption mechanism and favourable adsorption state of the two oligomers to each nanosurface. Subsequently the dynamic behaviour of the oligomers on each surface is investigated. Finally the umbrella sampling technique is used to quantify the free energy of dissociation of the apoC-II(60-70) dimer from the nanomaterial surface.

5.2 Introduction

Characteristic of amyloid fibril formation is the development of a small fibril nucleus or fibril seeds. These fibril seeds provide the basis for further peptide association and allow the quick growth of amyloid fibrils. In fact it has been suggested that these small oligomer species are the cytotoxic components causing amyloid diseases [46, 47, 48, 27, 49, 50].

Understanding the effects of nanomaterials on the structure and dynamics of these fibril seeds is crucial in determining the impact nanomaterials may have on the overall fibrillation process. If nanomaterials can disrupt these small oligomers they may slow down or stop the fibrillation process, conversely, if they stabilise the fibril seed, they may accelerate the growth of amyloid fibrils.

Computational methods are able to help understand the effects of nanomaterials on the early stages of amyloid fibril formation. Recently, several studies have investigated the response of amyloidogenic amyloid-β and hIAPP to the presence of carbonaceous nanomaterials [189, 204, 194]. These studies examined several free peptides in solution in the presence of either a C60 particle, a carbon nanotube or graphene surface. They showed that in general the nanomaterials reduced the propensity of the peptides to form fibrillar structures, when compared to their solution behaviour. However, the nanomaterial-peptide complexes were often simulated at a lower peptide concentration compared to nanomaterial-free simulations which affects the peptide propensity to aggregate. Furthermore, amyloid fibril formation is a slow process and often includes many energy barriers which can make it difficult to simulate the formation of a fibril nucleus in realistic time scales. Therefore it maybe more meaningful and useful to examine the dynamics, adsorption mechanism and stability of small amyloidogenic oligomers in the presence of these nanomaterials to extrapolate their impact on the propensity for fibrillation.

The peptide - nanoparticle adsorption mechanism can be crucial in determining how these, often amphipathic, amyloidogenic oligomers interact with and are affected by nanosurfaces. It has been established that the initial adsorption between peptides and surfaces in solution is mediated by the interactions between the peptide with the structured water at the interface [139, 406, 407, 408, 409]. Water forms hydration shells around solvated surfaces which consist of ordered water molecules which generally adopt a favoured orientation

towards the surface. This structuring has been shown to induce a charged "interfacial region" which may in fact be responsible for the biased diffusion of peptides towards strongly interacting surfaces through electrostatic interactions [408, 409]. While the orientational structure of water at hydrophobic surfaces, such as graphene, may also induce electrostatic attraction of peptides, it has been demonstrated that the biased diffusion is more likely driven by surface - peptide hydrophobic interactions [408, 409]. Additionally it has been demonstrated that peptides may undergo a reversible stepwise process during adsorption to hydrophobic surfaces, firstly through biased diffusion towards the surface, followed by interfacial association with the second water layer. The peptide can transition in the region between the first and second water layer where it becomes anchored in this region. Finally "lockdown" occurs, where the peptide undergoes conformation changes that maximise contacts between the peptide and nanomaterial. These processes are influenced by the peptide's primary structure and potentially by its amphipathic nature.

Amphiphilicity of peptides and proteins can have a big impact on how they adsorb to surfaces. For example, proteins such as hydrophobin, a fungal growth facilitating protein, are amphipathic and have the ability to spontaneously form monolayers at hydrophobic or hydrophilic surfaces. This monolayer can take on different roles depending on the environment, such as to protect the microorganism or facilitate its dispersion. Like hydrophobin, amyloid fibrils are often amphipathic and this characteristic may influence their adsorption to hydrophobic carbonaceous interfaces.

In this chapter two previously characterised pre-fibrillar aggregates, a dimer and tetramer of the amyloidogenic protein apolipoprotein C-II (apoC-II(60-70)), are simulated in the presence of three dimensionally different carbon nanomaterials. Chapter 3 contains an in-depth discussion of these two apoC-II(60-70) oligomers and nanomaterials investigated.

5.3 Computational details

5.3.1 Atomistic simulations of peptide-nanomaterial systems

To investigate the adsorption mechanism of apoC-II(60-70) oligomers on the surface of different carbonaceous nanomaterials a series of simulations were performed. The oligomers (dimer and tetramer) consisted of identical apoC-II(60-70) (MSTYTGIFTDQ) peptides

in an antiparallel configuration, designated D1 and D2 (dimer) and T1 - T4 (tetramer). These oligomers were shown to be stable in previous work [257, 258] which is discussed in detail in chapter 3. The three carbonaceous nanomaterials used are the same as those used in chapter 4 albeit with different size. Here the C60 particle was the same as described in chapter 4 while the carbon nanotube was modelled as a periodic (5,5) single-walled tube and the graphene modelled as a periodic single sheet to represent an infinite graphene surface.

A set of 300 MD simulations were conducted, with 50 simulations per oligomer - nanomaterial complex. Four different starting orientations of the apoC-II(60-70) oligomer to each nanomaterial were simulated. Different initial velocities were used for every simulation. The oligomers were initially positioned sufficiently apart (greater than 15 Å) from the nanosurface to allow spontaneous adsorption of the peptides to the surface to occur outside the nonbonded cutoff range (10 Å). These simulations were run for 30 ns each which allowed the adsorption mechanism of the apoC-II(60-70) oligomer to each nanomaterial to be characterised.

An additional 24 simulations were conducted, four simulations for each oligomer (dimer and tetramer) - nanomaterial (C60, CNT and graphene) complex. These additional simulations were run for at least 250 ns to investigate the dynamic properties of the apoC-II(60-70) oligomers while adsorbed to the nanomaterials for a longer time period.

The peptide-nanoparticle complexes were placed in a periodic simulation cell of at least 60 Å x 60 Å x 60 Å in dimension. The molecular dynamics (MD) simulations were performed with the Gromacs [410] simulation package using the united-atom Gromos forcefield and the 43A1 parameter set. The carbonaceous nanomaterials were modelled using the aromatic sp2 carbon parameters. The Lennard-Jones interactions were truncated at 10 Å, with the long-range electrostatic interactions accounted for by the Particle Mesh Ewald (PME) method [379]. The LINCS algorithm was used to constrain the bond lengths to their equilibrium values [278] enabling a timestep of 2 fs to be applied for all simulations. *In vacuo* energy minimization using steepest descent algorithm was initially performed on the peptide-nanoparticle system followed by solvation with the SPC water model [245]. To neutralise the overall negative charge of the system, two (dimer) and four (tetramer) unrestrained counterions (Na+) were included in the simulation cell. Energy minimisation

on the solvated system was performed to relax all atomic degrees of freedom. Subsequently, MD was conducted to allow the solvent to equilibrate around the solutes by keeping the peptide and nanomaterial restrained. A constant temperature of 300 K was maintained using the V-rescale thermostat [274]. In all simulations the geometry of the nanomaterial was restrained. The simulations used to investigate the spontaneous adsorption mechanism of apoC-II(60-70) to each nanomaterial resulted in 9 μs of data. The additional simulations used to investigate the dynamic properties of apoC-II(60-70) oligomers while adsorbed to each nanomaterial produced in 6 μs of data for analysis.

5.3.2 Dissociation free energy calculations

Using umbrella sampling together with the weighted histogram analysis method (WHAM) [385], potential of mean force (PMF) profiles were generated to evaluate the free energy of dissociation (ΔG) for the apoC-II(60-70) dimer bound to each nanomaterial in solution. The PMF was determined as a function of separation distance between the centre of mass of the nanomaterial and the α-carbon of the glycine residue of one of the apoC-II(60-70) monomers (D1). To acquire the PMF profiles, a series of simulations (windows) were performed at increasing distance between the peptide and nanomaterial, starting from selected initial structures (described later). The D1 monomer was restrained at each window using Hookean function with a force constant of 8000 kJmol^{-1}nm^{-2}. In the present work, ΔG and PMF both refer to the free energy required to bring D1 and the nanomaterial apart from an associated form, to some separation *d*. Adjacent windows were separated by 0.5 Å and each window was simulated for 15 ns with 35 windows used (until the restrained monomer was fully dissociated from the nanomaterial), resulting in a total simulation time of at least 525 ns per nanomaterial-peptide complex. WHAM was subsequently applied on the final 5 ns of simulations to remove the biasing potential and obtain the unbiased PMF profiles.

5.4 Results and discussions

Initially the structuring of water around each nanomaterial was examined, as it has been shown that water can influence the interactions between nanomaterials and peptides [139,

406, 407, 408, 409]. Subsequently the adsorption mechanism of the two oligomers on the surface of each nanomaterial was identified. The stability and dynamics of the oligomers while adsorbed to the nanomaterials was also investigated. Finally the potential of mean force required to remove a peptide from the nanomaterial was determined.

5.4.1 Water structuring on the surface of graphitic nanoparticles

The water structure around surfaces has been shown to influence the initial adsorption of peptides and proteins. Here, the water structuring was characterised by the density of the oxygen and hydrogen atoms of water molecules as a function of distance from the surface of each nanomaterial, Figure 5.1. The water charge density as a function of distance from the surface is also plotted, Figure 5.1. The density of the atoms is calculated by initially determining the number of atoms within a bin Δd at a distance d, where this bin is actually represented as a 3D volume. For the C60 particle the bin is a spherical shell, for the CNT it is cylindrical shell and for the graphene it is a rectangular slice. The number of atoms within each bin was then divided by the respective bin volume, in this way the density is normalised for the number of atoms and surface area of each nanomaterial. Finally the resulting density is normalised with respect to the density of bulk water to produce the variation density shown in Figure 5.1.

The density plots show that there are two well defined water shells that form around all the nanomaterials, albeit with differing peak density. The first and most structured water layer forms between 2 and 4.8 Å with a peak at $\approx$ 2 Å and the second forms at $\approx$ 6 Å. While these water layers form at the same distance from the surface of all the nanomaterials, regardless of the surface curvature, they do have differing peak heights. The water layer that forms around graphene is most structured with a peak density of 3.5 and 2.5 for the first and second water shell respectively. While the curved nanomaterials, C60 and CNT, have reduced order resulting in lower peak densities for the first peak at 3 and 2.9 respectively. This reduced ordering results in an attenuation in the 1st charge density trough at 3.5 Å, compared to the charge density trough of water at the graphene surface.

The difference in charge density was a result of the orientation of the water molecules with respect to the nanomaterial surface. The density profiles indicate that the hydrogen

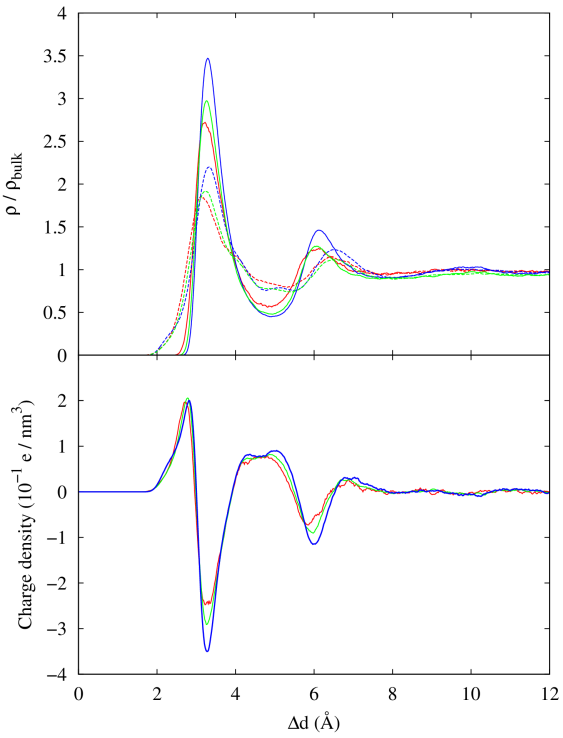

Figure 5.1: (a) Variation of density of oxygen (solid) and hydrogen (dashed) atoms of water molecules relative to the bulk phase density; and charge density resulting from the difference in oxygen and hydrogen atom distribution as a function of distance from the surface of C60 (red), CNT (green) and graphene (blue)

atoms of water are in closest contact with the nanomaterials and that in general the hydrogen atoms were oriented toward the surface while the oxygen atoms where oriented towards the bulk solvent. This ordering indicates the formation of an electrostatic double layer at the graphitic nanomaterial surface. It has been suggested that this orientational ordering of water can result in long range electrostatic interactions that may play a role in the initial adsorption of peptides and proteins to nanosurfaces [408, 409].

5.4.2 Amphipathicity characterisation of apoC-II(60-70) oligomers

As discussed in the introduction, Section 5.2, another factor that can play a role in peptide/protein adsorption to surfaces and interfaces is the inherent amphipathicity of some of these peptides/proteins. Here the amphipathicity is characterised using 3D hydrophobic moment vectors [411]. This tool identifies the hydrophobic moment (HM) of a molecule as a vector in three dimensions by evaluating the surface distribution of all hydrophilic and lipophilic regions. Additionally the electrostatic potential on the peptide surface is

calculated based on the atomic point charges. The hydrophobic moment is a vector normal to the most hydrophobic face of the peptide. Additionally the magnitude of this vector is a measure of the difference in hydrophobicity between the two faces of the molecule.

The hydrophobic moment vector and electrostatic potential have been calculated for the initial apoC-II(60-70) dimer and tetramer as shown in Figure 5.2a,b along with representative structures. The HM of the two oligomers is also shown in Figure 5.2a-iv and b-iv.

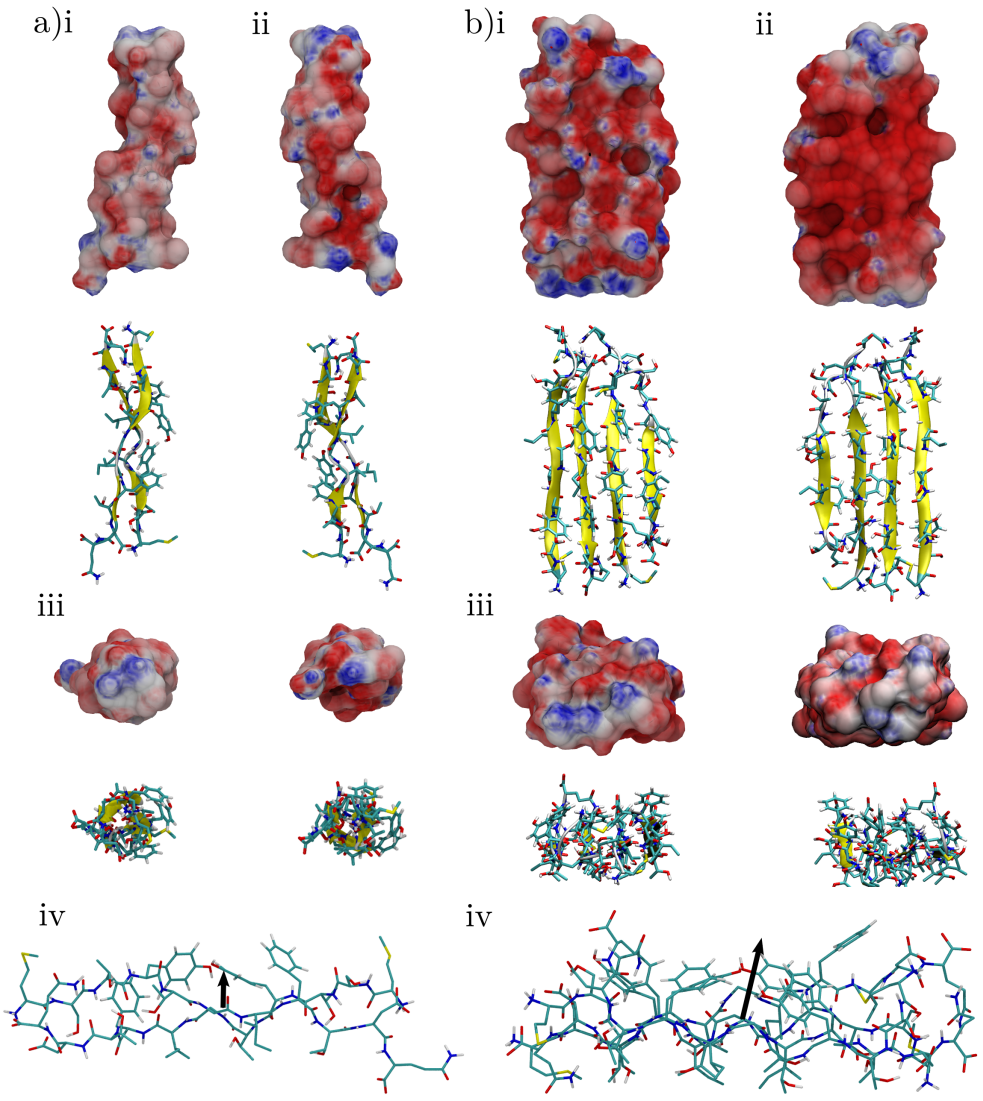

Figure 5.2: The electrostatic potential on the solvent-accessible surface area and representative structures of the apoC-II(60-70) dimer (a) and tetramer (b). The HM of the apoC-II(60-70) dimer (a-iv) and tetramer (b-iv) is shown as a black arrow.

The results show that the dimer has a mostly even electrostatic charge distribution

around its entire surface, for the twisted conformation that the apoC-II(60-70) dimer was found to adopt in solution [257]. This conformation results in flexible residue side chains leading to an even distribution of charges around the dimer surface. Conversely the tetramer has two distinct faces, a negatively charged face on the side of the threonine residue side chains (b-ii) and a more evenly distributed charged face on the side with the exposed aromatic residue side chains (b-i). These two faces are defined from here on as NF (negative face) and HF (hydrophobic face) respectively. The different electrostatic distributions between the two oligomers result in different magnitude HM's. The calculated HM is much smaller for the dimer than for the tetramer. The HM of the dimer is almost non-existent, with the small vector projected in the direction of the aromatic residues. The reduced magnitude HM vector is due to the twisted dimer conformation resulting in evenly distributed charged surface as discussed above. The restricted peptide chains of the tetramer produce the two distinctly different charged surfaces. This large charge distribution difference between the NF and HF faces results in the larger magnitude HM vectors compared to the dimer. The HM vector is directed from the NF towards the HF. It can be suggested that as the oligomer grows in size, ie. self assemble with like peptides along the fibril axis, the HM will increase resulting in greater amphipathicity.

Overall, the solution conformation of the apoC-II(60-70) dimer does not show any significant amphiphilic characteristics. In contrast, the solution conformation of the apoC-II(60-70) tetramer has two distinct hydrophilic and hydrophobic faces, NF and HF respectively. The NF is characterised by the presence of threonine side chains, Thr62, Thr64 and Thr68, while the HF is characterised by the presence of aromatic side chains, Tyr63 and Phe67 specifically. It is proposed that the amphipathic properties of the tetramer may have an effect on the adsorption mechanism to different nanomaterials. Although only the solution structures were examined here for their amphipathicity, they have been shown to be stable conformations in solution and do not undergo large conformational changes in the initial adsorption phase, see first 5 ns of RMSD results in section 5.4.4. However after adsorbing to the surface of the nanomaterial conformational changes do occur, see RMSD changes after adsorption, in section 5.4.4.

5.4.3 Adsorption mechanism of apoC-II(60-70) oligomers to graphitic nanoparticles

Determining the favourable adsorption process and the residues that are important in this interaction can guide the development of nanomaterials to target specific peptides and proteins. It is also important to consider other effects of protein conformation on adsorption processes such as conformation dependent amphiphilicity. It is well known that amphipathic proteins and peptides adsorb to hydrophobic and hydrophilic surfaces in very different ways. These different adsorption mechanisms may have a large impact on the final configurations of the peptide at the nanosurface and how they interact with other like peptide/proteins at these interfaces.

It has recently been proposed that peptides undergo a stepwise process upon adsorption to the surface of hydrophobic nanomaterials [409]. It was suggested that initially a biased diffusion of the peptide towards the surface takes place, mediated by electrostatic and hydrophobic interactions. The electrostatic interactions are driven by the orientation ordering of water at the surface water interface, discussed in section 5.4.1, while the hydrophobic interactions are driven by interactions between the surface and peptide. Once this diffusion brings the peptide to within a certain distance of the surface it begins interacting with the "interfacial region" (defined here as 7.8 - 10.8 Å from the surface). This association leads to an event termed "anchoring" whereby the peptide transitions through the outer most water layer, overcoming an energy barrier, to populate a region between water layers (defined as 4.8 - 7.8 Å from the surface). Once the peptide has transitioned through this water layer hydrophobic interactions between the surface and peptide induce closer interactions. The peptide is able to pass through and disrupt the first hydration shell and adsorb to the surface (less than 4.8 Å from the nanosurface). The recent work by Penna et al. investigated the adsorption mechanism of several monomeric peptide sequences at the graphene interface, herein the adsorption mechanism of more complex peptide configurations was considered, namely a dimer and tetramer of the apoC-II(60-70) peptide [257, 258]. Along with nanomaterials of different dimensionality the more complex peptides considered allow the investigation of stable peptide configuration and phenomena such as peptide amphipathicity on the adsorption process.

A total of 300 independent molecular dynamics simulations were conducted to investigate a large number of apoC-II(60-70) adsorption events. These simulations showed that apoC-II(60-70) oligomers would spontaneously absorb to all three nanomaterials within 30 ns of each simulation, albeit in differing configurations. Initially the residues that instigated interaction with the interfacial (I), anchoring (A) and contact (C) regions at the water - surface interface were investigated. To achieve this the following protocol was applied at each timeframe to determine the "residence time" for each residue of the apoC-II(60-70) peptides within each of the regions:

1. The minimum distance of the apoC-II(60-70) oligomer from the nanomaterial was determined.

2. If the oligomers minimum distance was within the range 7.8 - 10.8 Å, 4.8 - 7.8 Å or <4.8 Å it was assigned to region I, A or C respectively.

3. The minimum distance of all apoC-II(60-70) residue side chain/terminal (defined from here on as SC/T) was then determined.

4. If a residue SC/T minimum distance was within the same range as that of the peptide's minimum distance (determined at step 1), that residue SC/T was considered to be present in that region, and a count for the specific residue SC/T taken.

5. Once the peptide's minimum distance entered a new range, i.e. transitions from region I to A, only residue SC/Ts whose minimum distance within the same region were counted.

6. Once all timeframes had been processed, the residue SC/T residence results normalised with respect to the total time the peptide's minimum distance was within the respective region.

The per residue results for the residence time of each region were averaged over all 50 simulations for each peptide - nanomaterial system. In Figure 5.3 the per residue residence time is shown normalised by the number of peptide chains, for the residues in the interfacial region (a), anchoring region (b) and contact region (c). These results highlight the residue SC/Ts that are most populated within each region.

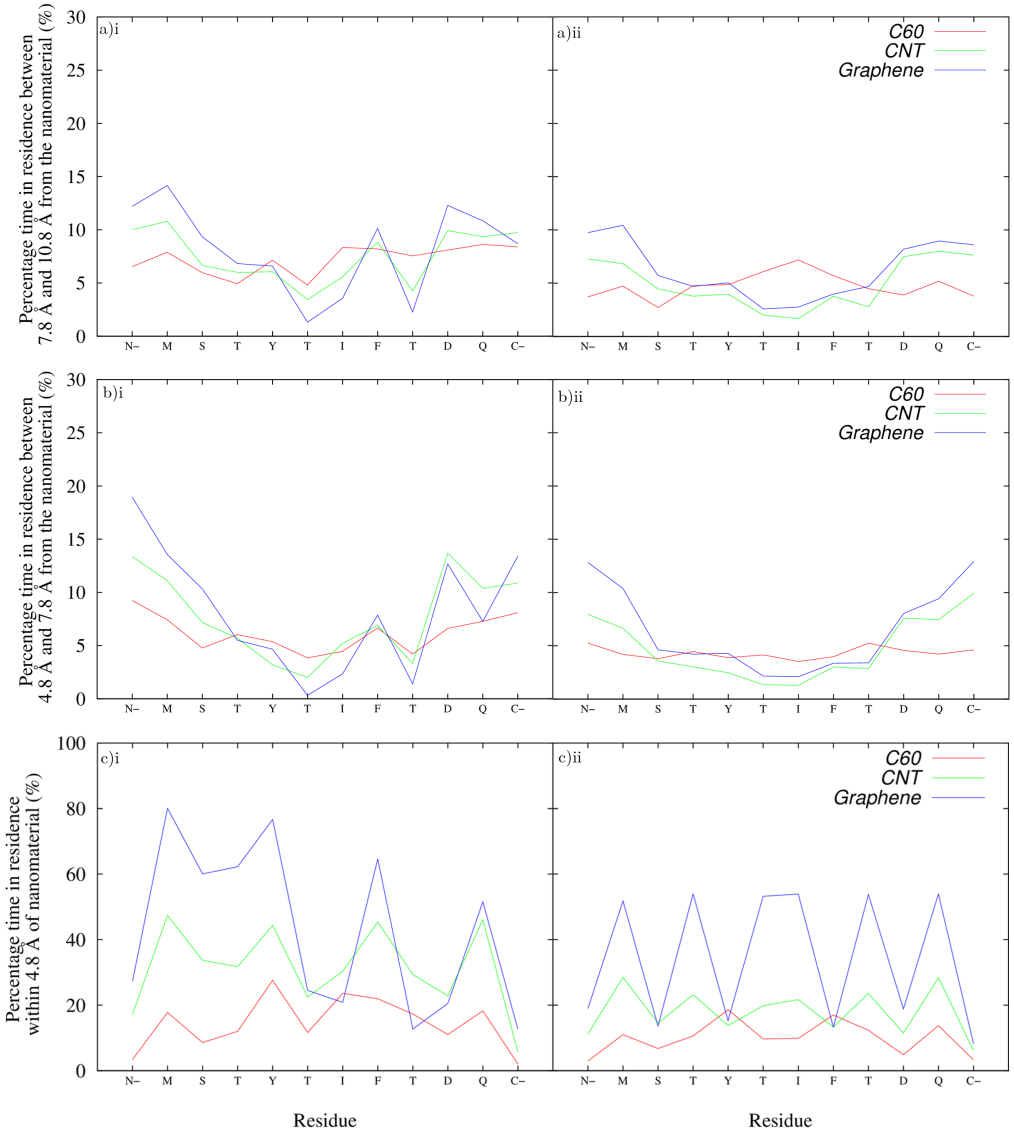

Figure 5.3: Residence time the residue side chains/terminals of the apoC-II(60-70) dimer (i) and tetramer (ii) are within the interface (a), anchoring (b) and contact regions (c), between 7.8 and 10.8 Å, 4.8 and 7.8 Å and <4.8 Å from the surface of the C60 (red), CNT (green) and graphene (blue) respectively

As discussed, peptides in the presence of surfaces can undergo a biased diffusion towards the surface, therefore, by investigating the interactions that initially take place between the peptide and the interfacial layer, the residues that drive this diffusion can be determined. Figure 5.3a shows the residue SC/Ts of the apoC-II(60-70) dimer (a-i) and tetramer (a-ii) that populate the interfacial region of the C60, CNT and graphene. The residence time of the residue SC/Ts of the dimer and tetramer with the interfacial region at the CNT and graphene interface had similar trends, while the oligomer - C60

interactions where quite different. Statistically the residue SC/T groups that had the highest residence within the interfacial layer at the CNT and graphene interface were the two terminal groups (N- and C- in Figure 5.3a) as well as the corresponding side chains of Met60 and Gln70. Additionally the charged Asp69 side chain showed significant presence in this region. While for the C60 particle there was less than 5% difference between the average percentage residence time of all the residue SC/Ts, with the C-terminal being the most populated. The results suggest that the interactions with the interfacial region at the CNT, graphene surface and to a minimal extent the C60 particle are driven by electrostatic forces. These interactions come about from the electrical double layer formed by water at these surfaces, where the graphene presents the most polarised surface, followed by the CNT and then the C60 particle, Figure 5.1. Recently polarisable graphitic nanomaterials (CNT, graphene) have been parameterised for use in the CHARMM forcefield, it was shown that water oriented toward the surface in the same way as demonstrated here albeit with significantly more structuring [251]. The interfacial region has a weak overall negative charge, as calculated by determining the area under the charge density profile between 7.8 and 10.8 Å (see appendix B), which results in long range electrostatic interactions with the positively charged N-terminal of the oligomers. This interaction results in the biased diffusion towards the surface and drives the interfacial association. The electrical double layer means that both the positive N-terminal and negative C-terminal can both populate the interfacial region by interacting with the negatively charged oxygen layer and positively charged hydrogen layer respectively. The attenuation of the polarised water surface around the C60 particle results in the reduced population of the terminal interactions with the interfacial region and more interactions with the hydrophobic residues are seen to dominate.

Following interfacial association the peptide undergoes "anchoring", whereby it transitions in between the first and second water layers. Figure 5.3b shows the residence time each residue SC/T of the apoC-II(60-70) dimer (b-i) and tetramer (b-ii) anchored within this region at the C60, CNT and graphene interface. The results for the anchoring region are similar to those at the interfacial region. That is, for the oligomers in the presence of the flatter CNT and graphene surfaces the most persistent interactions were between the N and C terminals as well as the charged Asp69 residue side chain. The increased

residence times of the charged SC/T at the A region compared to at the I region was a result of the electric double layer that water forms at these surfaces. The electric double layer drives the electrostatic interactions between the negative and positively charged terminal residues of the two oligomers. In the presence of the C60 particle, no residue SC/T dominates the anchoring within this region and as such the residence times for each residue SC/T is between 5 and 10% and $\approx$ 5% for the dimer and tetramer respectively.

Finally the oligomers transition into contact with the nanosurface. Figure 5.3c shows the residence time of each residue SC/T in the contact region while the apoC-II(60-70) dimer (c-i) and tetramer (c-ii) are adsorbed to the C60, CNT and graphene. Significantly different residue SC/T residence times are observed for the peptides in the contact region compared to the initial transition from the bulk solution into the interfacial and anchoring regions. The residence time for the residue SC/Ts of the apoC-II(60-70) dimer within the contact region of each nanomaterial exhibit similar trends. The residue side chains that had the highest residence time were the hydrophobic or aromatic side chains, with peaks at Met60, Tyr63 and Phe67, while the previously dominant terminals showed minimal presence within this region. The increased hydrophobic and aromatic interactions have been shown, in Chapter 4, to be the most favourable interaction at the surface of carbonaceous nanomaterials. Peptide contact with the surface has also been shown to induce dewetting of the peptide and nanomaterial water layers, Chapter 4. The dewetting of the graphitic nanomaterials explains the comparatively low residence time of the N and C terminals, <4%, <20% and <30% for the C60, CNT and graphene interfaces respectively. As discussed earlier the terminals interact with the electric double layer formed at nanomaterial interface thus while the peptide is adsorbed to the nanosurface they remain at a minimum distance greater than 4.8 Å which allows the interact within the electric double layer of water that has not been disrupted by the peptide adsorption. Overall the dimer has the greatest residue SC/T residence times while adsorbed to the graphene surface followed by the CNT and then the C60. The greater residence times observed on the graphene and CNT is due to the reduced curvature of these surfaces that allows a greater peptide contact area (see section 5.4.4 for more evidence). In contrast, the apoC-II(60-70) tetramer's most persistent interactions are between it's threonine residues and the CNT and graphene. Distinct peaks can be observed for the Met60, Thr62, Thr64, Ile66, Thr68,

Gln70 residue side chains. These side chains all correspond to the side chains exposed on the NF of the tetramer discussed in section 5.4.2. The negatively charged threonine residues interact with the positively charged hydrogen's of the water electric double layer. This interaction draws the threonine residues towards the nanosurface, explaining the counter intuitive adsorption of hydrophillic residues to the hydrophobic surface. Additionally it has recently been shown that for a β-sheet rich anti-freeze protein the threonine residues drive adsorption to a graphene surface [412]. Lv et al. suggested that the adsorption is stabilised by the CH-π interactions between the Thr side chains and the graphene carbon rings. A feature of the united-atom GROMOS FF, that is employed here, is that the CH groups are united as one interaction site. The results presented here correlate well with the all-atom molecular dynamics study conducted by Lv et al. and suggest that the CH-π interactions between the Thr residue sides chain and graphitic nanomaterials are captured adequately by the GROMOS force field.

At the CNT interface the tetramer also exhibits more stable interactions with the Met60, Thr62, Thr64, Ile66, Thr68, Gln70 residue side chains, however with lower population times compared to graphene. This reduction is a result of the increased curvature of the CNT compared to the flat graphene, which reduces the ability of the peptide to form stable CH-π interactions.

At the C60 interface the residue SC/Ts of the apoC-II(60-70) tetramer exhibit a markedly different persistence profile whereby the most persistent residue side chain interactions are those of the aromatic residues, Tyr63 and Phe67. This indicates that adsorption to the C60 surface takes place through the HF of the tetramer.

Having determined the specific residue SC/Ts that drive adsorption to the surface of these different nanomaterials the next step was to determine the favourable adsorption conformation. This has been achieved by plotting the free energy landscape of the adsorption process for each peptide - nanomaterial complex, Figures 5.5 and 5.6. The adsorption process is tracked at every timeframe by the following procedure:

1. The separation distance (Δd) between the nanomaterial surface and the C_α of the Gly65 residue of strand D2 for the apoC-II(60-70) dimer and T2 for the apoC-II(60-70) tetramer was determined.

2. The vector V1 was then produced, where V1 was the vector normal to the surface in the direction of the same C_α atom of the Gly65 as in step 1, see Figure 5.4.

3. Two angles were then produced with respect to vector V1, angle θ and angle ϕ.

4. Angle θ

   (a) θ is the angle produced by the two vectors V1 and V2, where

   (b) V2 is the vector formed between the C_α atom of the Tyr63 and the C_α atom of the Phe67, of strand D2 and T2 of the dimer and tetramer respectively, Figure 5.4a.

5. Angle ϕ

   (a) ϕ is the angle produced by the two vectors V1 and V3, where

   (b) V3 is the vector normal to the plane produced by the three C_α atoms of Tyr63 and Phe67 of strand D2 and T2 (apoC-II(60-70) dimer and tetramer respectively) and Gly65 of chain D1 (dimer) and chain T3 (tetramer), Figure 5.4b.

6. Finally two histograms were produced that tracked the angle θ at separation distance Δd and the angle ϕ at separation Δd. These histograms used the data from all trajectories for each peptide-nanomaterial complex.

7. A free energy map was produced from the two histograms using the relationship $\Delta G_{\Delta d,\theta} = -RT(log(f(\Delta d, \theta)))$ and $\Delta G_{\Delta d,\phi} = -RT(log(f(\Delta d, \phi)))$. These are shown in Figures 5.5 and 5.6.

The two angles, (θ, ϕ) show the relative orientation of the oligomers to the surface of the nanomaterials as they approach the surface and once adsorbed. A θ angle of 0 - 30° and 150 - 180° indicates the oligomer is oriented with the terminal residues toward the surface. At a θ angle of $\approx$ 90° the peptide plane is oriented perpendicular to the surface normal (as pictured in Figure 5.4a). Angle ϕ shows the orientation of the oligomer faces to the surface of the nanomaterial. At a ϕ angle of <30° the HF of the tetramer is solvent exposed while 150° <ϕ <180° the HF of the tetramer is oriented towards the nanosurface. Finally at a ϕ angle $\approx$ 90° the HF is directed perpendicular to the surface normal.

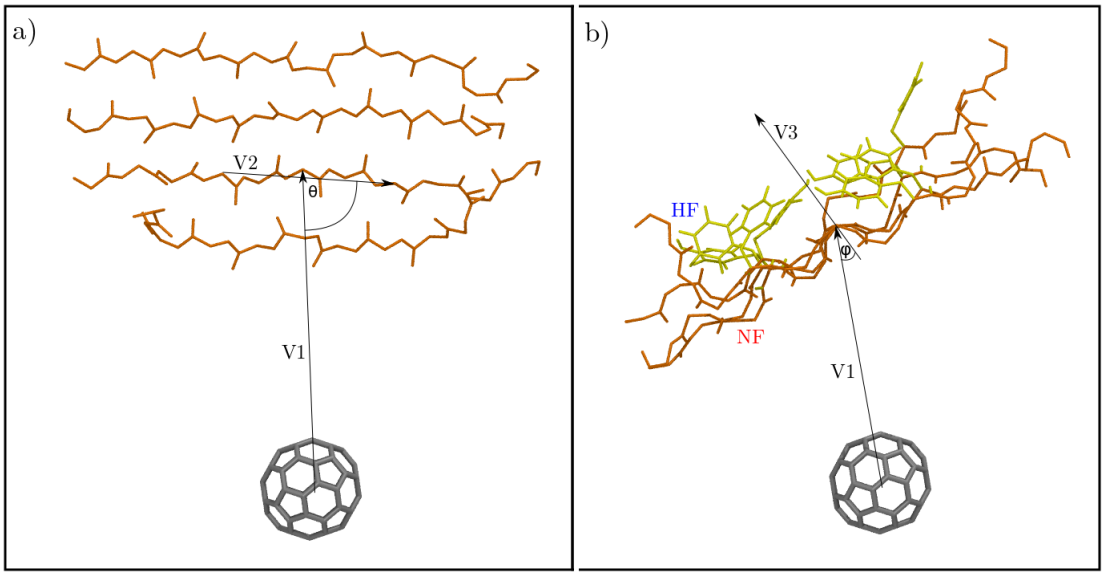

Figure 5.4: Representative image showing the angles θ (a) and ϕ (b) along with the vector V1, V2 and V3 used to generate these angles. Additionally the hydrophobic face (HF) and negativly charged face (NF) of the apoC-II(60-70) is labelled.

Figure 5.5 shows the free energy landscape of adsorption of the apoC-II(60-70) dimer to the C60 (a), CNT (b) and graphene (c). At a distance greater than 3 nm from the surface of the nanomaterial there was no distinctly favoured orientation for either the θ or ϕ angles. However once the peptide approaches the interfacial region, 1 $<\Delta$d $<$1.5 nm, there are distinct orientations that correspond to a θ angle of 0 - 40° and 140 - 180°. Here, the simulations show the dimer is tilted towards the surface with the terminal residues interacting with the interfacial layer, which was observed in the presence of each nanosurfaces. Once associated with the surface ($<$1 nm) the dimer populated a θ angle region around 90°, corresponding to dimer adsorbed in a configuration perpendicular to the surface normal of the nanomaterial (see inserts in Figure 5.4 for clarity).

The ϕ angle profiles are used to show the relative orientation of the aromatic face of the apoC-II(60-70) dimer to each nanosurface. In the presence of the C60 and CNT particles the dimer does not seem to adopt any favourable orientation, with several free energy wells present at separation distance $<$1 nm. While on the graphene surface there is a distinct shift towards a ϕ angle of greater than 130°. The dimer configuration at the surface here is highlighted by the inserts 1' and 2' which show the aromatic residues of the dimer π-π stacking with the surface. These results correlate well with the previous

characterisation of the stable residue SC/T groups.

Figure 5.6 shows the free energy adsorption profiles for the apoC-II(60-70) tetramer to the C60 (a), CNT (b) and graphene (c). Similar to the apoC-II(60-70) dimer, the tetramer does not adopt a favourable orientation for either the θ or ϕ angles at a distance of greater than 2 nm from the surface. Like the dimer however the tetramer does show favourable orientation towards the interfacial region at distances of 1 - 2 nm. This results in θ angles preferences between 0 - 50° and 130 - 180°. These configurations are representative of tetramers oriented with the terminal residues towards the nanomaterial surface, as proposed earlier. As the tetramer moves through the interfacial region and anchoring region it transitioned to an orientation with the peptide chains oriented across the surface (perpendicular to the surface normal). The inserts in figure 5.6 highlight these final adsorption configurations.

The ϕ angle shows the direction of the HF of the apoC-II(60-70) tetramer, whether it is oriented towards or away from the surface. Unlike the apoC-II(60-70) dimer the tetramer has very distinct free energy wells with respect to the ϕ angle. While in the presence of any nanomaterials the tetramers final configuration ended either adsorbed to the surface with the HF facing the surface or the solvent. On the C60 particle the favourable ϕ orientation is around 140°, with the aromatic residues π-π stacking and driving the adsorption, insert 1' and 2' Figure 5.6. There is also a small free energy well around 40°, this structure is shown by insert 3', Figure 5.6. Here the tetramer is interacting with the C60 surface via the threonine and isoleucine residues with the HF solvent exposed.

While adsorbed to the CNT and graphene surface the tetramer had a much greater propensity to adopt a configuration with the NF oriented to the surface and HF oriented to the solvent, in 24% of CNT simulations and 34% of graphene, compared to the simulations that resulted in the HF oriented to the surface,only 8% for the CNT and 4% for the graphene. This is additionally highlighted on the free energy profiles with the lowest free energies, $\approx$ -5 Kcal/mol, at ϕ angles of 0 - 40° and at a distance of $\approx$ 1 nm, Figure 5.6b-ii and c-ii. Additionally on both the CNT and graphene surface the tetramer had low free energies at $\approx$ 90° and between 1 - 1.5 nm from the surface, these regions correspond to structures that are typically adsorbed perpendicular to the nanosurface, examples shown as insert 2' for the CNT and 3' for the graphene in Figure 5.6. It is postulated that

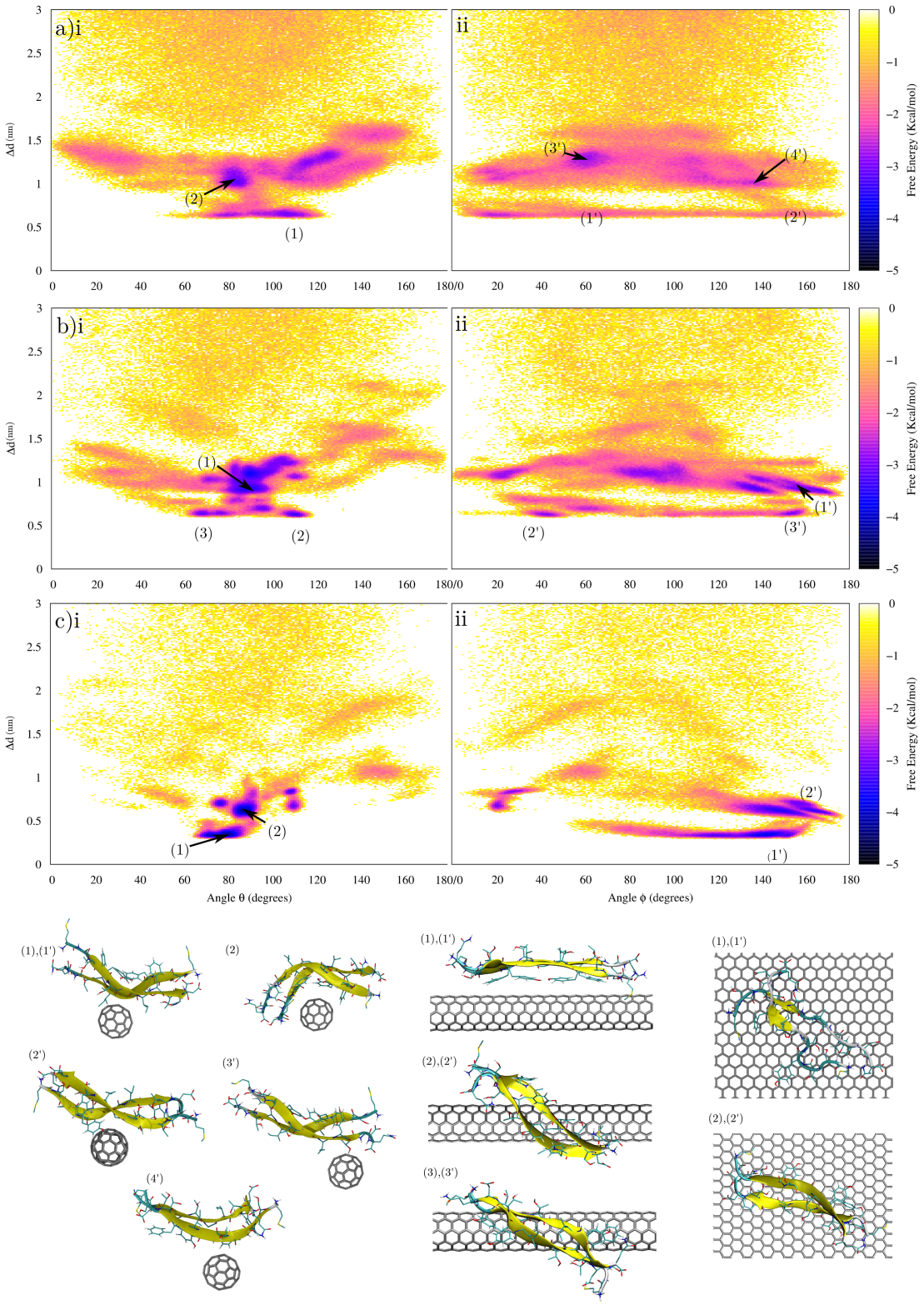

Figure 5.5: Free energy maps of adsorption of the apoC-II(60-70) dimer to the C60 (a) CNT (b) and graphene (c) with respect to the angle θ (i) and ϕ (ii)

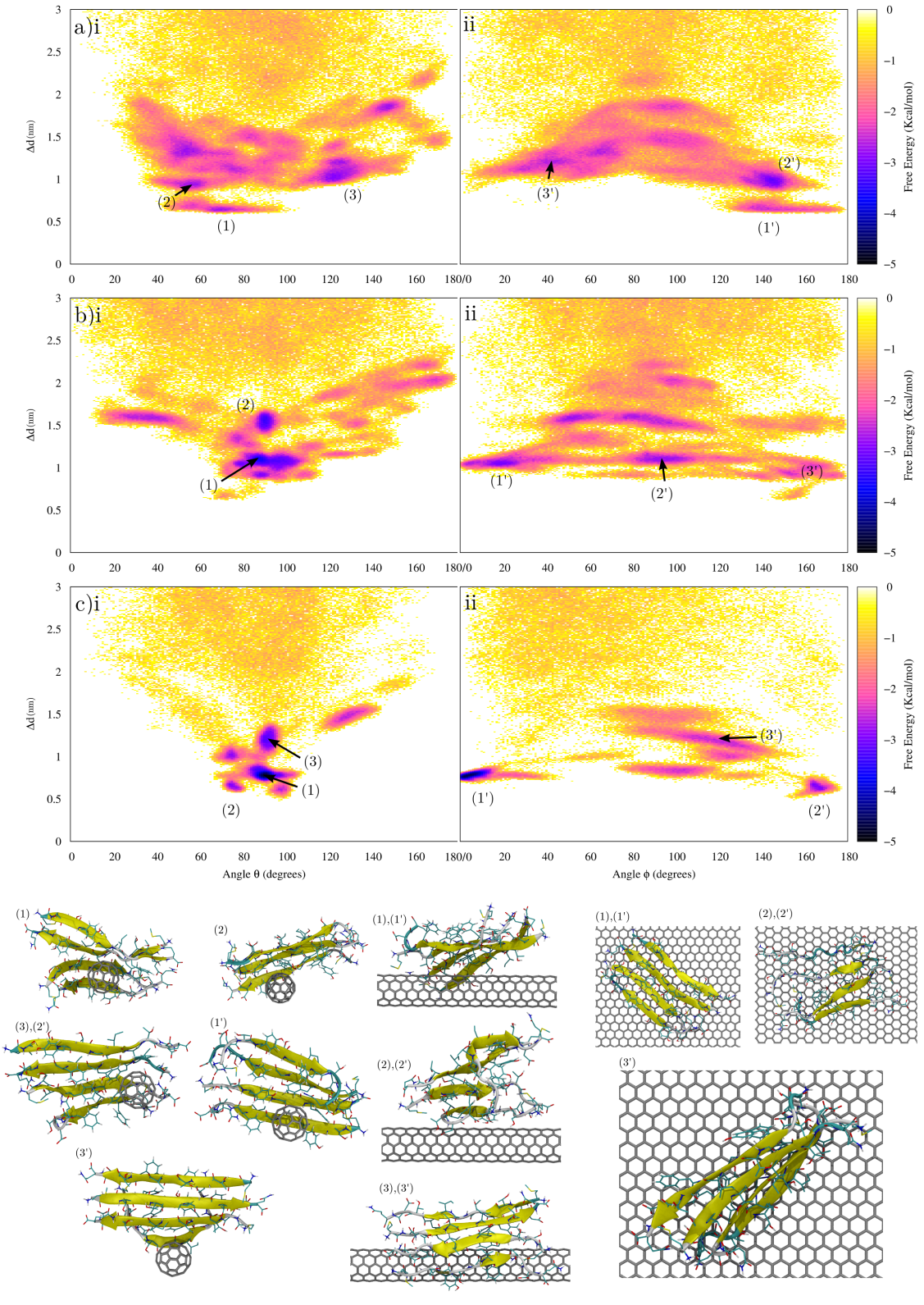

Figure 5.6: Free energy maps of adsorption of the apoC-II(60-70) tetramer to the C60 (a) CNT (b) and graphene (c) with respect to the angle θ (i) and ϕ (ii)

these structures would be short lived and will eventually transition to either of the most populated states where the tetramer HF was solvent exposed or the HF was surface bound.

Overall the results showed that the apoC-II(60-70) oligomers initiated interaction with the interfacial region by tilting toward the surface allowing the terminal residues to contact this region. This was driven by the long range electrostatic interactions between the water layers and the charged residues of the peptides. These initial contacts resulted in biased diffusion of both peptide oligomers toward the nanosurfaces. The oligomers then transition through the water layers via electrostatic interactions at the CNT and graphene surfaces or via more hydrophobic interactions at the C60 surface. Finally contact with the surface resulted in markedly different binding motifs for the apoC-II(60-70) dimer and tetramer. The dimer exhibited a favourable binding configuration with the peptide strands oriented across the nanosurface, perpendicular to the surface normal, which enables maximum contacts. However at the C60 and CNT surfaces there was no dominant dimer face that drove adsorption. While at the graphene surface it is clear that it was favorable for the aromatic residues to interact strongly with the surface. In contrast the tetramers amphiphilicity resulted in two well defined binding motifs, that were either HF solvent exposed or HF surface bound. At the surface of the C60 particle the tetramer favoured the HF surface bound motif while at the CNT and graphene interfaces the preferred configuration was with the HF solvent exposed.

5.4.4 Structure and dynamics of apoC-II(60-70) oligomers in the presence of graphitic nanoparticles

In general when peptides established contact with the surfaces, they reorient to induce closer interaction with the surface, in a process termed ”lockdown”. At carbonaceous surfaces, these close contacts are typically driven by hydrophobic or aromatic interactions. This behaviour has been shown in Chapter 4 where it was observed that the most prevalent interactions were between the aromatic residues of the monomeric apoC-II(60-70) and the carbonaceous surface. These interactions were driven by π-π stacking between the surface and nanomaterial and ultimately induced closer contacts between the carbon surface and peptide.

Figure 5.7 shows data collected from the trajectory of the exemplar MD simulation of

apoC-II(60-70) dimer (a,c) and tetramer (b,d) with each nanomaterial as they undergo adsorption and "lockdown" to the nanosurface. The contact area (a,b) between the apoC-II(60-70) oligomers and each nanomaterial is plotted along with the RMSD (c,d) of the two oligomers as a function of time over the course of the simulations. The results show an increase in contact area between both the apoC-II(60-70) dimer and tetramer upon adsorption to the nanomaterials. In all cases the contact area is greatest when adsorbed to the surface of the graphene ($\approx$ 7 nm^2 and $\approx$ 10 nm^2 for the dimer and tetramer respectively) followed by the CNT ($\approx$ 4 nm^2 and $\approx$ 10 nm^2) and finally the C60 particle ($\approx$ 2 nm^2 and $\approx$ 4 nm^2). These results correlate with the contact area results calculated for the monomeric apoC-II(60-70).

There is an increase in contact area over the course of the simulation between both oligomers and all nanomaterials. However, a larger increase (at least 65%) in contact area is observed for the apoC-II(60-70) tetramer while adsorbed to all the nanomaterials, a result of the greater number of atoms available to interact with the surface. Additionally both peptides undergo RMSD changes while adsorbed to the surface of all the nanomaterials, where some of these RMSD changes correlate with a change in contact area. This is particularly evident for the apoC-II(60-70) tetramer adsorbed to the surface of the graphene, whereby several structural changes result in large increases in the contact area between the peptide and nanosurface, specifically at 125 ns (an increase from $\approx$ 5.5 nm^2 to $\approx$ 7.4 nm^2) and 160 ns (an increase from $\approx$ 7.7 nm^2 to $\approx$ 9.7 nm^2).

While these figures show exemplar trajectories of the conformational rearrangement that optimises the contact area between the peptide and nanomaterial, this rearrangement is not always observed. Additional data showing such trajectories is shown in appendix B. The variation between the results highlights the difficulty that spontaneous classical molecular dynamics has to adequately sample oligomeric peptide conformations with short simulations (in this case $<$ 400 ns). Therefore, in Chapter 6 the replica exchange with solute tempering (REST) method is employed to enhance the conformational sampling of the apoC-II(60-70) dimer and tetramer while adsorbed to the each nanomaterial.

Overall the apoC-II(60-70) dimer and tetramer retained their preferred antiparallel arrangement of the peptide strands for the duration of the simulations, albeit with some structural changes caused by the nanoparticle curvature and interaction with the surfaces.

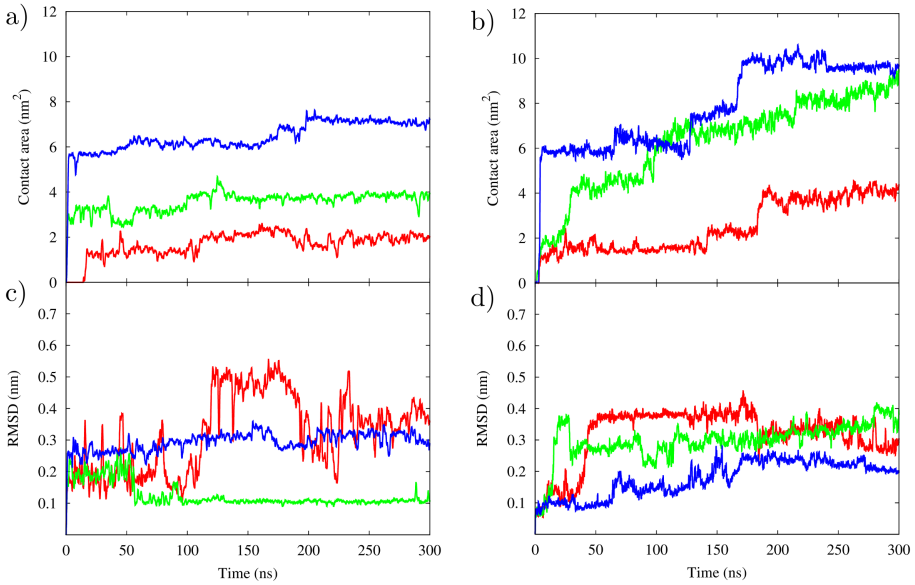

Figure 5.7: Trajectory data from the exemplar MD simulation of apoC-II oligomers on the surface of graphitic nanomaterials showing the contact area change between the apoC-II(60-70) dimer (a) and tetramer (b) with the C60 (red), CNT (green) and graphene (blue) nanoparticles. Root mean squared deviation of the apoC-II(60-70) dimer (c) and tetramer (d) while adsorbed to the C60 (red), CNT (green) and graphene (blue) nanoparticles.

Nanomaterial	Dimer average β-sheet content (%)	Tetramer average β-sheet content (%)
C60	54 ± 19	45 ± 8
CNT	49 ± 19	47 ± 11
Graphene	19 ± 17	64 ± 17

Table 5.1: Percent β-sheet content retained in the final 50 ns of simulation, averaged over the four simulations.

Root mean square fluctuation results (Figure 5.8) showed that the apoC-II(60-70) dimer and tetramer were the least dynamic on the flat graphene surface compared to the highly curved C60 particle and CNT. This indicates that nanoparticle curvature plays a role in oligomer dynamics, similar to the monomeric apoC-II(60-70). Secondary structure analysis shows that the flat graphene surface induces significant loss in β-sheet content of the apoC-II(60-70) dimer, Table 5.1. Conversely the apoC-II(60-70) tetramer retained the most β-sheet content while adsorbed to the graphene surface. These contrasting results are difficult to rationalise without additional simulations to ensure comprehensive sampling

of the oligomers in the presence of different nanoparticles.

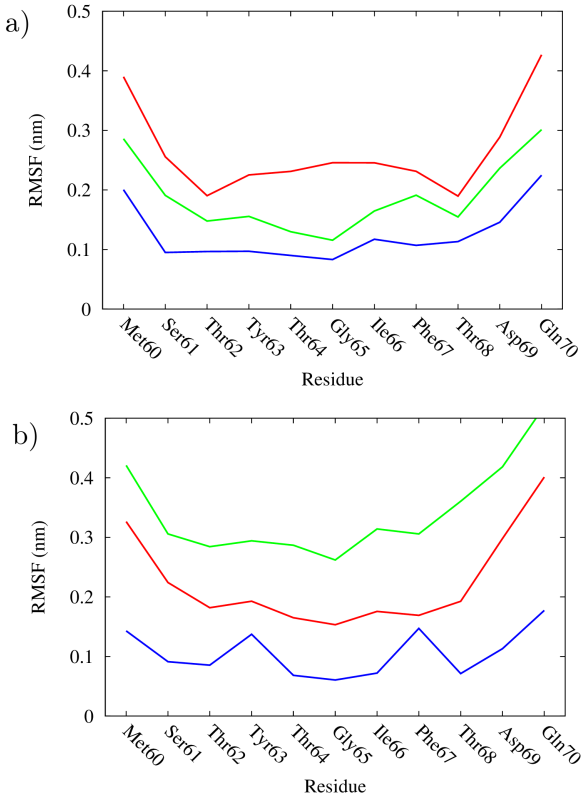

Figure 5.8: Root mean square fluctuation of the atomic positions in each residue of apoC-II(60-70) dimer (a) and tetramer (b) in the presence of C60 (red), nanotube (green) and graphene (blue).

5.4.5 Dissociation free energies of apoC-II(60-70) dimer from graphitic nanoparticles

To characterise the binding of the apoC-II(60-70) dimer to each nanomaterial the free energy of dissociation was calculated in explicit solvent. The apoC-II(60-70) dimer was chosen rather than the tetramer for the dissociation analysis as there was a lower number of potential pulling targets and significantly larger number of simulations would have been needed to determine the potential of mean force (PMF) for the tetramer. More important is the final conformation adopted by the tetramer while adsorbed to the nanomaterial thus a series of replica exchanges simulations have been used to obtain the free energy landscape of the dimer and tetramer adsorbed to each surface, presented in Chapter 6.

The PMF profiles detailing the dissociation pathway of the apoC-II(60-70) dimer from

each nanomaterial are presented in Figure 5.9. The results show that the apoC-II(60-70) dimer is weakly bound to the C60 particle ($\approx$ 1.7 kcal/mol), in agreement with the previous apoC-II(60-70) monomer results, which suggested that a higher degree of curvature reduces the surface area available for peptide adsorption. The peptide exhibited significant structural lability as it was "pulled" off the C60 surface, shown by the inserts in Figure 5.9a. The peaks and troughs observed correspond mostly to the transient π-stacking interactions, with peaks occurring when contacts are broken. The weak binding to the C60 surface contributed to the entire apoC-II(60-70) dimer dissociating from the nanoparticle, as seen from the inset in Figure 5.9a. Interestingly, after complete separation from the C60 particle the dimer regained its most stable antiparallel configuration observed in solution [257, 258].

In contrast, the umbrella sampling simulations of the apoC-II(60-70) dimer on the nanotube and graphene surfaces showed quite different behaviour. Here, during the translational pulling of the D1 strand, it completely separated from the other strand (D2), which remained adsorbed to the surface. The PMF calculations captured the separation of the D1 and D2 monomers, on the nanotube and graphene surfaces, with a flattening of the profiles occurring after a translation distance of $\approx$ 0.8 nm where the peptides in the dimer are completely dissociated. Interestingly, a similar dissociation free energy for both systems, $\approx$ 12 kcal/mol was calculated. The result indicates that the PMF profile represents the free energy required to separate the peptides in the dimer, while one peptide remains bound to the nanoparticle. It can be suggested that the separation of D1 from D2 results from the stronger π-π interactions between the aromatic residues of the D2 strand and the nanosurface relative to the interaction between the D1 and D2 strands. The transient π-π interactions between the aromatic rings of the peptides and between the peptides with the nanoparticles are represented by small peaks in the PMF profiles (Figure 5.9). These results confirmed the higher affinity of apoC-II(60-70) peptide for graphene and nanotube compared to the C60. Overall, the separation of the dimer strands while being "pulled" from the nanotube and graphene nanoparticles highlights the strong binding that exists between these surfaces and apoC-II(60-70) peptides. This result supports the hypothesis that the large surface area presented by elongated graphitic nanoparticles may induce a local increase in peptide concentration as a result of the tight binding that originates

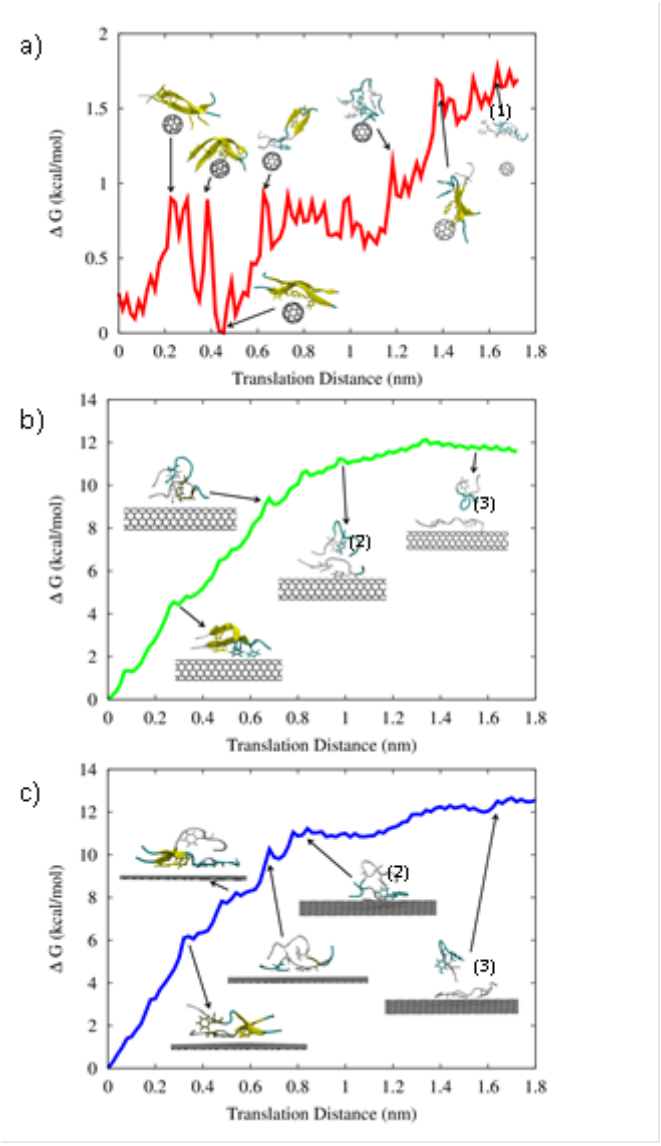

Figure 5.9: Potential of mean force profiles depicting the free energy of dissociation of apoC-II(60-70) dimer from a) C60 (red); b) nanotube (green) and c) graphene (blue) surface. Screenshots of typical events during the dissociation are shown as insets: (1) complete dissociation of the dimer from the C60 nanoparticle; (2) peptide D1 interacting with peptide D2 only; (3) D1 strand is completely dissociated from the nanotube and graphene while D2 remains adsorbed to the nanosurface.

from the π-π interactions between graphitic nanomaterials and the aromatic residues of the peptide. This observation confirms that extended graphitic nanoparticles can act as a template for peptide association, as suggested in Chapter 4. In contrast, the highly curved nanoparticles, such as C60, present a small area for adsorption, and induce conformational flexibility in peptides that has been shown to inhibit their aggregation [319]. It is important to note that the competitive aromatic interactions between the peptide

and the nanomaterial, and the peptides themselves, could have a destabilising effect on the peptide oligomer structure, as our umbrella sampling simulations identified for the dimer. Most importantly, the PMF revealed the mechanisms that were not evident in the brute-force MD simulations, which highlights the importance of an adequate conformational sampling. Hence, further work in this thesis has employed advanced computational sampling techniques, specifically, replica exchange with solute tempering (REST) [293, 294] to adequately explore the conformational landscape of apoC-II(60-70) amyloidogenic aggregates in different environments, described in Chapter 6.

5.5 Conclusions

Here extensive spontaneous classical molecular dynamics simulations have been used to investigate the adsorption, dynamics and dissociation of amyloidogenic apoC-II(60-70) peptide dimer and tetramer from the surface of three dimensionally different carbonaceous nanomaterials. Initially the water structuring around these nanomaterials was identified, showing the formation of several ordered water layers around each nanomaterial. These water layers resulted in an electric double layer that had a positive layer of hydrogen's oriented towards the surface and a layer of oxygen's oriented away from the surface, resulting in a polarised water layer at the interface. The most ordered water layer and thus the most polarised interface was at the graphene interface, followed by the CNT and finally the C60. Subsequently the amphiphilicity of the two apoC-II(60-70) oligomers was characterised. The dimer did not show any significant amphiphilicity, conversely the tetramer had two distinct faces, a hydrophobic face, characterised by the presence of aromatic residue, and a negatively charged face, characterised by the presence of threonine residue. It was postulated that the different amphipathic nature of the two oligomers would have an effect on their adsorption to the nanomaterials.

A series of 300 brute force MD simulations were conducted to investigate the adsorption mechanism of the apoC-II(60-70) dimer and tetramer to each nanosurface. These results showed that adsorption took place through a stepwise process, initially association was made to the interfacial water layer (7.8 to 10.8 Å from the nanosurface). This association was driven by long range electrostatic interactions between the ordered water layer

and the charged residues and terminals of the oligomers. These long range interactions would induce an orientational rotation in the oligomers so they orient with the terminal residues towards the nanosurface. Once associated, the oligomers anchored in between the first and second water layers (4.8 to 7.8 Å from the surface). This anchoring was also driven by electrostatic interactions at the CNT and graphene surface, while at the C60 interface it was not dominated by either polar or non-polar residues. The apoC-II(60-70) dimer adsorbed to the surface through hydrophobic and aromatic interactions with all the surfaces. In particular the interaction with the graphene surface was dominated by aromatic π-π interactions. Conversely the amphiphilicity of the tetramer resulted in contact with the CNT and graphene surface via the negative face, where the threonine residues were driving the initial contact via electrostatic interactions with the positively charged hydrogen layer of water at the surface. Resulting in the aromatic residues remaining solvent exposed. However when adsorbed to the C60 surface the tetramer interacted more favourably through the aromatic residues, a result of the reduced water structuring and more favourable hydrophobic interactions with this surface.

Additional extended timescale simulations were used to investigate the dynamic properties of the the amyloidogenic apoC-II(60-70) peptide dimer and tetramer. The simulations showed that these oligomers were more dynamic in the presence of the curved C60 and CNT nanoparticles compared to the flatter graphene surfaces, in line with the previous monomeric apoC-II(60-70) peptide investigation, Chapter 4. Additionally it was found that the dimer and tetramer underwent structural rearrangement to maximise contacts with the nanomaterials. This structural rearrangement resulted in a reduction in β-sheet content of the dimer while adsorbed to the graphene, while the tetramer actually gained β-sheet content. Extensive conformational sampling will be conducted to explore and rationalise these differences using replica exchange techniques, Chapter 6.

The dissociation free energy calculations showed that binding of the apoC-II(60-70) dimer to the C60 is weak, resulting in complete dissociation of the dimer during the pulling simulations. Conversely, the dimer is more strongly bound to the nanotube and graphene surfaces and is less dynamic in their proximity than on the C60 particle. The stronger peptide-surface interaction led to the separation of the peptide strands of apoC-II(60-70) dimer during the pulling simulations. This also indicated that the peptide interaction

with the elongated graphitic nanomaterials is stronger than the interaction between the peptide strands themselves. Our simulations support the hypothesis that extended nanomaterials can act as templates for peptide adsorption which can lead to a local increase in peptide concentration thus mediating peptide self-assembly and, possibly, fibril growth. Conversely, a small curved particle rich in aromatic residues, such as C60, induces high mobility to the amyloid prone peptides, which has been shown to have an inhibiting effect on the fibril growth. This C60 induced behaviour is remarkably similar to the inhibition mechanisms of the cyclic apoC-II (60-70) shown previously [319].

Chapter 6

Carbon nanomaterials effect on the structure, dynamics and aggregation of apoC-II(60-70) oligomers.

6.1 Overview

The amyloid-forming pathway involves self-assembly of soluble proteins into insoluble fibrils through a nucleation-dependent process [30, 31, 32]. It has been suggested that the nonfibrillar intermediates may in fact be the toxic species in amyloid related diseases [49, 47] and more recently that the development of small oligomers is an obligatory step in fibril formation [413]. Nanomaterials may inhibit or promote amyloid formation at three different stages of the fibrillation process; (1) by disruption of the nucleation phase, i.e. the formation of fibril seeds, (2) by influencing the fibril growth/elongation ability, and (3) by altering the amount of toxic species present and/or forming [150, 151, 367]. In this chapter the effect of nanomaterials on the stability of these fibril seeds and in turn the ability for fibril growth/elongation is explored. An advanced sampling method known as replica exchange with solute tempering (REST) is applied to investigate the stability and interactions of the apoC-II(60-70) dimer and tetramer while adsorbed to the carbonaceous

nanomaterials. Additionally, the binding free energy of the favourable structures of the apoC-II oligomers to the surface of the different nanomaterials, identified with the REST method, were also calculated. The results are used to rationalise how nanomaterial curvature, fibril seed size and peptide - nanomaterial binding free energy impact the oligomers stability and thus their fibrillation ability.

6.2 Introduction

Nanomaterials have a huge potential for applications in biotechnology ranging from drug delivery, sensing, and the development of novel therapeutic devices [51, 54, 353]. However, the implementation of nanomaterials for *in vivo* applications to target biological systems requires a detailed understanding of their chemical and physical effects in these environments. Numerous studies have been conducted into the potential impact of nanomaterials on major molecular components, including DNA, lipid membranes, and proteins as highlighted in several reviews [68, 60]. Some have shown that nanomaterials can affect the inherent behaviour of proteins and their conformations while adsorbed to their surfaces with the potential to induce protein misfolding, self-assembly and aggregation into amyloid fibrils [149, 350, 351, 73, 352]. An understanding of the adsorption mechanism and the subsequent dynamics of these proteins on the surface are key to determining if they may promote or inhibit amyloid fibril formation. Computational techniques provide an avenue for a fully atomistic and systematic approach to study the intricate bio-nano interactions and the contributing factors to amyloid fibril stability and growth on the surface of nanomaterials. However often the peptides of interest in these computational studies are small oligomeric systems, like the apoC-II(60-70) oligomers examined in Chapter 5. These fibril seeds are often stable in solution and at the surface of nanomaterials over the timescales accessible with traditional classical molecular dynamics techniques, as demonstrated in Chapter 5. This demonstrated that advanced conformational sampling methods need to be applied to overcome these sampling problems. The replica exchange-type methods (REM) have been widely employed to improve the conformational sampling in protein simulations [286, 294, 414, 293], where multiple replicas of the same system are simulated using a “bias” (higher temperature or potential energy) which allows the protein

to overcome energy barriers that it may otherwise be unable to do. Periodically swapping configurations between replicas, enables the exploration of a larger protein conformational landscape at the desired temperature/energy.

Recently the replica exchange molecular dynamics (REMD) approach has been applied to examine the effect of a single walled carbon nanotube on Aβ(16-22) octamers [194]. Initially, the solution behaviour and favourable structures of the oligomer were explored. The study showed that the structures that formed consisted mostly of disordered β-sheets, deemed prefibrillar conformations. To determine the effect that the CNT had on the initial fibril formation of the Aβ(16-22) octomer the authors used REMD to explore the same initial system as the ambient simulation with the addition of a CNT. They also examined the prefibrillar structure in the presence of the CNT. The Aβ(16-22) starting from the prefibrillar structure became destabilized in the presence of the CNT while the simulation starting from the random chains was not able to form β-sheet structures [194]. A draw back of the REMD method is that it is only computationally effective for model systems with minimal solvent content, as a consequence alternative approaches have been adopted and developed.

One approach has been to accelerate the dynamics of amyloidogenic peptide - nanomaterial systems by using coarse grained approaches. A type of coarse grained approach is dynamic monte carlo simulations, which removes the atomic detail of the system and replaces it with large particles that mimic, in this case, monomeric peptides and a large nanomaterial surface. The attractive potentials between the nanosurface and "peptides" are controllable. Vacha et al. used this technique to examine the fibrillation of 200-800 peptides in the presence of four nanosurfaces with differing attractive potentials (repulsive, weakly attractive, attractive and highly attractive) [166]. It was shown that weakly attractive surfaces lead to the retardation of fibril growth while strongly attractive surfaces lead to acceleration of the fibril growth [166]. Additionally it was suggested that the aggregation of peptides and proteins with an intrinsically high aggregation rate would be retarded by the presence of a nanomaterial, while the aggregation of peptides with an intrinsically low aggregation rate would be accelerated [166].

Coarse grained methods allow for the exploration of much longer time and length scales however the atomic detail that is lost can be important in determining the atomistic mech-

anisms that effect amyloid fibrillation. Therefore methods that retain the atomic detail but enable the exploration of a wider peptide conformation space with reduced computational expense are needed. Recently reformulations of the replica exchange methods have been developed to enable their application to larger systems. One such reformulation is replica exchange with solute tempering (REST). This method is a formulation of the Hamiltonian REM and has been shown to retain the same efficiency but reduced computational expense as other replica exchange techniques [57, 59]. Recently the REST method has been applied to investigate the dynamics of monomeric peptides at the surface of graphene and titanium [402]. However few studies have used this method to explore the interactions between larger protein assemblies and nanomaterials. The methodology behind replica exchange and REST methods are discussed in Chapter 2.

Here, the REST method is employed to examine the structural stability and interactions of apoC-II(60-70) oligomers with carbon nanomaterials. Several elements that affect the aggregate stability are addressed including, curvature and size of the nanomaterial, aggregate size and the role of π-π and CH-π interactions. These findings can be important for the rational design of amyloid fibril inhibitors as well as templates for self-assembled materials.

6.3 Computational details

6.3.1 Replica exchange with solvent tempering

Replica Exchange with Solute Tempering (REST) simulations were carried out to investigate the interactions, structure, dynamics and stability of the apoC-II(60-70) dimer and tetramer in the presence and absence of the different carbonaceous nanomaterials. The apoC-II(60-70) dimer and tetramer investigated in Chapter 5 and described in Chapter 3 were used in this chapter. These oligomers were shown to be stable and act as potential fibril seeds in our previous work [257, 258]. Additionally in Chapter 5 the apoC-II(60-70) tetramer was found to be amphipathic with a hydrophobic face (HF), that consisted of aromatic side chains, and a negative face (NF), that consisted of predominately threonine side chains. The same graphitic nanomaterials were used in this chapter as in the previous two chapters. Eight simulation were conducted, four with the apoC-II(60-70) dimer

and four with the apoC-II(60-70) tetramer. The four simulations were set up as follows: (1) apoC-II(60-70) dimer/tetramer in ambient conditions (no nanomaterials), (2) apoC-II(60-70) dimer/tetramer with C60, (3) apoC-II(60-70) dimer/tetramer with CNT and (4) apoC-II(60-70) dimer/tetramer with graphene. In the nanomaterial - peptide simulations the apoC-II(60-70) oligomers were initially positioned sufficiently apart (approximately 9 Å) from the nanosurface to prevent immediate contact with the nanomaterial. In all simulations the peptides were placed in a periodic simulation cell of at least dimensions of (60 Å x 60 Å x 60 Å). Simulations were performed with the Gromacs 4.6 [410] simulation package using the united-atom Gromos forcefield and the 43A1 parameter set. The Lennard-Jones interactions were truncated at 10 Å with the long-range electrostatic interactions accounted for by the Particle Mesh Ewald (PME) method [379]. The LINCS algorithm was used to constrain the bond lengths to their equilibrium values enabling a timestep of 2 fs to be applied for all simulations. *In vacuo* energy minimization using the steepest descent algorithm was initially performed on the oligomer-nanoparticle complex followed by solvation with the SPC water model [245]. To neutralize the overall negative charge of the system, two (dimer) and four (tetramer) unrestrained counterions (Na+) were included in each simulation cell. Energy minimization on the solvated system was performed to relax all atomic degrees of freedom. Subsequently, MD was conducted to allow the solvent to equilibrate around the solutes by keeping the peptide and nanomaterial restrained, at a constant temperature of 300 K maintained using the Berendsen thermostat [273]. For the production runs a constant temperature of 300 K was maintained using the weakly coupled thermostat by Bussi et al. [274]. Subsequent REST simulations were conducted on these apoC-II(60-70) dimer and tetramer systems. The results from the adsorption study, conducted in Chapter /refch:dimer, suggested that the apoC-II(60-70) dimer had no preferred adsorbed state on the surface of the C60 and CNT and only one on the graphene. Based on these results only one REST simulation was conducted for the apoC-II(60-70) dimer - nanomaterial systems. In contrast, the adsorption study revealed that are two adsorption states for the apoC-II(60-70) tetramer, (1) HF toward the nanosurface or (2) away from the nanosurface. Thus to ensure these states were sampled appropriately, two different starting orientations were used for the apoC-II(60-70) tetramer relative to the C60 and the CNT, and four starting orientations were used for

the apoC-II(60-70) tetramer relative to graphene. This ensured that there was substantial sampling of the conformational space as well as delineation of the influence of the starting arrangement (oligomer orientation). A single REST simulation was conducted for each of the apoC-II(60-70) oligomers in ambient conditions run for at least 100 ns.

Each oligomer - nanomaterial REST simulation was run for at least 150 ns and convergence of the simulations was verified by monitoring the secondary structure motifs (coil, turn and β-sheet) adopted by the oligomers between the final 50ns and the 50ns prior, the secondary structure was calculated using the STRIDE algorithm [397]. The convergence and sampling efficiency of each simulation was determined and shown in Appendix C.

The free energy perturbation and replica exchange codes within the Gromacs package were used to implement the REST method outlined by Terakawa et al. [294]. For each system, the potential energy of replica i was scaled according to:

$$V_i(X) = \frac{\beta_i}{\beta} V_{pp} + \sqrt{\frac{\beta_i}{\beta}} V_{ps}(X) + V_{ss}(X) \tag{6.1}$$

where V_{pp} is the intra-peptide, V_{ps} the peptide-water and peptide-surface, and V_{ss} the water-water, water-surface and surface-surface potential energies of the system X. β and β_i are the inverse of the system and 'effective' temperatures,

$$\beta = \frac{1}{KT} \tag{6.2}$$

and

$$\beta_H = \frac{1}{KT_H} \tag{6.3}$$

of replica i and are related via λ_i:

$$\beta_i = \beta(1 - \lambda_i) + \beta_H \lambda_i \tag{6.4}$$

where $0 < \lambda < 1$. Each system was simulated using 8 replicas in the NVT ensemble at an 'effective temperature' within the interval of 300 K to 410 K. The effective temperatures of the 8 replicas of each system were derived iteratively, following Terakawa et al [294]. Following Wang et al., only the nonbonded and dihedral angle terms of the

intra-peptide potential were scaled in each replica [341]. The average probability for an exchange attempt was approximately 0.5, with an exchange attempted every 2000 MD steps.

Analysis was conducted on the base replica, effective temperature of 300 K, over 100 ns of simulation time. For the apoC-II(60-70) oligomers in ambient conditions as well as the apoC-II(60-70) dimer simulations the final 100 ns of the simulation was used. However as two starting orientations were used for the apoC-II(60-70) tetramer - C60 and tetramer - CNT systems, the final 50 ns of these two separate REST simulations were combined for the analysis. As four starting orientations were used for the tetramer - graphene systems, the final 25ns of each of the four REST simulations was combined and used for the analysis. Initial clustering analysis was used to identify the most sampled structures, further analysis was then conducted on the most structures contained within the clusters found.

6.3.2 Binding free energy calculations

The binding free energy between the apoC-II(60-70) oligomers and various carbon nanomaterials was calculated using the g_mmpbsa tool [415] based on the molecular mechanics/Poisson-Boltzman surface area (MM/PBSA) method [416]. In this approximation the binding free energy (ΔG_{bind}) is decomposed into contributions from the gas-phase binding energy (ΔE_{gas}), solvation free energy (ΔG_{solv}), and entropy TΔS, as represented below.

$$\Delta G_{bind} = \Delta E_{gas} + \Delta G_{solv} - T\Delta S \tag{6.5}$$

Here, the gas-phase term is the sum of bonded and nonbonded energies, however in this work we are using the 'single trajectory' approach where the bonded terms cancel exactly and thus can be ignored, leaving only the non-bonded terms. The solvation energy term, ΔG_{solv}, contains polar and nonpolar solvation energies, the polar contributions are estimated using an implicit solvent model, in this case the Poisson-Boltzmann model. The non-polar solvation energy is linearly dependent on the solvent-accessible surface area (SASA), which is calculated to determine the non-polar solvation energy contribution. The binding free energy is determined by,

$$\Delta G_{bind} = \Delta E_{MM} + \Delta G_{polar} + \Delta G_{nonpolar} \tag{6.6}$$

The energy components, ΔE_{MM}, ΔG_{polar} and $\Delta G_{nonpolar}$, were calculated on the structures found in the four most populated clusters from the final 100 ns of the REST simulations. The additional parameters set are described in the g_mmpbsa developers publication [415].

6.4 Results and discussions

A total of 11 REST simulations were performed of the apoC-II(60-70) dimer and tetramer in the presence and absence of three different carbon nanomaterials. The converged portions of these simulations were combined as described in the methods section.

Initially the free energy map of the apoC-II(60-70) dimer and tetramer was produced for each system set up, that is ambient (1) and in the presence of the C60 (2), CNT (3) and graphene (4). Analysis was conducted on the clustered structures, with the results of the four most populated clusters are shown for each nanomaterials - oligomer complex. This included β-strand content, the contacts between peptide strands and the contacts, contact area and binding free energy between the peptide and nanomaterials.

6.4.1 Amyloid fibril seed stability

The fibril stability was characterised based on the radius of gyration of the apoC-II(60-70) oligomer as well as the inter-peptide hydrogen bonds over the combined 100 ns. The free energy profile was determined with respect to these two properties by $\Delta G = -RT(log(f(g_{\text{gyrate}}, H_{\text{Bonds}})))$, where f($R_{\text{gyrate}}$,$H_{\text{Bonds}}$) is the histogram formed by the oligomer radius of gyration (R_{gyrate}) and inter-strand hydrogen bonding normalised with respect to the number of peptide strands (H_{Bonds}). The free energy maps are shown in Figure 6.1 and 6.2. The structures that the apoC-II(60-70) oligomers adopted while adsorbed to the nanomaterials were assigned to three groups, determined as stable (S), unstable (US) and fibril incompetent (IN), as follows.

1. The average and standard deviation of the radius of gyration and hydrogen bonds per

peptide strand were determined for the most populated cluster of the apoC-II(60-70) dimer and tetramer in ambient conditions.

2. A series of cutoffs were generated from this data to determine the radius of gyration and inter strand hydrogen bonding that corresponded to a stable (S), unstable (US) or fibril incompetent (IN) oligomer structure.

   (a) The minimum R_{gyrate} cutoff for S to US states was defined as the R_{gyrate} that was two standard deviations less than the average R_{gyrate} for the ambient oligomer, dimer (0.87 nm) and tetramer (0.92 nm).

   (b) The minimum R_{gyrate} cutoff for US to IN states was defined as the R_{gyrate} that was four standard deviations less than the average R_{gyrate} for the ambient oligomer, dimer (0.81 nm) and tetramer (0.88 nm).

   (c) The maximum R_{gyrate} cutoff for S to US states was defined as the R_{gyrate} that was two standard deviations greater than the R_{gyrate} obtained from the initial starting oligomer structure, dimer (1.06 nm) and tetramer (1.14 nm).

   (d) The maximum R_{gyrate} cutoff for US to IN states was defined as the R_{gyrate} that was four standard deviations greater than the R_{gyrate} obtained from the initial starting oligomer structure, dimer (1.12 nm) and tetramer (1.18 nm).

   (e) The H_{Bonds} cutoff for S to US states was defined as a H_{Bonds} per peptide strand of 3, this value was chosen as it represents inter-strand hydrogen bonding that is likely to result in β-strand motifs.

   (f) The H_{Bonds} cutoff for US to IN states was defined as a H_{Bonds} per peptide strand of 2, this value was chosen as it represents inter-strand hydrogen bonding that is unlikely to result in β-strand motifs.

   (g) No maximum value for the H_{Bonds} was set, as a greater number of inter-strand hydrogen bonds is indicative of a greater degree of β-strand formation.

3. Two rectangles have also been placed on the free energy maps, one with a solid line (inner) and the other with a dashed line (outer). An oligomer structure with a R_{gyrate} and H_{Bonds} value within the inner rectangle the oligomer is considered

stable, between the inner and outer rectangles the oligomer is considered unstable and outside these rectangles it is considered fibril incompetent.

From this the stable region corresponds to R_{gyrate} and inter-strand H_{Bonds} of the oligomer that indicate a conformation capable of further ordered peptide association. The unstable region corresponds to conformations of the oligomers that are no longer exhibit the extended β-sheet conformation of a stable fibril seed, that is they have collapsed or the peptide strands have begun to dissociate. Finally the fibril incompetent region corresponds to oligomer conformations that have either become totally disorder, collapsed or the peptide strands have dissociated from one another, thus would be unable to allow for further ordered peptide association.

Cluster analysis of the peptide backbone (RMSD cutoff of 0.2 nm) was performed to identify the most frequently sampled structures over the combined 100 ns of each apoC-II(60-70) oligomer simulation. Additionally the representative structures of the four most populated clusters are shown in Figure 6.1 (dimer) and 6.2 (tetramer), as 1-4. The location of these clustered structures on the free energy maps allowed the oligomers to be identified as either stable (S), unstable (US) or fibril incompetent (IN). The cluster populations, β-strand content, R_{gyrate} and fibrillar stability for the top four clusters of each system is listed in Table 6.1 and 6.2.

The cluster analysis of the apoC-II(60-70) dimer in ambient conditions revealed the most significant cluster with a population of approximately 60% of the structures sampled. This cluster retains significant β-strand content, over 60%, and has an average R_{gyrate} of 0.93 nm that indicates an extended conformation. The third most populated cluster has the biggest deviation from the initial dimer conformation, with reduced β-sheet content, $\approx$ 55%, and significantly reduced R_{gyrate}, 0.74 nm. The insert, Figure 6.1a)3 shows that the dimer has adopted a curved conformation that is likely to be unstable. Overall the dimer retains the initial stable fibril conformation in ambient conditions.

The apoC-II(60-70) dimer adopts a curved conformation around the C60 particle in all of the top four clusters. This conformation leads to a $\approx$13% reduction in the average R_{gyrate} compared to the dimer in ambient conditions indicative of a more compact structure. The curved conformation also leads to a reduction in β-strand content, with a reduced β-sheet

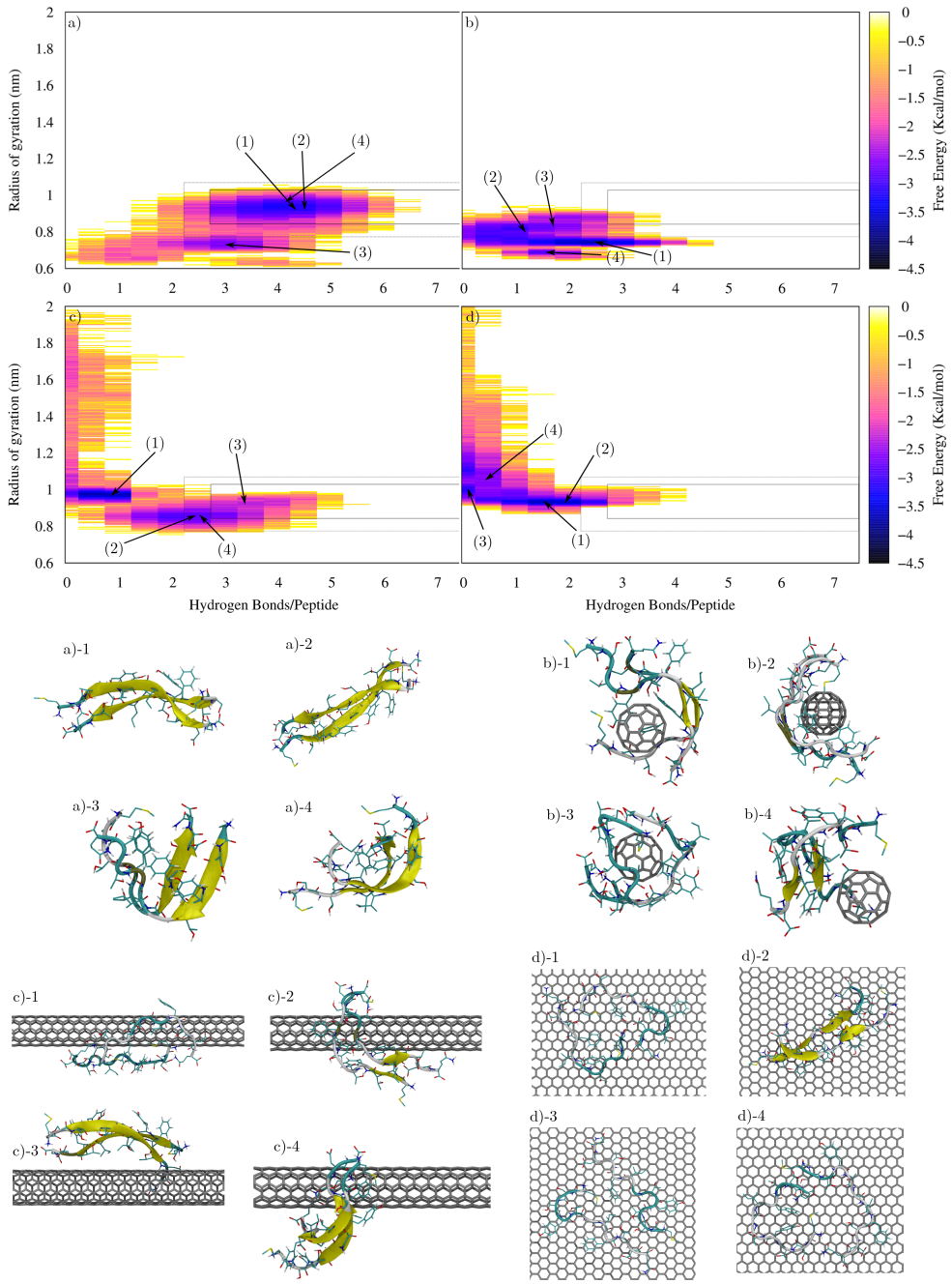

Figure 6.1: Free energy map of the apoC-II(60-70) dimer in the absence (a) and presence of a C60 particle (b) a CNT (c) and graphene surface (d). The free energy profiles (in kcal/mol) show the favourable radius of gyration and inter-chain hydrogen bonds (normalised per peptide strand). The representative structure of the four most populated clusters, a label is used to show their location on the free energy profile (1-4).

content of 29.3%. The low R_{gyrate} and β-strand content lead to conformations that were outside the R_{gyrate} and H_{Bonds} cutoff range and thus were deemed fibril incompetent.

The CNT induced a complete loss of β-strand content in the top cluster of the apoC-II(60-70) dimer (a population of 32%), indicating that the dimer has adopted a conformation that is fibril incompetent. However the second and third clusters of the dimer on the CNT surface, accounting for 31% of the structures obtained, retained more than 36% of its β-strand content, which corresponded to conformations that were either stable or unstable fibril seeds.

While adsorbed to the graphene surface the most populated cluster of the apoC-II(60-70) dimer (34%) was considered fibril incompetent with an no β-strand content recorded. However the second most populated cluster (7%) did exhibit a greater propensity to form β-strand with an average of 26% albeit these dimer conformations still had an average number of H_{Bonds} (1.96) below the cutoff (2) and thus were deemed fibril incompetent.

Cluster Number	Cluster Population	β-sheet content	R_{gyrate} (nm)	Fibril stability
		Ambient		
1	60.1%	65.5%	0.93±0.03	S
2	8.3%	67.1%	0.91±0.06	S
3	6.4%	55.3%	0.74±0.02	In
4	4.0%	61.5%	0.98±0.03	S
		C60		
1	41.0%	29.3%	0.75±0.01	In
2	9.4%	8.0%	0.81±0.02	In
3	6.4%	0.0%	0.83±0.03	In
4	6.2%	18.7%	0.69±0.01	In
		Carbon nanotube		
1	32.2%	0.0%	0.97±0.02	In
2	21.1%	37.0%	0.85±0.03	US
3	10.6%	56.5%	0.92±0.04	S
4	3.8%	36.7%	0.84±0.02	US
		Graphene		
1	34.6%	0.0%	0.95±0.03	In
2	7.6%	28.4%	0.95±0.03	US
3	7.2%	2.9%	0.99±0.03	US
4	4.9%	0.0%	1.04±0.05	In

Table 6.1: REST simulation cluster populations, average β-strand content and average radius of gyration (nm) along with the determined fibril stability of the top four clusters of the apoC-II(60-70) dimer in the presence and absence of different carbon nanomaterials.

However, overall the apoC-II(60-70) tetramer predominately formed stable fibril seed conformations. The tetramer in ambient conditions was less stable than the apoC-II(60-70) dimer. It did retain at least 39% β-strand content. The tetramer also begins to collapse which reduces the exposed hydrophobic face (HF, defined in Chapter 5), leading to a small reduction in the R_{gyrate} (average of 0.93 nm) compared to its initial state ($\approx$

1.0 nm), Figure 6.2a and Table 6.1.

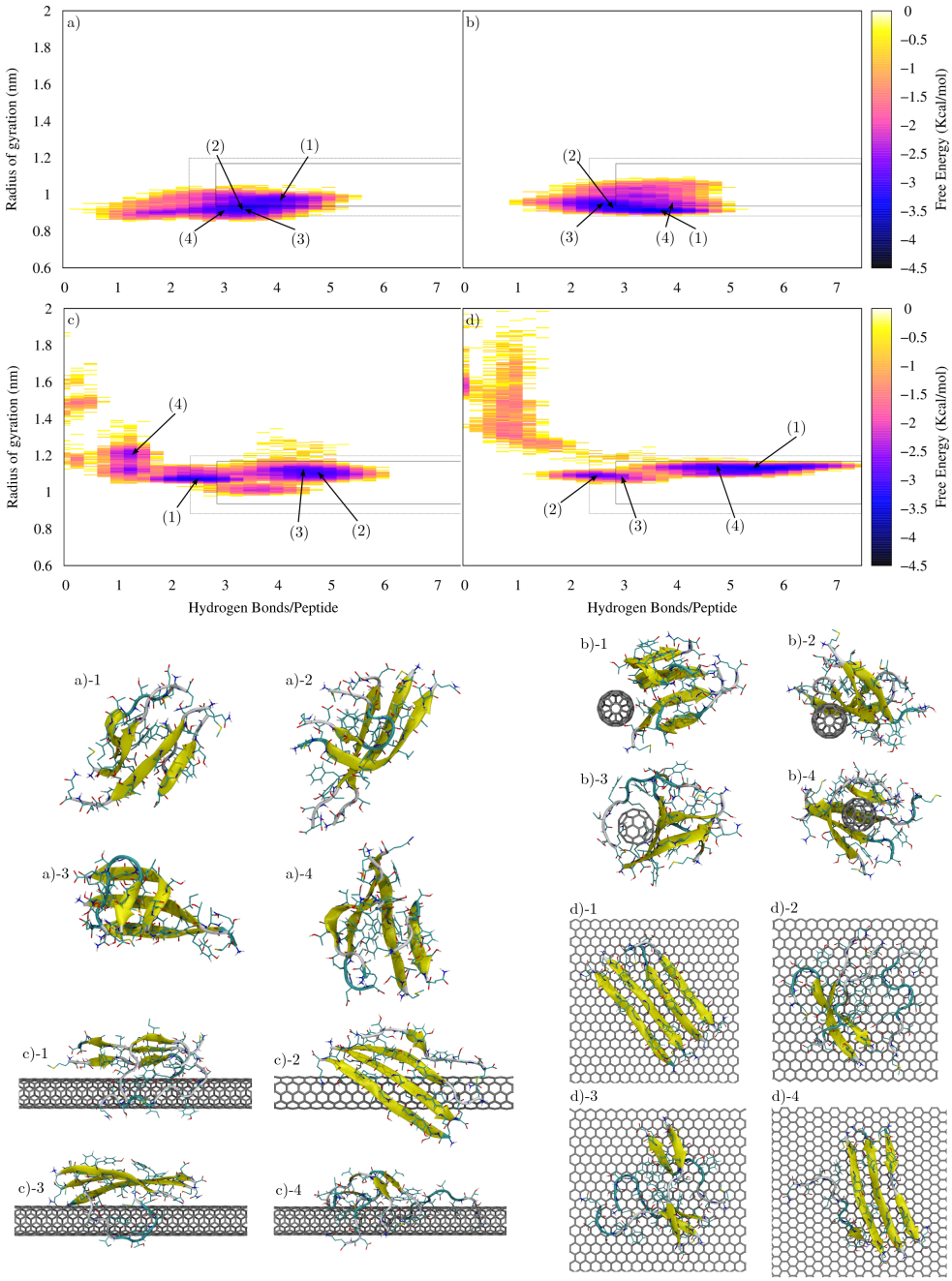

Figure 6.2: Free energy map of the apoC-II(60-70) tetramer in the absence (a) and presence of a C60 particle (b) a CNT (c) and graphene surface (d). The free energy profiles (in kcal/mol) show the favourable radius of gyration and inter-chain hydrogen bonds (normalised per peptide strand). The representative structure of the four most populated clusters, a label is used to show their location on the free energy profile (1-4).

Similar to the apoC-II(60-70) dimer adsorbed to the C60 particle the tetramer also adopted a curved conformation around the nanomaterial. The top populated cluster (41%) has the lowest average radius of gyration, 0.75 nm, of the four clusters, this is due to the different adsorbed conformations. In this cluster the negative face (NF), determined Chapter 5, is interacting with the C60 particle and the tetramer forms a curve around the Gly65 residue that shields the HF face from the solvent. The analysis in Chapter 5 predicted that this adsorption mechanism was actually less favourable than the HF interacting with the C60 particle. However when the HF is interacting with the C60 the tetramer undergoes more significant configurational changes compared to the NF forms an interface with the C60. This leads to the highest populated structures with different RMSD values, assigned to different clusters, as can be seen by the inserts in Figure 6.2b)-2 to b)-4, adsorbed through the HF of the tetramer. Therefore the favoured adsorption orientation is with the HF facing the surface, results in curved conformations that are fibril incompetent.

The elongated nanotube presented sufficient surface area for complete adsorption of the apoC-II(60-70) tetramer, however its high curvature induced disorder and partial separation of the peptide strands. This contributed to the top cluster (23%) having a β-strand content of only 30% and was determined to be unstable. However 32% of the apoC-II(60-70) tetramer structures had β-strand content greater than 57%. Interestingly these structures, clusters two and three, were adsorbed to the CNT surface via the NF face, whereas the disordered structures that formed were adsorbed via the HF face. These results indicate that in principle the CNT can induce the formation of disordered and unstable fibrillar structures as well as can stabilise the tetramer structure, dependant on the adsorption orientation.

The apoC-II(60-70) tetramer adsorbed to the surface of the graphene exhibited similar trends to the peptide adsorbed to the CNT, whereby disordered and unstable structures formed when the HF of the tetramer was interacting with the graphene (Figure 6.2d)-2,3) and stable structures when the NF was interacting with the surface, with the most populated cluster (66%) with the NF oriented toward the surface (Figure 6.2d)-1). The graphene surface increased the stability of the apoC-II(60-70) tetramer in comparison to the tetramer in ambient conditions, if it absorbed to the surface via the NF.

Cluster Number	Cluster Population	β-sheet content	R_{gyrate} (nm)	Fibril stability
		Ambient		
1	21.4%	55.9%	0.96±0.02	S
2	9.3%	39.2%	0.91±0.01	US
3	8.4%	49.0%	0.93±0.01	S
4	8.3%	37.2%	0.92±0.01	US
		C60		
1	41.0%	29.28%	0.75±0.01	In
2	9.4%	8.05%	0.81±0.02	In
3	6.4%	0.02%	0.83±0.01	In
4	6.2%	18.70%	0.69±0.02	In
		Carbon nanotube		
1	23.5%	30.2%	1.08±0.01	US
2	17.3%	62.3%	1.10±0.02	S
3	14.7%	57.1%	1.13±0.01	US
4	7.5%	13.7%	1.21±0.02	In
		Graphene		
1	66.5%	68.9%	1.13±0.02	S
2	8.3%	38.1%	1.10±0.01	US
3	4.4%	30.5%	1.08±0.01	US
4	2.7%	58.9%	1.14±0.01	S

Table 6.2: REST simulation cluster populations, average β-strand content and average radius of gyration (nm) along with the determined fibril stability of the top four clusters of the apoC-II(60-70) tetramer in the presence and absence of different carbon nanomaterials.

Overall the apoC-II(60-70) dimer is unstable or fibril incompetent on all of the nanomaterials in comparison to the dimer in ambient conditions. Specifically, the C60 particle induces curved, compact structures that are unlikely to form fibrils, while on the CNT and graphene there is total disruption of the β-sheet content. Similarly the C60 particle induced the apoC-II(60-70) tetramer to form curved conformations that were likely to be fibril incompetent. The CNT and graphene also induce the formation of unstable fibril seeds however they can also stabilise the tetramer structure and this seems to be dependent on the adsorption orientation, either NF toward the surface (more stable tetramer) or HF toward the surface (less stable tetramer).

6.4.2 Inter-strand peptide interactions

Contact maps of the adjacent peptide strands of the apoC-II(60-70) oligomers have been used to determine the most favourable interactions between the residues of the peptides while adsorbed to the nanomaterials surface. Figure 6.3 shows the contact maps, the probability that any two atoms of a residue are within 4 Å of each other, of the apoC-II(60-70) dimer in ambient conditions (a) and in the presence of the C60 (b), CNT (c)

and graphene (d). The contact maps of the top three clusters of the apoC-II(60-70) dimer are shown and labelled i - iii. Figure 6.4 shows the contact maps of adjacent peptide strands of the apoC-II(60-70) tetramer normalised with respect to number of peptide strands. Additionally this data has been used to quantify the overall contact between peptide strands, "contact fraction", which was calculated on each separate cluster of the apoC-II(60-70) dimer and tetramer. The contact fraction is the sum of all the contact probabilities divided by the total number of residues of the oligomer. A value of below 1 indicates that each residue has a probability of less than 100% of making a contact with a residue of the adjacent peptide strand, while a value larger than 1 indicates that each residue is in contact with at least one residue of the adjacent peptide strand in the majority of the structures clustered. Finally the inter chain hydrogen bonding for each cluster was also calculated and normalised with respect to the number of peptide strands. This data is shown in Table 6.3 and 6.4.

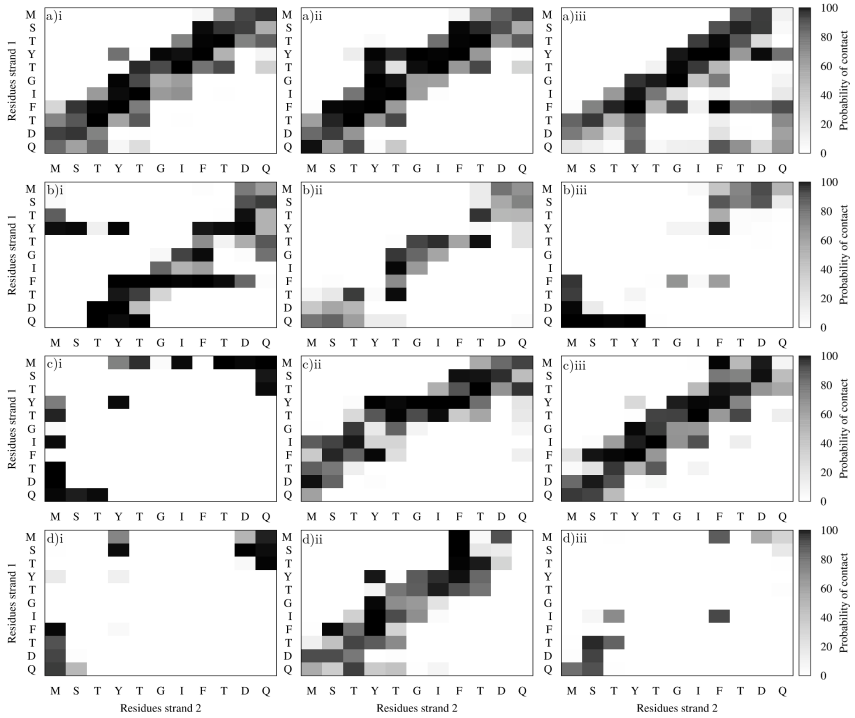

Figure 6.3: inter-strand contact maps, showing the percentage time in contact between residues of adjacent strands of the apoC-II(60-70) dimer in ambient (a), C60 (b), CNT (c) and graphene (d) of the top three cluster (i-iii).

Both the apoC-II(60-70) dimer and tetramer in ambient conditions exhibited persistent interactions between peptide chains, producing a profile that was indicative of an anti-

parallel arrangement. Figure 6.3a)iii and Figure 6.4a)iii had a reduced contact probability of most of the peptide residues. This coincided with an increase in contact probability between residues that were not typically adjacent in the anti-parallel configuration. These different contact stabilities are showing the changes in inter-strand interaction when the dimer and tetramer adopt compact conformations, as observed in cluster 3 of both the dimer and tetramer in ambient conditions.

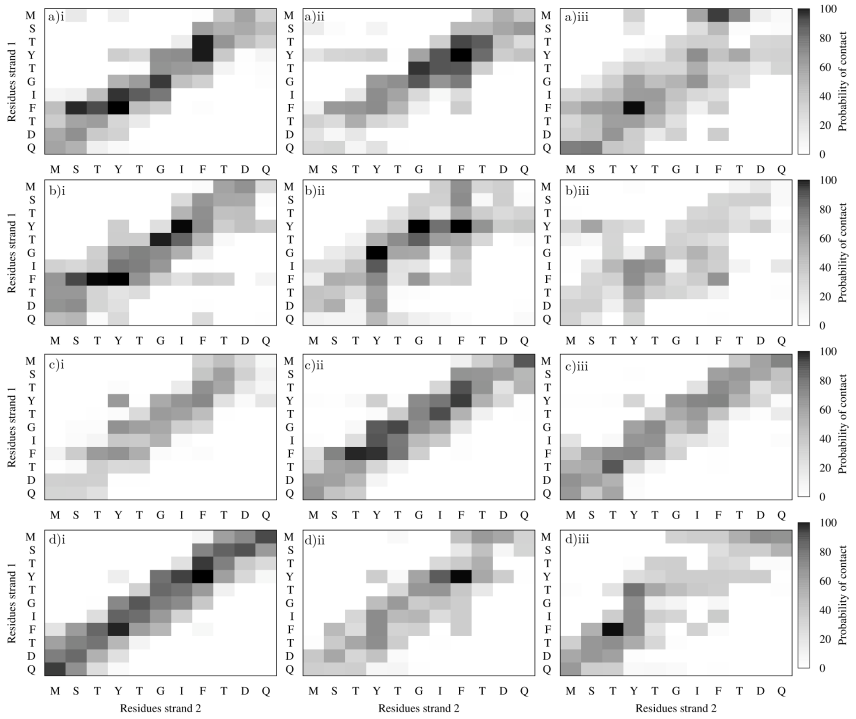

Figure 6.4: inter-strand contact maps, showing the percentage time in contact between residues of adjacent strands of the apoC-II(60-70) tetramer in ambient (a), C60 (b), CNT (c) and graphene (d) of the top three cluster (i-iii).

The apoC-II(60-70) dimer - C60 contact maps, Figure 6.3a)i, showed that both the F67 and Y63 of strand 1 show persistent contacts with a number of residues of strand 2, M60 – Y63 and Y63 - T68 respectively (probability of contact greater than 80%). The wrapped adsorption configuration adopted by the dimer around the C60 particle results in compact conformations that maintain close interactions between peptide strands but lose the original anti-parallel arrangement. This conformation is mediated by persistent interactions between M60 - Y63 of strand 1 and the aromatic residues, Y63 and F67 of strand 2.

The contact maps for the top two clusters of the apoC-II(60-70) dimer adsorbed to

Cluster Number	Hydrogen bond / peptide strand	Contact fraction
	Ambient	
1	4.16±0.82	1.77
2	4.29±0.76	1.81
3	3.03±0.60	1.84
4	4.04±0.80	1.66
	C60	
1	2.29±0.75	1.50
2	1.15±0.53	0.87
3	1.86±0.57	0.69
4	1.62±0.42	1.30
	Carbon nanotube	
1	0.67±0.34	0.74
2	2.38±0.76	1.51
3	3.30±0.82	1.63
4	2.32±0.73	1.56
	Graphene	
1	1.61±0.57	0.48
2	1.96±0.80	1.39
3	0.10±0.21	0.35
4	0.42±0.31	0.33

Table 6.3: Tabulated REST simulation results for the inter-strand interactions of apoC-II(60-70) dimer: inter-strand hydrogen bonds normalised per peptide strand as well as the contact fraction for the top four clusters of the apoC-II(60-70) dimer in the presence and absence of the carbon nanomaterials.

the surface of the CNT and graphene, Figure 6.3c)i and d)i, showed that minimal inter-strand contacts were retained with the exception of the charged terminal residues, M60 and Q70 as well as residues near the terminal. Unsurprisingly the persistent contact between the positively and negatively charged terminal residues is mediated by electrostatic interactions, while the absence of any other inter-strand contacts is indicative of peptide dissociation.

While adsorbed to the C60 particle the apoC-II tetramer retains persistent inter-strand backbone and sidechain contacts and most significantly between the aromatic residues of adjacent chains (Figure 6.4b)i. The contact maps of the tetramer - C60 generated from cluster two and three show less persistent contacts between peptide chains, these clusters correspond to the tetramer adsorbed to the surface of the C60 particle with the HF interacting with the nanosurface. Similarly the contact maps of the clustered tetramer structures that are adsorbed with the HF toward the surface of the CNT (cluster 1,4) and graphene (cluster 2,3) show an attenuation of the contact probability between adjacent chains, Figure 6.4c)i (CNT), d)ii (graphene) and d)iii (graphene), and a corresponding

Cluster Number	Hydrogen bond / peptide strand	Contact fraction
	Ambient	
1	4.03±0.50	1.78
2	3.36±0.45	1.73
3	3.32±0.43	1.90
4	2.90±0.42	1.57
	C60	
1	3.73±0.44	1.93
2	2.87±0.44	1.82
3	2.53±0.35	1.27
4	3.90±0.47	1.75
	Carbon nanotube	
1	2.47±0.41	1.19
2	4.77±0.50	1.85
3	4.38±0.47	1.65
4	1.20±0.22	1.11
	Graphene	
1	5.34±0.79	2.06
2	2.46±0.36	1.45
3	2.98±0.43	1.46
4	4.53±0.47	1.88

Table 6.4: Tabulated REST simulation results for the inter-strand interactions of apoC-II(60-70) tetramer: inter-strand hydrogen bonds normalised per peptide strand as well as the contact fraction for the top four clusters of the apoC-II(60-70) tetramer in the presence and absence of the carbon nanomaterials.

reduction in hydrogen bonding and contact fraction, Table 6.4. Conversely the clusters that correspond to the tetramer with the HF oriented away from the CNT (cluster 2,3) and graphene (cluster 1,4) have a more defined anti-parallel configuration, particularly cluster 1 of graphene (Figure **??**d)i), with dominate π-π interactions between peptide strands.

Overall the apoC-II(60-70) dimer has significantly reduced inter-strand interactions while adsorbed to the C60, graphene and in some instances the CNT. However in ambient conditions the dimer and tetramer largely retain their anti-parallel configuration and were stabilised by inter-strand π-π interactions. The apoC-II(60-70) tetramer on the other hand retains significantly more inter-strand contacts and hydrogen bonding (Table 6.4). Overall the tetramer had the highest contact fraction and inter-strand hydrogen bonding while adsorbed on the CNT and graphene surface via the NF.

6.4.3 Fibril seed – nanomaterial interactions

To determine the persistent interactions between the apoC-II(60-70) oligomers and nanomaterials the contact stabilities of each residue side chain/terminal were determined for

the top three clusters of all the systems. A contact was deemed made when an atom of the peptide was within 4.8 Å of the nanosurface. The contact stabilities for the apoC-II(60-70) dimer (a) and tetramer (b) while adsorbed to the C60 (red), CNT (green) and graphene (blue) for cluster 1 (i) to 3 (iii), are shown in Figure 6.6. Additionally the contact area between the oligomer and the nanomaterial has been calculated and normalised per peptide chain, Table 6.5 and 6.6. Finally the MMPB/SA method was used to determine the binding free energy of the apoC-II(60-70) dimer and tetramer to the different nanomaterial surfaces. The binding free energy was calculated by taking snapshots at least 12 ps apart which were extracted from each of the four most populated clusters for each peptide-nanomaterial complex. The binding free energy results have been normalised per peptide chain and are shown in Table 6.5 and 6.6. Here on in, all discussed binding energies will be assumed to be normalised per peptide strand unless otherwise stated. The contribution to the binding free energy from the nonbonded interactions and the poplar and non-polar solvation energies is shown in Appendix C. In this work the nanomaterials did not have any charge and thus there was no electrostatic contribution to the binding free energy. However it has recently been shown that the dominant interaction, between amyloidβ(17-40) hexamer and charged fullerene particles, were van der Waals interactions [189].

Cluster Number	Contact area / peptide strand (nm^2)	ΔG_{bind} / peptide strand (kcal/mol)
	C60	
1	1.33±0.06	-23.33±2.42
2	2.02±0.14	-37.26±2.64
3	1.82±0.31	-34.53±3.01
4	0.86±0.10	-11.98±3.26
	Carbon nanotube	
1	3.13±0.08	-67.49±2.30
2	2.04±0.12	-39.19±3.67
3	1.58±0.13	-28.53±3.31
4	1.58±0.14	-33.07±3.24
	Graphene	
1	4.31±0.11	-93.94±2.69
2	3.24±0.14	-69.16±3.84
3	4.90±0.15	-96.45±9.26
4	4.64±0.11	-101.17±3.63

Table 6.5: ApoC-II(60-70) dimer - nanomaterial contact area and binding free energy normalised per peptide strand for the top four clusters for each system.

The high curvature (low surface area) of the C60 contribute to minimal persistent

Cluster Number	Contact area/peptide strand (nm^2)	ΔG_{bind} / peptide strand (kcal/mol)
	C60	
1	0.46±0.03	-7.83±0.64
2	0.55±0.10	-9.27±1.60
3	0.67±0.04	-11.37±0.78
4	0.99±0.05	-18.07±1.29
	Carbon nanotube	
1	1.77±0.06	-39.87±1.66
2	1.53±0.25	-27.97±2.63
3	1.83±0.09	-36.09±2.32
4	2.54±0.06	-55.23±1.74
	Graphene	
1	2.43±0.16	-45.84±4.13
2	2.97±0.06	-62.39±1.89
3	2.74±0.06	-59.21±2.49
4	2.73±0.09	-52.82±2.02

Table 6.6: ApoC-II(60-70) tetramer - nanomaterial contact area and binding free energy normalised per peptide strand for the top four clusters for each system.

interactions with the apoC-II(60-70) dimer and tetramer. The contact stabilites of the most populated structure of the tetramer on the C60 surface show that the adsorption is driven by the Thr64 and Ile66, Figure 6.6a)i and b)i. Whereas the aromatic residues of the dimer are the most persistent interactions with the C60 and this leads to a much stronger binding, -26.78 kcal/mol, compared to the tetramer adsorbed to the C60, -11.64 kcal/mol. It is clear that the interaction between the dimer with the C60 is stronger and this is a result of not only the aromatics interacting with the surface but also the reduced inter-strand interactions compared to the apoC-II(60-70) tetramer, with average contact fraction of 1.09 (dimer-C60) and 1.69 (tetramer-C60).

The larger surface area of the CNT and graphene allow for more peptide-surface contacts, demonstrated by the overall greater contact area per strand, Table 6.6, compared to the oligomers adsorbed to the C60 surface. The apoC-II(60-70) dimer adsorbed to both these surfaces exhibits similar contacts stability profiles, Figure 6.6a. This correlates with the results obtained in Chapters 4 and 5. Additionally the most persistent contacts are between the aromatic residues of the dimer with the carbon surface, which has been shown in Chapter 4 to be the most favourable interaction with carbon nanomaterials leading to the formation of π-π stacking. The aromatic residues of the apoC-II dimer make the most stable contacts when in contact with the graphene and CNT followed by the C60 particle. Infact the high stability of the aromatic contacts with the elongated surfaces induces

destabilisation of the dimer β-strand structure, shown in Chapter 5. This is demonstrated by Figure 6.6a)i which showed a high number of persistent contacts between the aromatics of the dimer and the CNT (green line). This cluster was considered fibril incompetent due to a loss of all β-strand content and had a binding free energy of -67.49 kcal/mol . In contrast, Figure 6.6a)iii shows there were less persistent interactions with the residues from the N-terminal to Thr64 and this corresponds to a cluster that was determined to be unstable and had a reduced binding free energy of -28.53 kcal/mol. Interestingly some of the clustered structures of the apoC-II(60-70) dimer adsorbed to the CNT surface had a lower binding energy than the dimer adsorbed to the C60 surface. This was a result of the disorder caused by the C60 particle, embedding between the petpide strands, whereas the apoC-II(60-70) dimer adsorbed to the CNT surface did not dissociate in clusters 2, 3 and 4 and rather curved around the nanotube. These different configurations resulted in very similar contact areas between the dimer and two nanosurface, however the dimer at the CNT surface has a much greater capacity for contact as demonstrated by cluster 1 with a contact area of 3.13 nm^2.

As discussed in the previous section the apoC-II(60-70) tetramer has in general stronger inter-strand interactions, as such it's binding free energy to the nanomaterial is significantly less for all the complexes. Additionally the tetramer interacts with the nanomaterials via two different modes, as revealed by the adsorption investigation in Chapter 5, where it can adsorb via the HF (aromatics towards the surface) or via the NF (aromatics away from the surface). In the case of the C60 particle the apoC-II(60-70) tetramer interacts with the surface through the NF, resulting in conformations that exhibit turns and loops around the Gly65 residues, and a binding free energy of -7.83 kcal/mol. This turn at the Gly65 residue was a feature identified as an inherent property of apoC-II(60-70) peptides on-path to a β-hairpin formation [257, 258], which highlights the induced flexibility on the tetramer conformation by the C60 particle. Similarly, increased conformational lability in apoC-II(60-70) was also observed in the presence of the cyclic peptide, cyc(60-70), which was identified as a potential amyloid fibril inhibitor [319]. Interestingly the clustered structures that had the HF of the tetramer oriented towards the C60 exhibited similar curved conformations albeit with larger binding energies, -9.27 kcal/mol, -11.37 kcal/mol and -18.07 kcal/mol for cluster 2, 3 and 4, respectively. The increased binding energies observed

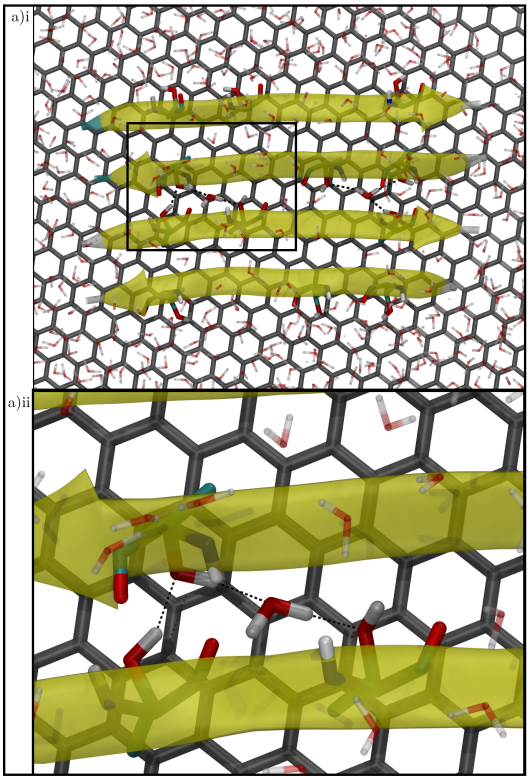

Figure 6.5: The trapped water molecules found between the apoC-II(60-70) tetramer and graphene surface. Dashed line indicates the formation of hydrogen bonds between the hydrogens and the Thr residues of strand 1 and 2.

here are a result of the increased aromatic interactions with the fullerene, however they still result in binding energies that are lower than the oligomers at the CNT and graphene surface, see below.

Similarly the apoC-II(60-70) tetramer adsorbed to both the CNT and graphene exhibited different interaction modes with the surface depending on how they adsorbed, either via the HF or NF. Adsorption via the HF on the CNT was observed within the clusters 1 and 4, with binding energies of -39.87 kcal/mol and -55.23 kcal/mol respectively. Clusters 2 and 3 of the tetramer had conformations that indicated adsorption to the CNT had proceeded via the NF and this produced weaker binding energies, -27.97 kcal/mol and -36.09 kcal/mol respectively. The same behaviour was observed for the tetramer adsorbed to the surface of the graphene, albeit with stronger binding energies overall. For cluster 1 of the tetramer on the graphene, which was considered the most stable fibrillar structure, the binding free energy was -45.84 kcal/mol, while for cluster 2 and 3, more disordered structures interacting through the HF, the binding energies were -62.39 kcal/mol and -59.21

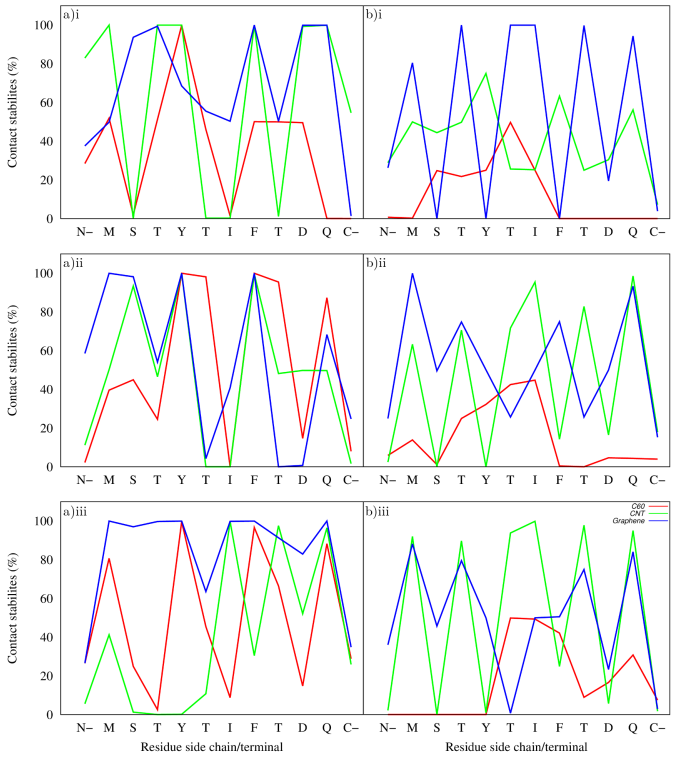

Figure 6.6: Contact stability plot of the top 3 clusters (a,b,c) of the apoC-II dimer(i) and tetramer (ii) adsorbed to C60 (red), carbon nanotubes (green) and graphene (blue). Here the contact stability has been averaged for the residues of each oligomer strand.

kcal/mol respectively. Figure 6.7 shows a snapshot of the apoC-II tetramer adsorbed to the graphene surface highlighting the conformation where the residues, Met60, Thr62, Thr64, Ile66, Thr68, Gln70 (colored red) are interacting with the surface and the residues, S61, Y63, G65, F67, D69 (colored blue) are solvent exposed. The solvent exposed residues have increased cross chain interacts in particular the aromatic residues, Tyr63 and Phe67, which form π-π-stack and stabilise the tetramer structure. Overall the interactions between the apoC-II(60-70) tetramer are either driven by π-π stacking or CH-π interactions (discussed in Chapter 5, with the former leading to peptide disorder and the later stabilising the oligomer.

Another mechanism that increases the stability of the apoC-II(60-70) tetramer at the graphene interface was revealed by examining the water structuring around the adsorbed tetramer. It showed that water molecules had been trapped between the tetramer and the graphene surface. Two water molecules formed a hydrogen bridge between the adjacent threonine residues, Thr62, Thr64 of strand 2 and Thr68 of strand 3 bonded with one

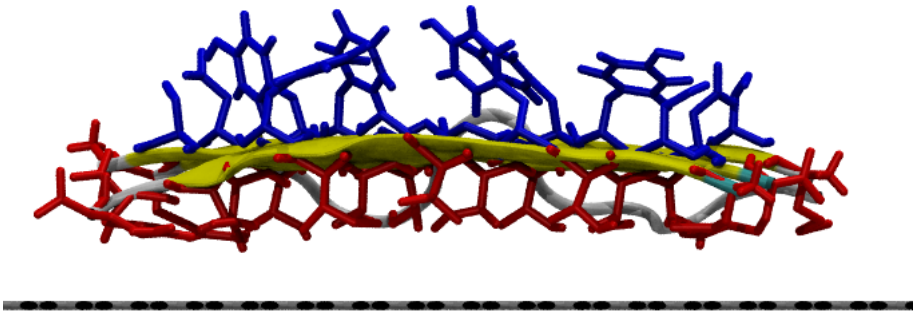

Figure 6.7: Snapshot from the most populated cluster, of the apoC-II(60-70) tetramer adsorbed to the graphene surface. Sidechains coloured red correspond to the residues that are in contact with the graphene surface and sidechains coloured blue correspond to residues that are solvent exposed.

water molecule while residues Thr62, Thr64 of strand 3 and Thr68 of strand 2 where hydrogen bonding with the other, shown in Figure 6.5. This hydrogen bridge stabilises the inner two peptide strands of the tetramer, and does not occur with the apoC-II(60-70) dimer suggesting that their maybe a critical fibril seed size that this behaviour occurs. It is postulated that as the oligomer grows in size additional hydrogen bridges will form thereby stabilising fibril growth, via increased cross chain π-π stacking and the addition of more hydrogen bridge formation, this mechanism has also been observed with a β-sheet structured protein adsorbed to a graphene surface [412]. Interestingly this behaviour is not observed while the tetramer is adsorbed to either the C60 or CNT nanomaterials, suggesting that it may be curvature dependent.

Overall the general trend observed for the binding free energy analysis was that C60 is the weakest binding followed by the CNT and then the graphene which correlates with our previous investigation, Chapter 4. However the difference in binding free energy between the peptides adsorbed to the CNT and graphene is similar, suggesting that binding free energy is dependant on the conformation adopted at the surface. It also appears that there was a competitive interaction while adsorbed to the nanomaterial, i.e peptide-peptide interactions are competing with the peptide-nanomaterial interactions, this is explored further in the next section. Furthermore the binding free energy was greatest when the apoC-II oligomers aromatic residues had a high contact stability with the nanosurface.

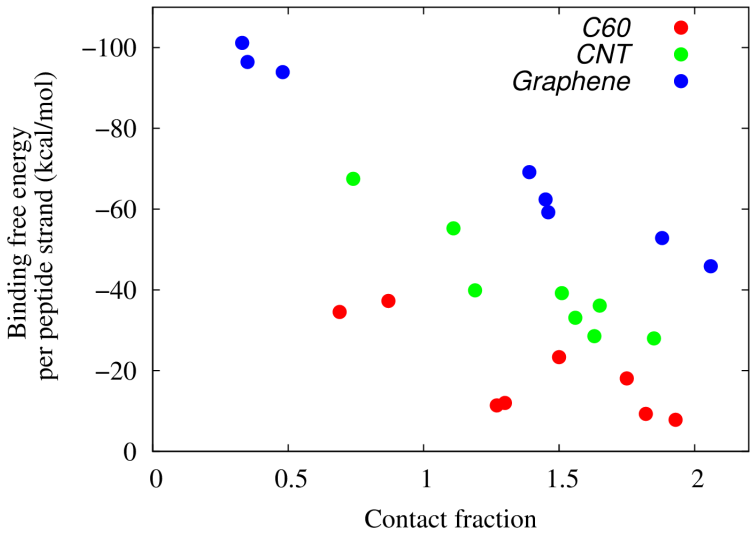

Figure 6.8: Binding free energy with respect to the contact fraction of each of the top four clusters for the apoC-II(60-70) dimer and tetramer adsorbed to the C60 (red), CNT (green) and graphene (blue).

These results suggest that the aromatic residues play an important role in binding and ultimately causing disorder in the structure of the oligomers.

6.5 Amyloid fibrillation propensity

Overall the results show that in general the apoC-II tetramer is more stable than the apoC-II dimer on all surfaces. It appears that the π-π stacking behaviour of the aromatic residues with the carbon nanosurface impacts on the stability of the fibril seed. In fact the cross strand π-π stacking between aromatic residues of neighbouring strands acts to stabilise the apoC-II tetramer [256, 257]. By disrupting these inter-strand π-π stacking interactions the overall stability of the oligomer was reduced. This is apparent, through the reduced β-strand content and calculated contact fraction of the apoC-II dimer on the surfaces of the CNT and graphene whereas the apoC-II tetramer on these same surfaces retains on average a larger contact fraction and more β-strand content. These results indicate that there was a competitive interaction between the residues of the peptide strands and the interaction of these residues with the surface. Figure 6.8 shows the normalised binding free energy vs the inter-strand contact fraction for each cluster of the apoC-II(60-70) dimer and tetramer in the presence of the C60, CNT and graphene. The trend of this graphene

shows that has the inter-strand contact fraction increases there is a linear decrease in binding free energy. Thus as an oligomer grows in size at the surface of a nanomaterial the overall interaction between the oligomer and surface will be reduced and therefore the oligomer will be more stable.

It has been determined throughout this thesis that the binding free energy between the peptide and nanomaterials is curvature dependant, with a larger curvature resulting in lower surface area and thus reduced binding free energy. Additionally it has been shown that peptide-nanosurface binding free energy and oligomer size are linked, with an increase in oligomer size resulting in a reduction in the binding free energy. In fact at the graphene interface there is a critical fibril size where the graphene nanomaterial stabilises the apoC-II(60-70) oligomers, through CH-π interactions and the trapping of water molecules between the tetramer and graphene surface. Figure 6.9 shows the proposed probability of peptide growth for each peptide size (monomer, dimer, tetramer and based on the trend, octomer). The probability was determined by taking the identified stability of each cluster of the apoC-II(60-70) oligomer at the different interfaces from the free energy maps generated in section 6.4.1. Equation 6.7 was then applied to determine the probability ($\mathrm{Pr_{fibrillation}}$) that the oligomer will adopt a structure that could lead to further peptide association while adsorbed to each nanomaterial. Here, $\mathrm{F_{Stability}}$ is the fibril stability identified in section 6.4.1 and is assigned the values 0, 0.5 and 1 for fibril incompetent, unstable and stable structures respectively. $\mathrm{C_{Population}}$ is the percentage population of each cluster, these values are calculated for each cluster and summed to determine the final $\mathrm{Pr_{fibrillation}}$.

$$Pr_{fibrillation} = \sum F_{Stability} C_{Population} \tag{6.7}$$

The monomeric fibrillation propensities are proposed based on results obtained in Chapter 4. The fibrillation propensities generated showed that the C60 particle induces conformations that are not able to lead to further ordered peptide association, while the CNT can induce either fibril favouring or fibril inhibiting conformations, however an increase in oligomer size can push the trend towards stability. Finally the graphene surface seems to have a critical fibril size that becomes stable at the interface, as the apoC-II(60-

70) dimer was disrupted and the apoC-II(60-70) tetramer was stabilised. From this data it is suggested that flatter surfaces such as CNTs and graphene may increase the stability of strongly bound oligomers (i.e. apoC-II(60-70) tetramer) while causing disorder in weakly bound oligomers (i.e. apoC-II(60-70) dimer). These results are inline with recent literature which suggested that strongly attractive surface accelerate the growth of fibril oligomers while weakly attractive surface would slow fibrillation [166].

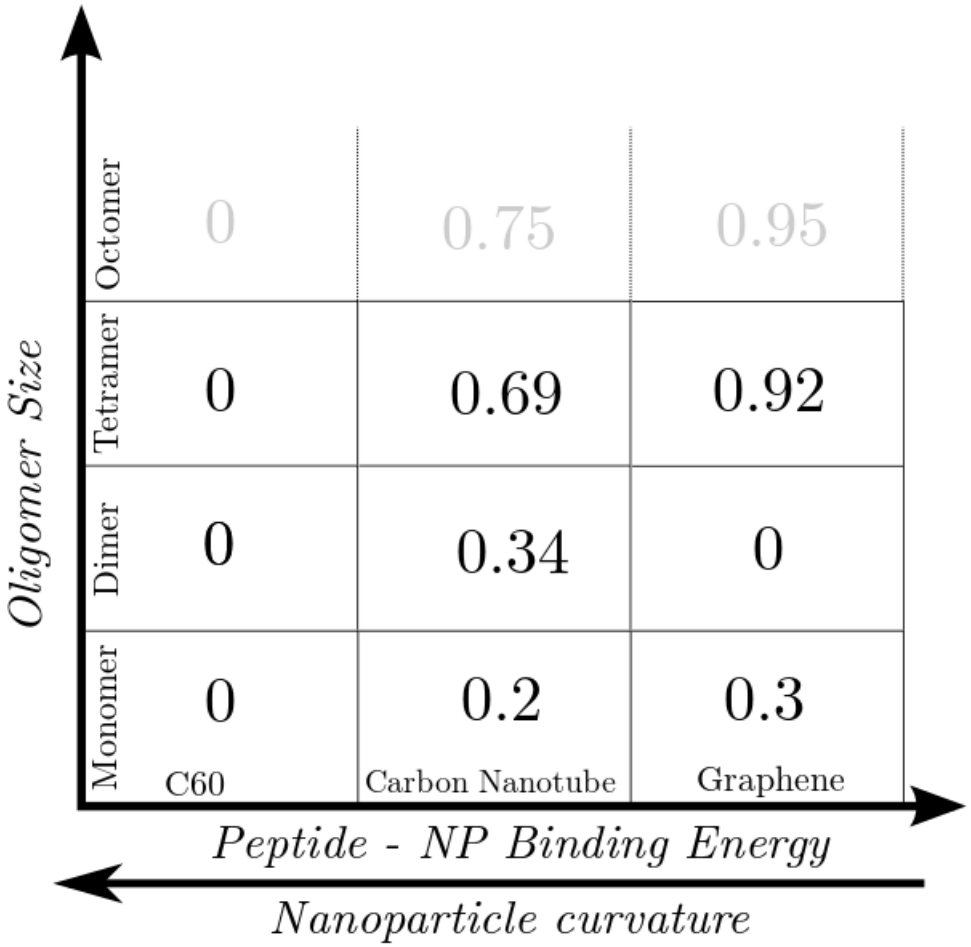

Figure 6.9: Diagram showing the determined effect that fibril size, binding free energy and nanomaterial curvature has on the fibril stability of apoC-II(60-70) oligomers.

6.6 Conclusions

Overall the REST results suggest that there are competing interactions when amyloidogenic peptides are in the presence of these nanomaterials. The peptide-peptide interactions

that stabilise the oligomer structure compete with the peptide-nanomaterial interactions that cause the formation of disordered aggregates. It has been shown that the disorder induced is dependant on the nanomaterial curvature, the initial adsorption to the nanomaterial and oligomer size. Highly curved surfaces lead to increased peptide lability and disorder, adsorption to the nanomaterial in a configuration that allows close aromatic contact with the surface induces oligomer disorder and stronger binding of the peptide to the nanomaterial. Finally we showed that small oligomers (dimers) become disordered in the presence of dimensionally different carbon nanomaterials, while larger oligomers (tetramers) retain more β-strand content and can be stabilised when adsorbed to flat graphene surfaces by promoting cross chain π-π stacking and surface - peptide CH-π interactions as well as trapping of water between the peptide and graphene surface resulting in a stable hydrogen bridge formation. It can be postulated that the carbon nanomaterials may disrupt unstable oligomers while encouraging stable oligomers to adopt conformations possible of further fibril growth. In this way nanomaterials may be used to reduce the overall concentration of the potentially toxic weakly bound oligomer intermediates by disruption of these oligomers or encouraging fibril growth of strongly bound oligomer species.

Chapter 7

Effect of graphitic nanomaterials on mature fibril seed of apoC-II(1-76)

7.1 Overview

In this chapter the structure and dynamics of the full length apoC-II fibril tetramer in the presence the three carbonaceous nanomaterials, C60, CNT and graphene, is investigated and compared to its known ambient behaviour. The fibril seed of the apoC-II protein has been characterised previously using NMR and X-ray diffraction analysis and optimised using molecular dynamics simulations [417]. The cross β-core of the apoC-II(1-79) fibril contains the 60 to 70 residues that have been examined as the peptide derivative apoC-II(60-70) in the previous chapters.

Here, long-time scale classical molecular dynamics simulations are used to explore the aggregate dynamics and structure of the preformed apoC-II tetramer in the presence the carbonaceous nanomaterials used throughout this thesis. The MMPBSA approach that was applied in Chapter 6 is also applied here to estimate the binding energy of the fibril seed to each nanomaterial. The results are compared to the peptide derivative apoC-II(60-70) and its oligomers in order to extrapolate the potential effect that these nanomaterials have to influence fibril formation of the full length apoC-II tetramer.

7.2 Introduction

Recently molecular dynamics studies have been applied to investigate proteins responsible for many amyloidogenic diseases, including amyloidβ, amylin and apolipoprotein C-II [417]. MD has been utilised to examine the structure and dynamics of monomeric and protofibril structures in solution, often in an attempt to optimise the structure [417] or identify conformational changes that may precede fibrillation [418]. Recently, studies have explored the effect that the presence of nanomaterials may have on these large protein structures.

Examining full length proteins such as Aβ and amylin require significantly more computational power and much longer timescales particularly in the presence of nanomaterials. As demonstrated in the previous Chapter, advanced conformational sampling techniques are needed to determine the favourable structures forming on the nanosurface. Several studies have used these sorts of techniques to understand the fibrillation propensity of Aβ monomers in the presence of carbonaceous nanomaterials. Jana et al. applied adaptive biasing force (ABF) methods to determine how the presence of a carbon nanotube can effect the collapse of an Aβ monomer [197]. They showed that the collapse of Aβ, a step in the fibrillation process, was reduced in the presence of the CNT [197]. Two other studies have recently focused on the binding of small carbonaceous nanomaterials to Aβ protofibrils. Huy et al. used docking, all-atom molecular dynamics and the MMPBSA method to determine the binding energy of different sized fullerene particles to 5Aβ(17-42) and 12Aβ(9-40) oligomers [189]. Their study demonstrated the larger the fullerene particle the higher the binding affinity. Additionally they showed that the C60 particle destroys the fibril structure to a greater extent compared to the other fullerenes [189]. The other study examined 1,2-(dimethoxymethano)fullerene (DMF) with a fibrillar hexamer of the full-length Aβ(1-42) [188]. DMF has been shown to be soluble in water and more recently was experimentally shown to reduce the fibrillation of Aβ [188]. Zhou et al. used classical molecular dynamics to identify three favourable binding sites of the DMF molecule on the Aβ protofibril [188]. Their binding energy analysis showed the importance of π-stacking interactions as well as curvature fitting mechanisms in binding of the DMF molecule. They also showed that the presence of DMF destabilised the D23-K28 salt bridge that is

considered important for the formation of amyloid fibrils [188].

In this chapter the full length apoC-II tetramer has been simulated using classical molecular dynamics in the presence of the three carbon nanomaterials used throughout this thesis. The apoC-II(1-79) tetramer has a simple 'letter-G-like' β-strand-loop-β-strand structure and two stable β-stand regions, between residues 20-36 (β1) and 58-74 (β2), described in Chapter 3.

7.3 Computational details

7.3.1 Atomistic simulations of peptide-nanomaterial systems

To investigate the effects of carbonaceous nanomaterials on the structure and dynamics of the apoC-II(1-79) tetramer (see Figure 3.4) a series of simulations were performed with different starting tetramer arrangements. Here, the same fullerene, CNT and graphene nanomaterials were used as those used in Chapters 4-6. As previous the CNT and graphene were modelled as periodic long while the C60 was a discrete particle. The initial configurations were constructed by positioning the tetramer 4.5-10 Å from the nanomaterial (see Appendix D for the initial configurations). The proteins together with the nanomaterial were then placed in a periodic simulation cell of at least 12.0 nm x 12.0 nm x 11.0 nm in dimension. The molecular dynamics simulations were performed using the Gromacs 4.6 [410] simulation package, with the interactions between the particles in the system described by the united-atom Gromos forcefield and the 43A1 parameter set. The carbonaceous nanomaterials were modelled using the aromatic sp2 carbon parameters.

The Lennard-Jones interactions were truncated at 10 Å, with the long-range electrostatic interactions accounted for by the Particle Mesh Ewald (PME) method [379]. The LINCS algorithm was used to constrain the bond lengths to their equilibrium values [278], enabling a timestep of 2 fs to be applied for all simulations. The VMD software package was used for visualization of the dynamics and analysis of the molecular trajectories [384]. *In vacuo* energy minimisation using steepest descent algorithm was initially performed on the tetramer-nanoparticle systems to remove steric clashes. The optimised system was then solvated using the SPC water model [245] at a water density of ≈ 1 g/cm^3. To neutralise the overall negative charge of the system, 16 unrestrained counterions (Na+) were

included in the simulation cell. Energy minimisation on the solvated system was performed to relax all of the atomic degrees of freedom. Subsequently, MD was conducted to allow the solvent to equilibrate around the solutes by keeping the tetramer and nanomaterial restrained. A constant temperature of 300 K was maintained through the equilbration process with the Berendsen thermostat [273] and the weak coupling thermostat of Bussi [274] was used for the production MD. In all simulations the geometry of the nanomaterial was restrained for ease of monitoring the protein dynamics. Four protein-nanomaterial complexes were simulated in the presence of each nanomaterial. These all had different starting orientations to enhance the conformational sampling, yielding a total 2 μs of data per nanomaterial-tetramer complex. The behaviour and structures observed in each system exhibited similar trends, therefore the results from representative simulations are shown.

7.3.2 Binding energy calculations

The binding free energy between the full length apoC-II and various carbon nanomaterials was calculated using the g_mmpbsa tool [415] based on the molecular mechanics/Poisson-Boltzman surface area (MM/PBSA) method [416]. In this approximation the binding free energy (ΔG_{bind}) is decomposed into contributions from the gas-phase binding energy (ΔE_{gas}), solvation free energy (ΔG_{solv}), and entropy TΔS, as represented below.

$$\Delta G_{bind} = \Delta E_{gas} + \Delta G_{solv} - T\Delta S \tag{7.1}$$

As in the previous chapter, the gas-phase term is the sum of bonded and nonbonded energies, however in this work we are using the 'single trajectory' approach where the bonded terms cancel exactly and thus can be ignored, leaving only the non-bonded terms. The solvation energy term, ΔG_{solv}, contains polar and nonpolar solvation energies, the polar contributions are estimated using an implicit solvent model, in this case the Poisson-Boltzmann model. The non-polar solvation energy is linearly dependant on the solvent-accessible surface area (SASA) which is calculated to determine this contribution. The binding free energy is determined by,

$$\Delta G_{bind} = \Delta E_{MM} + \Delta G_{polar} + \Delta G_{nonpolar} \tag{7.2}$$

The energy components, ΔE_{MM}, ΔG_{polar} and $\Delta G_{nonpolar}$, were calculated on the clustered structures from the final 100 ns of each of the independent MD simulations. The additional parameters set are described in the g_mmpbsa developers publication [415].

7.4 Results and discussions

Explicitly solvated molecular dynamics simulations were used to characterise the interactions between the amyloidogenic apoC-II(1-79) tetramer and three exemplar carbonaceous nanomaterials. The apoC-II(1-79) tetramer had a strong affinity to the nanomaterials, once the tetramer came in contact with each nanomaterial it remained adsorbed for the entire trajectory, as was reported for the peptide derivatives in the previous chapters. Below the structural changes that take place on the surface are analysed as well as the bound states from the final 100 ns of simulation.

7.4.1 Secondary structure analysis

Secondary structure analysis was performed to investigate the effects of the different nanomaterials and their dimensionality on the apoC-II fibril conformation. The STRuctural IDEntification (STRIDE) [397] algorithm was utilised to classify the β-strand propensity for each residue of the apoC-II tetramers. Figure 7.1 shows the amount of time each residue spends in a β-sheet backbone conformation during the final 100 ns of simulation. Percentages were taken as averages from the data for each monomer.

As previously shown the apoC-II(1-79) [299] has two well defined β-stranded regions between residues 20-36 (β1 strand) and residues 58-74 (β2 strand). These two regions largely retain their β-sheet rich content albeit with some difference between fibril - nanomaterial systems. In general the presence of the C60 particle resulted in a reduction in β-sheet content for the β2 region ($\approx$ 65% on average for the four simulations), due to the adsorption of the fullerene within this region of the tetramer. As discussed in Chapter 6, the peptide-peptide interactions are reduced when the fullerene adsorbs to the peptide resulting in the lower β-strand content. Additionally the C60 adsorbs to the tetramer on

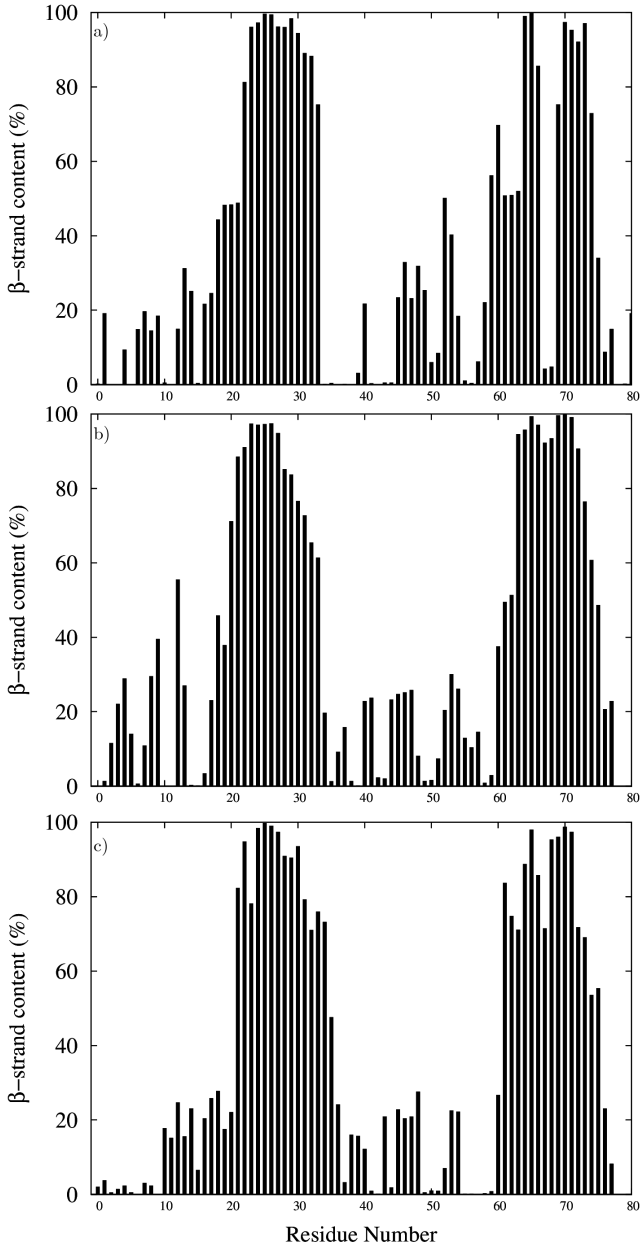

Figure 7.1: The percentage of time that each residue spends in a β-sheet conformation over the final 100ns of simulation for the apoC-II(1-79) tetramer in the presence of the C60 (a), CNT (b) and graphene(c).

the exposed fibril axis, Figure 7.2. It can be suggested that the C60 particle may block the fibril axis which would prevent any further ordered peptide association at this location.

The stability of the β1 and β2 regions, while the apoC-II(1-79) tetramer was adsorbed to the surface of the CNT and graphene, was dependent on the face of the protein that was in contact with the surface. In the case of graphene, one trajectory resulted in an average β1 strand percentage content of $\approx$ 86%, where the fibril axis of the tetramer was

oriented perpendicular to the graphene sheet. Whereas another trajectory resulted in the fibril axis oriented parallel with the graphene surface which lead to a reduction in both $\beta 1$ ($\approx 70\%$) and $\beta 2$ ($\approx 61\%$) strand content in comparison. Similarly when the apoC-II(1-79) tetramer was adsorbed with the fibril axis perpendicular to the CNT surface the β-strand content was increased in comparison to the other CNT-oligomer trajectories, with a $\beta 1$ content of $\approx 74\%$ and $\beta 2$ content of $\approx 74\%$.

7.4.2 ApoC-II(1-79) tetramer dynamics on the carbon nanomaterials

The per residue root mean square fluctuation (RMSF) results (Figure 7.3) showed that the apoC-II(1-79) tetramer was significantly less dynamic on the extended CNT and graphene surface compared to the highly curved C60 particle. These general trends are similar to the results presented in Chapters 4 and 5. As seen in Figure 7.2, while adsorbed to the C60 particle the tetramer is mostly solvent exposed, this contributes to the higher RMSF compared to the tetramer adsorbed to the CNT and graphene. The reduced dynamics on the extended surfaces suggest that the tetramer is more stable and structurally constrained. This may allow the surface to act as a template for further protein self-assembly. While the absolute RMSF is different between tetramer nanomaterial complexes, the RMSF profile exhibits very similar trends. The most dynamic residues were within the unstructured N-terminal region (residues 1-20), while the β-core has on average the lowest RMSF, albeit with a peak at the loop region (residues 37-57). This suggests that while adsorbed to the CNT and graphene the apoC-II(1-79) tetramer retains its initial structure.

Figure 7.4 shows the trajectory of the exemplar MD simulation of apoC-II(1-79) tetramer with each nanomaterial as they undergo adsorption and "lockdown" to the nanosurface. The lockdown procedure has been described previously, in Chapter 5 and 6, whereby the peptide/protein will undergo structural rearrangment to increase the contact with the surface. The RMSD of the apoC-II(1-79) tetramer and the contact area between the apoC-II(1-79) tetramer and the C60 (a), CNT (b) and graphene (c) is plotted over the 0.5 μs of simulation. The results show an increase in contact area upon adsorption to the nanomaterials and increasing over the course of the simulation. In all cases the contact area is greatest when adsorbed to the surface of graphene (≈ 25 nm^2) followed by the CNT (≈ 14 nm^2) and significantly less is the C60 particle (≈ 2 nm^2). The contact

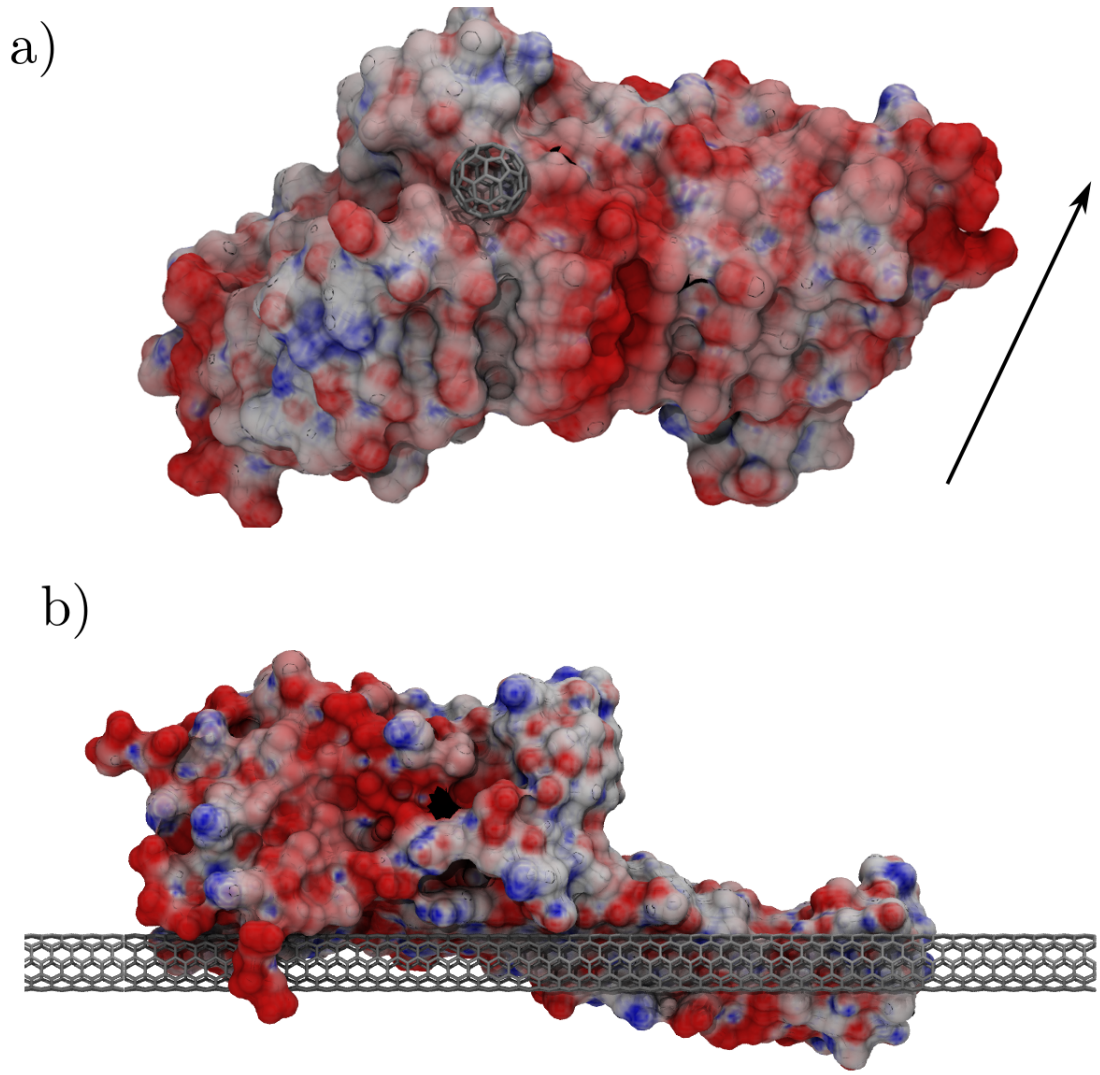

Figure 7.2: Snapshots taken of the apoC-II(1-79) tetramer adsorbed to the C60 (a) and CNT (b) nanomaterials, displayed with a surface of the electrostatic potential. The C60 particle can be seen adsorbed to the fibril axis (axes orientation shown by black arrow) side of the apoC-II(1-79) tetramer potentially blocking any further peptide association (a). The tetramer is also shown wrapping around the CNT surface (b).

area between the apoC-II(1-79) and the CNT and graphene surface, is much greater than the contact area recorded for the peptide derivatives, apoC-II(60-70) dimer and tetramer while adsorbed to these same surface. However the contact area between the apoC-II(1-79) and the C60 is not greater than the contact area obtained between the two peptide derivatives and the C60 particle. This indicates that the available interaction area of the

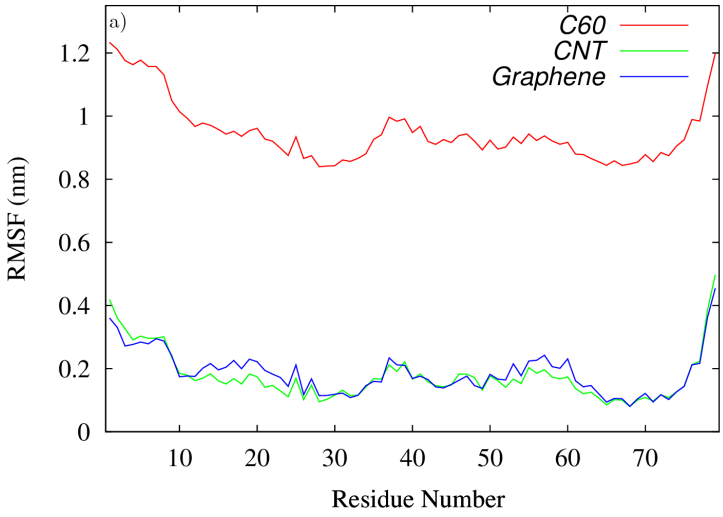

Figure 7.3: Root mean square fluctuation of the atomic positions in each residue of apoC-II(1-79) tetramer (a) in the presence of C60 (red), nanotube (green) and graphene (blue).

C60 is saturated even by the smaller apoC-II(60-70) peptide derivatives.

Furthermore, the apoC-II(1-79) tetramer undergoes the lockdown procedure albeit at a slower rate than the smaller peptide derivatives. Upon initial adsorption to the nanosurface the tetramer reorients to facilitate greater contacts with the surfaces, this does not always coincide with RMSD changes. This suggests that overall the apoC-II(1-79) is structurally stable and any significant conformational changes take place over longer time scales. On the surface of the CNT and graphene once the tetramer reorients to facilitate greater contacts there is few further changes that increase the contact area between the peptide and surfaces, Figure 7.4b,c, suggesting the tetramer adopts a favourable orientation structure for binding prior to the lock-down phase. The C60 particle however is much more dynamic and can induce some structural rearrangement resulting in changes in the contact area the fibril seed the nanomaterial. This is particluarly evident between 300 and 400 ns, Figure 7.4a, where a drop in contact area between the tetramer and C60 preceeds a RMSD change. Overall the results observed here with the apoC-II(1-79) tetramer follow the trends obtained for the apoC-II(60-70) peptides discussed in Chapter 5.

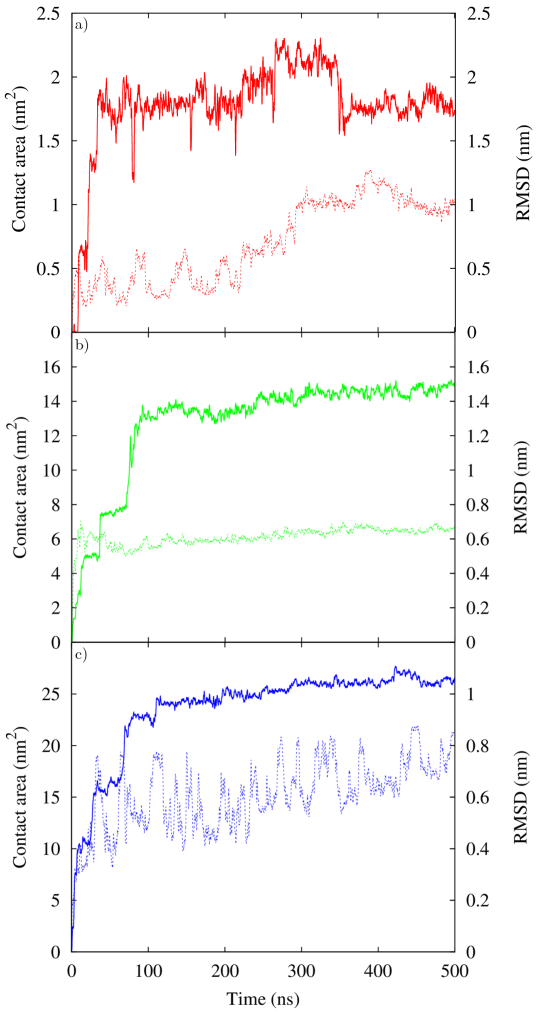

Figure 7.4: Properties from a typical MD simulation of apoC-II(1-79) tetramer on the surface of graphitic nanomaterials showing the RMSD change (dashed line) and contact area (solid line) change between the tetramer with the C60 (a), CNT (b) and graphene (c) nanoparticles.

7.4.3 Cluster analysis and binding energies

Cluster analysis of the peptide backbone (RMSD cutoff of 0.2 nm) over the final 100 ns of each trajectory was performed to identify the most frequently sampled structures. The representative structure of the most populated cluster for the exemplar trajectories is shown in Figure 7.5 and their populations shown in table 7.1. Additional structures are shown in in Appendix D. As discussed in the section 7.4.1, the cluster analysis also shows that the C60 predominately adsorbs to the β2 region. It can be suggested that this orientation may block further peptide association. The clusters of the apoC-II(1-79) tetramer adsorbed to the CNT surface show that the most favourable complex configura-

tion is with the fibril axis oriented perpendicular to the long axis of the CNT (Figure 7.5b). The clustered structures of the tetramer adsorbed on graphene showed a similar configuration where the fibril axis is oriented perpendicular to the extended graphene surface (Figure 7.5c). These configurations enable a large region of the amyloid fibril seed to be solvent exposed and which will enable further peptide association.

Trajectory Number	C60 Cluster Population	CNT Cluster Population	Graphene Cluster Population
1	80.9%	41.4%	51.7%
2	54.9%	96.1%	84.8%
3	57.7%	26.1%	51.8%
4	77.0%	99.9%	61.3%

Table 7.1: Populations of the top clusters from the four independent trajectories

It has been shown in the previous chapters that the binding affinity of the apoC-II peptide to the nano surface is important in determining the propensity of the peptide to form fibrils. Thus in this chapter the binding energy of the apoC-II(1-79) tetramer to each nanomaterial is determined using the MMPBSA approach, also used in Chapter 6. The structures used for the binding energy calculation were taken from the most populated cluster obtained from the cluster analysis. To ensure the structures were sufficiently decorrelated, each frame used in the calculation was at least 20 ps apart. The binding energy results are presented in Table 7.2. The results show that the peptide/protein adsorbs most strongly to the flat graphene and CNT and weakly binds to the C60, consistent with the results obtained previously for the peptide derivatives, Chapter 4 and 6.

The different binding energies observed on the independent trajectories with the same nanomaterial were a result of the different protein adsorbed states to each nanomaterial. This is evident for the tetramer - C60 complexes, where the C60 particle adsorbs to the fibril axis of the tetramer in three independent simulations resulting in a binding energy $\approx$ 20 - 30 kcal/mol (Figure 7.2a), while the fourth system, resulted in the C60 embedding between the peptide chains induced protein structural changes including maximised protein-surface interactions, a loss in β-sheet content and a more favourable binding energy of -43.94 kcal/mol (Figure 7.5a-iv). Additionally the weak binding of the tetramer to the

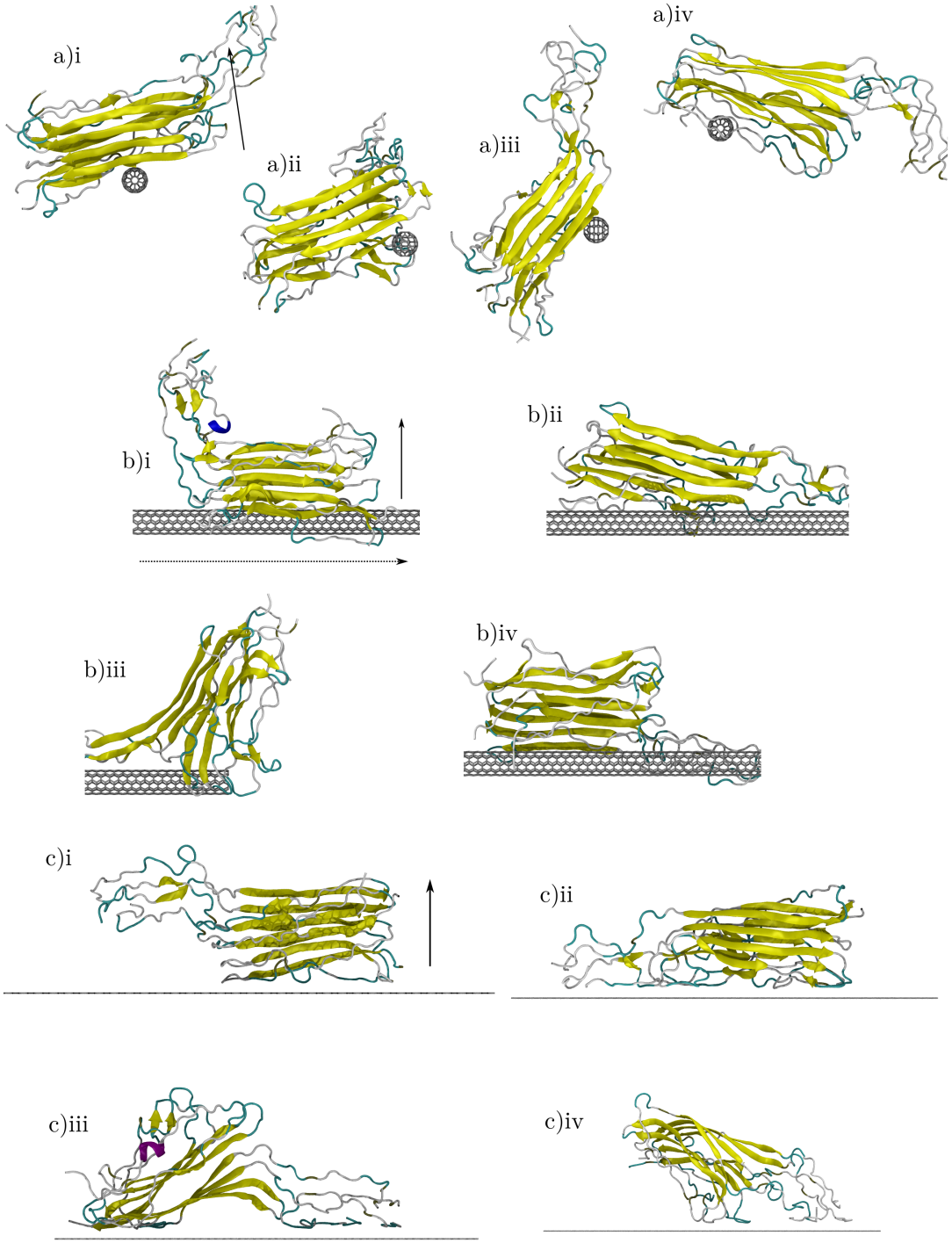

Figure 7.5: Exemplar structures of the highest populated cluster obtained through cluster analysis of the apoC-II(1-79) tetramer in the presence of the C60 (a), CNT (b) and graphene (c). Of the four independent trajectories for each nanomaterial - oligomer complex (i -iv). Solid black arrows show the direction of the fibril axes, dashed black line shows the CNT long axis.

Trajectory number	ΔE_{vdw} (kcal/mol)	ΔG_{PB} (kcal/mol)	ΔG_{sur} (kcal/mol)	ΔG_{bind} (kcal/mol)
		C60		
1	-38.64	13.31	-2.59	-27.92 ±3.62
2	-32.35	6.21	-2.16	-28.30 ±7.29
3	-29.63	8.83	-2.01	-22.82 ±8.38
4	-46.67	5.69	-2.97	-43.94 ±16.21
		Carbon nanotube		
1	-216.27	40.92	-10.92	-186.27 ±8.95
2	-375.57	72.49	-18.55	-321.63 ±9.30
3	-224.20	48.02	-12.08	-188.26 ±22.98
4	-353.06	73.11	-18.15	-298.09 ±10.99
		Graphene		
1	-308.01	97.39	-18.07	-228.69 ±13.46
2	-643.72	169.08	-35.50	-510.15 ±24.68
3	-674.15	103.21	-36.45	-607.40 ±19.72
4	-334.59	84.17	-19.03	-269.45 ±20.63

Table 7.2: Estimated binding energy of the most populated clusters taken from the four independant simulations of the full apoC-II tetramer in the presence of the C60, CNT and graphene. ΔE_{vdw} accounts for the van der Waals interactions between the tetramer and NP, the ΔG_{PB} and ΔG_{sur} account for the polar and non-polar solvation energies and ΔG_{bind} is the estimated binding energy.

C60 resulted in desorption of the tetramer from the C60 in trajectory 3, with re-adsorption occurring ≈ 100 ns later to the fibril axis of the tetramer. The tetramer similarly begins to wrap around the CNT in trajectories 2 and 4 thus explaining the high binding affinity (-321.63 kcal/mol and -298.09 kcal/mol), see Figure 7.5b-ii,b-iv and Figure 7.2b.

7.5 Conclusions

Using classical molecular dynamics it has been shown that an amyloidogenic apoC-II(1-79) fibril seed exhibits a strong affinity for graphitic nanomaterials. The proximity of the C60 fullerene contributed to an increase in conformational lability in the apoC-II(1-79) tetramer, resulting in reduced β-strand content, compared to the fibril in ambient

conditions [417]. It is postulated that the C60 may block further self-assembly by capping the fibril thus preventing any further ordered peptide association. Additionally it was shown that the CNT and graphene surface either do not have a significant effect on the β-sheet content or lead to an increased β-sheet content. Additionally they reduced the RMSF of the peptide residues suggesting that these nanomaterials may act as a fibril template for the larger protofibrils. These findings are in line with the previous work presented in the earlier chapters suggesting that apoC-II(60-70) fibril growth may be accelerated on the elongated surfaces, while the induced protein flexibility in the presence of the C60 particle maybe prohibitive for further fibril growth. The binding energy calculations showed the binding affinity of apoC-II(1-79) was weakest for the C60 particle, followed by the nanotube, and strongest for the graphene, in line with our peptide simulations, Chapter 4, 5 and 6. In all simulations these trends are due to the larger contact area available for peptide adsorption to the flatter graphene and nanotube than the highly curved C60.

In summary, our results show that the full length apoC-II(1-79) fibril seed exhibits the same trends as its peptide derivatives in the presence of dimensionally different carbonaceous nanomaterial. This highlights the effectiveness of using smaller peptide models and advanced sampling methods to explore the aggregation propensity of amyloidogenic peptides in the presence of nanomaterials.

Chapter 8

Summary

In this thesis computational modelling techniques were employed to investigate the behaviour of an amyloidogenic protein in the presence of dimensionally different carbonaceous nanomaterials. The work was motivated by experimental studies that have demonstrated nanoparticles can impact the rate of protein self-assembly, possibly interfering with the development of protein misfolding diseases such as Alzheimers and prion disease caused by aggregation and fibril formation of amyloid-prone proteins.

Here, the amyloidogenic protein apolipoprotein C-II (ApoC-II) and its peptides derivatives were simulated in the presence of differenent carbon allotropes; C60 fullerene, a single walled carbon nanotube and graphene sheet.

Initially the effect of the different carbon nanomaterials on the structure, dynamics and binding of the monomeric peptide apoC-II(60-70) was studied and compared to results obtained from previously characterised peptide behaviour in solution. A combination of computational methods, including large-scale electronic structure calculations and classical all-atom molecular dynamics were used. Additionally simulations were also conducted using a recently developed polarisable forcefield for graphitic nanomaterials and compared against the results using the a common non-polarisable forcefield. It was shown that the apoC-II(60-70) peptide exhibited a strong affinity for graphitic nanomaterials where the binding was facilitated through π-π interactions between the aromatic residues of the peptide and the surface of the nanomaterial. This was generally achieved by the exclusion of water molecules from the peptide-nanomaterial interface. The results showed that hydrophobic nanoparticles have multiple notable effects on the peptide structure,

dynamics and binding affinity. In particular it was demonstrated that dimensionality and different degree of curvature can either facilitate or hinder the interaction of amyloidogenic peptides with the nanosurfaces and make them adopt conformations capable of inhibiting or promoting fibril development. Specifically the proximity of the C60 fullerene contributed to an increase in conformational lability of apoC-II(60-70), which was shown to prevent it from adopting fibril-favouring structural features. Conversely, the less curved nanotube and flat graphene nanomaterials promote elongated peptide conformations previously shown to form fibril seeds. The electronic binding energy and solution free energy calculations showed the binding affinity of apoC-II(60-70) was weakest for the C60 particle, followed by the nanotube, and strongest for the graphene, this general trend was replicated throughout the thesis with a few exceptions. The observed agreement between the classical non-polarisable, polarisable forcefields and electronic structure calculations show that molecular dynamics simulations utilising fixed charge forcefields provide reasonable representation of the interactions between peptides and graphitic surfaces.

Understanding the effect nanomaterials may have on the early stages of fibril formation and in particular the small oligomeric species that drive the initial fibrillation behaviour was key to determining their potential to either inhibit or promote fibril growth. Initially the adsorption and desorption mechanism of two preformed oligomeric composits of apoC-II(60-70) peptide (dimer and tetramer) were investigated. This was followed by extensive REST simulations to investigate the dynamic properties of the oligomers while adsorbed to the surface. The adsorption study showed that adsorption took place through a stepwise process, initially association was made to the interfacial water layer driven by long range electrostatic interactions between the ordered water layer and the charged residues and terminals of the oligomers. Subsequently the oligomers associated between the first and second water layers. Finally the oligomers adsorbed to the surface albeit in different ways, the apoC-II(60-70) dimer through hydrophobic and aromatic interactions with the nanomaterials. Whereas the amphiphilicity of the tetramer resulted in contact with the CNT and graphene surface via the negatively charged face, where the threonine residues were driving the initial contact with the water layer and subsequently the nanosurface. This configuration resulted in the aromatic residues remaining solvent exposed. However when adsorbed to the C60 surface the tetramer interacted more favourably through

the aromatic residues, a result of the reduced water structuring and more favourable hydrophobic interactions with this surface.

Potential of mean force calculations of the dissociation of the apoC-II(60-70) dimer from the nanomaterials showed the same trends as the monomeric study, C60 was the weakest binder, followed by the CNT and finally graphene. In fact the stronger interaction with the CNT and graphene resulted in the separation of the peptide strands of apoC-II(60-70) dimer during the pulling simulations, indicating that the interaction with the surface was greater than between the petpide strands.

REST simulations were applied to investigate the stability and interactions of the apoC-II(60-70) dimer and tetramer while adsorbed to the carbonaceous nanomaterials. The results showed that the disorder experienced by the apoC-II(60-70) oligomers was dependant on the nanomaterial curvature, the initial adsorption to the nanomaterial and oligomer size. Highly curved surfaces lead to increased peptide lability and disorder. Initial adsorption to the nanomaterial in a configuration that allowed close aromatic contact with the surface induces oligomer disorder and stronger binding of the peptide to the nanomaterial. Additionally the instability experienced while at the nanosurface is dependent on oligomer size, with the apoC-II(60-70) dimer become disordered in the presence of of the different carbon nanomaterials, while the larger oligomer (tetramer) retained more β-strand content and was actually stabilised when adsorbed to flat graphene surfaces through cross chain π-π stacking and surface - peptide CH-π interactions.

Futhermore it was shown that the peptide-peptide interactions that stabilise the oligomer structure are in competition with the peptide-nanomaterial interactions, that can induce the formation of disordered aggregates. It is proposed that as the oligomer grows it will become more stable as there will be greater interchain interactions and thus less peptide-nanomaterial interactions. However additional studies would need to be conducted to confirm this hypothesis.

Finally the full length preformed apoC-II tetramer was investigated in the presence of the same carbonaceous nanomaterials. Overall the results showed the same trends as the peptide derivative studies, the proximity of the C60 fullerene contributed to an increase in conformational lability in the apoC-II(1-79) tetramer, resulting in reduced β-strand content, as has been shown throughout this thesis. Additionally it was hypothesised that

the C60 may block further self-assembly by capping the fibril thus preventing any further ordered peptide association. While it was shown that the CNT and graphene surface either do not have a significant effect on or lead to an increase in β-sheet content. The presence of these extended nanomaterials did lead to a reduction in the peptide structure fluctuations suggesting that they may act as a fibril template for the larger protofibrils. The binding energy calculations also showed the same trends as the peptide derivative work, with the C60 the weakest binder followed by the CNT and graphene. These results highlight the effectiveness of using smaller peptide models and advanced sampling methods to explore the aggregation propensity of amyloidogenic peptides in the presence of nanomaterials.

Overall, this thesis has shown that nanomaterials of different dimensionality can impact on the fibrillation process of an amyloidogenic peptide and its peptide derivatives. Specifically it has been shown that highly curved nanomaterials tend to induce conformational lability in the peptide a feature that may inhibit fibrillation. Flatter surfaces may also inhibit fibrillation by causing disorder in small and unstable aggregates it was shown however that for larger and more stable aggregates the flatter/extended surfaces may promote fibrillation by acting as a template for further peptide association. The results presented in this thesis may form the bases for the development of novel nano based therapeutics to combat amyloidogenic diseases or for ”safe by design” nanomaterial development.

Chapter 9

Future Work

9.1 Graphene-oxide as an amyloidogenic fibril inhibitor

Graphene has been described in Section 3.3.3, it is composed of sp2-hybridized carbon atoms in a hexagonally arranged in a two-dimensional structure. Graphene-oxide (GO) is another form of graphene that retains the 2D structure and hexagonally arranged carbon atoms with additional polar groups bonded to the surface. Typically these polar groups are epoxy and hydroxyl that are bonded to both sides of the basal plane of graphene, with carboxly groups attached to the edges of the graphene surface, Figure 9.1. The addition of these polar groups changes the chemical and physical properties of graphene. GO can be produced in large quantities and is easier to manipulate than pristine graphene, additionally it is highly dispersible in both water and organic solvents and surface modifications can be easily added. These properties have made it attractive for a range of applications including transparent conductive films [419], biomaterials in medicine, antibacterial materials [420] and coatings and interfaces [421].

Recently GO has been shown to inhibit the formation of amyloid-β fibrils *in vivo* [422] in a concentration dependant manner. Mahmoudi et al. showed that the large available surface of GO sheets was able to delay the process of Aβ fibrillation via adsorption of the amyloid monomers to the nanosurface. Additionally they showed that the protein corona can create a protective shell on the surface of the GO sheets, increasing the lag time for fibrillation. Finally an increase in protein concentration also lead to an increased inhibitory effect. Another recent study conducted by Wang et al., investigated the effect

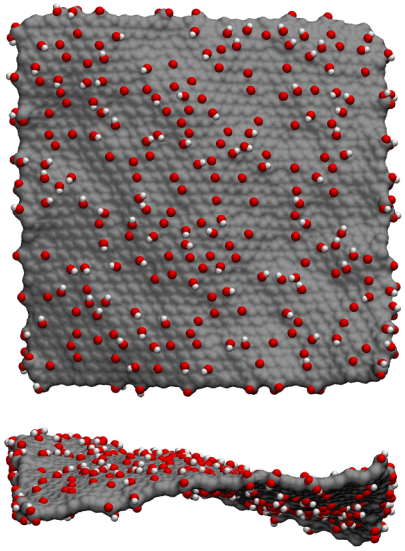

Figure 9.1: Top down and side on view of a 7 nm x 7 nm graphene-oxide flake.

that size of GO sheets could have on the fibrillation of Aβ(33-42) [423]. They showed that larger GO sheets had a relatively stronger inhibition of the fibrillation of Aβ, while they suggested that small sheets may infact promote the development of critical nuclei that may initiate the growth of amyloid fibrils [423].

These few studies highlight the potential of GO as an inhibitor of amyloid fibril formation, however the mechanism of this inhibition is largely unknown. Computational modelling techniques could be used to investigate the effect that GO has at the atomic scale on amyloid fibril forming proteins. These results could be used to rationalise the inhibitory effect that is proposed in these recent studies.

Additionally other carbon allotropes should not be discounted as potential amyloidogenic fibril inhibitors, these could include carbon nanodiamonds, multiwalled carbon nanotubes, graphite and possibly hypothetical carbon allotropes such as graphyne, graphdiyne and graphone [424].

9.2 Human islet amyloid polypeptide

This thesis has focused on a particular type of amyloidogenic protein and the effect that graphitic nanomaterials had on its structure, dynamics and aggregation propensity, however many proteins can readily form into amyloid fibrils and are related to a number of

other diseases. Some of these peptides and proteins have been discussed in Chapter 1, one particular fibril forming protein is human islet amyloid polypeptide (hIAPP), Figure 9.2. hIAPP has the ability to form amyloid fibrils and has been implicated in type II diabetes. Also known as Amylin, this 37 residue long peptide is co-secreted with insulin by the pancreatic islet β-cells and is involved in the regulation of glucose. However in some cases IAPP can be over expressed which can lead to formation of aggregates of the peptide that then form into amyloid fibrils, this aggregation has been linked to type II diabetes [425]. IAPP has been found in several other animal species, from marine species such as fish to the human variant that is related to type II diabetes. These variants often differ by just a few amino acid substitutions, which can lead to dramatically different aggregation propensities of the peptide. For example, the pig and rat IAPP do not spontaneously self-assemble into amyloid fibrils, while the cat and human variants have been shown to readily self assemble [426, 427]. The sequences of the aggregating human IAPP (hIAPP) and of the nonaggregating rat IAPP (rIAPP) been shown to be largely unstructured and contain some helical structure conserved in the N-terminal region [426, 427]. More recently computational modelling has been employed to probe the conformations of the intrinsically disordered IAPP family in an attempt to identify whether aggregate-prone conformations can be detected in the amyloidogenic sequences [428, 429, 430].

Limited studies investigating the effect that nanomaterials may have on the fibril formation propensity of IAPP. Understanding how nanomaterials can inhibit fibrillation of IAPP could help to develop novel nano based therapeutics to combat type II diabetes as well as identifying trends that exist between the effect that nanomaterials have on the fibrillation behaviour of amyloid fibril forming proteins.

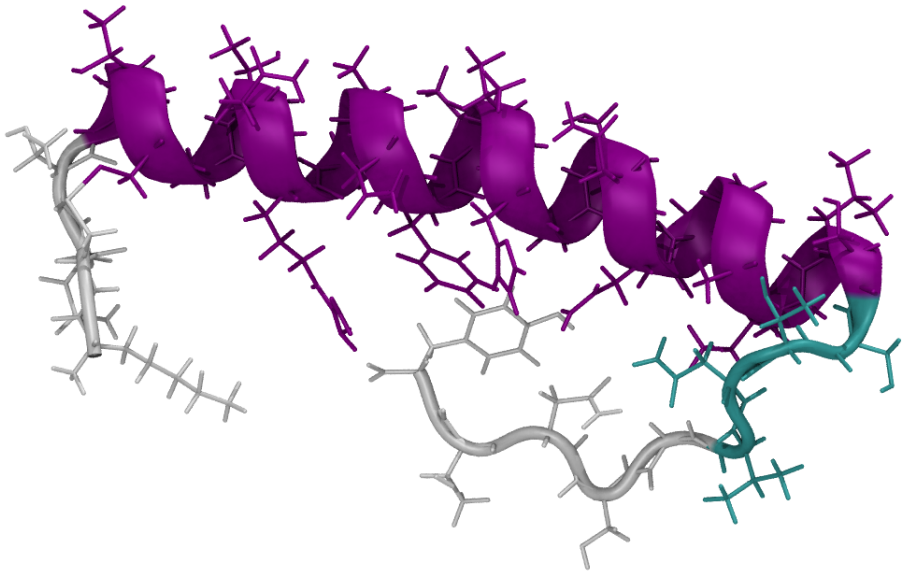

Figure 9.2: Human islet amyloid polypeptide monomer. Shown with cartoon representation.

Appendices

Appendix A

Group	C60 (%)	CNT (%)	Graphene (%)
No π-π stacking	77.1%	28.7%	12.9%
Offset π-π stacking	18.0%	61.9%	63.6%
Face-to-face π-π stacking	4.9%	9.4%	23.5%

Table 1: The total frame occupancy (%) within each main aromatic arrangement category: no π-stacking (arrangement 1), offset π-stacking (arrangements 2–5) and face-to-face π-stacking (arrangement 6) occurring on c60, nanotube and graphene as determined from the aromatic tracking and cluster analysis.

Aromatic Group	Relative Binding Energy (kcal/mol)	Absolute Binding Energy (kcal/mol)	Peptide Contact Area (nm^2)	Comments
		C60		
1	132.45	-33.56	1.12	Curved, terminal residues bound to C60
1	131.76	-34.25	1.21	Curved, terminal residues exposed to solvent
1	135.67	-30.34	1.21	Curved, terminal residues exposed to solvent
2	147.22	-18.79	0.76	Curved, terminal residues exposed to solvent
2	140.13	-25.88	0.9	Curved, terminal residues exposed to solvent
2	124.84	-41.17	1.18	Curved, terminal residues exposed to solvent
3	131.68	-34.33	1.37	Curved, terminal residues bound to C60
3	130.44	-35.57	1.65	Curved, terminal residues exposed to solvent, substantial H-bonding
3	131.04	-34.97	1.47	Curved, terminal residues bound to C60, some H-bonding
4	123.14	-42.87	1.35	Curved, terminal residues bound to C60, some H-bonding
4	131.94	-34.07	1.15	Curved, terminal residues bound to C60, some H-bonding
4	135.09	-30.92	1.46	Curved, terminal residues bound to C60, some H-bonding
5	122.85	-43.16	1.88	Curved, terminal residues exposed to solvent, substantial H-bonding
5	128.5	-37.51	1.41	Curved, terminal residues bound to C60, some H-bonding
5	144.89	-21.12	0.85	Curved, terminal residues exposed to solvent, substantial H-bonding
6	128.66	-37.35	1.95	Curved, terminal residues exposed to solvent, substantial H-bonding
6	128.96	-37.05	1.68	Curved, terminal residues exposed to solvent, substantial H-bonding
6	138.66	-27.35	1.01	Curved, terminal residues bound to C60, substantial H-bonding

Table 2: *In vacuo* binding energies (relative to the strongest bound complex, face-to-face π-stacking on graphene), and absolute binding energies together with total contact area of the representative frames for each arrangement category and C60. Structural comments for each frame are also included.

Aromatic Group	Relative Binding Energy (kcal/mol)	Absolute Binding Energy (kcal/mol)	Peptide Contact Area (nm^2)	Comments
		CNT		
1	91.14	-74.87	3.52	Curved, terminal residues bound to nanotube, substantial H-bonding
1	99.86	-66.15	3.33	Curved, terminal residues bound to nanotube, substantial H-bonding
1	100.05	-65.96	3.39	Curved, terminal residues bound to nanotube, substantial H-bonding
2	94.12	-71.89	2.92	Curved, terminal residues bound to nanotube, substantial H-bonding
2	71.01	-95	4.06	Elongated, terminal residues bound to nanotube
2	75.73	-90.28	4.1	Elongated, terminal residues bound to nanotube
3	80.02	-85.99	3.89	Elongated, terminal residues bound to nanotube, snorkelling effect
3	74	-92.01	4.01	Elongated, terminal residues bound to nanotube, snorkelling effect
3	74.18	-91.83	4.08	Elongated, terminal residues bound to nanotube, snorkelling effect
4	87.65	-78.36	2.94	Curved, terminal residues bound to nanotube, substantial H-bonding
4	39.7	-126.31	4.01	Elongated, terminal residues bound to nanotube, snorkeling effect
4	71.44	-94.57	4.22	
5	41.35	-124.66	4.38	Elongated, terminal residues bound to nanotube, snorkeling effect
5	74.58	-91.43	4.41	Curved, terminal residues bound to nanotube, substantial H-bonding
5	66.34	-99.67	4.26	Elongated, terminal residues bound to nanotube, snorkeling effect occurring, some H-bonding
6	53.2	-112.81	4.13	Elongated, terminal residues bound to nanotube, snorkeling effect
6	87.13	-78.88	3.28	Curved, MET60 terminal residue exposed to solvent
6	41.35	-124.66	4.21	Elongated, terminal residues bound to nanotube

Table 3: *In vacuo* binding energies (relative to the strongest bound complex, face-to-face π-stacking on graphene), and absolute binding energies together with total contact area of the representative frames for each arrangement category and CNT. Structural comments for each frame are also included.

Aromatic Group	Relative Binding Energy (kcal/mol)	Absolute Binding Energy (kcal/mol)	Peptide Contact Area (nm^2	Comments
		Graphene		
1	47.28	-118.73	4.92	Curved, terminal residues bound to graphene, substantial H-bonding, snorkeling effect occurring
1	42.64	-123.37	5.21	Curved, terminal residues bound to graphene, substantial H-bonding
1	69.97	-96.04	5.1	Curved, terminal residues bound to graphene, substantial H-bonding
2	49.14	-116.87	5.33	Curved, terminal residues bound to graphene, substantial H-bonding
2	18.02	-147.99	5.4	Curved, terminal residues bound to graphene, substantial H-bonding
2	26.15	-139.86	5.08	Curved, terminal residues bound to graphene, substantial H-bonding
3	3.06	-162.95	5.57	Elongated, terminal residues bound to graphene
3	2.81	-163.2	5.18	Elongated, terminal residues bound to graphene, snorkeling effect
3	42.42	-123.59	5.28	Elongated, terminal residues bound to graphene, snorkeling effect
4	51	-115.01	5.61	Curved, terminal residues bound to graphene, substantial H-bonding
4	26.96	-139.05	5.38	Curved, terminal residues bound to graphene, substantial H-bonding
4	28.72	-137.29	5.39	Curved, terminal residues bound to graphene, substantial H-bonding
5	39.23	-126.78	5.16	Elongated, terminal residues bound to graphene, snorkeling effect
5	10.55	-155.46	5.37	Elongated, terminal residues bound to graphene
5	26.37	-139.64	5.21	Elongated, terminal residues bound to graphene
6	61.85	-104.16	4.54	Elongated, terminal residues bound to graphene
6	53.6	-112.41	5.31	Curved, terminal residues bound to graphene, substantial H-bonding
6	0	-166.01	5.6	Elongated, MET60 and SER61 terminal residues exposed to solvent, snorkeling effect occurring

Table 4: *In vacuo* binding energies (relative to the strongest bound complex, face-to-face π-stacking on graphene), and absolute binding energies together with total contact area of the representative frames for each arrangement category and graphene. Structural comments for each frame are also included.

Appendix B

Nanomaterial Surface	0 - 4.8 Å	4.8 - 7.8 Å	7.8 - 10.8 Å
C60	+0.070	+0.018	-0.013
CNT	+0.032	+0.059	-0.030
GRAPH	-0.055	+0.094	-0.048

Table 5: The overall charge density of the water layer at different distances from each nanomaterials surface. Calculated by determining the area under the curve from figure 5.1.

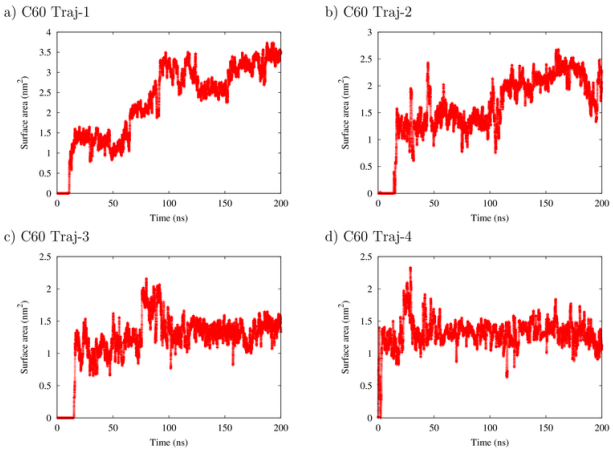

Figure 3: RMSD results for the four trajectories of the apoC-II dimer on the surface of C60 particle.

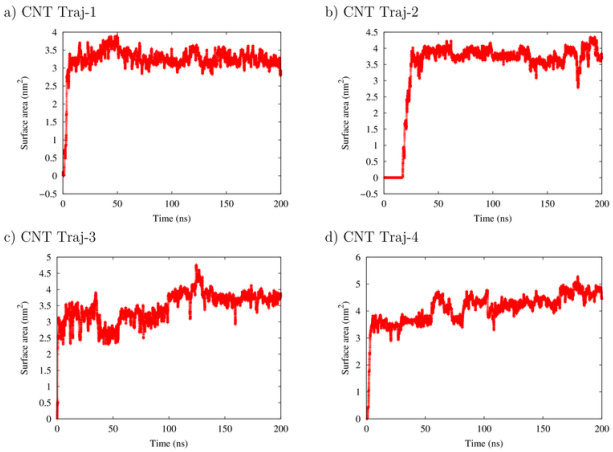

Figure 4: RMSD results for the four trajectories of the apoC-II dimer on the surface of the CNT.

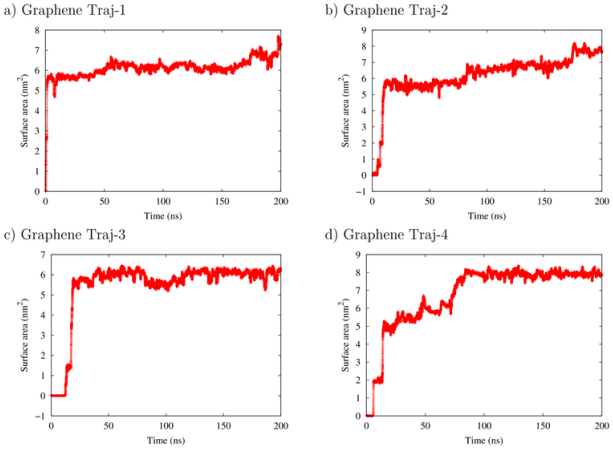

Figure 5: RMSD results for the four trajectories of the apoC-II dimer on the surface of Graphene.

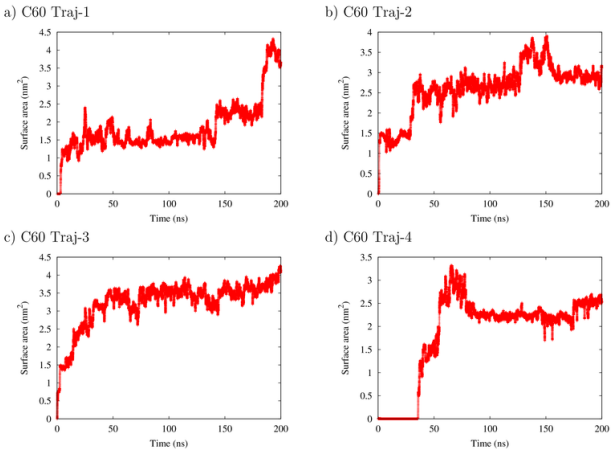

Figure 6: RMSD results for the four trajectories of the apoC-II tetramer on the surface of C60 particle.

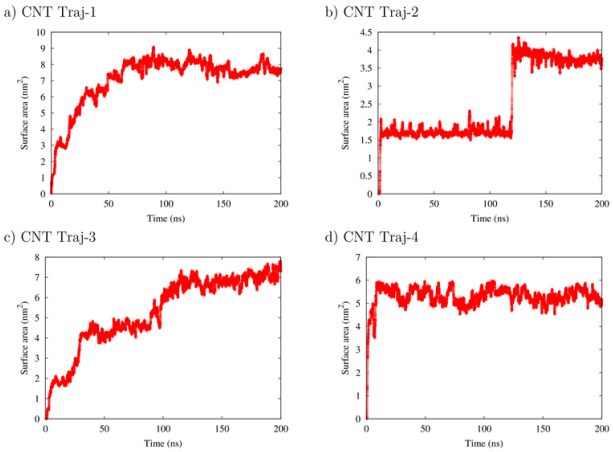

Figure 7: RMSD results for the four trajectories of the apoC-II tetramer on the surface of the CNT.

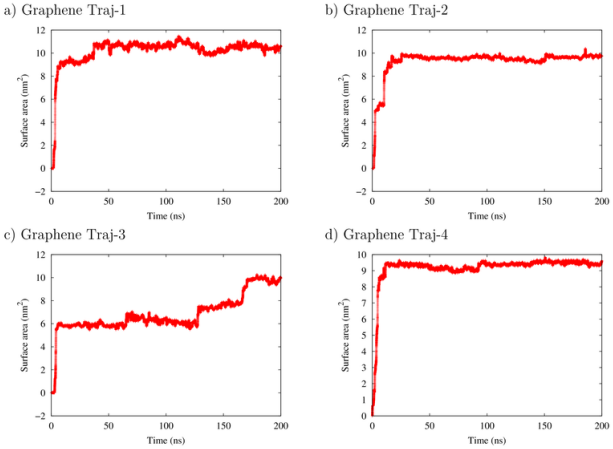

Figure 8: RMSD results for the four trajectories of the apoC-II tetramer on the surface of Graphene.

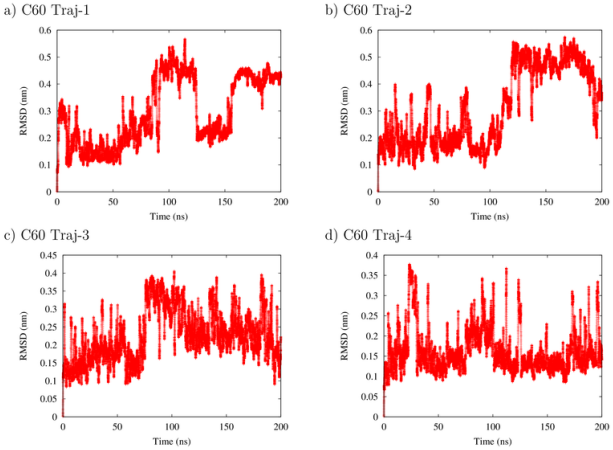

Figure 9: Contact area results for the four trajectories of the apoC-II dimer on the surface of C60 particle.

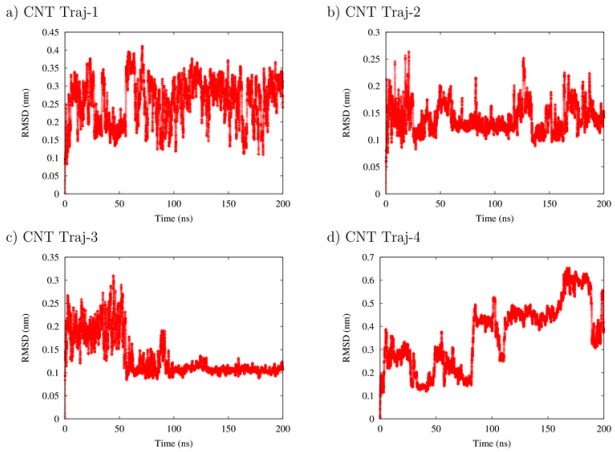

Figure 10: Contact area results for the four trajectories of the apoC-II dimer on the surface of the CNT.

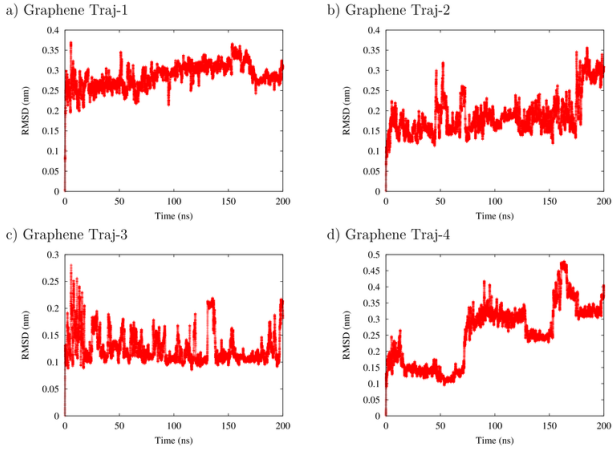

Figure 11: Contact area results for the four trajectories of the apoC-II dimer on the surface of Graphene.

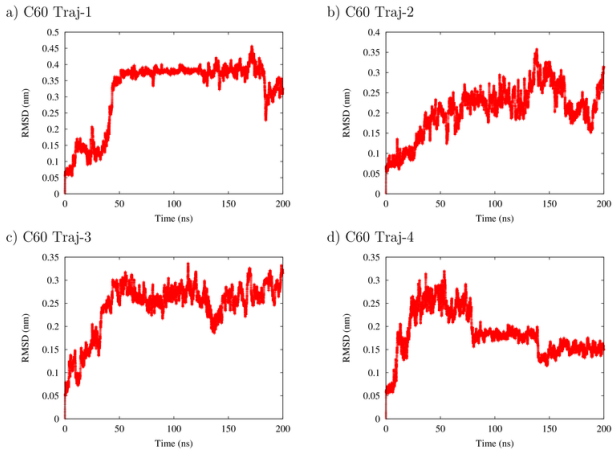

Figure 12: Contact area results for the four trajectories of the apoC-II tetramer on the surface of C60 particle.

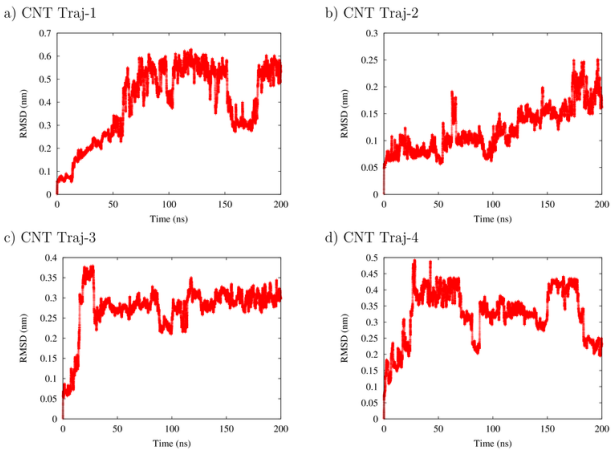

Figure 13: Contact area results for the four trajectories of the apoC-II tetramer on the surface of the CNT.

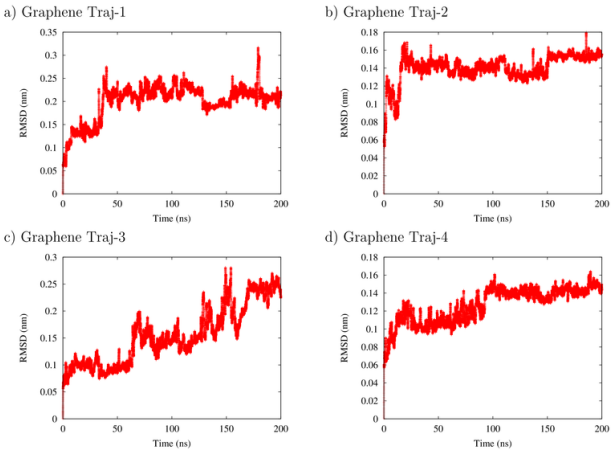

Figure 14: Contact area results for the four trajectories of the apoC-II tetramer on the surface of Graphene.

Appendix C

Trajectory number	ΔE_{vdw} (kcal/mol)	ΔG_{PB} (kcal/mol)	ΔG_{sur} (kcal/mol)	ΔG_{bind} (kcal/mol)
		C60		
1	-54.01	10.18	-2.83	-46.67±4.85
2	-82.24	11.78	-4.05	-74.51±5.28
3	-77.58	12.51	-4.00	-69.07±6.01
4	-29.55	7.58	-1.99	-23.96±6.53
		Carbon nanotube		
1	-152.31	24.87	-7.55	-134.99±4.60
2	-90.75	17.59	-5.21	-78.37±7.33
3	-66.83	14.00	-4.23	-57.06±6.62
4	-68.58	6.58	-4.15	-66.15±6.49
		Graphene		
1	-204.55	28.09	-11.42	-187.88±5.38
2	-149.56	20.02	-8.78	-138.32±7.68
3	-211.96	31.22	-12.16	-192.90±18.53
4	-222.94	33.04	-12.44	-202.35±7.25

Table 6: Estimated binding free energy of the top four most populated clusters taken from the REST simulations of the apoC-II(60-70) dimer in the presence of the C60, CNT and graphene. ΔE_{vdw} accounts for the van der Waals interactions between the tetramer and NP, the ΔG_{PB} and ΔG_{sur} account for the polar and non-polar solvation energies and ΔG_{bind} is the estimated binding energy.

Below the secondary structure of each residue of the apoC-II(60-70) dimer and tetramer is shown for the final time periods shown. These time periods are the convereged time of the simulation. As can be seen the plots overlap generally well, with greater difference at the terminal residues which are more flexible. This data indicates that a reasonable level of convergence has been achieved for each REST simulation.

Trajectory number	ΔE_{vdw} (kcal/mol)	ΔG_{PB} (kcal/mol)	ΔG_{sur} (kcal/mol)	ΔG_{bind} (kcal/mol)
		C60		
1	-33.59	4.38	-2.10	-31.30±2.56
2	-38.86	4.24	-2.46	-37.09±6.41
3	-48.83	6.27	-2.93	-45.49±3.10
4	-78.86	10.59	-4.02	-72.29±5.15
		Carbon nanotube		
1	-170.73	19.94	-8.67	-159.4±6.62
2	-123.02	18.57	-7.44	-111.89±10.51
3	-154.24	18.73	-8.85	-144.36±9.29
4	-246.51	37.71	-12.11	-220.91±6.97
		Graphene		
1	-196.04	26.25	-13.56	-183.35±16.51
2	-280.51	46.42	-15.47	-249.55±7.55
3	-265.48	43.02	-14.39	-236.85±9.86
4	-227.06	30.77	-15.00	-211.29±8.06

Table 7: Estimated binding free energy of the top four most populated clusters taken from the REST simulations of the apoC-II(60-70) tetramer in the presence of the C60, CNT and graphene. ΔE_{vdw} accounts for the van der Waals interactions between the tetramer and NP, the ΔG_{PB} and ΔG_{sur} account for the polar and non-polar solvation energies and ΔG_{bind} is the estimated binding energy.

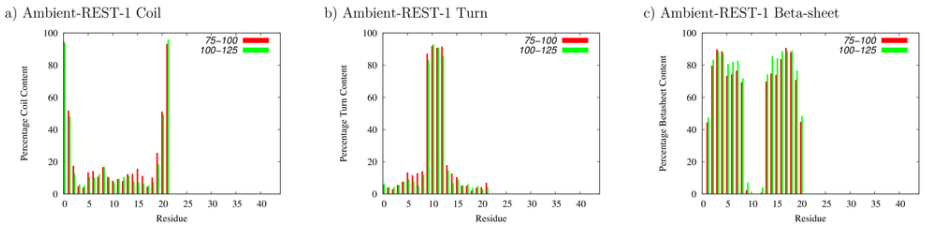

Figure 15: Percentage content of Coil, Turn and β-strand secondary structure motifs of the apoC-II(60-70) dimer in ambient conditions over the final 50 ns convergence period.

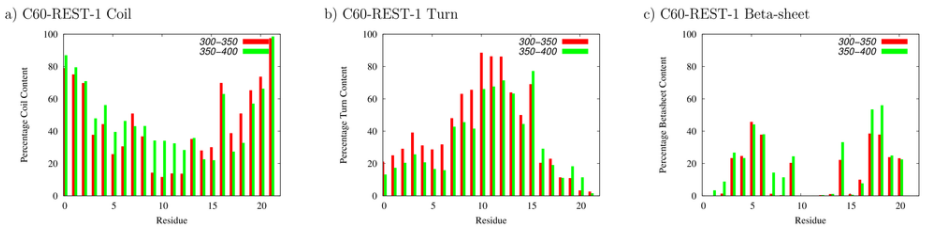

Figure 16: Percentage content of Coil, Turn and β-strand secondary structure motifs of the apoC-II(60-70) dimer adsorbed to the C60 over the final 100 ns convergence period.

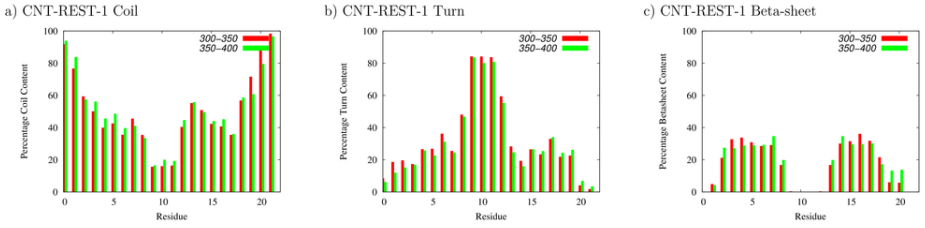

Figure 17: Percentage content of Coil, Turn and β-strand secondary structure motifs of the apoC-II(60-70) dimer adsorbed to the CNT over the final 100 ns convergence period.

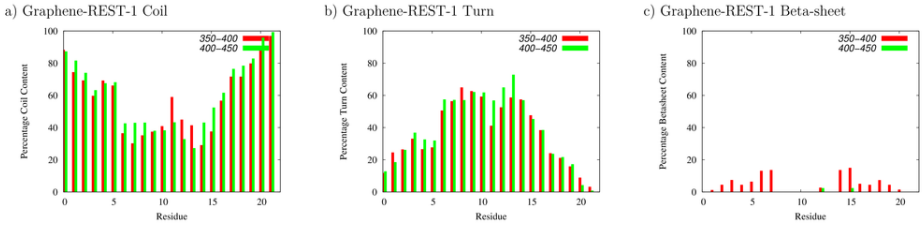

Figure 18: Percentage content of Coil, Turn and β-strand secondary structure motifs of the apoC-II(60-70) dimer adsorbed to the Graphene over the final 100 ns convergence period.

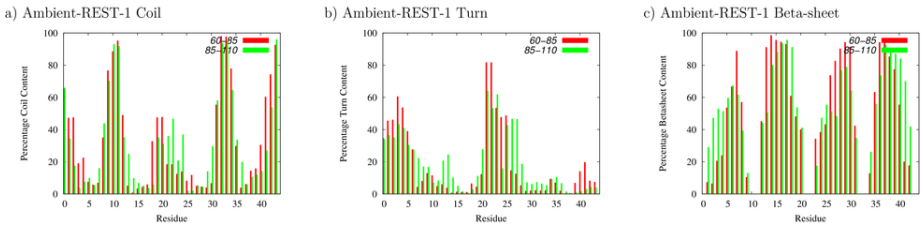

Figure 19: Percentage content of Coil, Turn and β-strand secondary structure motifs of the apoC-II(60-70) tetramer in ambient conditions over the final 50 ns convergence period.

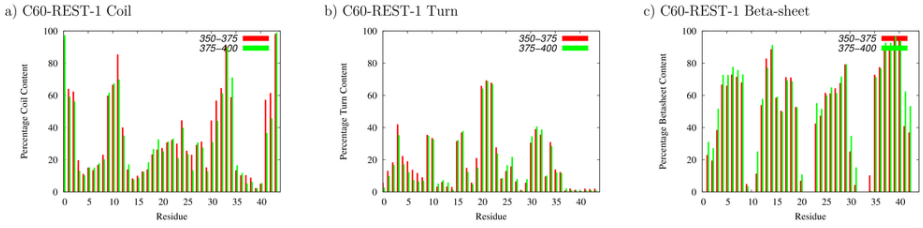

Figure 20: Percentage content of Coil, Turn and β-strand secondary structure motifs of the apoC-II(60-70) tetramer adsorbed to the C60 (REST1) over the final 50 ns convergence period.

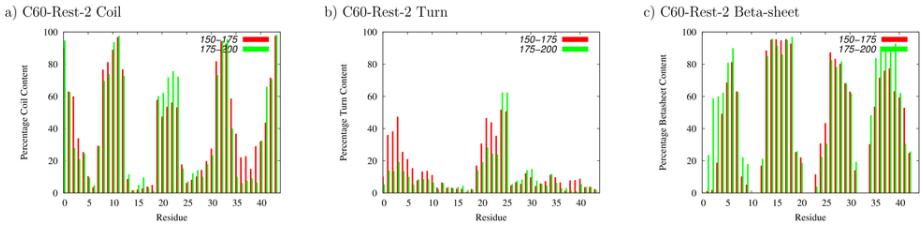

Figure 21: Percentage content of Coil, Turn and β-strand secondary structure motifs of the apoC-II(60-70) tetramer adsorbed to the C60 (REST2) over the final 50 ns convergence period.

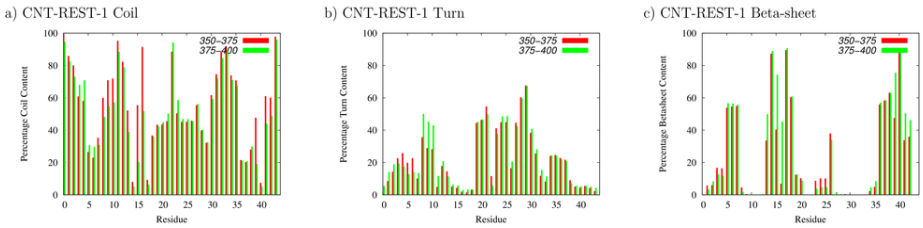

Figure 22: Percentage content of Coil, Turn and β-strand secondary structure motifs of the apoC-II(60-70) tetramer adsorbed to the CNT (REST1) over the final 50 ns convergence period.

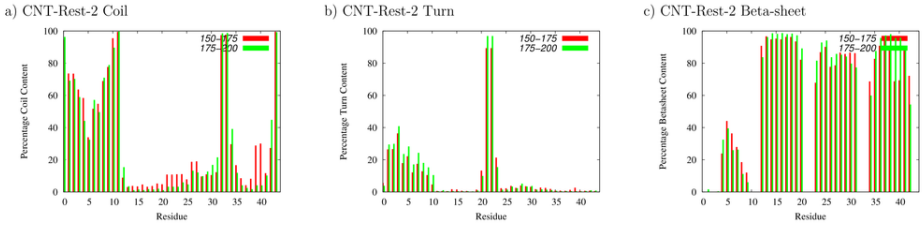

Figure 23: Percentage content of Coil, Turn and β-strand secondary structure motifs of the apoC-II(60-70) tetramer adsorbed to the CNT (REST2) over the final 50 ns convergence period.

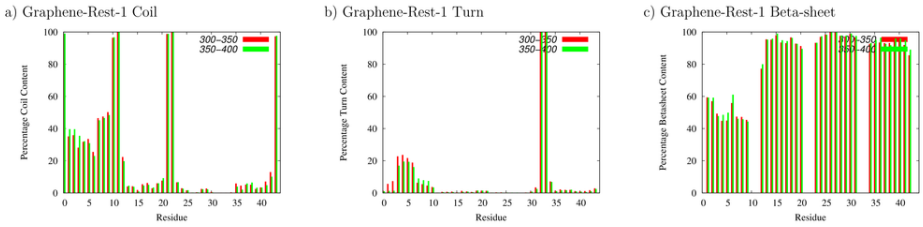

Figure 24: Percentage content of Coil, Turn and β-strand secondary structure motifs of the apoC-II(60-70) tetramer adsorbed to the Graphene (REST1) over the final 100 ns convergence period.

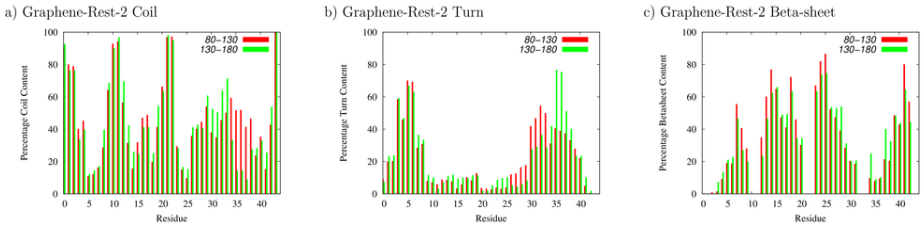

Figure 25: Percentage content of Coil, Turn and β-strand secondary structure motifs of the apoC-II(60-70) tetramer adsorbed to the Graphene (REST2) over the final 50 ns convergence period.

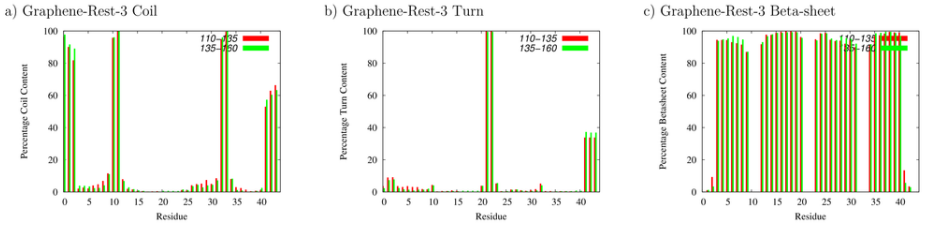

Figure 26: Percentage content of Coil, Turn and β-strand secondary structure motifs of the apoC-II(60-70) tetramer adsorbed to the Graphene (REST3) over the final 50 ns convergence period.

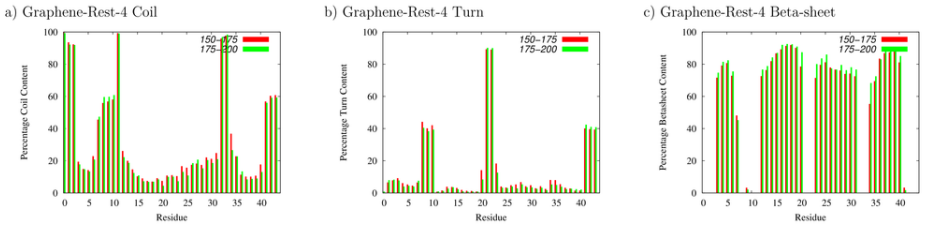

Figure 27: Percentage content of Coil, Turn and β-strand secondary structure motifs of the apoC-II(60-70) tetramer adsorbed to the Graphene (REST3) over the final 50 ns convergence period.

To determine the effectiveness of the REST method the sampling efficiency was checked. This was determined by examining the time evolution of a representative replica through the effective temperature space. The time evolution shows that the replicas have moved through the effective temperature space sufficiently.

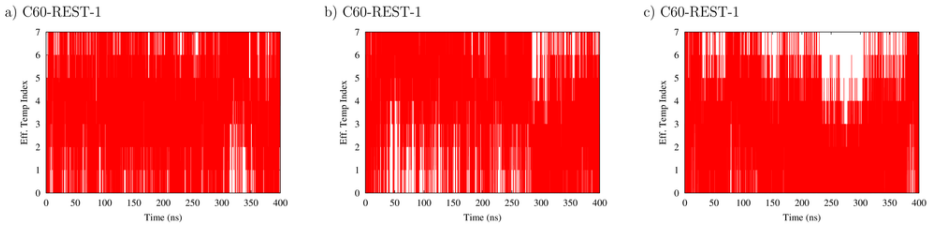

Figure 28: The swapping of several replicas through the 'effective temperature' space for the apoC-II(60-70) dimer adsorbed to the C60.

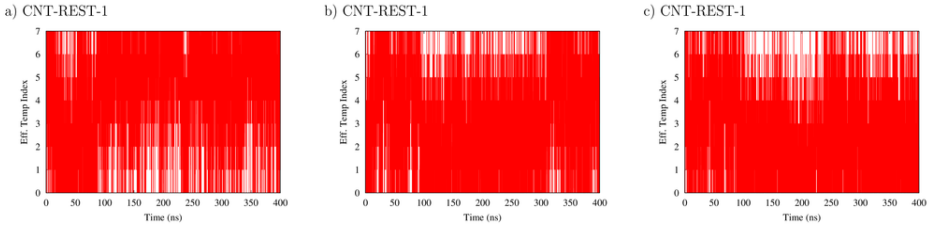

Figure 29: The swapping of several replicas through the 'effective temperature' space for the apoC-II(60-70) dimer adsorbed to the CNT.

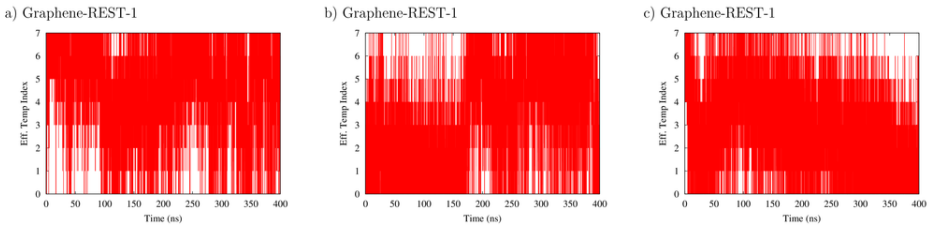

Figure 30: The swapping of several replicas through the 'effective temperature' space for the apoC-II(60-70) dimer adsorbed to the Graphene.

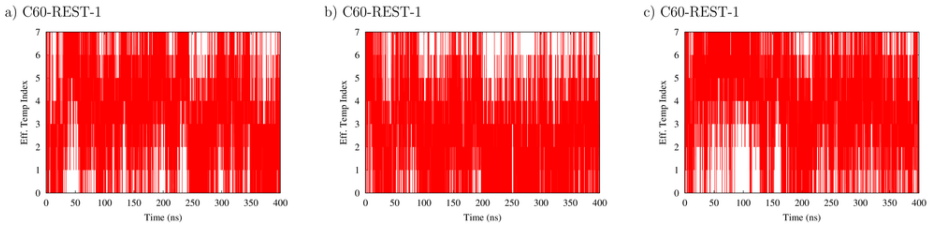

Figure 31: The swapping of several replicas through the 'effective temperature' space for the apoC-II(60-70) tetramer adsorbed to the C60.

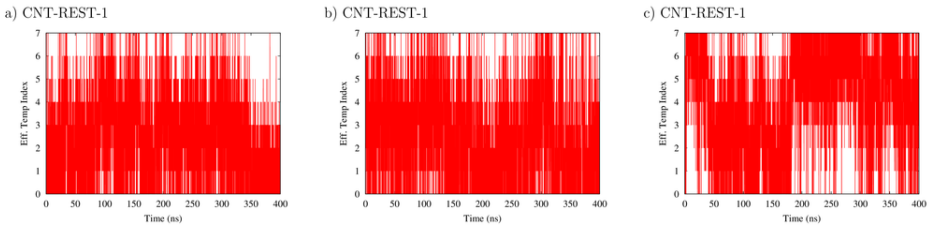

Figure 32: The swapping of several replicas through the 'effective temperature' space for the apoC-II(60-70) tetramer adsorbed to the CNT.

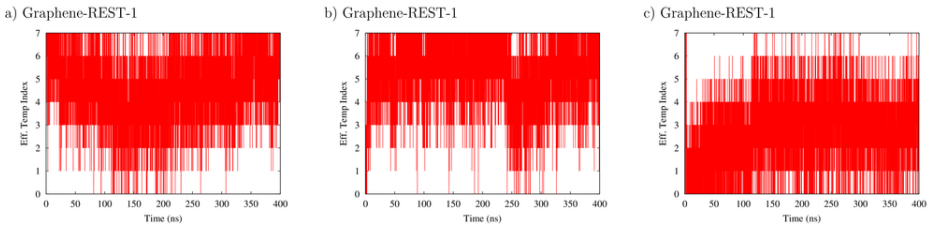

Figure 33: The swapping of several replicas through the 'effective temperature' space for the apoC-II(60-70) tetramer adsorbed to the Graphene.

Appendix D

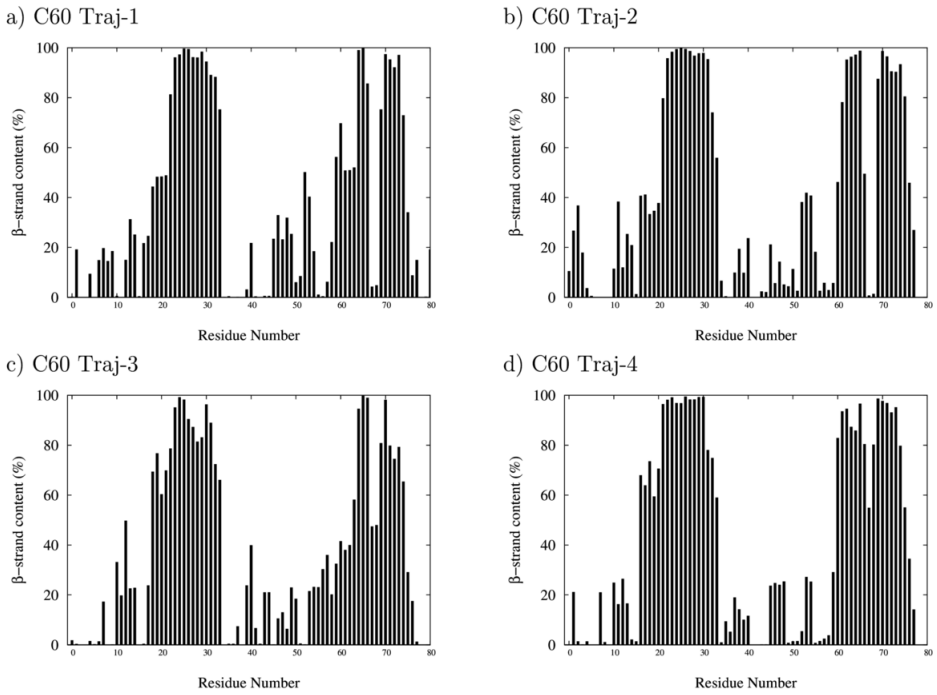

Figure 34: RMSD results for the four trajectories of the apoC-II dimer on the surface of C60 particle.

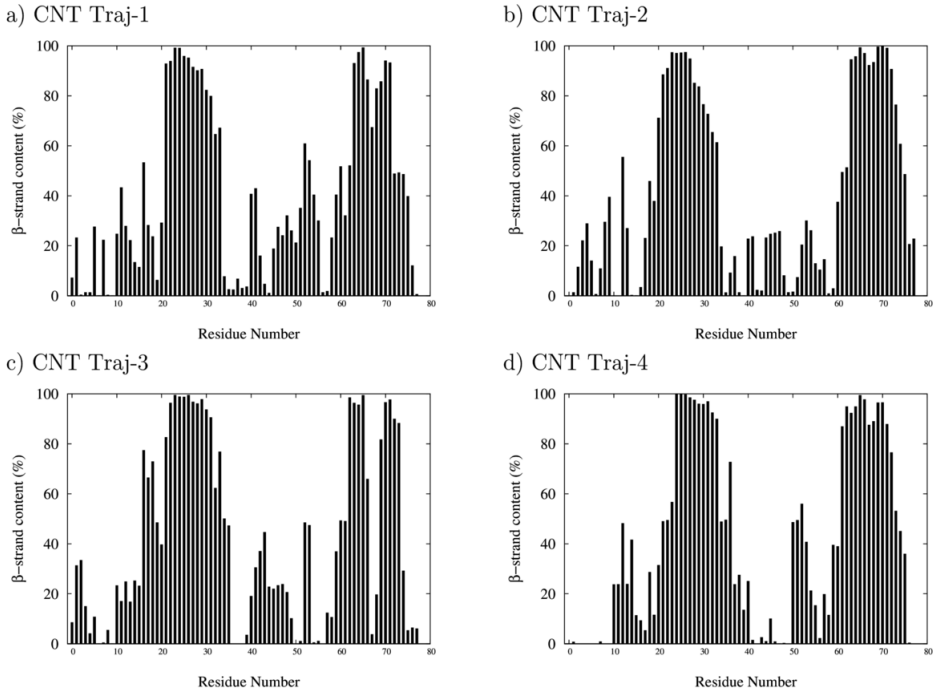

Figure 35: RMSD results for the four trajectories of the apoC-II dimer on the surface of the CNT.

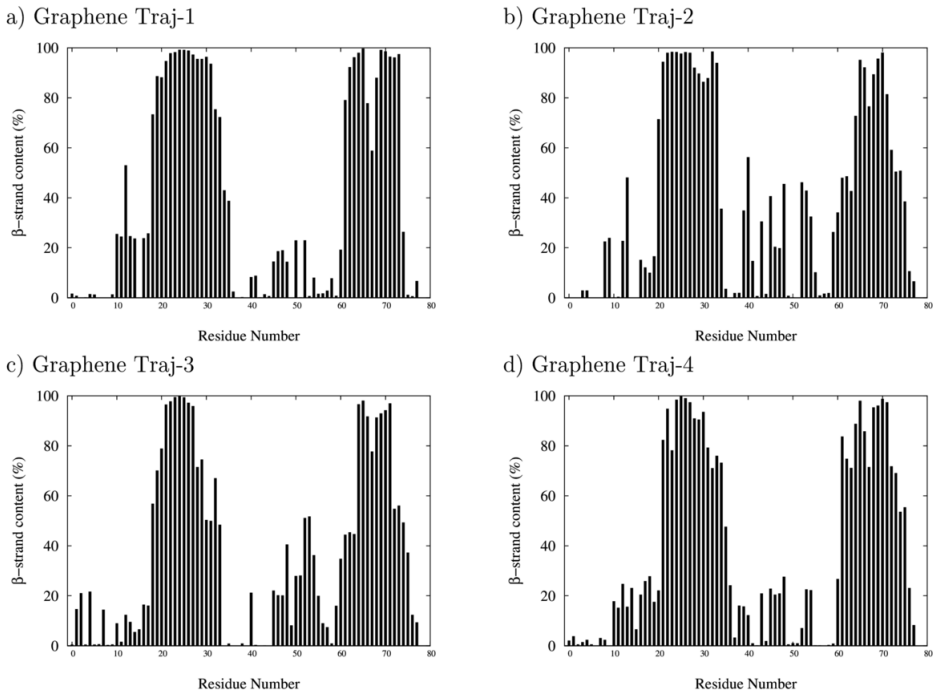

Figure 36: RMSD results for the four trajectories of the apoC-II dimer on the surface of Graphene.

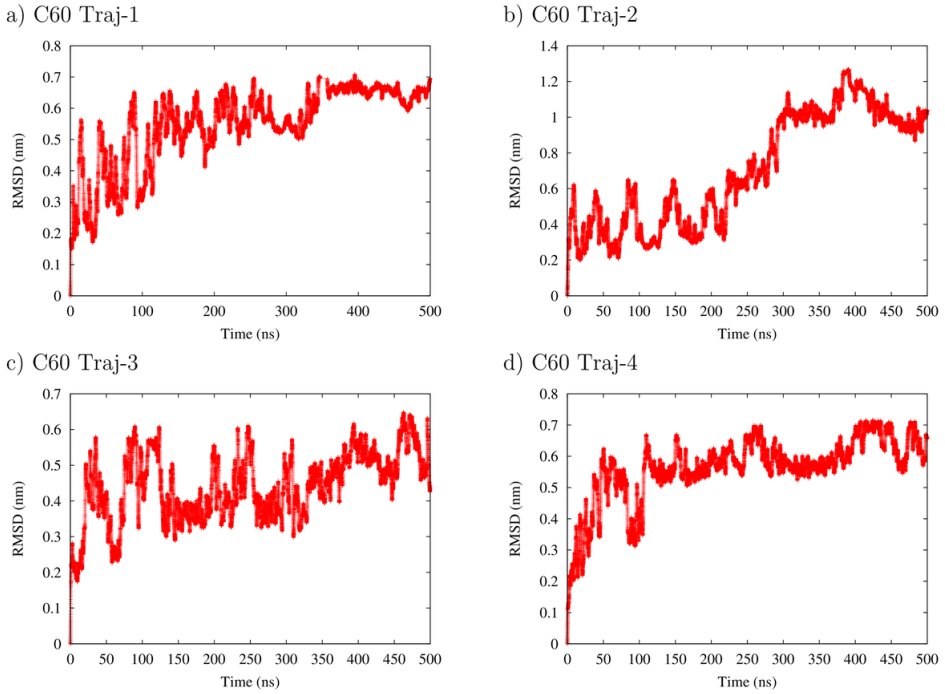

Figure 37: Contact area results for the four trajectories of the apoC-II dimer on the surface of C60 particle.

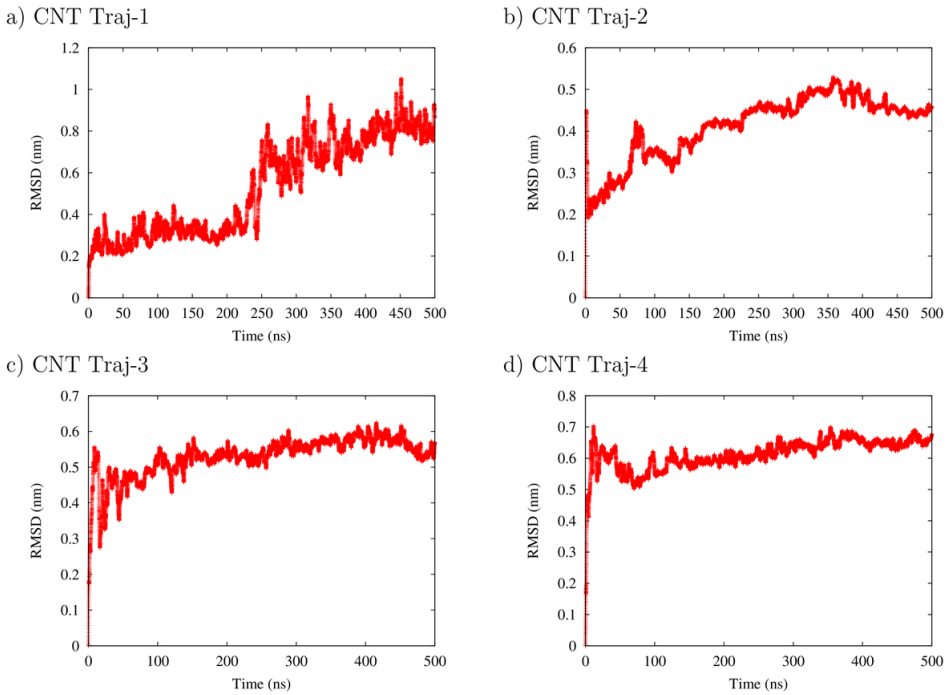

Figure 38: Contact area results for the four trajectories of the apoC-II dimer on the surface of the CNT.

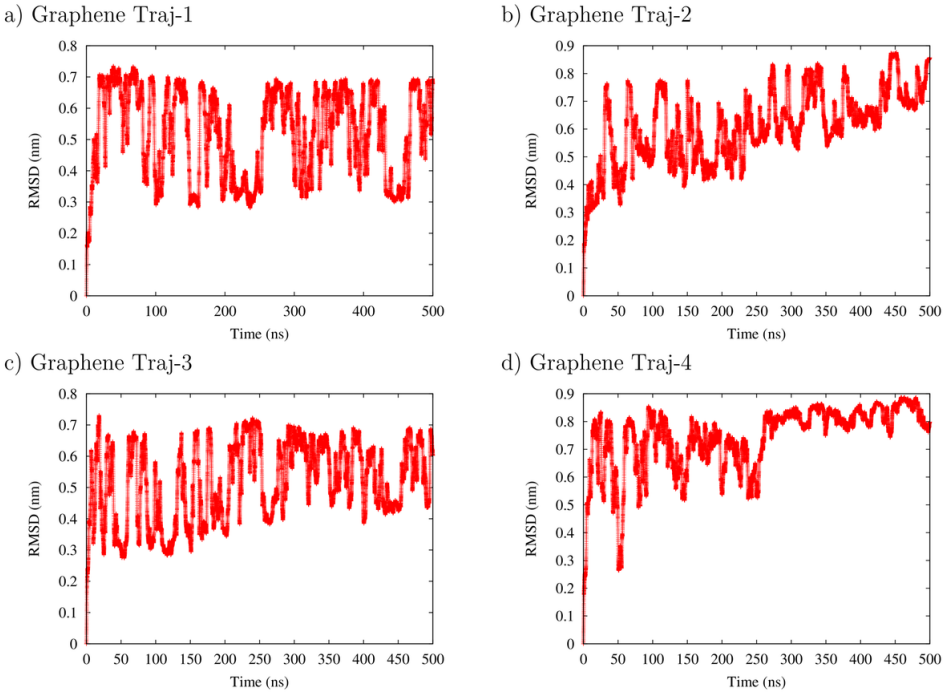

Figure 39: Contact area results for the four trajectories of the apoC-II dimer on the surface of Graphene.

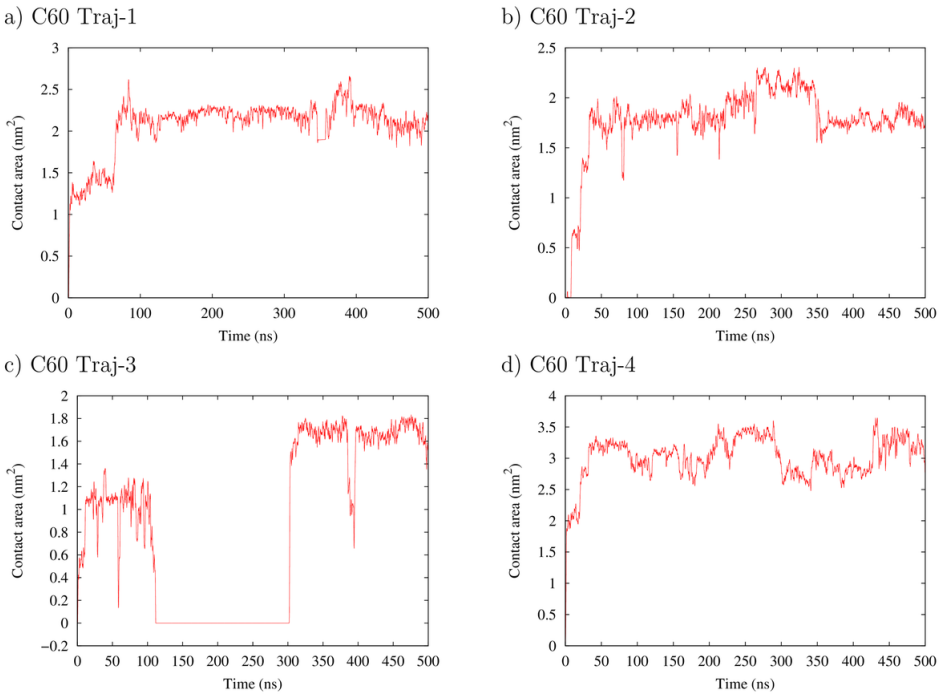

Figure 40: Contact area results for the four trajectories of the apoC-II tetramer on the surface of C60 particle.

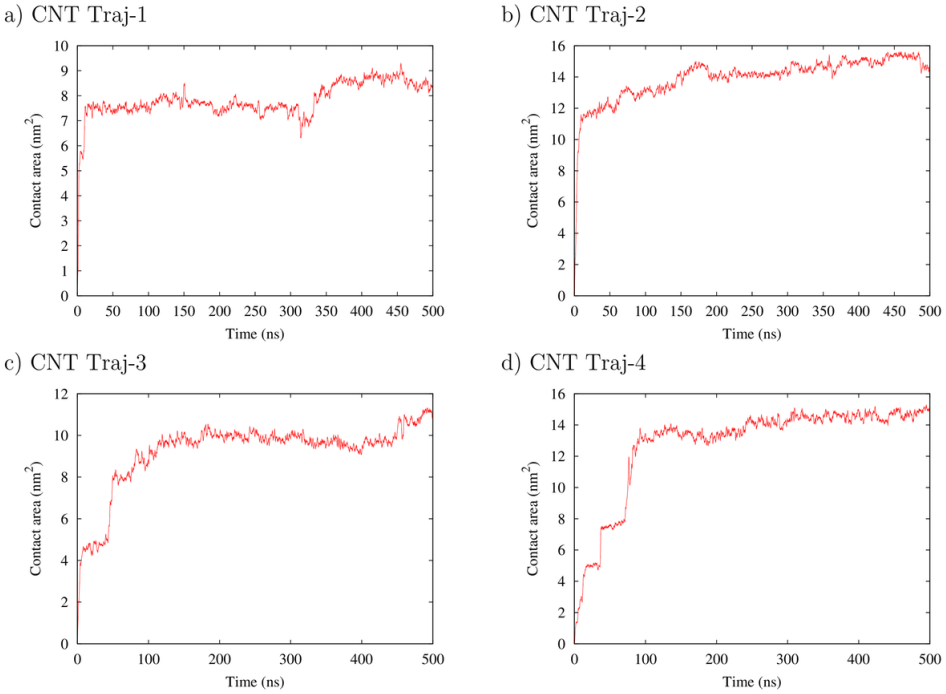

Figure 41: Contact area results for the four trajectories of the apoC-II tetramer on the surface of the CNT.

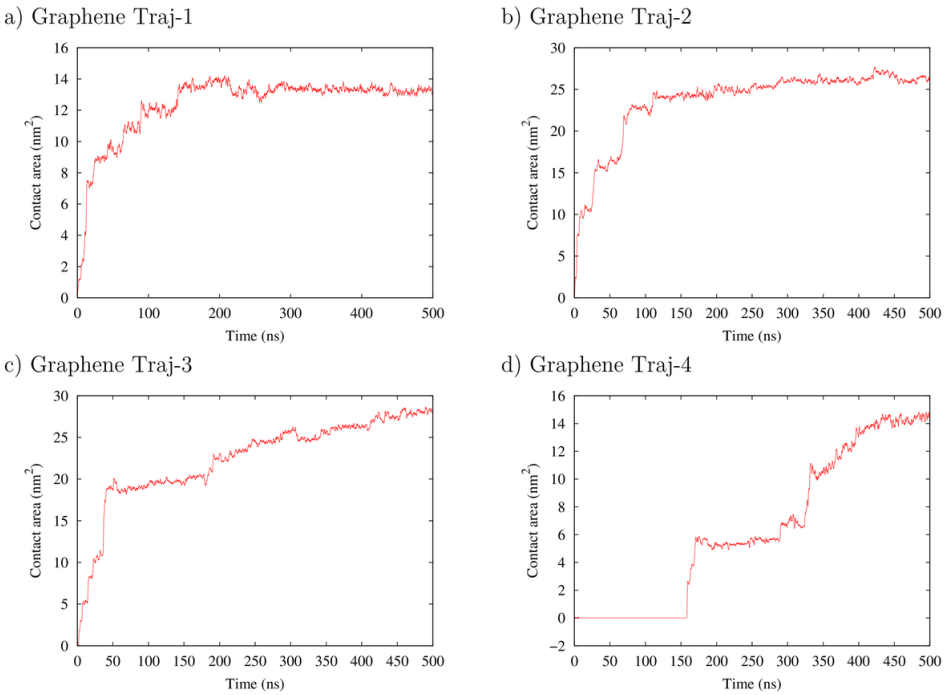

Figure 42: Contact area results for the four trajectories of the apoC-II tetramer on the surface of Graphene.

Bibliography

[1] C. B. Anfinsen. "Principles that Govern the Folding of Protein Chains". In: *Science* 181.4096 (July 20, 1973). PMID: 4124164, pp. 223–230. ISSN: 0036-8075, 1095-9203. DOI: 10.1126/science.181.4096.223.

[2] C. Levinthal. "Are There Pathways For Protein Folding?" In: *Extrait du Journal de Chimie Physique* 65.1 (1968).

[3] C. Levinthal. "How to Fold Graciously". In: Mossbauer Spectroscopy in Biological Systems: Proceedings of a meeting held at Allerton House, Monticello, Illinois. Ed. by J. Debrunnder and E. Munck. University of Illinois Press, 1969, pp. 22–24.

[4] K. Lindorff-Larsen et al. "How fast-folding proteins fold". In: *Science* 334.6055 (2011), pp. 517–520.

[5] R. Virchow. "Zur Cellulose-Frage". In: *Archiv für pathologische Anatomie und Physiologie und für klinische Medicin* 8.1 (Apr. 1, 1855), pp. 140–144. ISSN: 0720-8723, 1432-2307. DOI: 10.1007/BF01935322.

[6] R. Virchow. "Ueber eine im Gehirn und Rückenmark des Menschen aufgefundene Substanz mit der chemischen Reaction der Cellulose". In: *Archiv für pathologische Anatomie und Physiologie und für klinische Medicin* 6.1 (Mar. 1, 1854), pp. 135–138. ISSN: 0720-8723, 1432-2307. DOI: 10.1007/BF01930815.

[7] H. M. v. Hemsbach. *Die Speck-oder Cholestrinkrankheit*. A. W. Schade, 1853. 58 pp.

[8] P. D. N. Friedreich and P. D. A. Kekulé. "Zur Amyloidfrage". In: *Archiv für pathologische Anatomie und Physiologie und für klinische Medicin* 16.1-2 (Jan. 1, 1859), pp. 50–65. ISSN: 0720-8723, 1432-2307. DOI: 10.1007/BF01945246.

[9] H. Bennhold. “Specific staining of amyloid by Congo red”. In: *MuÈnchener Medizinische Wochenschrift* 69 (1922), pp. 1537–1538.

[10] P. Divry and M. Florkin. “Sur les proprietes optiques de l’amyloide”. In: *CR Soc. Biol* 97 (1927), pp. 1808–1810.

[11] H.-P. Missmahl and M. Hartwig. “Polarisationsoptische Untersuchungen an der Amyloidsubstanz”. In: *Virchows Archiv für pathologische Anatomie und Physiologie und für klinische Medizin* 324.4 (July 1, 1953), pp. 489–508. ISSN: 0376-0081, 1432-2307. DOI: 10.1007/BF00954791.

[12] H. Puchtler, F. Sweat, and M. Levine. “On the Binding of Congo Red by Amyloid”. In: *Journal of Histochemistry & Cytochemistry* 10.3 (May 1, 1962), pp. 355–364. ISSN: 0022-1554, 1551-5044. DOI: 10.1177/10.3.355.

[13] G. Legname et al. “Synthetic Mammalian Prions”. In: *Science* 305.5684 (July 30, 2004). PMID: 15286374, pp. 673–676. ISSN: 0036-8075, 1095-9203. DOI: 10.1126/science.1100195.

[14] F. Chiti and C. M. Dobson. “Protein misfolding, functional amyloid, and human disease”. In: *Annu. Rev. Biochem.* 75 (2006), pp. 333–366.

[15] T. P. J. Knowles, M. Vendruscolo, and C. M. Dobson. “The amyloid state and its association with protein misfolding diseases”. In: *Nature Reviews Molecular Cell Biology* 15.6 (June 2014), pp. 384–396. ISSN: 1471-0072. DOI: 10.1038/nrm3810.

[16] A. S. Cohen and E. Calkins. “Electron Microscopic Observations on a Fibrous Component in Amyloid of Diverse Origins”. In: *Nature* 183.4669 (Apr. 25, 1959), pp. 1202–1203. DOI: 10.1038/1831202a0.

[17] R. Caesar. “Die Feinstruktur von Milz und Leber bei experimenteller Amyloidose”. In: *Zeitschrift für Zellforschung und Mikroskopische Anatomie* 52.5 (Sept. 1, 1960), pp. 653–673. ISSN: 0044-3794, 1432-0878. DOI: 10.1007/BF00339852.

[18] L. Fruhling, J. Kempf, and A. Porte. “[Structure and formation of the amyloid substance in experimental amyloidosis in the mouse. Electron microscopic study]”. In: *Comptes Rendus Hebdomadaires Des Séances De l’Académie Des Sciences* 250 (Feb. 15, 1960). PMID: 13825438, pp. 1385–1386. ISSN: 0001-4036.

[19] S. Battaglia. "Electronoptic studies on liver amyloid in mice". In: *Beiträge zur pathologischen Anatomie und zur allgemeinen Pathologie* 126 (1962), p. 300. ISSN: 0366-2446.

[20] A. S. Cohen et al. "A Study of the Fine Structure of the Amyloid Associated with Familial Mediterranean Fever". In: *The American Journal of Pathology* 41.5 (Nov. 1962). PMID: 14022004 PMCID: PMC1949617, pp. 567–578. ISSN: 0002-9440.

[21] W. A. Heefner and G. D. Sorenson. "Experimental amyloidosis. I. Light and electron microscopic observation of spleen and lymph nodes". In: *Laboratory Investigation; a Journal of Technical Methods and Pathology* 11 (Aug. 1962). PMID: 13905899, pp. 585–593. ISSN: 0023-6837.

[22] T. Lührs et al. "3D structure of Alzheimer's amyloid-β(1–42) fibrils". In: *Proceedings of the National Academy of Sciences of the United States of America* 102.48 (Nov. 29, 2005). PMID: 16293696, pp. 17342–17347. ISSN: 0027-8424, 1091-6490. DOI: 10.1073/pnas.0506723102.

[23] H. Van Melckebeke et al. "Atomic-Resolution Three-Dimensional Structure of HET-s(218289) Amyloid Fibrils by Solid-State NMR Spectroscopy". In: *Journal of the American Chemical Society* 132.39 (Oct. 6, 2010), pp. 13765–13775. ISSN: 0002-7863. DOI: 10.1021/ja104213j.

[24] G. Comellas and C. M. Rienstra. "Protein Structure Determination by Magic-Angle Spinning Solid-State NMR, and Insights into the Formation, Structure, and Stability of Amyloid Fibrils". In: *Annual Review of Biophysics* 42.1 (2013). PMID: 23527778, pp. 515–536. DOI: 10.1146/annurev-biophys-083012-130356.

[25] A. W. P. Fitzpatrick et al. "Atomic structure and hierarchical assembly of a cross-β amyloid fibril". In: *Proceedings of the National Academy of Sciences* 110.14 (Apr. 2, 2013). PMID: 23513222, pp. 5468–5473. ISSN: 0027-8424, 1091-6490. DOI: 10.1073/pnas.1219476110.

[26] S. I. A. Cohen et al. "From Macroscopic Measurements to Microscopic Mechanisms of Protein Aggregation". In: *Journal of Molecular Biology.* Amyloid Structure, Function, and Molecular Mechanisms (Part I) 421.2–3 (Aug. 10, 2012), pp. 160–171. ISSN: 0022-2836. DOI: 10.1016/j.jmb.2012.02.031.

[27] S. I. A. Cohen et al. “Proliferation of amyloid-β42 aggregates occurs through a secondary nucleation mechanism”. In: *Proceedings of the National Academy of Sciences* 110.24 (June 11, 2013). PMID: 23703910, pp. 9758–9763. ISSN: 0027-8424, 1091-6490. DOI: 10.1073/pnas.1218402110.

[28] T. P. J. Knowles et al. “An Analytical Solution to the Kinetics of Breakable Filament Assembly”. In: *Science* 326.5959 (Dec. 11, 2009). PMID: 20007899, pp. 1533–1537. ISSN: 0036-8075, 1095-9203. DOI: 10.1126/science.1178250.

[29] A. Lomakin et al. “Kinetic theory of fibrillogenesis of amyloid β-protein”. In: *Proceedings of the National Academy of Sciences* 94.15 (July 22, 1997). PMID: 9223292, pp. 7942–7947. ISSN: 0027-8424, 1091-6490.

[30] N. Fay et al. “Assembly of the Yeast Prion Ure2p into Protein Fibrils THERMODYNAMIC AND KINETIC CHARACTERIZATION”. In: *Journal of Biological Chemistry* 278.32 (Aug. 8, 2003). PMID: 12777380, pp. 30199–30205. ISSN: 0021-9258, 1083-351X. DOI: 10.1074/jbc.M303000200.

[31] T. R. Serio et al. “Nucleated Conformational Conversion and the Replication of Conformational Information by a Prion Determinant”. In: *Science* 289.5483 (Aug. 25, 2000). PMID: 10958771, pp. 1317–1321. ISSN: 0036-8075, 1095-9203. DOI: 10.1126/science.289.5483.1317.

[32] D. M. Walsh and D. J. Selkoe. “Aβ Oligomers – a decade of discovery”. In: *Journal of Neurochemistry* 101.5 (2007), pp. 1172–1184. ISSN: 1471-4159. DOI: 10.1111/j.1471-4159.2006.04426.x.

[33] M. Jucker and L. C. Walker. “Pathogenic protein seeding in alzheimer disease and other neurodegenerative disorders”. In: *Annals of Neurology* 70.4 (2011), pp. 532–540. ISSN: 1531-8249. DOI: 10.1002/ana.22615.

[34] S. Meehan et al. “Characterisation of Amyloid Fibril Formation by Small Heat-shock Chaperone Proteins Human αA-, αB- and R120G αB-Crystallins”. In: *Journal of Molecular Biology* 372.2 (Sept. 14, 2007), pp. 470–484. ISSN: 0022-2836. DOI: 10.1016/j.jmb.2007.06.060.

[35] J. Juárez, P. Taboada, and V. Mosquera. "Existence of Different Structural Intermediates on the Fibrillation Pathway of Human Serum Albumin". In: *Biophysical Journal* 96.6 (Mar. 18, 2009), pp. 2353–2370. ISSN: 0006-3495. DOI: 10.1016/j.bpj.2008.12.3901.

[36] S. Yang et al. "An Equilibrium Model for Linear and Closed-Loop Amyloid Fibril Formation". In: *Journal of Molecular Biology*. Amyloid Structure, Function, and Molecular Mechanisms (Part I) 421.2–3 (Aug. 10, 2012), pp. 364–377. ISSN: 0022-2836. DOI: 10.1016/j.jmb.2012.02.026.

[37] M. J. Cannon et al. "Kinetic analysis of $\beta-amyloidfibrilelongation$". In: *Analytical Biochemistry* 328.1 (May 1, 2004), pp. 67–75. ISSN: 0003-2697. DOI: 10.1016/j.ab.2004.01.014.

[38] W. P. Esler et al. "Alzheimer's Disease Amyloid Propagation by a Template-Dependent Dock-Lock Mechanism†". In: *Biochemistry* 39.21 (2000), pp. 6288–6295. ISSN: 0006-2960. DOI: 10.1021/bi992933h.

[39] F. Massi and J. E. Straub. "Energy landscape theory for Alzheimer's amyloid β-peptide fibril elongation". In: *Proteins: Structure, Function, and Bioinformatics* 42.2 (2001), pp. 217–229. ISSN: 1097-0134. DOI: 10.1002/1097-0134(20010201)42:2<217::AID-PROT90>3.0.CO;2-N.

[40] P. H. Nguyen et al. "Monomer adds to preformed structured oligomers of Aβ-peptides by a two-stage dock–lock mechanism". In: *Proceedings of the National Academy of Sciences* 104.1 (Jan. 2, 2007). PMID: 17190811, pp. 111–116. ISSN: 0027-8424, 1091-6490. DOI: 10.1073/pnas.0607440104.

[41] C. B. Andersen et al. "Branching in Amyloid Fibril Growth". In: *Biophysical Journal* 96.4 (Feb. 18, 2009), pp. 1529–1536. ISSN: 0006-3495. DOI: 10.1016/j.bpj.2008.11.024.

[42] R. E. Samuel, E. D. Salmon, and R. W. Briehl. "Nucleation and growth of fibres and gel formation in sickle cell haemoglobin". In: *Nature* 345.6278 (June 28, 1990), pp. 833–835. DOI: 10.1038/345833a0.

[43] J. D. Harper et al. “Observation of metastable Aβ amyloid protofibrils by atomic force microscopy”. In: *Chemistry & Biology* 4.2 (1997), pp. 119–125. ISSN: 1074-5521. DOI: 10.1016/S1074-5521(97)90255-6.

[44] W.-F. Xue et al. “Fibril Fragmentation Enhances Amyloid Cytotoxicity”. In: *Journal of Biological Chemistry* 284.49 (Dec. 4, 2009). PMID: 19808677, pp. 34272–34282. ISSN: 0021-9258, 1083-351X. DOI: 10.1074/jbc.M109.049809.

[45] S. R. Collins et al. “Mechanism of Prion Propagation: Amyloid Growth Occurs by Monomer Addition”. In: *PLoS Biol* 2.10 (Sept. 21, 2004), e321. DOI: 10.1371/journal.pbio.0020321.

[46] C. Haass and D. J. Selkoe. “Soluble protein oligomers in neurodegeneration: lessons from the Alzheimer’s amyloid β-peptide”. In: *Nature Reviews Molecular Cell Biology* 8.2 (Feb. 2007), pp. 101–112. ISSN: 1471-0072. DOI: 10.1038/nrm2101.

[47] D. Eisenberg and M. Jucker. “The Amyloid State of Proteins in Human Diseases”. In: *Cell* 148.6 (Mar. 16, 2012), pp. 1188–1203. ISSN: 0092-8674. DOI: 10.1016/j.cell.2012.02.022.

[48] D. M. Walsh et al. “Naturally secreted oligomers of amyloid β protein potently inhibit hippocampal long-term potentiation in vivo”. In: *Nature* 416.6880 (Apr. 4, 2002), pp. 535–539. ISSN: 0028-0836. DOI: 10.1038/416535a.

[49] S. Campioni et al. “A causative link between the structure of aberrant protein oligomers and their toxicity”. In: *Nature Chemical Biology* 6.2 (Feb. 2010), pp. 140–147. ISSN: 1552-4450. DOI: 10.1038/nchembio.283.

[50] S. Baglioni et al. “Prefibrillar Amyloid Aggregates Could Be Generic Toxins in Higher Organisms”. In: *The Journal of Neuroscience* 26.31 (Aug. 2, 2006). PMID: 16885229, pp. 8160–8167. ISSN: 0270-6474, 1529-2401. DOI: 10.1523/JNEUROSCI.4809-05.2006.

[51] R. Mout et al. “Surface functionalization of nanoparticles for nanomedicine”. In: *Chemical Society Reviews* 41.7 (2012), p. 2539. ISSN: 0306-0012, 1460-4744. DOI: 10.1039/c2cs15294k.

[52] U. A. Gunasekera, Q. A. Pankhurst, and M. Douek. "Imaging applications of nanotechnology in cancer". In: *Targeted Oncology* 4.3 (Sept. 2009), pp. 169–181. ISSN: 1776-2596. DOI: 10.1007/s11523-009-0118-9.

[53] H. Houili, E. Tutis, and R. Izquierdo. "Modeling nanoparticle embedded organic memory devices". In: *Organic Electronics* 11.4 (Apr. 2010), pp. 514–520. ISSN: 1566-1199. DOI: 10.1016/j.orgel.2009.12.006.

[54] J. Lee, S. Mahendra, and P. J. J. Alvarez. "Nanomaterials in the Construction Industry: A Review of Their Applications and Environmental Health and Safety Considerations". In: *ACS Nano* 4.7 (July 27, 2010), pp. 3580–3590. ISSN: 1936-0851, 1936-086X. DOI: 10.1021/nn100866w.

[55] A. M. A. Elhissi et al. "Carbon Nanotubes in Cancer Therapy and Drug Delivery". In: *Journal of Drug Delivery* 2012 (2012), pp. 1–10. ISSN: 2090-3014, 2090-3022. DOI: 10.1155/2012/837327.

[56] K.-M. Kim et al. "Inorganic Nanomedicines and their Labeling for Biological Imaging". In: *Current Topics in Medicinal Chemistry* 13.4 (Feb. 1, 2013), pp. 488–503.

[57] K. Feris et al. "Electrostatic Interactions Affect Nanoparticle-Mediated Toxicity to Gram-Negative Bacterium Pseudomonas aeruginosa PAO1". In: *Langmuir* 26.6 (Mar. 16, 2010), pp. 4429–4436. ISSN: 0743-7463. DOI: 10.1021/La903491z.

[58] C. Hanley et al. "Preferential killing of cancer cells and activated human T cells using ZnO nanoparticles". In: *Nanotechnology* 19 (July 23, 2008). 29, pages. ISSN: 0957-4484. DOI: 10.1088/0957-4484/19/29/295103.

[59] M. I. Setyawati et al. "The influence of lysosomal stability of silver nanomaterials on their toxicity to human cells". In: *Biomaterials* 35.25 (Aug. 2014), pp. 6707–6715. ISSN: 0142-9612. DOI: 10.1016/j.biomaterials.2014.05.007.

[60] S. Sharifi et al. "Toxicity of nanomaterials". In: *Chemical Society Reviews* 41.6 (2012), p. 2323. ISSN: 0306-0012, 1460-4744. DOI: 10.1039/c1cs15188f.

[61] M. M. Khin et al. "A review on nanomaterials for environmental remediation". In: *Energy & Environmental Science* 5.8 (2012), p. 8075. ISSN: 1754-5692, 1754-5706. DOI: 10.1039/c2ee21818f.

[62] V. J. Morris. “Emerging roles of engineered nanomaterials in the food industry”. In: *Trends in Biotechnology* 29.10 (Oct. 2011), pp. 509–516. ISSN: 0167-7799. DOI: 10.1016/j.tibtech.2011.04.010.

[63] R. Singh and H. S. Nalwa. “Medical Applications of Nanoparticles in Biological Imaging, Cell Labeling, Antimicrobial Agents, and Anticancer Nanodrugs”. In: *Journal of Biomedical Nanotechnology* 7.4 (Aug. 1, 2011), pp. 489–503. DOI: 10.1166/jbn.2011.1324.

[64] P. Burcham. “Nanotoxicology: A primer for chemists”. In: *Chemistry in Australia* 77 (Sept. 2010). 8, pp. 18–22.

[65] H. Andresen et al. “Single-Step Homogeneous Immunoassays Utilizing Epitope-Tagged Gold Nanoparticles: On the Mechanism, Feasibility, and Limitations”. In: *Chemistry of Materials* 26.16 (2014), pp. 4696–4704. ISSN: 0897-4756. DOI: 10.1021/cm500535p.

[66] L. Zhang et al. “Development of Nanoparticles for Antimicrobial Drug Delivery”. In: *Current Medicinal Chemistry* 17.6 (Feb. 2010), pp. 585–594. ISSN: 0929-8673.

[67] H. C. Fischer and W. C. W. Chan. “Nanotoxicity: the growing need for in vivo study”. In: *Current Opinion in Biotechnology* 18.6 (Dec. 2007), pp. 565–571. ISSN: 0958-1669. DOI: 10.1016/j.copbio.2007.11.008.

[68] J. Klein. “Probing the interactions of proteins and nanoparticles”. In: *Proceedings of the National Academy of Sciences of the United States of America* 104.7 (Feb. 13, 2007), pp. 2029–2030. ISSN: 0027-8424. DOI: 10.1073/pnas.0611610104.

[69] N. Lewinski, V. Colvin, and R. Drezek. “Cytotoxicity of Nanoparticles”. In: *Small* 4.1 (Jan. 18, 2008), pp. 26–49. ISSN: 1613-6829. DOI: 10.1002/smll.200700595.

[70] N. L. Mills et al. “Diesel exhaust inhalation causes vascular dysfunction and impaired endogenous fibrinolysis”. In: *Circulation* 112.25 (Dec. 20, 2005), pp. 3930–6. ISSN: 1524-4539 (Electronic) 0009-7322 (Linking). DOI: 10.1161/CIRCULATIONAHA.105.588962.

[71] M. Geiser et al. “Ultrafine particles cross cellular membranes by nonphagocytic mechanisms in lungs and in cultured cells”. In: *Environ Health Perspect* 113.11 (Nov. 2005), pp. 1555–60. ISSN: 0091-6765 (Print) 0091-6765 (Linking).

[72] A. Nel et al. “Toxic potential of materials at the nanolevel”. In: *Science* 311.5761 (Feb. 3, 2006), pp. 622–627. ISSN: 0036-8075. DOI: 10.1126/science.1114397.

[73] S. Linse et al. “Nucleation of protein fibrillation by nanoparticles”. In: *Proceedings of the National Academy of Sciences of the United States of America* 104 (2007), pp. 8691–8696.

[74] C. I. Chang et al. “Adsorption mechanism of water molecules surrounding Au nanoparticles of different sizes”. In: *Journal of Chemical Physics* 128.15 (Apr. 21, 2008), pages. ISSN: 0021-9606. DOI: 10.1063/1.2897931.

[75] R. O. Dror et al. “Exploring atomic resolution physiology on a femtosecond to millisecond timescale using molecular dynamics simulations”. In: *The Journal of general physiology* 135.6 (2010), pp. 555–562.

[76] T. Roman et al. “Amino acid adsorption on single-walled carbon nanotubes”. In: *European Physical Journal D* 38.1 (Apr. 2006), pp. 117–120. ISSN: 1434-6060. DOI: 10.1140/epjd/e2006-00043-1.

[77] A. R. Leach. *Molecular Modelling: Principles and Applications*. Second Edition. Harlow, England: Pearson Education Limited, 2001.

[78] F. Carlsson et al. “Lysozyme adsorption to charged surfaces. A Monte Carlo study”. In: *Journal of Physical Chemistry B* 108.28 (July 15, 2004), pp. 9871–9881. ISSN: 1520-6106. DOI: 10.1021/Jp0495186.

[79] Q. X. Pei et al. “Molecular dynamics study on DNA oligonucleotide translocation through carbon nanotubes”. In: *Journal of Chemical Physics* 129.12 (Sept. 28, 2008), pages. ISSN: 0021-9606. DOI: 10.1063/1.2981798.

[80] H. Hwang, G. C. Schatz, and M. A. Ratner. “Coarse-Grained Molecular Dynamics Study of Cyclic Peptide Nanotube Insertion into a Lipid Bilayer”. In: *Journal of Physical Chemistry A* 113.16 (Apr. 23, 2009), pp. 4780–4787. ISSN: 1089-5639. DOI: 10.1021/Jp8080657.

[81] N. Todorova et al. “Systematic comparison of empirical forcefields for molecular dynamic simulation of insulin”. In: *The Journal of Physical Chemistry B* 112.35 (2008), pp. 11137–11146.

[82] P. Bjelkmar et al. “Conformational Changes and Slow Dynamics through Microsecond Polarized Atomistic Molecular Simulation of an Integral Kv1.2 Ion Channel”. In: *Plos Computational Biology* 5.2 (Feb. 2009), pages. ISSN: 1553-734X. DOI: 10.1371/journal.pcbi.1000289.

[83] J. Wong-Ekkabut et al. “Computer simulation study of fullerene translocation through lipid membranes”. In: *Nature Nanotechnology* 3.6 (June 2008), pp. 363–368. ISSN: 1748-3387. DOI: 10.1038/nnano.2008.130.

[84] X. H. Shi, Y. Kong, and H. J. Gao. “Coarse grained molecular dynamics and theoretical studies of carbon nanotubes entering cell membrane”. In: *Acta Mechanica Sinica* 24.2 (Apr. 2008), pp. 161–169. ISSN: 0567-7718. DOI: 10.1007/s10409-007-0131-0.

[85] E. J. Wallace and M. S. P. Sansom. “Blocking of carbon nanotube based nanoinjectors by lipids: A simulation study”. In: *Nano Letters* 8.9 (Sept. 2008), pp. 2751–2756. ISSN: 1530-6984. DOI: 10.1021/Nl801217f.

[86] S. J. Marrink et al. “The MARTINI force field: Coarse grained model for biomolecular simulations”. In: *Journal of Physical Chemistry B* 111.27 (July 12, 2007), pp. 7812–7824. ISSN: 1520-6106. DOI: 10.1021/Jp071097f.

[87] C. C. Chiu et al. “Size-dependent hydrophobic to hydrophilic transition for nanoparticles: A molecular dynamics study”. In: *Journal of Chemical Physics* 131.24 (Dec. 28, 2009), pages. ISSN: 0021-9606. DOI: 10.1063/1.3276915.

[88] J. J. Kuna et al. “The effect of nanometre-scale structure on interfacial energy”. In: *Nature Materials* 8.10 (Oct. 2009), pp. 837–842. ISSN: 1476-1122. DOI: 10.1038/Nmat2534.

[89] X. Zhao, A. Striolo, and P. T. Cummings. “C60 binds to and deforms nucleotides”. In: *Biophysical Journal* 89.6 (Dec. 2005), pp. 3856–62. ISSN: 0006-3495 (Print) 0006-3495 (Linking). DOI: 10.1529/biophysj.105.064410.

[90] H. J. Gao et al. “Spontaneous insertion of DNA oligonucleotides into carbon nanotubes”. In: *Nano Letters* 3.4 (Apr. 2003), pp. 471–473. ISSN: 1530-6984. DOI: 10.1021/Nl025967a.

[91] R. R. Johnson, A. T. Johnson, and M. L. Klein. “Probing the structure of DNA-carbon nanotube hybrids with molecular dynamics”. In: *Nano Letters* 8.1 (Jan. 2008), pp. 69–75. ISSN: 1530-6984 (Print) 1530-6984 (Linking). DOI: 10.1021/nl071909j.

[92] G. Lu, P. Maragakis, and E. Kaxiras. “Carbon nanotube interaction with DNA”. In: *Nano Letters* 5.5 (May 2005), pp. 897–900. ISSN: 1530-6984. DOI: 10.1021/Nl050354u.

[93] W. H. Noon, Y. F. Kong, and J. P. Ma. “Molecular dynamics analysis of a buckyball-antibody complex”. In: *Proceedings of the National Academy of Sciences of the United States of America* 99 (Apr. 30, 2002), pp. 6466–6470. ISSN: 0027-8424. DOI: 10.1073/pnas.022532599.

[94] C. C. Chiu, G. R. Dieckmann, and S. O. Nielsen. “Molecular Dynamics Study of a Nanotube-Binding Amphiphilic Helical Peptide at Different Water/Hydrophobic Interfaces”. In: *Journal of Physical Chemistry B* 112.51 (Dec. 25, 2008), pp. 16326–16333. ISSN: 1520-6106. DOI: 10.1021/Jp805313p.

[95] A. Kyani and B. Goliaei. “Binding free energy calculation of peptides to carbon nanotubes using molecular dynamics with a linear interaction energy approach”. In: *Journal of Molecular Structure-Theochem* 913.1-3 (Nov. 15, 2009), pp. 63–69. ISSN: 0166-1280. DOI: 10.1016/j.theochem.2009.07.018.

[96] L. W. Li et al. “A molecular dynamics simulation study of C-60 fullerenes inside a dimyristoylphosphatidylcholine lipid bilayer”. In: *Journal of Physical Chemistry B* 111.16 (Apr. 26, 2007), pp. 4067–4072. ISSN: 1520-6106. DOI: 10.1021/Jp064982r.

[97] D. Bedrov et al. “Passive transport of C-60 fullerenes through a lipid membrane: A molecular dynamics simulation study”. In: *Journal of Physical Chemistry B* 112.7 (Feb. 21, 2008), pp. 2078–2084. ISSN: 1520-6106. DOI: 10.1021/Jp075149c.

[98] R. Qiao et al. “Translocation of C-60 and its derivatives across a lipid bilayer”. In: *Nano Letters* 7.3 (Mar. 2007), pp. 614–619. ISSN: 1530-6984. DOI: 10.1021/Nl062515f.

[99] L. W. Li, D. Bedrov, and G. D. Smith. “Water-induced interactions between carbon nanoparticles”. In: *Journal of Physical Chemistry B* 110.21 (June 1, 2006), pp. 10509–10513. ISSN: 1520-6106. DOI: 10.1021/Jp060718m.

[100] D. R. Weiss, T. M. Raschke, and M. Levitt. “How hydrophobic Buckminsterfullerene affects surrounding water structure”. In: *Journal of Physical Chemistry B* 112.10 (Mar. 13, 2008), pp. 2981–2990. ISSN: 1520-6106. DOI: 10.1021/Jp076416h.

[101] G. Yiapanis et al. “Effect of surface composition and atomic roughness on interfacial adhesion between polyester and amorphous carbon”. In: *The Journal of Physical Chemistry C* 111.7 (2007), pp. 3000–3009.

[102] A. Verma and F. Stellacci. “Effect of Surface Properties on Nanoparticle-Cell Interactions”. In: *Small* 6.1 (Jan. 4, 2010), pp. 12–21. ISSN: 1613-6810. DOI: 10.1002/smll.200901158.

[103] G. D. Smith and D. Bedrov. “Transport of C-60 fullerenes through a lipid membrane: A molecular dynamics simulation study”. In: *Biophysical Journal* (Jan. 2007), 65a–66a. ISSN: 0006-3495.

[104] P. K. Ghorai and S. C. Glotzer. “Molecular dynamics simulation study of self-assembled monolayers of alkanethiol surfactants on spherical gold nanoparticles”. In: *Journal of Physical Chemistry C* 111.43 (Nov. 1, 2007), pp. 15857–15862. ISSN: 1932-7447. DOI: 10.1021/Jp0746289.

[105] V. Mailander and K. Landfester. “Interaction of Nanoparticles with Cells”. In: *Biomacromolecules* 10.9 (Sept. 2009), pp. 2379–2400. ISSN: 1525-7797. DOI: 10.1021/Bm900266r.

[106] W. T. Zhao, L. Lin, and I. M. Hsing. “Rapid Synthesis of DNA-Functionalized Gold Nanoparticles in Salt Solution Using Mononucleotide-Mediated Conjugation”. In: *Bioconjugate Chemistry* 20.6 (June 2009), pp. 1218–1222. ISSN: 1043-1802. DOI: 10.1021/Bc900080p.

[107] M. E. Aubin-Tam, W. Hwang, and K. Hamad-Schifferli. "Site-directed nanoparticle labeling of cytochrome c". In: *Proceedings of the National Academy of Sciences of the United States of America* 106.11 (Mar. 17, 2009), pp. 4095–4100. ISSN: 0027-8424. DOI: 10.1073/pnas.0807299106.

[108] C. Peetla, K. S. Rao, and V. Labhasetwar. "Relevance of Biophysical Interactions of Nanoparticles with a Model Membrane in Predicting Cellular Uptake: Study with TAT Peptide-Conjugated Nanoparticles". In: *Molecular Pharmaceutics* 6.5 (Sept. 2009), pp. 1311–1320. ISSN: 1543-8384. DOI: 10.1021/Mp900011h.

[109] L. Monticelli et al. "Effects of carbon nanoparticles on lipid membranes: a molecular simulation perspective". In: *Soft Matter* 5.22 (2009), pp. 4433–4445. ISSN: 1744-683X. DOI: 10.1039/B912310e.

[110] W. R. Yang et al. "Carbon nanotubes for biological and biomedical applications". In: *Nanotechnology* 18.41 (Oct. 17, 2007), pages. ISSN: 0957-4484. DOI: 10.1088/0957-4484/18/41/412001.

[111] R. S. D'Rozario et al. "The interaction of C60 and its derivatives with a lipid bilayer via molecular dynamics simulations". In: *Nanotechnology* 20.11 (Mar. 18, 2009), p. 115102. ISSN: 1361-6528 (Electronic). DOI: 10.1088/0957-4484/20/11/115102.

[112] V. V. Ginzburg and S. Balijepailli. "Modeling the thermodynamics of the interaction of nanoparticles with cell membranes". In: *Nano Letters* 7.12 (Dec. 2007), pp. 3716–3722. ISSN: 1530-6984. DOI: 10.1021/Nl0720531.

[113] E. J. Wallace and M. S. P. Sansom. "Carbon nanotube self-assembly with lipids and detergent: a molecular dynamics study". In: *Nanotechnology* 20.4 (Jan. 28, 2009), pages. ISSN: 0957-4484. DOI: 10.1088/0957-4484/20/4/045101.

[114] E. J. Wallace and M. S. P. Sansom. "Carbon nanotube/detergent interactions via coarse-grained molecular dynamics". In: *Nano Letters* 7.7 (July 2007), pp. 1923–1928. ISSN: 1530-6984. DOI: 10.1021/Nl070602h.

[115] S. Choe et al. "Molecular Dynamics Simulation Study of a Pulmonary Surfactant Film Interacting with a Carbonaceous Nanoparticle". In: *Biophysical Journal* 95.9

(Nov. 1, 2008), pp. 4102–4114. ISSN: 0006-3495. DOI: 10.1529/biophysj.107.123976.

[116] Y. Li, X. Chen, and N. Gu. "Computational Investigation of Interaction between Nanoparticles and Membranes: Hydrophobic/Hydrophilic Effect". In: *Journal of Physical Chemistry B* 112.51 (Dec. 25, 2008), pp. 16647–16653. ISSN: 1520-6106. DOI: 10.1021/Jp8051906.

[117] Y. Li and N. Gu. "Thermodynamics of Charged Nanoparticle Adsorption on Charge-Neutral Membranes: A Simulation Study". In: *Journal of Physical Chemistry B* 114.8 (Mar. 4, 2010), pp. 2749–2754. ISSN: 1520-6106. DOI: 10.1021/Jp904550b.

[118] J. N. Sachs and T. B. Woolf. "Understanding the Hofmeister effect in interactions between chaotropic anions and lipid bilayers: Molecular dynamics simulations". In: *Journal of the American Chemical Society* 125.29 (July 23, 2003), pp. 8742–8743. ISSN: 0002-7863. DOI: 10.1021/Ja0355729.

[119] F. Rueckerl, J. A. Kaes, and C. Selle. "Diffusion of nanoparticles in monolayers is modulated by domain size". In: *Langmuir* 24.7 (Apr. 1, 2008), pp. 3365–3369. ISSN: 0743-7463. DOI: 10.1021/La703140b.

[120] K. Yang and Y. Q. Ma. "Computer simulation of the translocation of nanoparticles with different shapes across a lipid bilayer". In: *Nature Nanotechnology* 5.8 (Aug. 2010), pp. 579–83. ISSN: 1748-3395 (Electronic) 1748-3387 (Linking). DOI: 10.1038/nnano.2010.141.

[121] A. Alexeev, W. E. Uspal, and A. C. Balazs. "Harnessing Janus nanoparticles to create controllable pores in membranes". In: *Acs Nano* 2.6 (June 2008), pp. 1117–1122. ISSN: 1936-0851. DOI: 10.1021/Nn8000998.

[122] J. Lin et al. "Penetration of lipid membranes by gold nanoparticles: insights into cellular uptake, cytotoxicity, and their relationship". In: *Acs Nano* 4.9 (Sept. 28, 2010), pp. 5421–9. ISSN: 1936-086X (Electronic) 1936-0851 (Linking). DOI: 10.1021/nn1010792.

[123] A. V. Titov, P. Kral, and R. Pearson. "Sandwiched graphene–membrane superstructures". In: *Acs Nano* 4.1 (Jan. 26, 2010), pp. 229–34. ISSN: 1936-086X (Electronic) 1936-0851 (Linking). DOI: 10.1021/nn9015778.

[124] H. W. Wang et al. "Molecular Dynamics Study of Dipalmitoylphosphatidylcholine Lipid Layer Self-Assembly onto a Single-Walled Carbon Nanotube". In: *Nano Research* 2.12 (Dec. 2009), pp. 945–954. ISSN: 1998-0124. DOI: 10.1007/s12274-009-9097-5.

[125] W. H. De Jong and P. J. A. Borm. "Drug delivery and nanoparticles: Applications and hazards". In: *International Journal of Nanomedicine* 3.2 (2008), pp. 133–149. ISSN: 1176-9114.

[126] Y. H. Xie et al. "Electric field-induced translocation of single-stranded DNA through a polarized carbon nanotube membrane". In: *Journal of Chemical Physics* 127.22 (Dec. 14, 2007), pages. ISSN: 0021-9606. DOI: 10.1063/1.2799989.

[127] R. R. Johnson et al. "Free Energy Landscape of a DNA-Carbon Nanotube Hybrid Using Replica Exchange Molecular Dynamics". In: *Nano Letters* 9.2 (Feb. 2009), pp. 537–541. ISSN: 1530-6984. DOI: 10.1021/Nl802645d.

[128] W. Martin, W. Zhu, and G. Krilov. "Simulation Study of Noncovalent Hybridization of Carbon Nanotubes by Single-Stranded DNA in Water". In: *Journal of Physical Chemistry B* (Aug. 19, 2008). ISSN: 1520-5207 (Electronic) 1520-5207 (Linking). DOI: 10.1021/jp8040567.

[129] D. J. Duggan et al. "Expression profiling using cDNA microarrays". In: *Nature Genetics* 21.1 Suppl (Jan. 1999), pp. 10–4. ISSN: 1061-4036 (Print) 1061-4036 (Linking). DOI: 10.1038/4434.

[130] C. S. Shan et al. "Direct Electrochemistry of Glucose Oxidase and Biosensing for Glucose Based on Graphene". In: *Analytical Chemistry* 81.6 (Mar. 15, 2009), pp. 2378–2382. ISSN: 0003-2700. DOI: 10.1021/Ac802193c.

[131] O. S. Lee and G. C. Schatz. "Interaction between DNAs on a Gold Surface". In: *Journal of Physical Chemistry C* 113.36 (Sept. 10, 2009), pp. 15941–15947. ISSN: 1932-7447. DOI: 10.1021/Jp905469q.

[132] I. Yarovsky, M. L. Aguilar, and M. T. W. Hearn. "Influence of the Chain-Length and Surface-Density on the Conformation and Mobility of N-Alkyl Ligands Chemically Immobilized onto a Silica Surface". In: *Analytical Chemistry* 67.13 (July 1, 1995), pp. 2145–2153. ISSN: 0003-2700.

[133] K. Kubiak and P. A. Mulheran. "Molecular Dynamics Simulations of Hen Egg White Lysozyme Adsorption at a Charged Solid Surface". In: *Journal of Physical Chemistry B* 113.36 (Sept. 10, 2009), pp. 12189–12200. ISSN: 1520-6106. DOI: 10.1021/Jp901521x.

[134] D. Pellenc et al. "New insights on growth mechanisms of protein clusters at surfaces: an AFM and simulation study". In: *Langmuir* 24.17 (Sept. 2, 2008), pp. 9648–9655. ISSN: 0743-7463. DOI: 10.1021/La801246k.

[135] Y. Ohno et al. "Electrolyte-Gated Graphene Field-Effect Transistors for Detecting pH Protein Adsorption". In: *Nano Letters* 9.9 (Sept. 2009), pp. 3318–3322. ISSN: 1530-6984. DOI: 10.1021/Nl901596m.

[136] A. J. Patil et al. "Aqueous Stabilization and Self-Assembly of Graphene Sheets into Layered Bio-Nanocomposites using DNA". In: *Advanced Materials* 21.31 (Aug. 21, 2009), pp. 3159–+. ISSN: 0935-9648. DOI: 10.1002/adma.200803633.

[137] L. J. Liang et al. "Molecular Dynamics Simulation on Stability of Insulin on Graphene". In: *Chinese Journal of Chemical Physics* 22.6 (Dec. 27, 2009), pp. 627–634. ISSN: 1674-0068. DOI: 10.1088/1674-0068/22/06/627-634.

[138] G. Raffaini and F. Ganazzoli. "Molecular dynamics simulation of the adsorption of a fibronectin module on a graphite surface". In: *Langmuir* 20.8 (Apr. 13, 2004), pp. 3371–3378. ISSN: 0743-7463. DOI: 10.1021/La0357716.

[139] A. Hung et al. "Ordering Surfaces on the Nanoscale: Implications for Protein Adsorption". In: *Journal of the American Chemical Society* 133.5 (Feb. 9, 2011), pp. 1438–1450. ISSN: 0002-7863. DOI: 10.1021/ja108285u.

[140] A. M. Jackson, J. W. Myerson, and F. Stellacci. "Spontaneous assembly of subnanometre-ordered domains in the ligand shell of monolayer-protected nanoparticles". In:

Nature Materials 3.5 (May 2004), pp. 330–336. ISSN: 1476-1122. DOI: 10.1038/Nmat1116.

[141] S. Auer, A. Trovato, and M. Vendruscolo. "A Condensation-Ordering Mechanism in Nanoparticle-Catalyzed Peptide Aggregation". In: *Plos Computational Biology* 5.8 (Aug. 2009), pages. ISSN: 1553-734X. DOI: 10.1371/journal.pcbi.1000458.

[142] J. W. Shen et al. "Molecular simulation of protein adsorption and desorption on hydroxyapatite surfaces". In: *Biomaterials* 29.5 (Feb. 2008), pp. 513–532. ISSN: 0142-9612. DOI: 10.1016/j.biomaterials.2007.10.016.

[143] C. C. Chiu et al. "Molecular Dynamics Study of a Carbon Nanotube Binding Reversible Cyclic Peptide". In: *Acs Nano* 4.5 (May 2010), pp. 2539–2546. ISSN: 1936-0851. DOI: 10.1021/Nn901484w.

[144] S. R. Friling, R. Notman, and T. R. Walsh. "Probing diameter-selective solubilisation of carbon nanotubes by reversible cyclic peptides using molecular dynamics simulations". In: *Nanoscale* 2.1 (Jan. 2010), pp. 98–106. ISSN: 2040-3364. DOI: 10.1039/B9nr00226j.

[145] Q. Chen et al. "Energetics investigation on encapsulation of protein/peptide drugs in carbon nanotubes". In: *Journal of Chemical Physics* 131.1 (July 7, 2009), p. 015101. ISSN: 1089-7690 (Electronic) 0021-9606 (Linking). DOI: 10.1063/1.3148025.

[146] K. L. Kilpadi, P.-L. Chang, and S. L. Bellis. "Hydroxylapatite binds more serum proteins, purified integrins, and osteoblast precursor cells than titanium or steel". In: *Journal of biomedical materials research* 57.2 (2001), pp. 258–267.

[147] O. Suzuki et al. "Bone formation enhanced by implanted octacalcium phosphate involving conversion into Ca-deficient hydroxyapatite". In: *Biomaterials* 27.13 (2006), pp. 2671–2681.

[148] X. L. Dong et al. "Understanding adsorption-desorption dynamics of BMP-2 on hydroxyapatite (001) surface". In: *Biophysical Journal* 93.3 (Aug. 2007), pp. 750–759. ISSN: 0006-3495. DOI: 10.1529/biophysj.106.103168.

[149] R. Khan et al. “Nanoparticles in relation to peptide and protein aggregation”. In: *International Journal of Nanomedicine* (Feb. 2014), p. 899. ISSN: 1178-2013. DOI: 10.2147/IJN.S54171.

[150] M. Zhang et al. “Nanomaterials for Reducing Amyloid Cytotoxicity”. In: *Advanced Materials* 25.28 (July 26, 2013), pp. 3780–3801. ISSN: 09359648. DOI: 10.1002/adma.201301210.

[151] C. Li and R. Mezzenga. “The interplay between carbon nanomaterials and amyloid fibrils in bio-nanotechnology”. In: *Nanoscale* (2013). ISSN: 2040-3364, 2040-3372. DOI: 10.1039/c3nr01644g.

[152] S. Supattapone et al. “Branched Polyamines Cure Prion-Infected Neuroblastoma Cells”. In: *Journal of Virology* 75.7 (Apr. 1, 2001). PMID: 11238871, pp. 3453–3461. ISSN: 0022-538X, 1098-5514. DOI: 10.1128/JVI.75.7.3453-3461.2001.

[153] B. Klajnert et al. “Influence of heparin and dendrimers on the aggregation of two amyloid peptides related to Alzheimer’s and prion diseases”. In: *Biochemical and Biophysical Research Communications* 339.2 (Jan. 13, 2006), pp. 577–582. ISSN: 0006-291X. DOI: 10.1016/j.bbrc.2005.11.053.

[154] A. Rekas et al. “PAMAM Dendrimers as Potential Agents against Fibrillation of $\alpha - Synuclein, a Parkinson's Disease - Related Protein$”. In: *Macromolecular Bioscience* 9.3 (2009), pp. 230–238. ISSN: 1616-5195. DOI: 10.1002/mabi.200800242.

[155] K. Milowska, M. Malachowska, and T. Gabryelak. “PAMAM G4 dendrimers affect the aggregation of $\alpha - synuclein$”. In: *International Journal of Biological Macromolecules* 48.5 (June 1, 2011), pp. 742–746. ISSN: 0141-8130. DOI: 10.1016/j.ijbiomac.2011.02.021.

[156] B. Klajnert et al. “Dendrimers reduce toxicity of Aβ 1-28 peptide during aggregation and accelerate fibril formation”. In: *Nanomedicine: Nanotechnology, Biology and Medicine* 8.8 (Nov. 2012), pp. 1372–1378. ISSN: 1549-9634. DOI: 10.1016/j.nano.2012.03.005.

[157] A. Assarsson et al. “Charge Dependent Retardation of Amyloid β Aggregation by Hydrophilic Proteins”. In: *ACS Chemical Neuroscience* 5.4 (2014), pp. 266–274. DOI: 10.1021/cn400124r.

[158] P. M. H. Heegaard et al. “Amyloid aggregates of the prion peptide PrP106–126 are destabilised by oxidation and by the action of dendrimers”. In: *FEBS Letters* 577.1–2 (Nov. 5, 2004), pp. 127–133. ISSN: 0014-5793. DOI: 10.1016/j.febslet.2004.09.073.

[159] L. Giehm et al. “Dendrimers destabilize proteins in a generation-dependent manner involving electrostatic interactions”. In: *Biopolymers* 89.6 (2008), pp. 522–529. ISSN: 1097-0282. DOI: 10.1002/bip.20921.

[160] B. Klajnert, J. Cladera, and M. Bryszewska. “Molecular Interactions of Dendrimers with Amyloid Peptides: pH Dependence”. In: *Biomacromolecules* 7.7 (2006), pp. 2186–2191. ISSN: 1525-7797. DOI: 10.1021/bm060229s.

[161] B. Klajnert et al. “Influence of dendrimer’s structure on its activity against amyloid fibril formation”. In: *Biochemical and Biophysical Research Communications* 345.1 (June 23, 2006), pp. 21–28. ISSN: 0006-291X. DOI: 10.1016/j.bbrc.2006.04.041.

[162] C. Cabaleiro-Lago et al. “Inhibition of IAPP and IAPP(2029) Fibrillation by Polymeric Nanoparticles”. In: *Langmuir* 26.5 (2009), pp. 3453–3461. ISSN: 0743-7463. DOI: 10.1021/la902980d.

[163] C. Cabaleiro-Lago et al. “Inhibition of Amyloid β Protein Fibrillation by Polymeric Nanoparticles”. In: *Journal of the American Chemical Society* 130.46 (2008), pp. 15437–15443. ISSN: 0002-7863. DOI: 10.1021/ja8041806.

[164] O. Szczepankiewicz et al. “Interactions in the native state of monellin, which play a protective role against aggregation”. In: *Molecular BioSystems* 7.2 (2011), p. 521. ISSN: 1742-206X, 1742-2051. DOI: 10.1039/c0mb00155d.

[165] C. Cabaleiro-Lago, O. Szczepankiewicz, and S. Linse. “The Effect of Nanoparticles on Amyloid Aggregation Depends on the Protein Stability and Intrinsic Aggregation Rate”. In: *Langmuir* 28.3 (2011), pp. 1852–1857. ISSN: 0743-7463. DOI: 10.1021/la203078w.

[166] R. Vácha, S. Linse, and M. Lund. "Surface Effects on Aggregation Kinetics of Amyloidogenic Peptides". In: *Journal of the American Chemical Society* 136.33 (Aug. 20, 2014), pp. 11776–11782. ISSN: 0002-7863, 1520-5126. DOI: 10.1021/ja505502e.

[167] C. P. Shaw et al. "Amyloid-Derived Peptide Forms Self-Assembled Monolayers on Gold Nanoparticle with a Curvature-Dependent β-Sheet Structure". In: *ACS Nano* 6.2 (2012), pp. 1416–1426. ISSN: 1936-0851. DOI: 10.1021/nn204214x.

[168] Y.-H. Liao et al. "Negatively Charged Gold Nanoparticles Inhibit Alzheimer's Amyloid-β Fibrillization, Induce Fibril Dissociation, and Mitigate Neurotoxicity". In: *Small* 8.23 (2012), pp. 3631–3639. ISSN: 1613-6829. DOI: 10.1002/smll.201201068.

[169] D. Zhang et al. "Gold Nanoparticles Can Induce the Formation of Protein-based Aggregates at Physiological pH". In: *Nano Letters* 9.2 (2009), pp. 666–671. ISSN: 1530-6984. DOI: 10.1021/nl803054h.

[170] A. Antosova et al. "Anti-amyloidogenic activity of glutathione-covered gold nanoparticles". In: *Materials Science and Engineering: C* 32.8 (Dec. 1, 2012), pp. 2529–2535. ISSN: 0928-4931. DOI: 10.1016/j.msec.2012.07.036.

[171] H.-M. Chan et al. "Effect of surface-functionalized nanoparticles on the elongation phase of $\beta - amyloid(1–40)fibrillogenesis$". In: *Biomaterials* 33.18 (June 2012), pp. 4443–4450. ISSN: 0142-9612. DOI: 10.1016/j.biomaterials.2012.03.024.

[172] M. Hoefling et al. "Interaction of β-Sheet Folds with a Gold Surface". In: *PLoS ONE* 6.6 (June 7, 2011), e20925. DOI: 10.1371/journal.pone.0020925.

[173] I. Lynch, K. A. Dawson, and S. Linse. "Detecting cryptic epitopes created by nanoparticles". In: *Science Signaling* 2006.327 (2006), pe14.

[174] G. Brancolini, D. Toroz, and S. Corni. "Can small hydrophobic gold nanoparticles inhibit β2-microglobulin fibrillation?" In: *Nanoscale* 6.14 (2014), p. 7903. ISSN: 2040-3364, 2040-3372. DOI: 10.1039/c4nr01514b.

[175] L.-Y. Zhang et al. “CdTe quantum dots as a highly selective probe for prion protein detection: Colorimetric qualitative, semi-quantitative and quantitative detection”. In: *Talanta* 83.5 (Feb. 15, 2011), pp. 1716–1720. ISSN: 0039-9140. DOI: 10.1016/j.talanta.2010.11.075.

[176] C. H. Vannoy, J. Xu, and R. M. Leblanc. “Bioimaging and Self-Assembly of Lysozyme Fibrils Utilizing CdSe/ZnS Quantum Dots”. In: *The Journal of Physical Chemistry C* 114.2 (2009), pp. 766–773. ISSN: 1932-7447. DOI: 10.1021/jp907839j.

[177] S. Gupta, P. Babu, and A. Surolia. “Biphenyl ethers conjugated CdSe/ZnS core/shell quantum dots and interpretation of the mechanism of amyloid fibril disruption”. In: *Biomaterials* 31.26 (Sept. 2010), pp. 6809–6822. ISSN: 0142-9612. DOI: 10.1016/j.biomaterials.2010.05.031.

[178] C. H. Vannoy and R. M. Leblanc. “Effects of DHLA-Capped CdSe/ZnS Quantum Dots on the Fibrillation of Human Serum Albumin”. In: *The Journal of Physical Chemistry B* 114.33 (2010), pp. 10881–10888. ISSN: 1520-6106. DOI: 10.1021/jp1045904.

[179] L. Xiao et al. “Inhibition of β1–40*amyloidfibrillationwithN*$-$*acetyl*$-$*l*$-$*cysteinecappedquantumdots*” In: *Biomaterials* 31.1 (Jan. 2010), pp. 91–98. ISSN: 0142-9612. DOI: 10.1016/j.biomaterials.2009.09.014.

[180] A. S. Barnard, S. P. Russo, and I. K. Snook. “Size dependent phase stability of carbon nanoparticles: Nanodiamond versus fullerenes”. In: *The Journal of Chemical Physics* 118.11 (Mar. 15, 2003), pp. 5094–5097. ISSN: 0021-9606, 1089-7690. DOI: 10.1063/1.1545450.

[181] V. N. Mochalin et al. “The properties and applications of nanodiamonds”. In: *Nature Nanotechnology* 7.1 (Jan. 2012), pp. 11–23. ISSN: 1748-3387. DOI: 10.1038/nnano.2011.209.

[182] V. C. Sanchez et al. “Biological Interactions of Graphene-Family Nanomaterials: An Interdisciplinary Review”. In: *Chemical Research in Toxicology* 25.1 (Jan. 13, 2012), pp. 15–34. ISSN: 0893-228X, 1520-5010. DOI: 10.1021/tx200339h.

[183] E. E. Tuppo and L. J. Forman. "Free radical oxidative damage and Alzheimer's disease". In: *JAOA: Journal of the American Osteopathic Association* 101.12 suppl 1 (Dec. 1, 2001), 11S–15S. ISSN: 0098-6151, 1945-1997.

[184] L. L. Dugan et al. "Carboxyfullerenes as neuroprotective agents". In: *Proceedings of the National Academy of Sciences* 94.17 (Aug. 19, 1997), pp. 9434–9439. ISSN: 0027-8424, 1091-6490.

[185] J. E. Kim and M. Lee. "Fullerene inhibits β-amyloid peptide aggregation". In: *Biochemical and Biophysical Research Communications* 303.2 (Apr. 2003), pp. 576–579. ISSN: 0006291X. DOI: 10.1016/S0006-291X(03)00393-0.

[186] C.-M. Lee et al. "C60 fullerene-pentoxifylline dyad nanoparticles enhance autophagy to avoid cytotoxic effects caused by the β-amyloid peptide". In: *Nanomedicine: Nanotechnology, Biology and Medicine* 7.1 (Feb. 2011), pp. 107–114. ISSN: 1549-9634. DOI: 10.1016/j.nano.2010.06.009.

[187] I. Y. Podolski et al. "Effects of Hydrated Forms of C60 Fullerene on Amyloid - Peptide Fibrillization In Vitro and Performance of the Cognitive Task". In: *Journal of Nanoscience and Nanotechnology* 7.4-1 (Apr. 1, 2007), pp. 1479–1485. DOI: 10.1166/jnn.2007.330.

[188] X. Zhou et al. "Interactions of a Water-Soluble Fullerene Derivative with Amyloid-β Protofibrils: Dynamics, Binding Mechanism, and the Resulting Salt-Bridge Disruption". In: *The Journal of Physical Chemistry B* (May 23, 2014). ISSN: 1520-6106. DOI: 10.1021/jp503458w.

[189] P. D. Q. Huy and M. S. Li. "Binding of fullerenes to amyloid $\beta fibrils : sizematters$". In: *Physical Chemistry Chemical Physics* 16.37 (Aug. 7, 2014), p. 20030. ISSN: 1463-9076, 1463-9084. DOI: 10.1039/C4CP02348J.

[190] X. Xue et al. "Single-Walled Carbon Nanotubes Alleviate Autophagic/Lysosomal Defects in Primary Glia from a Mouse Model of Alzheimer's Disease". In: *Nano Letters* 14.9 (2014), pp. 5110–5117. ISSN: 1530-6984. DOI: 10.1021/nl501839q.

[191] A. V. Ghule et al. "Carbon nanotubes prevent 2, 2, 2 trifluoroethanol induced aggregation of protein". In: *Carbon* 45.7 (2007), pp. 1586–1589. ISSN: 0008-6223.

[192] J. Luo et al. "The Aβ peptide forms non-amyloid fibrils in the presence of carbon nanotubes". In: *Nanoscale* 6.12 (2014), p. 6720. ISSN: 2040-3364, 2040-3372. DOI: 10.1039/c4nr00291a.

[193] Z. Fu et al. "Induced β-Barrel Formation of the Alzheimer's Aβ25–35 Oligomers on Carbon Nanotube Surfaces: Implication for Amyloid Fibril Inhibition". In: *Biophysical Journal* 97.6 (Sept. 2009), pp. 1795–1803. ISSN: 00063495. DOI: 10.1016/j.bpj.2009.07.014.

[194] H. Li et al. "Carbon Nanotube Inhibits the Formation of β-Sheet-Rich Oligomers of the Alzheimer's Amyloid-β(16-22) Peptide". In: *Biophysical Journal* 101.9 (Nov. 2011), pp. 2267–2276. ISSN: 00063495. DOI: 10.1016/j.bpj.2011.09.046.

[195] J. Khandogin and C. L. Brooks. "Linking folding with aggregation in Alzheimer's β-amyloid peptides". In: *Proceedings of the National Academy of Sciences* 104.43 (Oct. 23, 2007), pp. 16880–16885. ISSN: 0027-8424, 1091-6490. DOI: 10.1073/pnas.0703832104.

[196] A. T. Petkova et al. "A structural model for Alzheimer's β-amyloid fibrils based on experimental constraints from solid state NMR". In: *Proceedings of the National Academy of Sciences* 99.26 (Dec. 24, 2002), pp. 16742–16747. ISSN: 0027-8424, 1091-6490. DOI: 10.1073/pnas.262663499.

[197] A. K. Jana and N. Sengupta. "Adsorption Mechanism and Collapse Propensities of the Full-Length, Monomeric Aβ1-42 on the Surface of a Single-Walled Carbon Nanotube: A Molecular Dynamics Simulation Study". In: *Biophysical Journal* 102.8 (Apr. 2012), pp. 1889–1896. ISSN: 00063495. DOI: 10.1016/j.bpj.2012.03.036.

[198] A. K. Jana, J. C. Jose, and N. Sengupta. "Critical roles of key domains in complete adsorption of Aβ peptide on single-walled carbon nanotubes: insights with point mutations and MD simulations". In: *Physical Chemistry Chemical Physics* 15.3 (2013), p. 837. ISSN: 1463-9076, 1463-9084. DOI: 10.1039/c2cp42933k.

[199] T. Kowalewski and D. M. Holtzman. "In situ atomic force microscopy study of Alzheimer's β-amyloid peptide on different substrates: new insights into mechanism of β-sheet formation". In: *Proceedings of the National Academy of Sciences* 96.7 (1999), pp. 3688–3693.

[200] J. J. Valle-Delgado et al. “Self-assembly of human amylin-derived peptides studied by atomic force microscopy and single molecule force spectroscopy”. In: *Soft Matter* 8.4 (2012), p. 1234. ISSN: 1744-683X, 1744-6848. DOI: 10.1039/c1sm06764h.

[201] C. L. Brown et al. “Template-Directed Assembly of a de Novo Designed Protein”. In: *Journal of the American Chemical Society* 124.24 (2002), pp. 6846–6848. ISSN: 0002-7863. DOI: 10.1021/ja0261271.

[202] F. T. Arce et al. “Polymorphism of amyloid β peptide in different environments: implications for membrane insertion and pore formation”. In: *Soft Matter* 7.11 (2011), p. 5267. ISSN: 1744-683X, 1744-6848. DOI: 10.1039/c1sm05162h.

[203] D. Losic et al. “β-Amyloid fibril formation is promoted by step edges of highly oriented pyrolytic graphite”. In: *Biopolymers* 84.5 (2006), pp. 519–526. ISSN: 0006-3525, 1097-0282. DOI: 10.1002/bip.20549.

[204] J. Guo et al. “Exploring the Influence of Carbon Nanoparticles on the Formation of β-Sheet-Rich Oligomers of IAPP22–28 Peptide by Molecular Dynamics Simulation”. In: *PLoS ONE* 8.6 (June 5, 2013). Ed. by J. Zheng, e65579. ISSN: 1932-6203. DOI: 10.1371/journal.pone.0065579.

[205] J. Liu et al. “Dewetting transition assisted clearance of (NFGAILS) amyloid fibrils from cell membranes by graphene”. In: *The Journal of Chemical Physics* 141.22 (Dec. 14, 2014), p. 22D520. ISSN: 0021-9606, 1089-7690. DOI: 10.1063/1.4901113.

[206] G. G. Hall. “The Molecular Orbital Theory of Chemical Valency. VIII. A Method of Calculating Ionization Potentials”. In: *Proceedings of the Royal Society of London A: Mathematical, Physical and Engineering Sciences* 205.1083 (Mar. 7, 1951). An analysis of the ’linear combination of atomic orbitals’ approximation using the accurate molecular orbital equations shows that it does not lead to equations of the form usually assumed in the semi-empirical molecular orbital method. A new semi-empirical method is proposed, therefore, in terms of equivalent orbitals. The equations obtained, which do have the usual form, are applicable to a large class of molecules and do not involve the approximations that were thought necessary. In this method the ionization potentials are calculated by treating certain integrals as semi-empirical parameters. The value of these parameters is discussed in terms of

the localization of equivalent orbitals and some approximate rules are suggested. As an illustration the ionization potentials of the paraffin series are considered and good agreement between the observed and calculated values is found., pp. 541–552. ISSN: 0080-4630. DOI: 10.1098/rspa.1951.0048.

[207] C. C. J. Roothaan. "New Developments in Molecular Orbital Theory". In: *Reviews of Modern Physics* 23.2 (Apr. 1, 1951), pp. 69–89. DOI: 10.1103/RevModPhys.23.69.

[208] W. J. Hehre, R. F. Stewart, and J. A. Pople. "SelfConsistent MolecularOrbital Methods. I. Use of Gaussian Expansions of SlaterType Atomic Orbitals". In: *The Journal of Chemical Physics* 51.6 (Sept. 15, 1969), pp. 2657–2664. ISSN: 0021-9606, 1089-7690. DOI: 10.1063/1.1672392.

[209] D. Maurice and M. Head-Gordon. "Analytical second derivatives for excited electronic states using the single excitation configuration interaction method: theory and application to benzo[a]pyrene and chalcone". In: *Molecular Physics* 96.10 (May 20, 1999), pp. 1533–1541. ISSN: 0026-8976. DOI: 10.1080/00268979909483096.

[210] G. D. P. Iii and R. J. Bartlett. "A full coupledcluster singles and doubles model: The inclusion of disconnected triples". In: *The Journal of Chemical Physics* 76.4 (Feb. 15, 1982), pp. 1910–1918. ISSN: 0021-9606, 1089-7690. DOI: 10.1063/1.443164.

[211] C. Møller and M. S. Plesset. "Note on an Approximation Treatment for Many-Electron Systems". In: *Physical Review* 46.7 (Oct. 1, 1934), pp. 618–622. DOI: 10.1103/PhysRev.46.618.

[212] J. A. P. R. Krishnan. "Approximate fourthorder perturbation theory of the electron correlation energy". In: *International Journal of Quantum Chemistry* 14.1 (2004), pp. 91–100. ISSN: 1097-461X. DOI: 10.1002/qua.560140109.

[213] E. R. Johnson and A. D. Becke. "A post-Hartree–Fock model of intermolecular interactions". In: *The Journal of Chemical Physics* 123.2 (July 8, 2005), p. 024101. ISSN: 0021-9606, 1089-7690. DOI: 10.1063/1.1949201.

[214] A. Szabo and N. S. Ostlund. *Modern Quantum Chemistry: Introduction to Advanced Electronic Structure Theory*. Courier Corporation, June 8, 2012. 484 pp. ISBN: 9780486134598.

[215] M. J. S. Spencer, K. W. J. Wong, and I. Yarovsky. "Surface defects on ZnO nanowires: implications for design of sensors". In: *Journal of Physics: Condensed Matter* 24.30 (Aug. 1, 2012), p. 305001. ISSN: 0953-8984. DOI: 10.1088/0953-8984/24/30/305001.

[216] F. Oba et al. "Defect energetics in ZnO: A hybrid Hartree-Fock density functional study". In: *Physical Review B* 77.24 (June 9, 2008), p. 245202. DOI: 10.1103/PhysRevB.77.245202.

[217] J. Paier et al. "${{Cu}}_{2}{{ZnSnS}}_{4}$ as a potential photovoltaic material: A hybrid Hartree-Fock density functional theory study". In: *Physical Review B* 79.11 (Mar. 25, 2009), p. 115126. DOI: 10.1103/PhysRevB.79.115126.

[218] S. Kristyán and P. Pulay. "Can (semi)local density functional theory account for the London dispersion forces?" In: *Chemical Physics Letters* 229.3 (Oct. 28, 1994), pp. 175–180. ISSN: 0009-2614. DOI: 10.1016/0009-2614(94)01027-7.

[219] J. Pérez-Jordá and A. D. Becke. "A density-functional study of van der Waals forces: rare gas diatomics". In: *Chemical Physics Letters* 233.1–2 (Feb. 3, 1995), pp. 134–137. ISSN: 0009-2614. DOI: 10.1016/0009-2614(94)01402-H.

[220] J. Kussmann, M. Beer, and C. Ochsenfeld. "Linear-scaling self-consistent field methods for large molecules". In: *Wiley Interdisciplinary Reviews: Computational Molecular Science* 3.6 (Nov. 1, 2013), pp. 614–636. ISSN: 1759-0884. DOI: 10.1002/wcms.1138.

[221] C. Yam et al. "Linear-scaling quantum mechanical methods for excited states". In: *Chemical Society Reviews* 41.10 (Apr. 30, 2012), pp. 3821–3838. ISSN: 1460-4744. DOI: 10.1039/C2CS15259B.

[222] R. Z. Khaliullin, J. VandeVondele, and J. Hutter. "Efficient Linear-Scaling Density Functional Theory for Molecular Systems". In: *Journal of Chemical Theory and*

Computation 9.10 (Oct. 8, 2013), pp. 4421–4427. ISSN: 1549-9618. DOI: 10.1021/ct400595k.

[223] C. K. Skylaris et al. "Linear-scaling density functional theory with the ONETEP program". In: *Abstracts of Papers of the American Chemical Society* 241 (Mar. 27, 2011). ISSN: 0065-7727.

[224] G. Galli. "Linear scaling methods for electronic structure calculations and quantum molecular dynamics simulations". In: *Current Opinion in Solid State and Materials Science* 1.6 (Dec. 1996), pp. 864–874. ISSN: 1359-0286. DOI: 10.1016/S1359-0286(96)80114-8.

[225] S. Goedecker. "Linear scaling electronic structure methods". In: *Reviews of Modern Physics* 71.4 (July 1, 1999), pp. 1085–1123. DOI: 10.1103/RevModPhys.71.1085.

[226] W. Kohn. "Analytic Properties of Bloch Waves and Wannier Functions". In: *Physical Review* 115.4 (Aug. 15, 1959), pp. 809–821. DOI: 10.1103/PhysRev.115.809.

[227] W. Kohn. "Density Functional and Density Matrix Method Scaling Linearly with the Number of Atoms". In: *Physical Review Letters* 76.17 (Apr. 22, 1996), pp. 3168–3171. DOI: 10.1103/PhysRevLett.76.3168.

[228] R. G. Parr and W. Yang. *Density-Functional Theory of Atoms and Molecules*. Oxford University Press, Apr. 13, 1989. 345 pp. ISBN: 9780195357738.

[229] E. Blount. "Solid State Physics". In: *Academic, New York* 13 (1962), p. 305.

[230] N. Marzari and D. Vanderbilt. "Maximally localized generalized Wannier functions for composite energy bands". In: *Physical Review B* 56.20 (Nov. 15, 1997), pp. 12847–12865. DOI: 10.1103/PhysRevB.56.12847.

[231] C.-K. Skylaris et al. "Nonorthogonal generalized Wannier function pseudopotential plane-wave method". In: *Physical Review B* 66.3 (July 30, 2002), p. 035119. DOI: 10.1103/PhysRevB.66.035119.

[232] C.-K. Skylaris et al. "Accurate kinetic energy evaluation in electronic structure calculations with localized functions on real space grids". In: *Computer Physics Communications* 140.3 (Nov. 1, 2001), pp. 315–322. ISSN: 0010-4655. DOI: 10.1016/S0010-4655(01)00248-X.

[233] R. Baer and M. Head-Gordon. “Sparsity of the Density Matrix in Kohn-Sham Density Functional Theory and an Assessment of Linear System-Size Scaling Methods”. In: *Physical Review Letters* 79.20 (Nov. 17, 1997), pp. 3962–3965. DOI: 10.1103/PhysRevLett.79.3962.

[234] S. Ismail-Beigi and T. Arias. “Locality of the density matrix in metals, semiconductors, and insulators”. In: *arXiv preprint cond-mat/9805147* (1999).

[235] L. He and D. Vanderbilt. “Exponential Decay Properties of Wannier Functions and Related Quantities”. In: *Physical Review Letters* 86.23 (June 4, 2001), pp. 5341–5344. DOI: 10.1103/PhysRevLett.86.5341.

[236] R. McWeeny. “Some recent advances in density matrix theory”. In: *Reviews of Modern Physics* 32.2 (1960), p. 335.

[237] P. D. Haynes and M. C. Payne. “Localised spherical-wave basis set for O(N) total-energy pseudopotential calculations”. In: *Computer Physics Communications* 102.1–3 (May 2, 1997), pp. 17–27. ISSN: 0010-4655. DOI: 10.1016/S0010-4655(97)00028-3.

[238] C. A. White et al. “Linear scaling density functional calculations via the continuous fast multipole method”. In: *Chemical Physics Letters* 253.3–4 (May 3, 1996), pp. 268–278. ISSN: 0009-2614. DOI: 10.1016/0009-2614(96)00175-3.

[239] M. C. Strain, G. E. Scuseria, and M. J. Frisch. “Achieving Linear Scaling for the Electronic Quantum Coulomb Problem”. In: *Science* 271.5245 (Jan. 5, 1996), pp. 51–53. ISSN: 0036-8075, 1095-9203. DOI: 10.1126/science.271.5245.51.

[240] J. M. Soler et al. “The SIESTA method for ab initio order-N materials simulation”. In: *Journal of Physics: Condensed Matter* 14.11 (Mar. 25, 2002), p. 2745. ISSN: 0953-8984. DOI: 10.1088/0953-8984/14/11/302.

[241] E. Schwegler and M. Challacombe. “Linear scaling computation of the Hartree–Fock exchange matrix”. In: *The Journal of Chemical Physics* 105.7 (Aug. 15, 1996), pp. 2726–2734. ISSN: 0021-9606, 1089-7690. DOI: 10.1063/1.472135.

[242] C. K. Skylaris et al. “Using ONETEP for accurate and efficient O(N) density functional calculations”. In: *Journal of Physics-Condensed Matter* 17 (Sept. 21, 2005). 37, pp. 5757–5769. ISSN: 0953-8984. DOI: 10.1088/0953-8984/17/37/012.

[243] K. A. Wilkinson, N. D. M. Hine, and C.-K. Skylaris. “Hybrid MPI-OpenMP Parallelism in the ONETEP Linear-Scaling Electronic Structure Code: Application to the Delamination of Cellulose Nanofibrils”. In: *Journal of Chemical Theory and Computation* 10.11 (Nov. 11, 2014), pp. 4782–4794. ISSN: 1549-9618, 1549-9626. DOI: 10.1021/ct500686r.

[244] W. L. Jorgensen et al. “Comparison of simple potential functions for simulating liquid water”. In: *The Journal of Chemical Physics* 79.2 (July 15, 1983), pp. 926–935. ISSN: 0021-9606, 1089-7690. DOI: 10.1063/1.445869.

[245] H. J. C. Berendsen, J. P. M. Postma, and W. F. VanGunsteren. “Interaction Models for Water in Relation to Protein Hydration”. In: *Intermolecular Forces*. Ed. by B. Pullman. Dordrecht: D. Reidel Publishing Company, 1981, pp. 331–342.

[246] A. D. MacKerell et al. “All-Atom Empirical Potential for Molecular Modeling and Dynamics Studies of Proteins”. In: *The Journal of Physical Chemistry B* 102.18 (1998), pp. 3586–3616. ISSN: 1520-6106. DOI: 10.1021/jp973084f.

[247] W. D. Cornell et al. “A Second Generation Force Field for the Simulation of Proteins, Nucleic Acids, and Organic Molecules”. In: *Journal of the American Chemical Society* 117.19 (1995), pp. 5179–5197. ISSN: 0002-7863. DOI: 10.1021/ja00124a002.

[248] W. L. Jorgensen, D. S. Maxwell, and J. Tirado-Rives. “Development and Testing of the OPLS All-Atom Force Field on Conformational Energetics and Properties of Organic Liquids”. In: *Journal of the American Chemical Society* 118.45 (1996), pp. 11225–11236. ISSN: 0002-7863. DOI: 10.1021/ja9621760.

[249] C. Oostenbrink et al. “A biomolecular force field based on the free enthalpy of hydration and solvation: The GROMOS force-field parameter sets 53A5 and 53A6”. In: *Journal of Computational Chemistry* 25.13 (2004), pp. 1656–1676. ISSN: 1096-987X. DOI: 10.1002/jcc.20090.

[250] L. B. Wright et al. “GolP-CHARMM: First-Principles Based Force Fields for the Interaction of Proteins with Au(111) and Au(100)”. In: *Journal of Chemical Theory and Computation* 9.3 (Mar. 12, 2013), pp. 1616–1630. ISSN: 1549-9618. DOI: 10.1021/ct301018m.

[251] Z. E. Hughes, S. M. Tomásio, and T. R. Walsh. “Efficient simulations of the aqueous bio-interface of graphitic nanostructures with a polarisable model”. In: *Nanoscale* 6.10 (Apr. 23, 2014), pp. 5438–5448. ISSN: 2040-3372. DOI: 10.1039/C4NR00468J.

[252] S. De Miranda Tomásio and T. R. Walsh. “Atomistic modelling of the interaction between peptides and carbon nanotubes”. In: *Molecular Physics* 105.2-3 (2007), pp. 221–229.

[253] H. Sun. “COMPASS: An ab Initio Force-Field Optimized for Condensed-Phase ApplicationsOverview with Details on Alkane and Benzene Compounds”. In: *The Journal of Physical Chemistry B* 102.38 (Sept. 1, 1998), pp. 7338–7364. ISSN: 1520-6106. DOI: 10.1021/jp980939v.

[254] J. R. Maple et al. “Derivation of class II force fields. I. Methodology and quantum force field for the alkyl functional group and alkane molecules”. In: *Journal of Computational Chemistry* 15.2 (Feb. 1, 1994), pp. 162–182. ISSN: 1096-987X. DOI: 10.1002/jcc.540150207.

[255] A. Hung et al. “Lipids enhance apolipoprotein C-II-derived amyloidogenic peptide oligomerization but inhibit fibril formation”. In: *Journal of Physical Chemistry B* 113 (2009), pp. 9447–53.

[256] A. Hung et al. “Effects of oxidation, pH and lipids on amyloidogenic peptide structure: implications for fibril formation?” In: *European Biophysics Journal* 38.1 (2008), pp. 99–110.

[257] N. Todorova, A. Hung, and I. Yarovsky. “Lipid concentration effects on the amyloidogenic apoC-II(60-70) peptide: a computational study”. In: *Journal of Physical Chemistry B* 114 (2010), pp. 7974–82.

[258] N. Todorova et al. “Effects of mutation on the amyloidogenic propensity of apolipoprotein C-II60–70 peptide”. In: *Physical Chemistry Chemical Physics* 12 (2010), p. 14762.

[259] B. G. Dick and A. W. Overhauser. "Theory of the Dielectric Constants of Alkali Halide Crystals". In: *Physical Review* 112.1 (Oct. 1, 1958), pp. 90–103. DOI: 10.1103/PhysRev.112.90.

[260] F. Iori and S. Corni. "Including image charge effects in the molecular dynamics simulations of molecules on metal surfaces". In: *Journal of Computational Chemistry* 29.10 (July 30, 2008), pp. 1656–1666. ISSN: 1096-987X. DOI: 10.1002/jcc.20928.

[261] G. Lamoureux and B. Roux. "Modeling induced polarization with classical Drude oscillators: Theory and molecular dynamics simulation algorithm". In: *The Journal of Chemical Physics* 119.6 (Aug. 8, 2003), pp. 3025–3039. ISSN: 0021-9606, 1089-7690. DOI: 10.1063/1.1589749.

[262] H. Bekker et al. "An Efficient, Box Shape Independent Non-Bonded Force and Virial Algorithm for Molecular Dynamics". In: *Molecular Simulation* 14.3 (Apr. 1, 1995), pp. 137–151. ISSN: 0892-7022. DOI: 10.1080/08927029508022012.

[263] P. P. Ewald. "Die Berechnung optischer und elektrostatischer Gitterpotentiale". In: *Annalen der Physik* 369.3 (1921), pp. 253–287. ISSN: 1521-3889. DOI: 10.1002/andp.19213690304.

[264] T. Darden, D. York, and L. Pedersen. "Particle mesh Ewald: An Nlog(N) method for Ewald sums in large systems". In: *The Journal of Chemical Physics* 98.12 (June 15, 1993), pp. 10089–10092. ISSN: 0021-9606, 1089-7690. DOI: 10.1063/1.464397.

[265] U. Essmann et al. "A smooth particle mesh Ewald method". In: *The Journal of Chemical Physics* 103.19 (Nov. 15, 1995), pp. 8577–8593. ISSN: 0021-9606, 1089-7690. DOI: 10.1063/1.470117.

[266] B. A. Luty, I. G. Tironi, and W. F. v. Gunsteren. "Latticesum methods for calculating electrostatic interactions in molecular simulations". In: *The Journal of Chemical Physics* 103.8 (Aug. 22, 1995), pp. 3014–3021. ISSN: 0021-9606, 1089-7690. DOI: 10.1063/1.470490.

[267] K. Zimmermann. "ORAL: All purpose molecular mechanics simulator and energy minimizer". In: *Journal of Computational Chemistry* 12.3 (Apr. 1, 1991), pp. 310–319. ISSN: 1096-987X. DOI: 10.1002/jcc.540120305.

[268] L. Verlet. “Computer ”Experiments” on Classical Fluids. I. Thermodynamical Properties of Lennard-Jones Molecules”. In: *Physical Review* 159.1 (July 5, 1967), pp. 98–103. DOI: 10.1103/PhysRev.159.98.

[269] R. Hockney, R. Warriner, and M. Reiser. “Two-dimensional particle models in semiconductor-device analysis”. In: *Electronics Letters* 10.23 (1974), p. 484. ISSN: 00135194. DOI: 10.1049/el:19740386.

[270] W. C. Swope et al. “A computer simulation method for the calculation of equilibrium constants for the formation of physical clusters of molecules: Application to small water clusters”. In: *The Journal of Chemical Physics* 76.1 (Jan. 1, 1982), pp. 637–649. ISSN: 0021-9606, 1089-7690. DOI: 10.1063/1.442716.

[271] S. Nosé. “A molecular dynamics method for simulations in the canonical ensemble”. In: *Molecular Physics* 52.2 (1984), pp. 255–268. ISSN: 0026-8976. DOI: 10.1080/00268978400101201.

[272] W. G. Hoover. “Canonical dynamics: Equilibrium phase-space distributions”. In: *Physical Review A* 31.3 (Mar. 1, 1985), pp. 1695–1697. DOI: 10.1103/PhysRevA.31.1695.

[273] H. J. C. Berendsen et al. “Molecular dynamics with coupling to an external bath”. In: *The Journal of Chemical Physics* 81.8 (Oct. 15, 1984), pp. 3684–3690. ISSN: 0021-9606, 1089-7690. DOI: 10.1063/1.448118.

[274] G. Bussi, D. Donadio, and M. Parrinello. “Canonical sampling through velocity rescaling”. In: *The Journal of Chemical Physics* 126.1 (2007), p. 014101. ISSN: 0021-9606, 1089-7690. DOI: 10.1063/1.2408420.

[275] H. J. C. Berendsen et al. “Molecular dynamics with coupling to an external bath”. In: *The Journal of Chemical Physics* 81.8 (Oct. 15, 1984), pp. 3684–3690. ISSN: 0021-9606, 1089-7690. DOI: 10.1063/1.448118.

[276] M. Parrinello and A. Rahman. “Polymorphic transitions in single crystals: A new molecular dynamics method”. In: *Journal of Applied Physics* 52.12 (Dec. 1, 1981), pp. 7182–7190. ISSN: 0021-8979, 1089-7550. DOI: 10.1063/1.328693.

[277] J.-P. Ryckaert, G. Ciccotti, and H. J. C. Berendsen. "Numerical integration of the cartesian equations of motion of a system with constraints: molecular dynamics of n-alkanes". In: *Journal of Computational Physics* 23.3 (Mar. 1977), pp. 327–341. ISSN: 0021-9991. DOI: 10.1016/0021-9991(77)90098-5.

[278] B. Hess et al. "LINCS: a linear constraint solver for molecular simulations". In: *Journal of computational chemistry* 18.12 (1997), pp. 1463–1472. ISSN: 0192-8651.

[279] T. Huber, A. E. Torda, and W. F. v. Gunsteren. "Local elevation: A method for improving the searching properties of molecular dynamics simulation". In: *Journal of Computer-Aided Molecular Design* 8.6 (Dec. 1, 1994), pp. 695–708. ISSN: 0920-654X, 1573-4951. DOI: 10.1007/BF00124016.

[280] H. Grubmüller. "Predicting slow structural transitions in macromolecular systems: Conformational flooding". In: *Physical Review E* 52.3 (Sept. 1, 1995), pp. 2893–2906. DOI: 10.1103/PhysRevE.52.2893.

[281] S. Kirkpatrick and M. Vecchi. "Optimization by simmulated annealing". In: *science* 220.4598 (1983), pp. 671–680. ISSN: 0036-8075.

[282] B. Mao and A. R. Friedman. "Molecular dynamics simulation by atomic mass weighting". In: *Biophysical Journal* 58.3 (Sept. 1990), pp. 803–805. ISSN: 0006-3495.

[283] Y. Okamoto. "Generalized-ensemble algorithms: enhanced sampling techniques for Monte Carlo and molecular dynamics simulations". In: *Journal of Molecular Graphics and Modelling*. Conformational Sampling 22.5 (May 2004), pp. 425–439. ISSN: 1093-3263. DOI: 10.1016/j.jmgm.2003.12.009.

[284] A. Laio and M. Parrinello. "Escaping free-energy minima". In: *Proceedings of the National Academy of Sciences* 99.20 (Oct. 1, 2002), pp. 12562–12566. ISSN: 0027-8424, 1091-6490. DOI: 10.1073/pnas.202427399.

[285] G. M. Torrie and J. P. Valleau. "Nonphysical sampling distributions in Monte Carlo free-energy estimation: Umbrella sampling". In: *Journal of Computational Physics* 23.2 (Feb. 1977), pp. 187–199. ISSN: 0021-9991. DOI: 10.1016/0021-9991(77)90121-8.

[286] Y. Sugita and Y. Okamoto. "Replica-exchange molecular dynamics method for protein folding". In: *Chemical Physics Letters* 314.1–2 (Nov. 26, 1999), pp. 141–151. ISSN: 0009-2614. DOI: 10.1016/S0009-2614(99)01123-9.

[287] P. Raiteri et al. "Efficient Reconstruction of Complex Free Energy Landscapes by Multiple Walkers Metadynamics†". In: *The Journal of Physical Chemistry B* 110.8 (Mar. 1, 2006), pp. 3533–3539. ISSN: 1520-6106. DOI: 10.1021/jp054359r.

[288] G. Bussi et al. "Free-Energy Landscape for β Hairpin Folding from Combined Parallel Tempering and Metadynamics". In: *Journal of the American Chemical Society* 128.41 (Oct. 1, 2006), pp. 13435–13441. ISSN: 0002-7863. DOI: 10.1021/ja062463w.

[289] S. Piana and A. Laio. "A Bias-Exchange Approach to Protein Folding". In: *The Journal of Physical Chemistry B* 111.17 (May 1, 2007), pp. 4553–4559. ISSN: 1520-6106. DOI: 10.1021/jp067873l.

[290] S. Kumar et al. "THE weighted histogram analysis method for free-energy calculations on biomolecules. I. The method". In: *Journal of Computational Chemistry* 13.8 (Oct. 1, 1992), pp. 1011–1021. ISSN: 1096-987X. DOI: 10.1002/jcc.540130812.

[291] N. Metropolis et al. "Equation of State Calculations by Fast Computing Machines". In: *The Journal of Chemical Physics* 21.6 (June 1, 1953), pp. 1087–1092. ISSN: 0021-9606, 1089-7690. DOI: 10.1063/1.1699114.

[292] H. Fukunishi, O. Watanabe, and S. Takada. "On the Hamiltonian replica exchange method for efficient sampling of biomolecular systems: Application to protein structure prediction". In: *The Journal of Chemical Physics* 116.20 (2002), p. 9058. ISSN: 00219606. DOI: 10.1063/1.1472510.

[293] P. Liu et al. "Replica exchange with solute tempering: A method for sampling biological systems in explicit water". In: *Proceedings of the National Academy of Sciences of the United States of America* 102.39 (2005), pp. 13749–13754.

[294] T. Terakawa, T. Kameda, and S. Takada. "On easy implementation of a variant of the replica exchange with solute tempering in GROMACS". In: *Journal of*

Computational Chemistry 32.7 (May 2011), pp. 1228–1234. ISSN: 01928651. DOI: 10.1002/jcc.21703.

[295] M. C. Jong, M. H. Hofker, and L. M. Havekes. "Role of ApoCs in Lipoprotein Metabolism Functional Differences Between ApoC1, ApoC2, and ApoC3". In: *Arteriosclerosis, Thrombosis, and Vascular Biology* 19.3 (Mar. 1, 1999), pp. 472–484. ISSN: 1079-5642, 1524-4636. DOI: 10.1161/01.ATV.19.3.472.

[296] R. J. Havel et al. "Cofactor activity of protein components of human very low density lipoproteins in the hydrolysis of triglycerides by lipoprotein lipase from different sources". In: *Biochemistry* 12.9 (1973), pp. 1828–1833. ISSN: 0006-2960. DOI: 10.1021/bi00733a026.

[297] E. Rh. "Lipoprotein lipase. A multifunctional enzyme relevant to common metabolic diseases." In: *The New England journal of medicine* 320.16 (Apr. 1989), pp. 1060–1068. ISSN: 0028-4793.

[298] A. A. Kei et al. "A review of the role of apolipoprotein C-II in lipoprotein metabolism and cardiovascular disease". In: *Metabolism* 61.7 (July 2012), pp. 906–921. ISSN: 0026-0495. DOI: 10.1016/j.metabol.2011.12.002.

[299] C. L. Teoh et al. "A Structural Model for Apolipoprotein C-II Amyloid Fibrils: Experimental Characterization and Molecular Dynamics Simulations". In: *Journal of Molecular Biology* 405 (2011), pp. 1246–1266.

[300] C. A. MacRaild et al. "NMR structure of human apolipoprotein C-II in the presence of sodium dodecyl sulfate". In: *Biochemistry* 40.18 (2001), pp. 5414–5421.

[301] J. Zdunek et al. "Global structure and dynamics of human apolipoprotein CII in complex with micelles: evidence for increased mobility of the helix involved in the activation of lipoprotein lipase". In: *Biochemistry* 42.7 (2003), pp. 1872–1889.

[302] C. A. MacRaild, G. J. Howlett, and P. R. Gooley. "The structure and interactions of human apolipoprotein C-II in dodecyl phosphocholine". In: *Biochemistry* 43.25 (2004), pp. 8084–8093.

[303] C. E. MacPhee et al. “HelixHelix Association of a Lipid-Bound Amphipathic α-Helix Derived from Apolipoprotein C-II”. In: *Biochemistry* 38.33 (1999), pp. 10878–10884. ISSN: 0006-2960. DOI: 10.1021/bi990726b.

[304] J. P. Segrest et al. “The amphipathic helix in the exchangeable apolipoproteins: a review of secondary structure and function.” In: *Journal of Lipid Research* 33.2 (Feb. 1, 1992), pp. 141–166. ISSN: 0022-2275, 1539-7262.

[305] S. S. Fojo et al. “Donor splice site mutation in the apolipoprotein (Apo) C-II gene (Apo C-IIHamburg) of a patient with Apo C-II deficiency.” In: *Journal of Clinical Investigation* 82.5 (Nov. 1988), pp. 1489–1494. ISSN: 0021-9738.

[306] T. A. Musliner, P. N. Herbert, and E. C. Church. “Activation of lipoprotein lipase by native and acylated peptides of apolipoprotein C-II”. In: *Biochimica et Biophysica Acta (BBA) - Lipids and Lipid Metabolism* 573.3 (June 21, 1979), pp. 501–509. ISSN: 0005-2760. DOI: 10.1016/0005-2760(79)90224-8.

[307] Y. Shen et al. “Functional Analyses of Human Apolipoprotein CII by Site-directed Mutagenesis IDENTIFICATION OF RESIDUES IMPORTANT FOR ACTIVATION OF LIPOPROTEIN LIPASE”. In: *Journal of Biological Chemistry* 277.6 (Feb. 8, 2002), pp. 4334–4342. ISSN: 0021-9258, 1083-351X. DOI: 10.1074/jbc.M105421200.

[308] D. M. Hatters et al. “Human apolipoprotein C-II forms twisted amyloid ribbons and closed loops”. In: *Biochemistry* 39.28 (2000), pp. 8276–8283.

[309] L. A. Medeiros et al. “Fibrillar amyloid protein present in atheroma activates CD36 signal transduction”. In: *Journal of Biological Chemistry* 279.11 (2004), pp. 10643–10648.

[310] C. A. MacRaild et al. “Sedimentation Velocity Analysis of Flexible Macromolecules: Self-Association and Tangling of Amyloid Fibrils”. In: *Biophysical Journal* 84.4 (Apr. 2003), pp. 2562–2569. ISSN: 0006-3495. DOI: 10.1016/S0006-3495(03)75061-9.

[311] K. J. Binger, M. D. Griffin, and G. J. Howlett. “Methionine Oxidation Inhibits Assembly and Promotes Disassembly of Apolipoprotein C-II Amyloid Fibrils†”. In: *Biochemistry* 47.38 (2008), pp. 10208–10217.

[312] D. M. Hatters, A. P. Minton, and G. J. Howlett. “Macromolecular crowding accelerates amyloid formation by human apolipoprotein C-II”. In: *Journal of Biological Chemistry* 277.10 (2002), pp. 7824–7830.

[313] D. M. Hatters, L. J. Lawrence, and G. J. Howlett. “Sub-micellar phospholipid accelerates amyloid formation by apolipoprotein C-II”. In: *FEBS Letters* 494.3 (Apr. 13, 2001), pp. 220–224. ISSN: 0014-5793. DOI: 10.1016/S0014-5793(01)02355-9.

[314] M. D. Griffin et al. “Phospholipid interaction induces molecular-level polymorphism in apolipoprotein C-II amyloid fibrils via alternative assembly pathways”. In: *Journal of Molecular Biology* 375 (2008), pp. 240–56.

[315] C. R. Stewart et al. “Serum amyloid P colocalizes with apolipoproteins in human atheroma: functional implications”. In: *Journal of lipid research* 48.10 (2007), pp. 2162–2171.

[316] F. S. Legge et al. “Effect of Oxidation and Mutation on the Conformational Dynamics and Fibril Assembly of Amyloidogenic Peptides Derived from Apolipoprotein C-II”. In: *The Journal of Physical Chemistry B* 113.42 (Oct. 22, 2009), pp. 14006–14014. ISSN: 1520-6106, 1520-5207. DOI: 10.1021/jp903842u.

[317] L. M. Wilson et al. “A structural core within apolipoprotein C-II amyloid fibrils identified using hydrogen exchange and proteolysis”. In: *Journal of molecular biology* 366.5 (2007), pp. 1639–1651.

[318] M. D. W. Griffin et al. “A Cyclic Peptide Inhibitor of ApoC-II Peptide Fibril Formation: Mechanistic Insight from NMR and Molecular Dynamics Analysis”. In: *Journal of Molecular Biology* 416.5 (Mar. 9, 2012), pp. 642–655. ISSN: 0022-2836. DOI: 10.1016/j.jmb.2011.12.059.

[319] N. Todorova et al. ""Janus" cyclic peptides: a new approach to amyloid fibril inhibition?" In: *Plos One* 8 (2013). 2, e57437. ISSN: 1932-6203 (Electronic) 1932-6203 (Linking). DOI: 10.1371/journal.pone.0057437.

[320] Y. Gogotsi and V. Presser. *Carbon Nanomaterials, Second Edition.* CRC Press, Oct. 24, 2013. 516 pp. ISBN: 9781466502420.

[321] P. J. Krusic et al. "Radical Reactions of C60". In: *Science* 254.5035 (Nov. 22, 1991), pp. 1183–1185. ISSN: 0036-8075, 1095-9203. DOI: 10.1126/science.254.5035.1183.

[322] M.-C. Tsai, Y. H. Chen, and L. Y. Chiang. "Polyhydroxylated C60, Fullerenol, a Novel Free-radical Trapper, Prevented Hydrogen Peroxide- and Cumene Hydroperoxide-elicited Changes in Rat Hippocampus In-vitro". In: *Journal of Pharmacy and Pharmacology* 49.4 (Apr. 1, 1997), pp. 438–445. ISSN: 2042-7158. DOI: 10.1111/j.2042-7158.1997.tb06821.x.

[323] L. Xiao et al. "The water-soluble fullerene derivative 'Radical Sponge®' exerts cytoprotective action against UVA irradiation but not visible-light-catalyzed cytotoxicity in human skin keratinocytes". In: *Bioorganic & Medicinal Chemistry Letters* 16.6 (Mar. 2006), pp. 1590–1595. ISSN: 0960894X. DOI: 10.1016/j.bmcl.2005.12.011.

[324] A. W. Jensen, S. R. Wilson, and D. I. Schuster. "Biological applications of fullerenes". In: *Bioorganic & Medicinal Chemistry* 4.6 (June 1996), pp. 767–779. ISSN: 0968-0896. DOI: 10.1016/0968-0896(96)00081-8.

[325] S. Foley et al. "Cellular localisation of a water-soluble fullerene derivative". In: *Biochemical and Biophysical Research Communications* 294.1 (May 31, 2002), pp. 116–119. ISSN: 0006-291X. DOI: 10.1016/S0006-291X(02)00445-X.

[326] S. Iijima. "Helical microtubules of graphitic carbon". In: *Nature* 354.6348 (Nov. 7, 1991), pp. 56–58. DOI: 10.1038/354056a0.

[327] P. Avouris, M. Freitag, and V. Perebeinos. "Carbon-nanotube photonics and optoelectronics". In: *Nature Photonics* 2.6 (June 2008), pp. 341–350. ISSN: 1749-4885. DOI: 10.1038/nphoton.2008.94.

[328] Y. Gogotsi and V. Presser. *Carbon Nanomaterials, Second Edition*. CRC Press, Oct. 24, 2013. 532 pp. ISBN: 9781439897812.

[329] P. C. Ke and R. Qiao. "Carbon nanomaterials in biological systems". In: *Journal of Physics: Condensed Matter* 19.37 (Sept. 19, 2007), p. 373101. ISSN: 0953-8984, 1361-648X. DOI: 10.1088/0953-8984/19/37/373101.

[330] F. Lu et al. "Advances in Bioapplications of Carbon Nanotubes". In: *Advanced Materials* 21.2 (Jan. 12, 2009), pp. 139–152. ISSN: 1521-4095. DOI: 10.1002/adma.200801491.

[331] B. S. Harrison and A. Atala. "Carbon nanotube applications for tissue engineering". In: *Biomaterials* 28.2 (Jan. 2007), pp. 344–353. ISSN: 01429612. DOI: 10.1016/j.biomaterials.2006.07.044.

[332] J. P. Ryman-Rasmussen et al. "Inhaled carbon nanotubes reach the subpleural tissue in mice". In: *Nature Nanotechnology* 4.11 (Nov. 2009), pp. 747–751. ISSN: 1748-3387, 1748-3395. DOI: 10.1038/nnano.2009.305.

[333] J. Kolosnjaj, H. Szwarc, and F. Moussa. "Toxicity Studies of Carbon Nanotubes". In: *Bio-Applications of Nanoparticles*. Ed. by W. C. W. Chan. Advances in Experimental Medicine and Biology 620. Springer New York, 2007, pp. 181–204. ISBN: 978-0-387-76712-3 978-0-387-76713-0.

[334] A. E. Porter et al. "Direct imaging of single-walled carbon nanotubes in cells". In: *Nature nanotechnology* 2.11 (2007), pp. 713–717.

[335] L. Ma-Hock et al. "Comparative inhalation toxicity of multi-wall carbon nanotubes, graphene, graphite nanoplatelets and low surface carbon black". In: *Particle and fibre toxicology* 10.1 (2013), p. 23.

[336] M. L. Schipper et al. "A pilot toxicology study of single-walled carbon nanotubes in a small sample of mice". In: *Nature nanotechnology* 3.4 (2008), pp. 216–221.

[337] L. A. Mitchell et al. "Mechanisms for how inhaled multiwalled carbon nanotubes suppress systemic immune function in mice". In: *Nature nanotechnology* 4.7 (2009), pp. 451–456.

[338] X. Lu et al. “Tailoring graphite with the goal of achieving single sheets”. In: *Nanotechnology* 10.3 (Sept. 1, 1999), p. 269. ISSN: 0957-4484. DOI: 10.1088/0957-4484/10/3/308.

[339] K. S. Novoselov et al. “Electric Field Effect in Atomically Thin Carbon Films”. In: *Science* 306.5696 (Oct. 22, 2004), pp. 666–669. ISSN: 0036-8075, 1095-9203. DOI: 10.1126/science.1102896.

[340] M. J. Allen, V. C. Tung, and R. B. Kaner. “Honeycomb carbon: a review of graphene”. In: *Chemical reviews* 110.1 (2009), pp. 132–145. ISSN: 0009-2665.

[341] L. Wang, R. A. Friesner, and B. J. Berne. “Replica Exchange with Solute Scaling: A More Efficient Version of Replica Exchange with Solute Tempering (REST2)”. In: *The Journal of Physical Chemistry B* 115.30 (Aug. 4, 2011), pp. 9431–9438. ISSN: 1520-6106, 1520-5207. DOI: 10.1021/jp204407d.

[342] S. Agarwal et al. “Interfacing Live Cells with Nanocarbon Substrates”. In: *Langmuir* 26.4 (Feb. 16, 2010), pp. 2244–2247. ISSN: 0743-7463. DOI: 10.1021/la9048743.

[343] N. V. S. Vallabani et al. “Toxicity of Graphene in Normal Human Lung Cells (BEAS-2B)”. In: *Journal of Biomedical Nanotechnology* 7.1 (Jan. 1, 2011), pp. 106–107. DOI: 10.1166/jbn.2011.1224.

[344] M. C. Duch et al. “Minimizing Oxidation and Stable Nanoscale Dispersion Improves the Biocompatibility of Graphene in the Lung”. In: *Nano Letters* 11.12 (Dec. 14, 2011), pp. 5201–5207. ISSN: 1530-6984. DOI: 10.1021/nl202515a.

[345] A. Schinwald et al. “Graphene-Based Nanoplatelets: A New Risk to the Respiratory System as a Consequence of Their Unusual Aerodynamic Properties”. In: *ACS Nano* 6.1 (Jan. 24, 2012), pp. 736–746. ISSN: 1936-0851. DOI: 10.1021/nn204229f.

[346] C. Chung et al. “Biomedical Applications of Graphene and Graphene Oxide”. In: *Accounts of Chemical Research* 46.10 (Oct. 15, 2013), pp. 2211–2224. ISSN: 0001-4842. DOI: 10.1021/ar300159f.

[347] X. Hu and Q. Zhou. “Health and Ecosystem Risks of Graphene”. In: *Chemical Reviews* 113.5 (May 8, 2013), pp. 3815–3835. ISSN: 0009-2665. DOI: 10.1021/cr300045n.

[348] W. Bao et al. “Controlled ripple texturing of suspended graphene and ultrathin graphite membranes”. In: *Nature Nanotechnology* 4.9 (Sept. 2009), pp. 562–566. ISSN: 1748-3387, 1748-3395. DOI: 10.1038/nnano.2009.191.

[349] J. C. Meyer et al. “The structure of suspended graphene sheets”. In: *Nature* 446.7131 (Mar. 1, 2007), pp. 60–63. ISSN: 0028-0836, 1476-4687. DOI: 10.1038/nature05545.

[350] C. Cabaleiro-Lago, O. Szczepankiewicz, and S. Linse. “The Effect of Nanoparticles on Amyloid Aggregation Depends on the Protein Stability and Intrinsic Aggregation Rate”. In: *Langmuir* 28.3 (Jan. 24, 2012), pp. 1852–1857. ISSN: 0743-7463, 1520-5827. DOI: 10.1021/la203078w.

[351] R. Cukalevski et al. “Structural Changes in Apolipoproteins Bound to Nanoparticles”. In: *Langmuir* 27.23 (Dec. 6, 2011), pp. 14360–14369. ISSN: 0743-7463, 1520-5827. DOI: 10.1021/la203290a.

[352] M. Mahmoudi et al. “The Protein Corona Mediates the Impact of Nanomaterials and Slows Amyloid Beta Fibrillation”. In: *ChemBioChem* 14.5 (2013), pp. 568–572.

[353] R. de la Rica and H. Matsui. “Applications of peptide and protein-based materials in bionanotechnology”. In: *Chemical Society Reviews* 39.9 (2010), p. 3499. ISSN: 0306-0012, 1460-4744. DOI: 10.1039/b917574c.

[354] M. Mahmoudi et al. “ProteinNanoparticle Interactions: Opportunities and Challenges”. In: *Chemical Reviews* 111.9 (Sept. 14, 2011), pp. 5610–5637. ISSN: 0009-2665, 1520-6890. DOI: 10.1021/cr100440g.

[355] S. A. Love et al. “Assessing Nanoparticle Toxicity”. In: *Annual Review of Analytical Chemistry* 5.1 (July 19, 2012), pp. 181–205. ISSN: 1936-1327, 1936-1335. DOI: 10.1146/annurev-anchem-062011-143134.

[356] M. van der Zande et al. “Carbon Nanotubes in Animal Models: A Systematic Review on Toxic Potential”. In: *Tissue Engineering Part B: Reviews* 17.1 (Feb. 2011), pp. 57–69. ISSN: 1937-3368, 1937-3376. DOI: 10.1089/ten.teb.2010.0472.

[357] J. Kayat et al. “Pulmonary toxicity of carbon nanotubes: a systematic report”. In: *Nanomedicine: Nanotechnology, Biology and Medicine* 7.1 (Feb. 2011), pp. 40–49. ISSN: 15499634. DOI: 10.1016/j.nano.2010.06.008.

[358] S.-T. Yang et al. “Biosafety and Bioapplication of Nanomaterials by Designing Protein-Nanoparticle Interactions”. In: *Small* (Jan. 23, 2013), n/a–n/a. ISSN: 16136810. DOI: 10.1002/smll.201201492.

[359] M. P. Monopoli et al. “Biomolecular coronas provide the biological identity of nanosized materials”. In: *Nature Nanotechnology* 7.12 (Dec. 5, 2012), pp. 779–786. ISSN: 1748-3387, 1748-3395. DOI: 10.1038/nnano.2012.207.

[360] A. Gajewicz et al. “Advancing risk assessment of engineered nanomaterials: Application of computational approaches”. In: *Advanced Drug Delivery Reviews* 64.15 (Dec. 2012), pp. 1663–1693. ISSN: 0169409X. DOI: 10.1016/j.addr.2012.05.014.

[361] A. J. Makarucha, N. Todorova, and I. Yarovsky. “Nanomaterials in biological environment: a review of computer modelling studies”. In: *European Biophysics Journal* 40 (2010), pp. 103–115.

[362] G. Zuo et al. “Interactions Between Proteins and Carbon-Based Nanoparticles: Exploring the Origin of Nanotoxicity at the Molecular Level”. In: *Small* (Oct. 5, 2012), n/a–n/a. ISSN: 16136810. DOI: 10.1002/smll.201201381.

[363] A. Albanese, P. S. Tang, and W. C. Chan. “The Effect of Nanoparticle Size, Shape, and Surface Chemistry on Biological Systems”. In: *Annual Review of Biomedical Engineering* 14.1 (Aug. 15, 2012), pp. 1–16. ISSN: 1523-9829, 1545-4274. DOI: 10.1146/annurev-bioeng-071811-150124.

[364] D et al. “The interaction of C60 and its derivatives with a lipid bilayer via molecular dynamics simulations”. In: *Nanotechnology* 20 (2009), p. 115102.

[365] G. Zuo et al. “Adsorption of Villin Headpiece onto Graphene, Carbon Nanotube, and C60: Effect of Contacting Surface Curvatures on Binding Affinity”. In: *The Journal of Physical Chemistry C* 115.47 (Dec. 2011), pp. 23323–23328. ISSN: 1932-7447, 1932-7455. DOI: 10.1021/jp208967t.

[366] A. A. Shvedova et al. “Mechanisms of carbon nanotube-induced toxicity: Focus on oxidative stress”. In: *Toxicology and Applied Pharmacology* 261.2 (June 2012), pp. 121–133. ISSN: 0041008X. DOI: 10.1016/j.taap.2012.03.023.

[367] V. L. Colvin and K. M. Kulinowski. "Nanoparticles as catalysts for protein fibrillation". In: *Proceedings of the National Academy of Sciences of the United States of America* 104 (May 22, 2007). 21, pp. 8679–8680. ISSN: 0027-8424. DOI: 10.1073/pnas.0703194104.

[368] M. Zhu. "Surface-catalyzed Amyloid Fibril Formation". In: *Journal of Biological Chemistry* 277.52 (Sept. 27, 2002), pp. 50914–50922. ISSN: 00219258, 1083351X. DOI: 10.1074/jbc.M207225200.

[369] A. Hung et al. "Amphiphilic amino acids: a key to adsorbing proteins to nanopatterned surfaces?" In: *Chemical Science* 4 (2013). 3, p. 928. ISSN: 2041-6520 2041-6539. DOI: 10.1039/c2sc21639f.

[370] A. Hung et al. "Ordering Surfaces on the Nanoscale: Implications for Protein Adsorption". In: *Journal of the American Chemical Society* 133.5 (Feb. 9, 2011), pp. 1438–1450. ISSN: 0002-7863, 1520-5126. DOI: 10.1021/ja108285u.

[371] T. R. Walsh. "Modelling the nanoscale patterning of nucleic acid base pairs deposited on graphite". In: *Molecular Physics* 106.12 (June 2008), pp. 1613–1619. ISSN: 0026-8976. DOI: 10.1080/00268970802225533.

[372] F. Iori et al. "GolP: An atomistic force-field to describe the interaction of proteins with Au(111) surfaces in water". In: *Journal of Computational Chemistry* 30.9 (July 15, 2009), pp. 1465–1476. ISSN: 1096-987X. DOI: 10.1002/jcc.21165.

[373] C. A. MacRaild et al. "NMR structure of human apolipoprotein C-II in the presence of sodium dodecyl sulfate". In: *Biochemistry* 40 (2001), pp. 5414–21.

[374] C. A. MacRaild, G. J. Howlett, and P. R. Gooley. "The structure and interactions of human apolipoprotein C-II in dodecyl phosphocholine". In: *Biochemistry* 43 (2004), pp. 8084–93.

[375] Q. Sun et al. "Long-term Air Pollution Exposure and Acceleration of Atherosclerosis and Vascular Inflammation in an Animal Model". In: *JAMA: The Journal of the American Medical Association* 294.23 (Dec. 21, 2005), pp. 3003–3010. DOI: 10.1001/jama.294.23.3003.

[376] L. K. Vesterdal et al. “Modest vasomotor dysfunction induced by low doses of C60 fullerenes in apolipoprotein E knockout mice with different degree of atherosclerosis”. In: *Particle and Fibre Toxicology* 6 (), pp. 5–5. DOI: 10.1186/1743-8977-6-5.

[377] S. M. Tomásio and T. R. Walsh. “Modeling the Binding Affinity of Peptides for Graphitic Surfaces. Influences of Aromatic Content and Interfacial Shape”. In: *The Journal of Physical Chemistry C* 113.20 (May 21, 2009), pp. 8778–8785. ISSN: 1932-7447, 1932-7455. DOI: 10.1021/jp8087594.

[378] D. Van Der Spoel et al. “GROMACS: fast, flexible, and free”. In: *J Comput Chem* 26.16 (Dec. 2005), pp. 1701–18.

[379] T. E. CHEATHAM et al. “MOLECULAR-DYNAMICS SIMULATIONS ON SOLVATED BIOMOLECULAR SYSTEMS - THE PARTICLE MESH EWALD METHOD LEADS TO STABLE TRAJECTORIES OF DNA, RNA, AND PROTEINS”. In: *Journal of the American Chemical Society* 117.14 (1995), pp. 4193–4194.

[380] E. Neria, S. Fischer, and M. Karplus. “Simulation of activation free energies in molecular systems”. In: *The Journal of Chemical Physics* 105.5 (Aug. 1, 1996), pp. 1902–1921. ISSN: 0021-9606, 1089-7690. DOI: 10.1063/1.472061.

[381] A. D. MacKerell et al. “All-Atom Empirical Potential for Molecular Modeling and Dynamics Studies of Proteins”. In: *The Journal of Physical Chemistry B* 102.18 (Apr. 1, 1998), pp. 3586–3616. ISSN: 1520-6106. DOI: 10.1021/jp973084f.

[382] S. Piana, K. Lindorff-Larsen, and D. E. Shaw. “How Robust Are Protein Folding Simulations with Respect to Force Field Parameterization?” In: *Biophysical Journal* 100.9 (May 4, 2011), pp. L47–L49. ISSN: 0006-3495. DOI: 10.1016/j.bpj.2011.03.051.

[383] W. G. Hoover. “Canonical dynamics: Equilibrium phase-space distributions”. In: *Physical Review A* 31.3 (Mar. 1, 1985), pp. 1695–1697. DOI: 10.1103/PhysRevA.31.1695.

[384] W. Humphrey, A. Dalke, and K. Schulten. “VMD: Visual molecular dynamics”. In: *Journal of Molecular Graphics* 14.1 (1996), pp. 33–&.

[385] B. Roux. “The Calculation of the Potential of Mean Force Using Computer-Simulations”. In: *Computer Physics Communications* 91 (Sept. 1995). 1-3, pp. 275–282. ISSN: 0010-4655.

[386] G. Lever et al. “Electrostatic considerations affecting the calculated HOMO–LUMO gap in protein molecules”. In: *Journal of Physics: Condensed Matter* 25.15 (Apr. 17, 2013), p. 152101. ISSN: 0953-8984, 1361-648X. DOI: 10.1088/0953-8984/25/15/152101.

[387] D. J. Cole et al. “Interrogation of the Protein-Protein Interactions between Human BRCA2 BRC Repeats and RAD51 Reveals Atomistic Determinants of Affinity”. In: *PLoS Computational Biology* 7.7 (July 14, 2011). Ed. by S. C. Kowalczykowski, e1002096. ISSN: 1553-7358. DOI: 10.1371/journal.pcbi.1002096.

[388] J. Dziedzic et al. “Large-scale DFT calculations in implicit solvent-A case study on the T4 lysozyme L99A/M102Q protein”. In: *International Journal of Quantum Chemistry* 113.6 (Mar. 15, 2013), pp. 771–785. ISSN: 00207608. DOI: 10.1002/qua.24075.

[389] L. P. Lee et al. “Natural bond orbital analysis in the ONETEP code: Applications to large protein systems”. In: *Journal of Computational Chemistry* 34.6 (Mar. 5, 2013), pp. 429–444. ISSN: 01928651. DOI: 10.1002/jcc.23150.

[390] N. Hine et al. “Linear-scaling density-functional theory with tens of thousands of atoms: Expanding the scope and scale of calculations with ONETEP”. In: *Computer Physics Communications* 180.7 (July 2009), pp. 1041–1053. ISSN: 00104655. DOI: 10.1016/j.cpc.2008.12.023.

[391] A. A. Mostofi et al. “Preconditioned iterative minimization for linear-scaling electronic structure calculations”. In: *Journal of Chemical Physics* 119 (Nov. 1, 2003). 17, pp. 8842–8848. ISSN: 0021-9606. DOI: 10.1063/1.1613633.

[392] J. P. Perdew, K. Burke, and M. Ernzerhof. “Generalized Gradient Approximation Made Simple”. In: *Physical Review Letters* 77.18 (Oct. 28, 1996), p. 3865. DOI: 10.1103/PhysRevLett.77.3865.

[393] Q. Hill and C.-K. Skylaris. “Including dispersion interactions in the ONETEP program for linear-scaling density functional theory calculations”. In: *Proceedings of the Royal Society A: Mathematical, Physical and Engineering Sciences* 465.2103 (Mar. 8, 2009), pp. 669–683. ISSN: 1364-5021, 1471-2946. DOI: 10.1098/rspa.2008.0398.

[394] S. Ehrlich, J. Moellmann, and S. Grimme. “Dispersion-Corrected Density Functional Theory for Aromatic Interactions in Complex Systems”. In: *Accounts of Chemical Research* 46.4 (Apr. 16, 2013), pp. 916–926. ISSN: 0001-4842, 1520-4898. DOI: 10.1021/ar3000844.

[395] J. Antony and S. Grimme. “Fully ab initio protein-ligand interaction energies with dispersion corrected density functional theory”. In: *Journal of Computational Chemistry* 33.21 (Aug. 5, 2012), pp. 1730–1739. ISSN: 01928651. DOI: 10.1002/jcc.23004.

[396] G. B. McGaughey, M. Gagne, and A. K. Rappe. “pi-stacking interactions - Alive and well in proteins”. In: *Journal of Biological Chemistry* 273 (June 19, 1998). 25, pp. 15458–15463. ISSN: 0021-9258.

[397] D. Frishman and P. Argos. “Knowledge-based protein secondary structure assignment”. In: *Proteins: Structure, Function, and Genetics* 23 (Dec. 1995). 4, pp. 566–579. ISSN: 0887-3585.

[398] S. A. Andujar et al. “Amyloid-β fibril disruption by C60-molecular guidance for rational drug design”. In: *Physical Chemistry Chemical Physics* 14.24 (2012), p. 8599. ISSN: 1463-9076, 1463-9084. DOI: 10.1039/c2cp40680b.

[399] G. Zuo et al. “Plugging into Proteins: Poisoning Protein Function by a Hydrophobic Nanoparticle”. In: *ACS Nano* 4.12 (Dec. 28, 2010), pp. 7508–7514. ISSN: 1936-0851, 1936-086X. DOI: 10.1021/nn101762b.

[400] A. d. Leon, A. F. Jalbout, and V. A. Basiuk. “Fullerene–amino acid interactions. A theoretical study”. In: *Chemical Physics Letters* 452.4-6 (Feb. 2008), pp. 306–314. ISSN: 00092614. DOI: 10.1016/j.cplett.2007.12.065.

[401] A. de Leon, A. F. Jalbout, and V. A. Basiuk. “SWNT–amino acid interactions: A theoretical study”. In: *Chemical Physics Letters* 457.1-3 (May 2008), pp. 185–190. ISSN: 00092614. DOI: 10.1016/j.cplett.2008.03.079.

[402] Z. E. Hughes and T. R. Walsh. “What makes a good graphene-binding peptide? Adsorption of amino acids and peptides at aqueous graphene interfaces”. In: *Journal of Materials Chemistry B* (Feb. 27, 2015). ISSN: 2050-7518. DOI: 10.1039/C5TB00004A.

[403] A. K. Chamberlain et al. “Snorkeling Preferences Foster an Amino Acid Composition Bias in Transmembrane Helices”. In: *Journal of Molecular Biology* 339.2 (May 2004), pp. 471–479. ISSN: 00222836. DOI: 10.1016/j.jmb.2004.03.072.

[404] J. P. Segrest et al. “Amphipathic Helix Motif - Classes and Properties”. In: *Proteins-Structure Function and Genetics* 8 (1990). 2, pp. 103–117. ISSN: 0887-3585. DOI: 10.1002/prot.340080202.

[405] V. Z. Poenitzsch et al. “Effect of electron-donating and electron-withdrawing groups on peptide/single-walled carbon nanotube interactions”. In: *Journal of the American Chemical Society* 129 (Nov. 28, 2007). 47, pp. 14724–14732. ISSN: 0002-7863. DOI: 10.1021/ja0750827.

[406] A. Hung et al. “Amphiphilic amino acids: a key to adsorbing proteins to nanopatterned surfaces?” In: *Chemical Science* 4.3 (Feb. 4, 2013), pp. 928–937. ISSN: 2041-6539. DOI: 10.1039/C2SC21639F.

[407] A. A. Skelton, T. Liang, and T. R. Walsh. “Interplay of Sequence, Conformation, and Binding at the PeptideTitania Interface as Mediated by Water”. In: *ACS Applied Materials & Interfaces* 1.7 (July 29, 2009), pp. 1482–1491. ISSN: 1944-8244, 1944-8252. DOI: 10.1021/am9001666.

[408] M. J. Penna, M. Mijajlovic, and M. J. Biggs. “Molecular-Level Understanding of Protein Adsorption at the Interface between Water and a Strongly Interacting Uncharged Solid Surface”. In: *Journal of the American Chemical Society* 136.14 (Apr. 9, 2014), pp. 5323–5331. ISSN: 0002-7863, 1520-5126. DOI: 10.1021/ja411796e.

[409] M. J. Penna et al. “Molecular-level understanding of the adsorption mechanism of a graphite-binding peptide at the water/graphite interface”. In: *Soft Matter* (Apr. 29, 2015). ISSN: 1744-6848. DOI: 10.1039/C5SM00123D.

[410] S. Pronk et al. “GROMACS 4.5: a high-throughput and highly parallel open source molecular simulation toolkit”. In: *Bioinformatics (Oxford, England)* 29.7 (Apr. 1, 2013), pp. 845–854. ISSN: 1367-4811. DOI: 10.1093/bioinformatics/btt055.

[411] S. Reißer et al. “3D Hydrophobic Moment Vectors as a Tool to Characterize the Surface Polarity of Amphiphilic Peptides”. In: *Biophysical Journal* 106.11 (Mar. 6, 2014), pp. 2385–2394. ISSN: 0006-3495. DOI: 10.1016/j.bpj.2014.04.020.

[412] W. Lv et al. “Interlayer Water Regulates the Bio-nano Interface of a β-sheet Protein stacking on Graphene”. In: *Scientific Reports* 5 (Jan. 5, 2015). DOI: 10.1038/srep07572.

[413] Y. Bram et al. “Monitoring and Targeting the Initial Dimerization Stage of Amyloid Self-Assembly”. In: *Angewandte Chemie International Edition* (Dec. 22, 2014), n/a–n/a. ISSN: 14337851. DOI: 10.1002/anie.201408744.

[414] A. Laio and F. L. Gervasio. “Metadynamics: a method to simulate rare events and reconstruct the free energy in biophysics, chemistry and material science”. In: *Reports on Progress in Physics* 71.12 (Dec. 1, 2008), p. 126601. ISSN: 0034-4885. DOI: 10.1088/0034-4885/71/12/126601.

[415] R. Kumari, R. Kumar, and A. Lynn. “g_mmpbsa—A GROMACS Tool for High-Throughput MM-PBSA Calculations”. In: *Journal of Chemical Information and Modeling* 54.7 (July 28, 2014), pp. 1951–1962. ISSN: 1549-9596. DOI: 10.1021/ci500020m.

[416] N. Homeyer and H. Gohlke. “Free Energy Calculations by the Molecular Mechanics PoissonBoltzmann Surface Area Method”. In: *Molecular Informatics* 31.2 (2012), pp. 114–122. ISSN: 1868-1751. DOI: 10.1002/minf.201100135.

[417] C. L. Teoh, M. D. W. Griffin, and G. J. Howlett. “Apolipoproteins and amyloid fibril formation in atherosclerosis”. In: *Protein & Cell* 2.2 (Mar. 12, 2011), pp. 116–127. ISSN: 1674-800X, 1674-8018. DOI: 10.1007/s13238-011-1013-6.

[418] L. E. Buchanan et al. “Mechanism of IAPP amyloid fibril formation involves an intermediate with a transient -sheet”. In: *Proceedings of the National Academy of Sciences* 110.48 (Nov. 26, 2013), pp. 19285–19290. ISSN: 0027-8424, 1091-6490. DOI: 10.1073/pnas.1314481110.

[419] J. Zhao et al. “Efficient preparation of large-area graphene oxide sheets for transparent conductive films”. In: *Acs Nano* 4.9 (2010), pp. 5245–5252.

[420] W. Hu et al. “Graphene-Based Antibacterial Paper”. In: *ACS Nano* 4.7 (July 27, 2010), pp. 4317–4323. ISSN: 1936-0851. DOI: 10.1021/nn101097v.

[421] J. Kim et al. “Graphene Oxide Sheets at Interfaces”. In: *Journal of the American Chemical Society* 132.23 (June 16, 2010), pp. 8180–8186. ISSN: 0002-7863. DOI: 10.1021/ja102777p.

[422] M. Mahmoudi et al. “Graphene oxide strongly inhibits amyloid beta fibrillation”. In: *Nanoscale* 4.23 (2012), p. 7322. ISSN: 2040-3364, 2040-3372. DOI: 10.1039/c2nr31657a.

[423] J. Wang et al. “Size Effect of Graphene Oxide on Modulating Amyloid Peptide Assembly”. In: *Chemistry - A European Journal* 21.27 (June 26, 2015), pp. 9632–9637. ISSN: 09476539. DOI: 10.1002/chem.201500577.

[424] Q. Peng et al. “New materials graphyne, graphdiyne, graphone, and graphane: review of properties, synthesis, and application in nanotechnology”. In: *Nanotechnology, Science and Applications* 7 (Apr. 10, 2014), pp. 1–29. ISSN: 1177-8903. DOI: 10.2147/NSA.S40324.

[425] P. Cao, A. Abedini, and D. P. Raleigh. “Aggregation of islet amyloid polypeptide: from physical chemistry to cell biology”. In: *Current opinion in structural biology* 23.1 (2013), pp. 82–89.

[426] J. A. Williamson and A. D. Miranker. “Direct detection of transient -helical states in islet amyloid polypeptide”. In: *Protein Science* 16.1 (2007), pp. 110–117.

[427] I. T. Yonemoto et al. “Amylin proprotein processing generates progressively more amyloidogenic peptides that initially sample the helical state†”. In: *Biochemistry* 47.37 (2008), pp. 9900–9910.

[428] A. S. Reddy et al. “Stable and metastable states of human amylin in solution”. In: *Biophysical journal* 99.7 (2010), pp. 2208–2216.

[429] Q. Qiao, G. R. Bowman, and X. Huang. “Dynamics of an intrinsically disordered protein reveal metastable conformations that potentially seed aggregation”. In: *Journal of the American Chemical Society* 135.43 (2013), pp. 16092–16101.

[430] N. F. Dupuis et al. “Human islet amyloid polypeptide monomers form ordered -hairpins: a possible direct amyloidogenic precursor”. In: *Journal of the American Chemical Society* 131.51 (2009), pp. 18283–18292.